UNIVERSIDAD COMPLUTENSE DE MADRID
FACULTAD DE CIENCIAS FÍSICAS

TESIS DOCTORAL

Transporte cuántico en materiales de Dirac bajo campos externos y desorden

Quantum transport in Dirac materials under external fields and disorder

MEMORIA PARA OPTAR AL GRADO DE

DOCTORA PRESENTADA POR

Yuriko Caterina Baba

Directores

Rafael A. Molina Fernández
Francisco Domínguez-Adame Acosta

Madrid

UNIVERSIDAD COMPLUTENSE DE MADRID
FACULTAD DE CIENCIAS FÍSICAS

TESIS DOCTORAL

Transporte cuántico en materiales de Dirac bajo campos externos y desorden
Quantum transport in Dirac materials under external fields and disorder

MEMORIA PARA OPTAR AL GRADO DE DOCTORA

PRESENTADA POR

Yuriko Caterina Baba

DIRECTORES

Rafael A. Molina Fernández
Francisco Domínguez-Adame Acosta

ACKNOWLEDGEMENTS

It goes without saying that this thesis would not have been possible without the constant support of many people who, with their love, time, and dedication, have accompanied me throughout this long process. Even if the thesis is written in english, I will switch languages in the acknowledgements to spanish, except for the international collaborators of course.

En primer lugar, me gustaría agradecer a mis directores, cuya ayuda ha sido esencial en la realización de esta tesis. Francisco Domínguez-Adame Acosta y Rafael A. Molina Fernández, gracias por las discusiones científicas, por la paciencia y por vuestra guía. Gracias a todo el grupo QNG de la UCM y al Condensed Matter Theory Group del IEM por las interesantes discusiones científicas y el ambiente inmejorable y, en especial, a Leonor Chico, Elena Díaz, Andrey Malyshev, Olga Arroyo, Enrique Benito, Marta García. Gracias a los antiguos miembros de QNG Marta Saiz y Álvaro Díaz, que me ayudaron en mis primeros proyectos científicos y a Irián Sánchez y Carolina Martínez, dos soles con los que tuve el honor de trabajar (¡Mucha suerte con la tesis!). Quiero agradecer especialmente también a Gloria Platero y al grupo de Nanotecnología de la Universidad de Salamanca, Enrique Diez y Mario Amado por las interesantes colaboraciones y por recibirme siempre con la más cálida bienvenida.

Next, I would like to express my gratitude to the Klaus Richter group in Regensburg University for making my stay there an excellent experience. Klaus Richter, Juan Diego Urbina and Angelika Knothe, thank you for your warm welcome. Vanessa Junk, Wolfgang Hogger (and Alex!) and Alexander Riedel, thank you for the patience, the scientific discussions and the hearty welcome. Lukas, Florian, thank you for hosting me in the office and making me feel at home. Jacob, thank you for the cakes, the music and the conversations. Thanks to Jordi Picó for the coffees and the walks near the Donau. Michael, Maxi, Fabian, Georg, Mathias, Torsten, Denis... Thank you all for your hospitality.

Y de vuelta al español... me gustaría dar las gracias a mi familia por apoyarme incansablemente en todo momento: a mis padres Emilia y Kenji y a Keiko por aguantarme estresada y animarme a seguir siempre con mis proyectos. Gracias a Manuel por estar a mi lado, soportar mis excentricidades y por reconfortarme siempre. Gracias a mis maestros (y queridísimos amigos) Elena R. Chamón, Cristina Aguilar y Yuri Ananiev por su pasión por enseñarme y por la inmensa dedicación.

No puede faltar un agradecimiento a mis amigos. Empezaré por orden (geográfico) desde mi escritorio en la Facultad hacia el exterior, ¡así que ya sabéis cuál es el criterio de ordenación! Gracias a mis amigos físicos Jesús Mateos, Beatriz Rodríguez, Javier García; y a las nuevas incorporaciones Dunkan Martínez y Sandra López por aguantarme todos los días (¡No es tarea fácil!), por los cafés y los planes. Gracias a Sofía Mañero, Carmen Hernández, Violeta Carballo por los desayunos, las conversaciones y las recomendaciones en todo momento. ¡Gracias por estar siempre cerca de mí! Gracias a mis amigos físicos de la carrera, ahora desperdigados por el mundo, pero antes tan cerquita de la UCM siempre, a Fernando Alvarado, Beatriz Arregui, Francisco Arizo, Ana Contreras, Álvaro Espada, Ángel Rojas... A María Hita, Diego García y a Teresa Palomo por hacer de Noviciado un piso encantador y acogedor. Gracias a mis amigos músicos por la buena música y los buenos ratos: Jaime Augusto Serrano por tu incansable energía y proyectos; Marta Lorenzana por las meriendas y los viajes; Pablo Calderón por las cenas y los paseos; Alberto Molina por ser un sol. Gracias a mis amigos amanielos Ángel, Elena, Jaime, Cecilia, Álvaro. En definitiva, gracias a todos aquellos que han hecho de estos cuatro años una etapa inolvidable.

Este trabajo ha sido financiado por el Ministerio de Universidades del Gobierno de España a través de la Ayuda FPU19/04862. Además, ha contado el apoyo económico del Ministerio de Ciencia e Innovación a través de los proyectos MAT2016-75955, PGC2018-094180-B-I00 y PID2019-106820RB-C21 y de la Comunidad de Madrid - Unión Europea con el proyecto “Materiales Disruptivos Bidimensionales (2D)” (MAD2D-CM)-UCM5.

CONTENTS

ABSTRACT

Recent years have seen the rapid development of the so-called *topological* states of matter. This field represents an important advance in the band theory of solids, which was established after the pioneering work of Schrödinger in the 1920s.

In topological materials, global properties of the quantum states appear at the macroscopic level, and characteristic metallic states typically emerge at the Fermi energy. The first observation of a quantum topological state dates back to the work of von Klitzing in the 1980s [134]. In a 2D electron gas under strong magnetic fields, a quantized Hall conductance was measured at low temperature in plateaus proportional to e^2/h, following an integer progression for increasing magnetic fields. The *integer* quantum Hall effect was the first observation of a quantized response in a macroscopic sample.

In 1988, Haldane showed that the integer quantum Hall effect could be realized in a lattice system with zero total magnetic flux [105], paving the way to the topological phases in the absence of an external magnetic field. In particular, a quantum *spin* Hall state, where the quantized conductance is spin-polarized and opposite for opposite spins, was predicted by Bernevig, Hughes and Zhang in CdHgTe quantum wells in 2006 [19]. In this model, the total conductance cancels out as a result of the contribution of the two spins. The quantum *anomalous* Hall effect with nonzero total conductance from a single channel without external fields was predicted by breaking the time-reversal symmetry in magnetically doped systems in reference [308]. The quantum spin Hall effect in CdHgTe quantum wells was measured in 2007 [139], and the quantum anomalous Hall effect in Cr-doped $(\mathrm{Bi},\mathrm{Sb})_2\mathrm{Te}_3$ was observed in 2013 [33].

The quantized response of these systems is related to topological edge states that are localized at the surfaces of the samples. These states are a consequence of the topological nature of the bulk bands and they appear in finite systems due to the bulk-boundary correspondence. In gapped systems, the so-called *topological insulators*, the topological states appear inside the gap and usually resemble a linearly dispersive band. Hence, the topological states are described by the Dirac equation, which characterizes linearly dispersive fermions. Equivalent states are also found in gapless phases such as the *topological semimetals*.

This thesis focuses on the role of external fields in the topological states. The interest is double, on the one hand, the resilience of the topological

states under external perturbations is studied; on the other hand, the possibilities of tuning the states and their properties are also addressed. The materials considered resemble three categories: topological insulators, topological semimetals, and graphene-based systems.

The topological semimetals are covered in chapter 2. In these materials the dispersion relation closes at isolated points in the reciprocal space. The degeneracy points are connected by topological states called Fermi arcs. These states can be tuned by an external electric field in the direction of the localization of the states. The external field shifts the crossing of the Dirac bands of the Fermi arcs and modifies the Fermi velocity in a chiral dependent way in Na_3Bi. In the case of an electric field that couples the Fermi arcs with opposite chirality due to the breaking of inversion symmetry, the external field can be used to design a spin-switching device such that the spin-polarization of the current is flipped in certain regimes.

In chapter 3, the effect of the external electric field is studied in magnetically doped heterostructures of topological insulators. It is found that in these systems, the electric field is indeed a tool to tune the number of channels and to manipulate the transverse current driven by the topological channels.

Graphene systems are treated in chapter 4 in the context of two problems related to transport in nanoribbons: the effect of electron-electron interaction and the influence of broken inversion symmetry due to encapsulation in hBN. For the electron-electron interaction, the unrestricted Hartree-Fock model is used and electron transport in nanoribbons with monovacancies at the edge is studied. A magnetization appears in certain regimes due to the interaction, which leads to a local breaking of the time-reversal symmetry that impacts the transport at the edge. On the other hand, the hBN affect the transport by generating a valley-dependent drift of the currents, which can be measured by non-local resistances.

The effect of disorder in topological insulators and semimetals is discussed in several sections of the thesis. The impact of impurities on transport is considered in chapters 2 and 3. Chapter 5 studies the effect of impurities on the surface states of 3D topological insulators using analytical techniques such as the self-consistent Born approximation and the coherent potential approximation. These two formalisms are derived and compared in the case of the 2D effective model for the surface states of a topological insulator.

The effect of a time-dependent external electromagnetic field driving the surface states of topological insulators is considered in chapter 6. The well-known Floquet formalism is extended in this chapter to include non-periodic drivings. Due to the external pumping, the states absorb and emit photons in such a way that their energy is modified by the external

pulse. It is found that the Floquet formalism correctly describes these phenomena as long as the time evolution is adiabatic.

In conclusion, this thesis explores fundamental properties of topological states and the effect of external fields in tuning their properties. A special effort has been made to propose experimentally feasible scenarios by including the effect of disorder and finite size devices.

RESUMEN

Los últimos años han visto el rápido desarrollo de los así denominados estados *topológicos* de la materia. Este campo representa un avance importante en la teoría de bandas de los sólidos, que se estableció a partir del trabajo de Schrödinger en la década de 1920.

En los materiales topológicos, las propiedades globales de los estados cuánticos aparecen a nivel macroscópico, y estados metálicos característicos emergen típicamente en la energía de Fermi. La primera observación de un estado topológico cuántico se remonta al trabajo de von Klitzing en la década de 1980 [135]. En un gas de electrones 2D bajo fuertes campos magnéticos, se midió una conductancia Hall cuantizada a baja temperatura en *plateaus* proporcionales a e^2/h, siguiendo una progresión entera en función del campo magnéticos. El efecto Hall cuántico *entero* fue la primera observación de una respuesta cuantizada en una muestra macroscópica.

En 1988, Haldane demostró que el efecto Hall cuántico entero podía obtenerse en una red con flujo magnético total cero [105], abriendo el camino hacia las fases topológicas sin campo magnético externo. En particualr, Bernevig, Hughes y Zhang predijeron en 2006 [19] un estado Hall cuántico de *espín* en pozos de CdHgTe. En este modelo, la conductancia cuantizada está polarizada en espín y es opuesta para espines contrarios tal que la conductancia total se cancela como resultado de la contribución de los dos espines. El efecto Hall cuántico *anómalo* con conductancia mediada por la contribución de un solo canal sin campos externos se predijo rompiendo la simetría de inversión temporal en sistemas dopados magnéticamente en la referencia [308]. El efecto Hall cuántico de espín en pozos de CdHgTe se midió en 2007 [139], y el efecto Hall anómalo cuántico se observó en 2013 [33] en $(\mathrm{Bi},\mathrm{Sb})_2\mathrm{Te}_3$ dopado con Cr.

La respuesta cuantizada de estos sistemas está relacionada con los estados de borde topológicos que se localizan en las superficies de las muestras. Estos estados son una consecuencia de la naturaleza topológica de las bandas masivas y aparecen en sistemas finitos debido al teorema de la correspondencia entre bandas masivas y estados de superficie. En los sistemas con intervalo prohibido de energía, los *aislantes topológicos*, los estados topológicos aparecen dentro de la banda prohibida y generalmente muestran una dispersión lineal. Por lo tanto, se describen mediante la ecuación de Dirac, que caracteriza a fermiones linealmente dispersivos. Estados equivalentes también se obtenen en fases sin intervalo prohibido

de energía, como los *semimetales topológicos*.

Esta tesis se centra en el papel de los campos externos en los estados topológicos. El interés es doble, por un lado, se estudia la resiliencia de los estados topológicos ante perturbaciones externas; por otro lado, se abordan las posibilidades de control de los estados y sus propiedades topológicas. Los materiales considerados se agrupan en tres categorías: aislantes topológicos, semimetales topológicos y sistemas basados en grafeno.

Los semimetales topológicos se estudian en el capítulo 2. En estos materiales la relación de dispersión se cierra en puntos aislados del espacio recíproco. Los puntos de degeneración de las bandas están conectados por estados topológicos llamados arcos de Fermi. Estos estados se pueden controlar mediante un campo eléctrico externo en la dirección de la localización de los estados. El campo externo desplaza el cruce de las bandas de Dirac de los arcos de Fermi y modifica la velocidad de Fermi dependiendo de la quiralidad del estado para el Na_3Bi. En el caso de un campo eléctrico que acopla los arcos de Fermi con quiralidad opuesta debido a la ruptura de la simetría de inversión, el campo externo se puede usar para diseñar un dispositivo de conmutación de espín de modo que la polarización de la correinte en espín se invierte en ciertos regímenes.

En el capítulo 3, se estudia el efecto de un campo eléctrico externo en heterostructuras de aislantes topológicos dopados magnéticamente. En estos sistemas, el campo eléctrico es una herramienta para controlar el número de canales y manipular la corriente transversal de los canales topológicos.

Los sistemas de grafeno se tratan en el capítulo 4 en el contexto de dos problemas relacionados con el transporte en nanocintas: el efecto de la interacción electrón-electrón y la influencia de la ruptura de la simetría de inversión debido a la encapsulación en hBN. Para la interacción electrón-electrón se emplea el modelo de Hartree-Fock no restringido y se estudia el transporte en nanocintas con una vacante en el borde. La magnetización que aparece en ciertos regímenes debido a la interacción genera una ruptura local de la simetría de inversión temporal y modifica el transporte de los estados de borde. Por otro lado, el hBN afecta el transporte al generar una deriva de las corrientes de valle, que puede medirse mediante resistencias no locales.

El efecto del desorden en aislantes topológicos y semimetales se discute en varias secciones de la tesis. El efecto de las impurezas en el transporte se considera en los capítulos 2 y 3. El capítulo 5 estudia el efecto de las impurezas en los estados superficiales de los aislantes topológicos tridimensionales empleando técnicas analíticas como la aproximación autoconsistente de Born y la aproximación de potencial coherente. Estos

dos formalismos se derivan y comparan en el caso del modelo efectivo bidimensional para los estados superficiales de un aislante topológico.

En el capítulo 6 se estudia el efecto de un campo electromagnético externo dependiente del tiempo que modula los estados de superficie de los aislantes topológicos. El conocido formalismo de Floquet se amplía en este capítulo para incluir pulsos no periódicos. Debido al pulso externo, los estados absorben y emiten fotones de tal forma que su energía se modifica. En el capítulo, se prueba que el formalismo de Floquet describe correctamente estos fenómenos cuando la evolución temporal es adiabática.

En conclusión, esta tesis explora propiedades fundamentales de los estados topológicos y su modificación mediante campos externos. Se ha hecho un especial esfuerzo por proponer escenarios experimentalmente accesibles incluyendo el efecto del desorden y estudiando dispositivos de tamaño finito.

LIST OF PUBLICATIONS

Publications related to this thesis

1. **Electric field manipulation of surface states in topological semimetals**
   Yuriko Baba, Álvaro Díaz-Fernández, Elena Díaz, Francisco Domínguez-Adame, Rafael A. Molina
   Physical Review B **100**, 165105 (2019).
   The content of this paper is discussed in chapter 2.

2. **Rashba coupling, spin switching through surface states of Dirac semimetals**
   Yuriko Baba, Francisco Domínguez-Adame, Gloria Platero, Rafael A. Molina
   New Journal of Physics **23**, 023008 (2021).
   The content of this paper is discussed in chapter 2.

3. **Impact of electron-electron interactions on the thermoelectric efficiency of graphene quantum point contacts**
   Irián Sánchez-Ramírez, Yuriko Baba, Leonor Chico, Francisco Domínguez-Adame
   Physical Review B **106**, 045129 (2022).
   The content of this paper is discussed in chapter 4.

4. **Many-impurity scattering on the surface of a topological insulator**
   José Luis Hernando*, Yuriko Baba*, Elena Díaz, Francisco Domínguez-Adame
   Scientific Reports **11**, 5810 (2021).
   * The two authors contributed equally.
   The content of this paper is discussed in chapter 5.

5. **Effect of external fields in high Chern number quantum anomalous Hall insulators**
   Yuriko Baba, Mario Amado, Enrique Diez, Francisco Domínguez-Adame, Rafael A. Molina
   Physical Review B **106**, 245305 (2022).
   The content of this paper is discussed in chapter 3.

6. **Generation, control of non-local chiral currents in graphene superlattices by orbital Hall effect**
J. Salvador-Sánchez, L. M. Canonico, A. Pérez-Rodríguez, T. P. Cysne, Y. Baba, V. Clericò, M. Vila, D. Vaquero, J. A. Delgado-Notario, J. M. Caridad, K. Watanabe, T. Taniguchi, R. A. Molina, F. Domínguez-Adame, S. Roche, E. Diez, T. G. Rappoport, M. Amado
Submitted (2023). Arxiv: 2206.04565.
The content of this paper is discussed in chapter 4.

7. **Treating disorder in introductory solid state physics**
Dunkan Martinez Camacho, Yuriko Baba, Francisco Dominguez-Adame
Accepted in American Journal of Physics (2023).
The content of this paper is discussed in chapter 5.

Other publications

8. **Spin-dependent electronic lenses based on hybrid graphene nanostructures**
Yuriko Baba, Marta Saiz-Bretín
Physica E **115**, 113769 (2020).

9. **Persistence of symmetry-protected Dirac points at the surface of the topological crystalline insulator SnTe upon impurity doping**
Olga Arroyo-Gascón, Yuriko Baba, Jorge I. Cerdá, Oscar de Abril, Ruth Martínez, Francisco Domínguez-Adame, Leonor Chico
Nanoscale **14**, 7151 (2022).

10. **Tailoring topological states of core–shell nanoparticles**
Carolina Martínez-Strasser, Yuriko Baba, Álvaro Díaz-Fernández, Francisco Domínguez-Adame
Physica E **136**, 115000 (2022).

ACRONYMS

1BZ first Brillouin zone. 12–17, 33, 94, 116, 123

aGNR armchair graphene nanoribbon. 100–102, 196

ARPES angle-resolved photoemission spectroscopy. 23, 33, 38, 70, 155, 156, 163, 164, 169, 170, 176, 185

BHZ Bernevig, Hughes and Zhang (model). 19–22, 28–30, 69–71, 74, 75, 148

BZ Brillouin zone. 26, 28, 99, 207

CNP charge neutrality point. 118, 119

CPA coherent potential approximation. 128, 130–132, 137, 138, 140, 141, 144–153, 188

CSS chiral surface states. 54–57

DFT density functional theory. 23, 30, 34, 38, 54, 61, 64, 70, 104, 119, 120

DOS density of states. 141, 142, 146–153, 162, 165–167, 174–176, 185, 188

DSM Dirac semimetal. 26, 29, 30, 33–36, 38, 41, 42, 44, 46, 48, 49, 58, 59, 63–65, 187, 188

e-e electron-electron (interaction). 52, 94, 103–106, 110–112, 124, 125, 187

FBZ Floquet Brillouin zone. 158, 163, 167, 180, 182

GSS general surface states. 54–57

hBN hexagonal boron nitride. 94, 97, 103, 114–117, 119, 120, 124, 125, 187, 188

KM Kane-Mele (model). 98, 99, 102, 106, 109, 112, 113, 187

LAPE laser-assisted photoemission. 164, 174, 176

LL Landau level. 49, 50, 64, 65

PBC periodic boundary conditions. 10, 21, 22, 25, 27, 39, 77, 81, 83–86, 108, 121

PR participation ratio. 86–88

QAH quantum anomalous Hall. 67–71, 75, 78, 80, 98, 155

QHE quantum Hall effect. 48, 49, 51

QSH quantum spin Hall. 18, 31, 52, 67–69, 71, 98, 99, 103, 106, 112, 115

RSOC Rashba spin-orbit coupling. 34, 52–55, 57–66, 187

SCBA self-consistent Born approximation. 128, 130, 138–153, 188

TDSE time-dependent Schrödinger equation. 157–160, 162–165, 169–172, 178, 180, 181, 183, 184

TI topological insulator. 5, 6, 9, 13, 18, 23, 26, 31, 49, 50, 52, 53, 67–69, 71, 72, 75, 78–82, 91, 127, 128, 140, 152, 156, 164, 187

TR time-reversal. 12, 18, 20, 21, 23, 28–30, 33, 36, 38, 41, 52, 54, 59, 67–71, 89, 93, 96–98, 112, 125, 187, 189–191

TSM topological semimetal. 5, 26, 30, 31, 33, 34, 41, 53, 64, 187

VCA virtual crystal approximation. 128, 130, 138, 141, 142, 145, 147

WSM Weyl semimetal. 26–28, 33–35, 37, 39, 41, 44, 64, 144, 148, 187

zGNR zigzag graphene nanoribbon. 100–103, 109–111, 113, 114, 120–123, 125, 198

0 INTRODUCTION

The advent of topology in condensed matter systems has revolutionised the interpretation of Bloch band theory, which was established a century ago to understand the electronic structures of materials. Topology is a branch of mathematics that studies the properties of manifolds that are invariant under continuous transformations [176]. In condensed matter systems, the topology of the Hilbert space in which the electron wavefunctions live has been found to have an important influence on the properties of the system itself. The work of D. Thouless, D. Haldane, and M. Kosterlitz was awarded with the Nobel Prize in 2016 for their seminal contributions to this field [106, 140, 141, 262, 264].

The classification of one-particle Hamiltonians within the usual Bloch band theory was based on the spectrum of the systems, and it clearly predicted the electronic transport properties. Thus, the usual basic categories were roughly distinguished by the size of the gap in metals, semimetals, semiconductors, and insulators. However, when topology is added to this classification, a new point of view emerges by considering the properties of the wave functions and not only the spectrum itself. In this way, the standard classification is extended depending on how the wavefunction of the system is defined in the reciprocal space [42].

Topological materials reflect the global property of quantum states in mesoscopic systems by the appearance of characteristic edge states. These states are resilient to disorder and edge roughness and typically exhibit linearly dispersive bands resembling a Dirac cone. For this reason, topological materials are promising for future applications in electronics. The various members of the family of topological materials manifest a wide range of interesting electronic properties, but the most important is dissipationless electron transport through boundary states.

The first measurement of a topological channel in an experimental setup was made in 1980 by K. von Klitzing. In a quantum Hall setup, a quantized signal in multiples of e^2/h was measured in a sample of a 2D electron gas with a strong magnetic field and low temperature [134]. As a function of the external field, the Hall resistance shows quantized plateaus while the longitudinal signal drops to zero. For the discovery of the *integer quantum Hall effect*, K. von Klitzing was awarded with the Nobel Prize in 1985. The introduction of the resistance standard based on the quantum Hall effect is a prominent example of the applications of topo-

logical properties of materials, as it was a groundbreaking advance in metrology [135].

Nowadays, the family of quantum Hall effects has been extended by the fractional Hall effect first obtained in 1982 [268], the quantum spin Hall effect measured in 2007 [139], and the quantum anomalous Hall effect observed in 2013 [33]. The latter two can be modeled by single-particle Hamiltonians and no external fields are needed to obtain the topological channels. The topological state is encoded in the bands by the band inversion that occurs due to the strong spin-orbit coupling [19] and, in the case of the quantum anomalous Hall, by a magnetization that breaks the time-reversal symmetry [308].

In fact, symmetries play a fundamental role in the topological states of matter. Together with dimensionality, a periodic table of topological insulators and superconductors has been constructed by S. Ryu and collaborators [131, 223, 233, 234]. This classification, also called the tenfold way, takes into account the presence or absence of fundamental symmetries, such as time-reversal, particle-hole, and chiral symmetries, in a given dimensionality and defines a topological invariant that characterizes the topological phase [42]. The topological invariant is conserved under adiabatic transformations, and thus it is a quantity that intrinsically defines the topology of the bands.

In the systems considered in this thesis, the topological invariant is related to the Chern number, which is a specific invariant for 2D systems with broken time-reversal symmetry [105, 109]. The Chern number is related to the winding of the phase of the states around the Brillouin zone [12]. It is calculated over the bulk bands [82], but it gives the number of boundary states that appear when an edge is cut. This is known as the bulk-boundary correspondence theorem and was proved by Y. Hatsugai in 1993 [109].

The main focus of this thesis is the study of topological boundary states under external perturbations. In the literature, the effect of external fields has been studied both from a theoretical perspective and experimentally. It has been found that the electric fields can induce a topological phase transition depending on their strength in topological insulators [129, 315, 319] and topological semimetals [44, 181, 197]. The application of external electric fields can renormalize the Fermi velocity and control the decay of surface states in Dirac materials [55, 56]. Time-dependent electromagnetic fields can also be used to control the topological properties of matter [31, 32, 54, 93, 94, 153, 170, 188, 274, 310].

In this thesis the external fields are studied in topological Dirac semimetals in chapter 2 and in heterostructures of magnetically doped topological insulators in chapter 3. Chapter 4 examines the effect in non-local resis-

tance measurements of the breaking of the inversion symmetry due to the encapsulation of graphene nanoribbons in hBN. The effect of impurities in topological insulators is covered in chapter 5 and the combined effect of vacancies and electron-electron interaction is discussed in chapter 4 for the topological Kane-Mele model. The time-dependent fields are treated using the Floquet formalism in chapter 6 in the case of the surface states of topological insulators.

The interest in studying these perturbations is twofold. On the one hand the resilience of topological channels under external fields [13, 14] and disorder [111, 228] is investigated. On the other hand, the possibilities of tuning the topological properties such as the Chern number [13] or the properties of the states such as the spin [15], the Fermi velocity and the localisation [14] are explored. Special emphasis is placed on transport calculations in order to establish a direct comparison with experiments. Hall bar setups and two lead devices with spin-polarised leads are used, and the transport signatures of the topological channels are calculated within the Landauer-Büttiker formalism.

In conclusion, this thesis aims to deepen in the tuning of the topological boundary states in different materials and setups and provide transport signatures associated with the topological channels.

1 THE DIRAC EQUATION IN CONDENSED MATTER SYSTEMS

Preamble

The main topic of this thesis is the study of electron dynamics in Dirac materials and their transport properties under externals fields and disorder. In these materials, the low-energy quasiparticles are described by the Dirac equation and exhibit a linear dispersion relation. Dirac fermions appear in various and diverse condensed matter systems, including purely 2D materials such as graphene or 3D phases such as Weyl and Dirac semimetals. In the case of topological semimetals (TSMs) and topological insulators (TIs), the linearly dispersive (Dirac) bands appear at the Fermi energy due to the topological properties of the bulk bands and correspond to edge-localised states.

The Dirac equation was first formulated in 1928 by Paul Dirac in the context of particle physics to describe elementary spin-1/2 particles [57]. As a consequence of the expansion of the low energy band structure, many effective continuum models for the extended family of topological materials have a mathematical structure that resembles the Dirac equation with the gap playing the role of mass. The exploration of the Dirac equation in the context of condensed matter systems is a wide field of the recent research.

In this introductory chapter, the general concepts of topology in condensed matter are discussed, together with minimal models that provide a first approximation to the systems studied in this thesis, namely TIs and TSMs. The graphene-based systems, even though they share the Dirac dispersion and the topological properties of the Kane-Mele model, are strongly related to the geometry of the hexagonal lattice and are therefore covered separately in chapter 4. The discussion in this chapter is based on established results presented in reviews on TIs such as references [12, 18, 107, 206, 245].

The chapter is organised as follows:

- First, the linear Dirac equation is introduced and the interface states of the linear Dirac Hamiltonian with changing mass are calculated in section 1.1.1.
- Next, the quadratic corrections to the Dirac equation are introduced in section 1.1.2 to obtain an interface state without the need for

two media with masses of opposite sign. This makes it possible to obtain a boundary state in a single medium. The existence of the boundary state depends on the relative sign of the parameter of the quadratic curvature of the bands and the constant gap term. Up to this point, the boundary states are derived by imposing a finite gap Dirac system and searching for solutions within the gap. However, the existence of such states is actually encoded in intrinsic properties of the band structure. In fact, the topological properties of the band dictate the existence of the boundary states.

- In order to study the topology of bands, some important quantities and concepts are introduced in section 1.2. The central quantity is the Chern number, which encodes the topological nature of a 2D band. The topological number is calculated in section 1.2.2 for the 2D Chern insulator, which is the lattice realisation of the Dirac equation modified with the quadratic terms.

- Section 1.3 introduces some relevant models that will be used in the following chapters of the thesis. The topological properties of all of them are related to the Chern number by arguments that exploit the possibility of factorising the Hamiltonians into independent blocks. In this way, the quantum spin Hall state is built up from two Chern insulators that are time-reversal partners in section 1.3.1, and the Weyl and Dirac semimetals are obtained in section 1.3.3 by introducing the third spatial direction as a parameter. The model for the 3D TIs is briefly discussed in section 1.3.2.

- Finally, the chapter ends with a conclusion in section 1.4, which highlights the main concepts introduced in the chapter and summarises the key findings.

1.1 The Dirac equation and the bound state at the interface

The Dirac equation appears in the context of relativistic quantum field theory with the idea of fulfilling both the postulates of relativistic and quantum mechanics. On the one hand, relativistic mechanics suggests an identification of momentum and energy in such a way that both enter on the same footing and linearly[1], i.e. roughly speaking $\epsilon = \sqrt{\mathbf{k}^2 + m^2}$. On the other hand, quantum mechanics describes the dynamics by the

[1]Here and in the following it was set $\hbar = 1$ and $c = 1$ for simplicity.

Schrödinger equation

$$\mathcal{H}\psi = \epsilon\psi \ . \tag{1.1}$$

where ψ is the wavefunction, ϵ the energy and $\mathcal{H}$ is the Hamiltonian of the system. For a free particle with mass described by the Schrödinger equation, the momentum usually enters quadratically in the energy, i.e. $\epsilon = \mathbf{k}^2/2m$.

By coupling the momentum components to the Dirac matrices, the Dirac Hamiltonian was proposed as a solution that satisfies both the Schrödinger equation and the relativistic constraints encoded in Lorentz invariance [2]. The simplest form of the Dirac Hamiltonian is the following

$$\mathcal{H} = v\boldsymbol{\alpha}\cdot\mathbf{k} + \beta m_0 \ , \tag{1.2}$$

where α is a vector of Dirac matrices and β is another Dirac matrix. The length of the vector and the matrix size of the Dirac matrices depend on the dimensionality of the space, being $\boldsymbol{\alpha} = (\alpha_x, \alpha_y)$ in the case of 2D and $\boldsymbol{\alpha} = (\alpha_x, \alpha_y, \alpha_z)$ in the case of 3D. The Dirac matrices satisfy the following anticommutator relations

$$\{\alpha_i, \alpha_j\} = 2\delta_{ij} \ , \quad \{\alpha_i, \beta\} = 0 \ , \quad \beta^2 = 1 \ . \tag{1.3}$$

The Pauli matrices fulfil the conditions of equation (1.3) and therefore in 2D the three Dirac matrices can be chosen as the three Pauli matrices.

$$\alpha_x = \sigma_x \ , \alpha_y = \sigma_y \ , \beta = \sigma_z \ . \tag{1.4}$$

In 3D, four Dirac matrices are needed, and the properties of the Pauli matrices can still be used to define them in terms of the Pauli matrices, as follows

$$\alpha_i = \begin{pmatrix} 0 & \sigma_i \\ \sigma_i & 0 \end{pmatrix} \ , \quad \beta = \begin{pmatrix} \sigma_0 & 0 \\ 0 & -\sigma_0 \end{pmatrix} \ , \tag{1.5}$$

where $\sigma_0 = \mathbb{1}_2$ is the identity matrix in 2D.

The Schrödinger equation (1.1) is solved for the Dirac Hamiltonian by

$$\epsilon_\pm = \pm\sqrt{v^2\mathbf{k}^2 + m_0^2} \ , \tag{1.6}$$

with eigenstates, in 2D, given by

$$\psi_\pm = A_\pm \begin{pmatrix} v(k_x - k_y) \\ \epsilon_\pm - m_0 \end{pmatrix} \ , \tag{1.7}$$

[2] The Lorentz convariance is outside of the scope of this thesis. For the reference of the reader, the intuitive idea that the energy should enter in the same footing of the mass is sufficient. The properties of the Lorentz covariance are encoded in the anticommutator relations that the Dirac matrices have to fulfil.

where $A_\pm$ is a normalization constant. The dispersion (1.6) resembles the gapped linear cone plotted in figure 1.1 (a) and (b) and the states are in general multicomponent wavefunctions as expressed by equation (1.7).

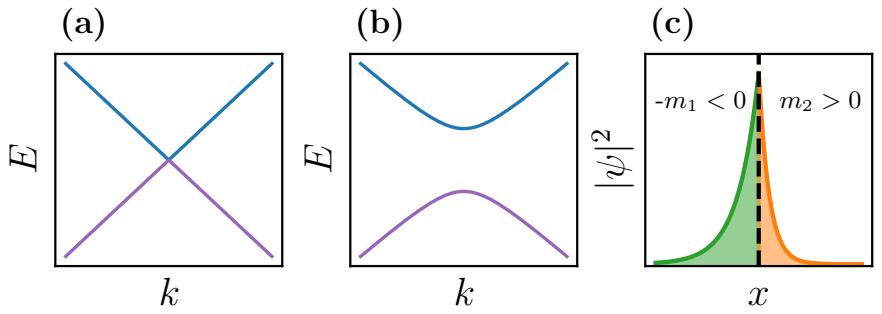

Figure 1.1: Dispersion relation for the linear Dirac model given by equation (1.6) for the massless case, i.e. for $m = 0$ in (a) and for the gapped case in (b). In (c) the solution for the mass inverted Dirac equation (1.10) is schematically represented. The vertical line indicates the interface between the two media with different masses.

1.1.1 Bound states and mass inversion

In the case of an inhomogeneous medium, for example when the mass changes in one direction, bound states are obtained at the interface between the two media. These states are particularly interesting because they exhibit spatial localisation and appear within the bulk gap. Next, the derivation of such states is sketched for a mass change in the x-direction, given by

$$m(x) = \begin{cases} -m_1 & \text{if } x < 0 \ , \\ +m_2 & \text{if } x \geq 0 \ , \end{cases} \tag{1.8}$$

where $m_1 > 0$ and $m_2 > 0$ without loss of generality. In condensed matter systems the mass inversion corresponds to the inversion of bands.

Considering the mass term in equation (1.8), the Hamiltonian (1.2) has a well defined momentum only in the y-direction and upon substitution of $k_x \to -i\partial_x$ it reads as

$$\mathcal{H}(x) = -iv\partial_x\sigma_x + vk_y\sigma_y + m(x)\sigma_z \ . \tag{1.9}$$

This Hamiltonian is easily solvable for the specific case of $k_y = 0$ and for the zero-energy solutions. An exponential decaying ansatz is used so that

the state is given by

$$\psi(x) = \begin{cases} e^{+\lambda_1 x}\phi_1 & \text{if } x < 0 \ , \\ e^{-\lambda_2 x}\phi_2 & \text{if } x \geq 0 \ , \end{cases} \tag{1.10}$$

where ϕ_j is a constant spinor and $\lambda_j > 0$ for $j = 1, 2$.

In the specific case of the zero-energy solutions for $k_y = 0$, the state is solved by applying the Hamiltonian twice and exploiting the properties of the Pauli matrices:

$$\mathcal{H}(x, k_y = 0)^2\psi(x) = 0 \qquad \Rightarrow -(v\lambda_j)^2 + m_1^2 = 0 \ . \tag{1.11}$$

The decay lengths are determined by this condition leading to

$$\lambda_j = m_j/v \ , \quad j = 1, 2 \ , \tag{1.12}$$

and the spinor is solved by

$$\phi_j = A_j \begin{pmatrix} i \\ 1 \end{pmatrix} \ , \tag{1.13}$$

where A_j is a constant that is obtained by matching the wavefuntion at $x = 0$ and by the normalization condition. The interface bound state is the first example we encounter of a TI-like surface state. It is indeed a metallic state, with energy at the Fermi level and it appears inside the bulk gap, thus resembling two main properties of the topological surface states. This solution was first obtained by Jackiw and Rebbi in 1976 [118] and it is schematically represented in figure 1.1 (c).

The Dirac Hamiltonian is invariant under the transformation of $m \to -m$ together with $\beta \to -\beta$, where $-\beta$ still satisfies the anticommutator relations (1.3). This symmetry implies that the overall sign of the mass itself does not determine whether the bound state appears or not. A linear Dirac system is not topologically distinct because a unitary transformation relates the two systems with opposite mass signs [244, 245]. Therefore, the simple linear Dirac Hamiltonian has to be extended to define the topological properties.

1.1.2 Quadratic correction to the Dirac Hamiltonian

In order to study the topological properties of the Dirac Hamiltonian, a quadratic correction is introduced in the mass term

$$\mathcal{H} = v\boldsymbol{\alpha} \cdot \mathbf{k} + (m_0 - m_1\mathbf{k}^2)\beta \ , \tag{1.14}$$

where m_1 is a parameter that breaks the symmetry between the sign exchange in the Dirac Hamiltonian.

Bound states can be obtained for the modified Dirac Hamiltonian without introducing two media. In fact, for a semi-infinite material extended at $x \geq 0$ and with vacuum on the left side, the zero energy solutions are obtained similarly to the previous derivation by replacing the momentum in the x-direction by the derivative and by employing an *ansatz* with an exponential decay $\psi(x) \sim e^{-\lambda x}$:

$$\mathcal{H}(x, k_y = 0)^2 \psi(x) = 0 \quad \Rightarrow \; (m_1\lambda^2 + m_0)^2 = (v\lambda)^2 \; . \tag{1.15}$$

If $m_0 m_1 > 0$, two roots of the polinomial equation fulfill the condition of $\lambda > 0$ and they are given by

$$\lambda_\pm = \frac{v \pm \sqrt{v^2 - 4m_1 m_0}}{2|m_1|} \; . \tag{1.16}$$

The spinorial part is also solved in this case by

$$\phi = A \begin{pmatrix} \mathrm{sgn}(m_1) \\ i \end{pmatrix} \; . \tag{1.17}$$

where $\mathrm{sgn}(m_1)$ indicates the sign of the quadratic term and A is the normalization constant.

A solution that satisfies the Dirichlet boundary conditions, i.e. that the wavefunction is zero at the boundary $\psi(x = 0) = 0$, can be obtained by combining the two decay lengths as

$$\psi(x) = A(e^{-\lambda_+ x} - e^{-\lambda_- x})\phi \; . \tag{1.18}$$

In figure 1.2 the dispersion relation is computed numerically for a nanoribbon of length L in the y-direction and periodic boundary conditions (PBC) in the x-direction for the regime of $m_0 m_1 > 0$ in (a) and for $m_0 m_1 < 0$ in (b). Note that linearly dispersive bands appear inside the gap only in the case depicted in panel (a). The state corresponding to the Fermi energy is represented in panel (c) in orange, showing a clear localisation at the two boundaries. On the other hand, for $m_0 m_1 < 0$ in (b) no states appear at the Fermi energy and the first occupied state below the Fermi energy corresponds to the bulk delocalised state plotted in green in panel (c).

In conclusion, by numerical and analytical methods a boundary state for the modified Dirac equation is obtained at zero energy whenever $m_0 m_1 > 0$. On the other hand, the system has no localised state if $m_0 m_1 < 0$. In contrast to the linear Dirac Hamiltonian, the condition for the existence of the states is encoded in the parameters of the model itself, without the need to introduce a second medium.

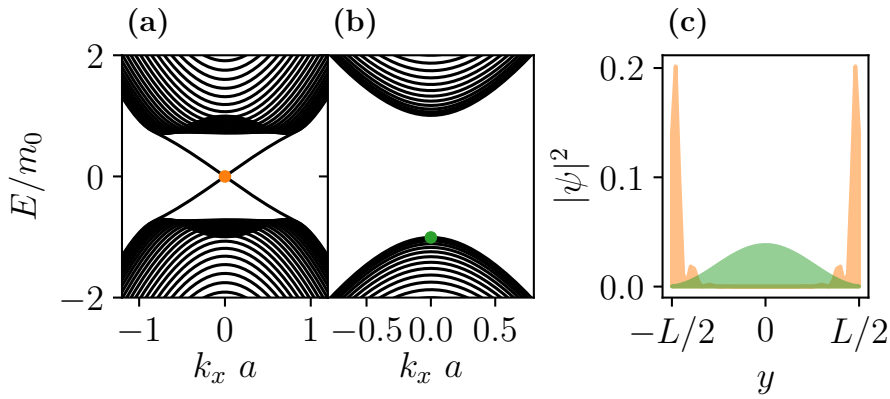

Figure 1.2: Dispersion relation and $|\psi|^2$ for a nanoribbon of $L = 50a$ with Hamiltonian given by equation (1.14) for two parameters sets. In (a) the parameters are $v/(am_0) = 1$, $m_1/(a^2m_0) = 1.5$ and hence the system is expected to show boundary states. In (b) The parameters employed are $v/(am_0) = 1$, $m_1/(a^2m_0) = -1.5$. In (c) the probability density $|\psi|^2$ is plotted for the first state below the Fermi energy for the nanoribbon with parameters corresponding to (a) in orange and to (b) in green. The dot in the panels (a) and (b) indicates the energy of the state plotted in (c). The lattice constant a and the gap m_0 are employed to adimensionalize the quantities.

1.2 Topology and the Dirac equation

1.2.1 Pedestrian introduction to topology

The existence condition of the surface state obtained in the previous section was extracted from the algebraic solution of the states of the Hamiltonian (1.14) in a finite system. However, the presence of the boundary state is actually related to the more general concepts of topology applied to condensed matter systems and can be obtained from the properties of the bulk Hamiltonian without finding the states in a finite system. This section is devoted to introducing the main concepts of topology needed to characterise the properties of the systems and in particular the 2D Dirac Hamiltonians.

Topology is the branch of mathematics that studies continuity [176]. Given two physical systems, they are considered topologically equivalent if a smooth parameter transformation relates them, i.e. they are connected by an *adiabatic* transformation. In the context of Bloch band theory, smoothness always refers to a transformation that deforms the bands but preserves the gaps; no new level crossings are created by the

transformation. Thus the topological transitions are related to gap closings.

The topological equivalence of two condensed matter systems is usually proved by computing a *topological invariant* for the bulk system. These quantities remain unchanged under smooth deformations and thus define the topological state of a set of equivalent Hamiltonians. A complete classification of the topological phases of single-particle crystalline systems according to dimensionality and symmetries is the so-called Altland-Zirnbauer classification [6, 42, 131, 233, 321]. By this classification, the Hamiltonians of topological insulators and superconductors are sorted in terms of TR, particle-hole and chiral symmetries in a periodic table formed by ten generic symmetry classes which are related to random-matrix ensembles [6, 321]. The topological classification can be extended to non-crystalline systems, which is beyond the scope of this work, although it is a promising new field [3, 45].

The topological invariants in crystalline systems are based on the representation within the Bloch theorem. Due to the periodicity of the crystalline structure, the eigenstates of a given Hamiltonian are Bloch wavefunctions, factorised as

$$|\psi_{\mathbf{k}}(\mathbf{r})\rangle = e^{i\mathbf{k}\cdot\mathbf{r}}|u_{\mathbf{k}}(\mathbf{r})\rangle \ , \tag{1.19}$$

where $|u_{\mathbf{k}}(\mathbf{r})\rangle$ is the cell-periodic part of the wavefunction such that $|u_{\mathbf{k}}(\mathbf{r})\rangle = |u_{\mathbf{k}}(\mathbf{R}+\mathbf{r})\rangle$ with $\mathbf{R}$ a vector of the Bravais lattice. The $|u_{\mathbf{k}}\rangle$ are labelled by the momentum $\mathbf{k}$ which is in the first Brillouin zone (1BZ). Determining the energies as a function of momenta gives the concept of *band*

$$\mathcal{H}(\mathbf{k})|u_n(\mathbf{k})\rangle = \epsilon_n(\mathbf{k})|u_n(\mathbf{k})\rangle \ , \tag{1.20}$$

where n is the band index and denotes the n-th solution of the eigenvalue equation from the Schrödinger equation (1.1) for a given $\mathbf{k}$ with the decomposition in expression (1.19) and energy $\epsilon_n(\mathbf{k})$. The topological properties studied in this thesis relate to the so-called *band topology* where the topological invariants are computed over the bands and their eigenstates.

In a square lattice with parameter a, the 1BZ is given by $k_x \in (-\pi/a, \pi/a)$ and $k_y \in (-\pi/a, \pi/a)$ such that the components of the momentum at $k_i = \pi/a$ and $k_i = -\pi/a$ are identified, for $i = x, y$. This implies that the 1BZ contains a closed surface in two directions and it can be mapped onto the geometric figure of the torus. The topological invariants are usually defined over closed paths (surfaces or loops) so that they are intrinsically path independent. The 1BZ itself is a suitable region to compute them, thanks to its periodicity.

Assuming a non-interacting 2D Hamiltonian with Fermi energy inside the gap, i.e. an insulator state, an integer-valued topological invariant $C^{(n)} \in \mathbb{Z}$ can be computed for each band n. This invariant is related to the times that the phase of the n-th state winds around the 1BZ.

The evolution of the phase is captured by the so-called Berry connection, defined as

$$\mathcal{A}_i^{(n)}(\mathbf{k}) = -i\langle u_{\mathbf{k}}^{(n)} | \partial_{k_i} | u_{\mathbf{k}}^{(n)} \rangle \ , \tag{1.21}$$

where ∂_{k_i} indicates the partial derivative with respect to momenta k_i and $i = x, y, z$ stands for the spatial directions. The superscripts indicate the n-th band and they will be omitted for simplicity in the following.

The integral of the Berry connection over a closed loop L gives the Berry phase, or more precisely the Zak phase[3]

$$\gamma = \oint_L \mathcal{A}(\mathbf{k}) \cdot d\mathbf{k} \ . \tag{1.22}$$

Note that due to the definition of the Berry connection, the Zak phase is related to the expectation value of the position operator in the i-th direction over the bands, see equation (1.21). The operator inside the brackets is the position operator in the momentum representation and this relates the topological properties of the bands to the spatial distribution of the eigenfunctions.

Using the Stokes theorem, expression (1.22) can be written as

$$\gamma = \int_S d\mathbf{S} \ \cdot \ \mathbf{\Omega}(\mathbf{k}) \ , \tag{1.23a}$$

$$\mathbf{\Omega}(\mathbf{k}) = \boldsymbol{\nabla}_{\mathbf{k}} \times \mathcal{A}(\mathbf{k}) \ , \tag{1.23b}$$

with S the surface enclosed by the loop L. The quantity $\mathbf{\Omega}$ is named Berry curvature and it resembles the form of a vector field for the vector potential $\mathcal{A}$.

When the surface S coincides with the 1BZ of a 2D system, the Berry curvature is expected to be zero. In fact, the edges of the 1BZ are identified and therefore the integration in the closed (continuous) surface of a soft function should return the same value. However, this is not the case for topological materials where the Berry curvature is discontinuous, so the integral in equation (1.23a) is non-zero when integrated over the 1BZ.

In a TI, the Zak phase, integrated over the 1BZ, is related to an integer number named as *Chern number* C

$$\gamma = 2\pi C \ . \tag{1.24}$$

[3] Usually, the name Berry phase is related to a general parameter dependence, while when the phase is computed over the 1BZ is named Zak phase. In the literature both terms are used indistinguishably.

The quantization of the phase follows from the Chern's theorem [264, 275]. A simple demonstration of the quantization property is obtained by defining the Wilson loops. The idea is to decouple the integration in equation (1.22) in two parameters λ_1 and λ_2, which for simplicity are bounded between 0 and 2π. The integration over the closed path L in the 1BZ is parametrised by λ_1 and λ_2. Then, equation (1.22) can be rewritten as

$$\gamma = \int_0^{2\pi} d\lambda_2 \; \phi(\lambda_2) \; , \tag{1.25a}$$

$$\phi(\lambda_2) = \int_0^{2\pi} d\lambda_1 \mathcal{A}(\lambda_1, \lambda_2) \cdot \mathbf{u}_1 \; , \tag{1.25b}$$

where $\mathbf{u}_1$ gives the direction of λ_1. With these definitions, the Zak phase can be interpreted geometrically as the winding of the phase of the eigenstates over the line given by λ_2. In figure 1.3 two Wilson loops are plotted as a function of λ_2. In the case of the trivial state in panel (a), the line does not wind. On the other hand, in the topological state in panel (b), the Wilson loop winds once as it circulates the closed path given by λ_2. Since the winding is an integer number, the Zak phase is related to the integer Chern number C.

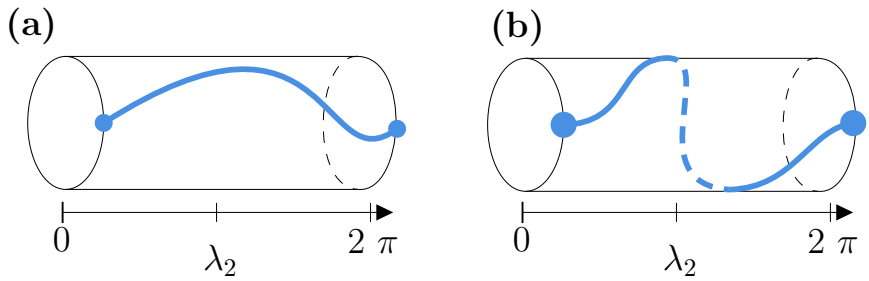

Figure 1.3: Schematic representation of two Wilson loops as a function of λ_2 for the case of no winding around the 1BZ (a) and for a case with one wind (b).

The numerical computation of the Chern number is usually related to the Wilson loops and the tracking of the spatial distribution of the eigenfunctions in the Wannier basis thanks to the relation between the Berry connection and the expectation value of the position [82, 275]. This is, for example, the case of the `Z2pack` [100] employed in chapter 3.

1.2.2 2D Chern insulator

In this section, as an example of the previously presented quantities, the case of the 2D modified Dirac Hamiltonian in its lattice realisation is discussed. This is usually known as the 2D Chern insulator. The problem is easily formulated using the properties of the two-band models. Any two-band Hamiltonian can be expressed in the basis of Pauli matrices as

$$\mathcal{H}(\mathbf{k}) = R_0(\mathbf{k})\sigma_0 + \mathbf{R}(\mathbf{k}) \cdot \boldsymbol{\sigma} \ , \tag{1.26a}$$

$$\mathbf{R}(\mathbf{k}) = (\ R_x(\mathbf{k}),\ R_y(\mathbf{k}),\ R_z(\mathbf{k})\ ). \tag{1.26b}$$

where $\boldsymbol{\sigma} = (\sigma_x, \sigma_y, \sigma_z)$ denotes a vector of Pauli matrices. The spectrum can be easily computed using the anticonmutation properties of the Pauli matrices obtaining

$$\epsilon_\pm = R_0 \pm R \ , \tag{1.27}$$

where $R \equiv \sqrt{R_x^2 + R_y^2 + R_z^2}$. The eigenvectors for a gapped system are given by

$$|\psi_\pm^N\rangle = \frac{1}{\sqrt{2R\,(R \pm R_z)}} \begin{pmatrix} \pm R + R_z \\ R_x + iR_y \end{pmatrix} \ . \tag{1.28a}$$

Within this gauge choice for the eigenvectors, the valence state has a singularity at $\mathbf{R}(\mathbf{k}) = (0, 0, r)$ if $r > 0$. The superscript N indicates the singularity being in the *north pole*. This singularity can be shifted, but not eliminated. For example, by expressing the states in a different gauge we get

$$|\psi_\pm^S\rangle = \frac{1}{\sqrt{2R\,(R \mp R_z)}} \begin{pmatrix} R_x - iR_y \\ -R_z \mp R \end{pmatrix} \ , \tag{1.28b}$$

which is also singular in the valence state, but for $\mathbf{R}(\mathbf{k}) = (0, 0, -r)$ if $r > 0$ and hence with the singularity in the *south pole* S.

For the modified Dirac equation (1.14), the vector $\mathbf{R}$ in a square lattice with lattice parameter a is given within the tight-binding approximation as [12, 205]

$$\mathbf{R}(\mathbf{k}) = \begin{pmatrix} \nu \sin(k_x a) \\ \nu \sin(k_y a) \\ m_0 - 4\mu \sum_{i=x,y} \sin^2(k_i a/2) \end{pmatrix} \ , \tag{1.29}$$

where $\nu = v/a$, $\mu = m_1/a^2$. The tight-binding model is obtained by replacing $k_i \to a^{-1} \sin k_i a$ and by $k_i^2 \to 2a^{-2}(1 - \cos k_i a)$ in the continuous model given by equation (1.14). The tight-binding formulation is particularly convenient because it incorporates the periodicity of the 1BZ. The continuous model and the tight-binding model coincide for small

momenta as long as the quadratic term is present. When $m_1 = 0$, the linear Dirac equation encounters the well-known fermion doubling problem, which forces the existence of two merging points in a lattice realisation [180].

From equation (1.27), the spectrum for the modified Dirac equation is gapless in three cases

- if $m_0 = 0$ the conduction and valence band touch at $\mathbf{k}_0 = (0, 0)$,
- if $m_0 = 4\mu$ the bands touch at $\mathbf{k}_1 = (0, \pm\pi/a)$ and $\mathbf{k}_2 = (\pm\pi/a, 0)$,
- if $m_0 = 8\mu$ the bands touch at $\mathbf{k}_\pi = (\pi/a, \pi/a)$. This point, due to the period conditions of the 1BZ is equivalent to $(-\pi/a, -\pi/a)$ and $(\pm\pi/a, \mp\pi/a)$.

Therefore, depending on the value of m_0 and μ, there are four regimes regarding the sign of R_z:

1. If $m_0 < 0$: $R_z < 0$ over the whole 1BZ.
2. If $0 < m_0 < 4\mu$: $R_z > 0$ near the $\mathbf{k}_0 = (0, 0)$. and $R_z < 0$ near the boundaries of the 1BZ (i.e. $k_x = \pm\pi/a$ and $k_y = \pm\pi/a$).
3. If $4\mu < m_0 < 8\mu$: the sign of R_z is negative near the $\mathbf{k}_\pi = (\pi/a, \pi/a)$ and in all its equivalent points, while $R_z > 0$ at $\mathbf{k}_0 = (0, 0)$.
4. If $m_0 > 8\mu$: $R_z > 0$ over the whole 1BZ.

Figure 1.4 shows the R_z over the 1BZ for the four regimes listed above.

The eigenstates of the Hamiltonian can be chosen to be continuous in the case of (1) and (4) by selecting the states in equations (1.28a) and (1.28b) respectively. However, whenever the system is described by the parameters of (2) and (3), two gauges are needed to avoid the singularities. The impossibility of defining the states in the full 1BZ with a single gauge is indeed a signal of the obstruction that rules out the Stokes theorem and hence of the topological non-triviality of the states.

The Chern number can be computed by its definition in equation (1.24) via the Berry connection (1.21), but in the specific case of the considered model a more instructive method can be exploited by switching the derivatives with respect to the momenta to the $\mathbf{R}$ space. To do this, the Berry connection over the momentum space (1.21) is rewritten in a more convenient form as

$$\mathcal{A}_i^{(\pm)}(\mathbf{k}) = -i\frac{\partial R_j}{\partial k_i}\langle u_{\mathbf{k}}^{(\pm)}|\partial_{R_j}|u_{\mathbf{k}}^{(\pm)}\rangle \equiv -i\frac{\partial R_j}{\partial k_i}a_j^{\pm}(\mathbf{R}) \ . \tag{1.30}$$

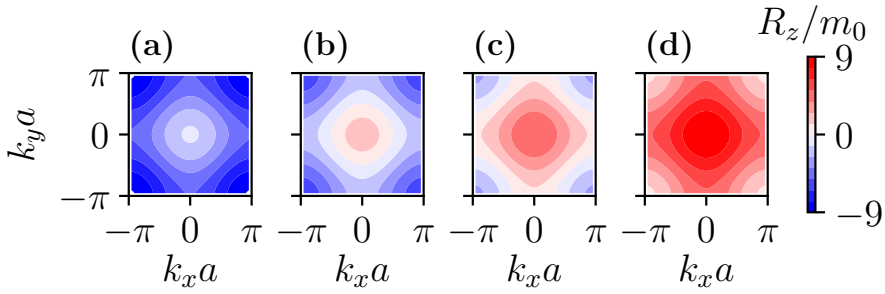

Figure 1.4: R_z as a function of k_x and k_y for the four different regimes listed in the text. The numerical value of the parameters is $\mu/m_0 = -1, 2, 5, 9$ in panels (a), (b), (c) and (d), respectively.

where the superscript corresponds to the band, valence $(-)$ or conduction $(+)$. Employing this result and after some algebra, it can be proven that

$$\mathbf{\Omega}_z^{\pm} = \frac{\partial \mathcal{A}_y^{\pm}}{\partial k_x} - \frac{\partial \mathcal{A}_x^{\pm}}{\partial k_y} = \pm \frac{\mathbf{u_R}}{2R^2} \cdot \left(\frac{\partial \mathbf{R}}{\partial k_x} \times \frac{\partial \mathbf{R}}{\partial k_y} \right) , \tag{1.31}$$

where $\mathbf{u_R} \equiv \mathbf{R}/R$. By integrating equation (1.23a) over the thoroidal 1BZ surface, the only component of the Berry connection that contributes is in the z-direction, leading to a Chern number

$$C^{(\pm)} = \pm \frac{1}{2\pi} \int_{BZ} dk_x dk_y \frac{\mathbf{u_R}}{2R^2} \cdot \left(\frac{\partial \mathbf{R}}{\partial k_x} \times \frac{\partial \mathbf{R}}{\partial k_y} \right) . \tag{1.32}$$

The former expression corresponds to the integral of the area of the surface of $\mathbf{R}$ in fact,

$$\mathbf{u_R} \cdot d^2\mathbf{S} = \mathbf{u_R} \cdot \left(\frac{\partial \mathbf{R}}{\partial k_x} dk_x \right) \times \left(\frac{\partial \mathbf{R}}{\partial k_y} dk_y \right) . \tag{1.33}$$

Dividing by R^2, the integration gives the solid angle subtended by the surface. In the case of a closed surface, the solid angle is $4\pi w$, where w is an integer number that quantifies the times that the surface wraps around the unit sphere. The Chern number is thus directly given by the winding number w.

$$C^{(\pm)} = w^{\pm} . \tag{1.34}$$

For the modified Dirac equation, depending on the parameters, the wrapping of the surface of $\mathbf{R}$ can be easily obtained by the sign of R_z:

1. If $m < 0$: the surface is not wrapped due to the negative sign of R_z over the whole 1BZ. The Chern number is then $C^{(\pm)} = 0$.

2. If $0 < m < 4\mu$: the surface is wrapped once by the $\mathbf{R}$ due to the sign change of R_z. Hence the Chern number is $C^{(\pm)} = \pm 1$.

3. If $4\mu < m < 8\mu$: the sign of R_z changes in the opposite way of the case (2) leading to the opposite sign in the winding number and hence $C^{(\pm)} = \mp 1$.

4. If $m > 8\mu$: similarly to the case (1), the constant positive sign of R_z implies that the surface can not be wrapped by $\mathbf{R}$ and $C^{(\pm)} = 0$.

The sign convention of the winding number w and consequently of the Chern number C is arbitrary, but it must be consistent when the winding direction is reversed. In conclusion, the modified Dirac equation has topological bulk bands for some range of parameters, and the topological nature is captured by the Chern number of the bands, which is modified when the band gap closes.

1.3 Models for topological insulators and semimetals

The modified Dirac equation, or equivalently the 2D Chern insulator, is a simplified case of the more general class of 2D insulators with broken time-reversal (TR) symmetry[4]. In the classification of topological single-particle phases [42], this class is the class A and the topology is encoded in the Chern number. The Chern number, also known as TKNN from the work of Thouless-Kohmoto-Nightingale-Nijs [264], is a specific topological invariant for gapped systems with broken TR symmetry. However, in order to describe systems with TR symmetry, with higher dimensions or with gap closure, other topological invariants are defined. In this thesis the derivation of the other topological invariants is traced back to the Chern number. In fact, the systems studied in this work can always be related to effective 2D systems with a well-defined Chern number. In the following, the main models used in the upcoming chapters are introduced and related to the 2D Chern state.

1.3.1 Quantum spin Hall

The first example of a realistic Hamiltonian based on the modified Dirac equation is the quantum spin Hall (QSH) state. The QSH state was the first TI to be experimentally observed by Koenig et al. in 2007 [139].

[4] See appendix A for a more detailed discussion about TR symmetry.

The existence of such a phase had been predicted a few years earlier in a graphene system by Kane and Mele [123] and a year later in HgTe/CdTe quantum well structures by Bernevig, Hughes and Zhang [19].

The model for semiconductor quantum wells, also known as the BHZ model after the initials of Bernevig, Hughes and Zhang, can be directly related to the modified Dirac equation and is discussed below. The Kane-Mele model is based on the symmetry of the hexagonal lattice and is discussed in more detail in section 4.1.2, where graphene-based systems are treated.

The BHZ model describes the four bands close to the Fermi level near the Γ point of HgTe/CdTe quantum wells. The wells consist of a layer of HgTe with thickness d embedded in CdTe. The CdTe band structure is similar to that of other semiconductors and shows two conduction states with s symmetry and two valence states with p symmetry. The double degeneracy of the states is due to the spin. On the other hand, in HgTe the p states have a higher energy with respect to the s states due to the strong spin-orbit coupling, and hence the bands are *inverted* with respect to the ordering in CdTe.

The effective Hamiltonian for the quantum well describes the subbands of the well formed by the hybridisation of the bulk bands coming from the two materials. The band ordering of the subbands depends on the width of the HgTe layer. If $d < d_c$, the quantum well bounded states obtained show the same band ordering of CdTe. On the other hand if $d > d_c$ the bound states have an inverted band order. The critical value for the thickness is $d_c = 6.3\,\mathrm{nm}$ [19].

In the basis set of the quantum well subbands, the effective Hamiltonian is expressed by [19]

$$H = \sum_{\mathbf{k}} (c^\dagger_{s\uparrow}, c^\dagger_{p\uparrow}, c^\dagger_{s\downarrow}, c^\dagger_{p\downarrow}) \begin{pmatrix} h(\mathbf{k}) & h_I(\mathbf{k}) \\ h_I^\dagger(\mathbf{k}) & h^*(-\mathbf{k}) \end{pmatrix} \begin{pmatrix} c_{s\uparrow} \\ c_{p\uparrow} \\ c_{s\downarrow} \\ c_{p\downarrow} \end{pmatrix}, \tag{1.35}$$

where the creation and annihilation operators are labelled by their parity symmetry s or p.

If the system is inversion symmetric and the symmetry around the growth axis is preserved, the interblock element $h_I(\mathbf{k})$ vanishes [19]. The Bloch Hamiltonian is then reduced to two blocks of 2×2. The $h(\mathbf{k})$ block

can be written by equation (1.26) with the vector $\mathbf{R}(\mathbf{k})$ given by

$$R_x(\mathbf{k}) = vk_x \ , \tag{1.36a}$$
$$R_y(\mathbf{k}) = vk_y \ , \tag{1.36b}$$
$$R_z(\mathbf{k}) = m_0 - m_1(k_x^2 + k_y^2) \ , \tag{1.36c}$$
$$R_0(\mathbf{k}) = c_0 - c_1(k_x^2 + k_y^2) \ , \tag{1.36d}$$

where v, m_0, m_1, c_0, c_1 are constants of the model that depend on the material and the width. The form of $h(\mathbf{k})$ is equivalent to the modified Dirac Hamiltonian (1.14) by including the additional term $R_0(\mathbf{k})$. The term $R_0(\mathbf{k})$ has no effect on the topology of the bands. In fact it does not change the winding of the vector $\mathbf{R}$ when computing the Chern number according to the discussion in section 1.2.2. Then, each of the sectors of the BHZ model is topological if $m_0 m_1 > 0$.

For CdHgTe quantum wells of 55 Å and 70 Å the parameters are listed in table 1.1. Note that even if all the parameters are modified by the width, only the mass term m_0 changes sign, while m_1 remains negative. The sign change in the gap defines the topological transition between a trivial state for $d = 55$ Å and a topological state for $d = 70$ Å.

d	55 Å	70 Å
v [eV Å]	3.87	3.65
m_1 [eVÅ^2]	-48.0	-68.6
c_1 [eV]	-30.6	-51.1
m_0 [eV]	0.009	-0.010

Table 1.1: Values for the parameters of CdHgTe wells from reference [157, 221]. The values of c_0 in equation (1.36d) are not reported as they are a constant term that only shifts the Fermi energy.

Up to this point, the topology of the BHZ model has only been discussed in terms of the topology of each of the subblocks. However, the total Hamiltonian includes two sectors that are found to be TR partners. In the basis of the BHZ mode, the TR operator is given by the usual form for a 1/2-spin particle, as discussed in appendix A.2

$$\Theta = i\sigma_y \mathcal{K} \tau_0 \ , \tag{1.37}$$

where the τ_0 is the 2×2 unit matrix that acts on the orbital basis and the σ_y acts on the spin basis. Since the Θ operator converts $h(\mathbf{k}) \to h^*(-\mathbf{k})$ and also exchanges the spin up and spin down, the BHZ Hamiltonian is TR symmetric and $h(\mathbf{k})$ and $h^*(-\mathbf{k})$ are TR partners.

The TR symmetry has an important effect on the states due to the so-called Kramers degeneracy, which follows from the Kramers' theorem

proved in appendix A.3. The Kramers degeneracy implies that a Bloch state $u_{\mathbf{k},s}$ with energy $\epsilon_{\mathbf{k},s}$ and its TR partner $\Theta u_{\mathbf{k},s}$ have the same energy and both states are orthogonal. The pairs of states are called Kramers states and they cannot scatter as long as the TR symmetry is preserved.

The forbidden backscattering of Kramers pairs is easy to prove. For a non-magnetic potential described by a TR invariant operator V, from the Kramers' theorem and the antiunitary property of Θ it follows that

$$\begin{aligned}\langle u_{\mathbf{k},s}|V|\Theta u_{\mathbf{k},s}\rangle &= -\langle u_{\mathbf{k},s}|\Theta V\Theta|\Theta u_{\mathbf{k},s}\rangle \\ &= -\langle \Theta u_{\mathbf{k},s}|V|u_{\mathbf{k},s}\rangle^* = -\langle u_{\mathbf{k},s}|V|\Theta u_{\mathbf{k},s}\rangle = 0\ . \end{aligned} \tag{1.38}$$

Thus the TR symmetry enforces the degeneracy of the levels but protects them from backscattering. In particular, in the BHZ model, the Hamiltonian is TR symmetric and any non-magnetic perturbation does not produce backscattering between the Kramers states.

This kind of protection is due to a topological property of the bands. However, the Chern number cannot determine directly the topology of TR systems. In fact, the Kramers partners show opposite $C^{(n)}$ due to the sign exchange of the momentum in the derivatives of equation (1.21) and (1.23b). Hence, the added Chern number of the two Kramers bands is always zero.

A related quantity to the Chern number, called the $\mathbb{Z}_2$ invariant, is defined in TR invariant systems. The $\mathbb{Z}_2$ invariant has been formulated in several ways [125]. In systems with a well-defined spin projection in z it can be obtained from the Chern number of the TR sectors [246]. In a more general situation, the Pfaffian [79, 124] has to be calculated.

In the case of the BHZ model, the $\mathbb{Z}_2$ invariant can be obtained by counting the number of topological Kramers pairs [246] or equivalently by the Chern number of one of the TR sectors. The scattering between the two Chern sectors is prevented by the symmetries of the system [19] and the conservation of the z-component of the spin.

In conclusion, the BHZ model is topological whenever $h(\mathbf{k})$ has a topological Chern number, i.e. when $m_0 m_1 > 0$. In figure 1.5, the dispersion relation and the probability density for the two states below the Fermi level are plotted for a ribbon of 100 nm in the trivial and topological regimes. In the trivial regime, the system is gapped and the states below the Fermi energy are bulk states delocalised along the transverse direction of the ribbon width, see panels (a) of figure 1.5. For the topological regime, the dispersion relation shows two degenerate bands corresponding to the edge states, see panel (c) of figure 1.5. The probability density of these states peaks near the boundaries, as shown in figure 1.5(d). In the direction of PBC, the edge states show a Dirac-like linear dispersion relation, as shown in figure 1.5 (c).

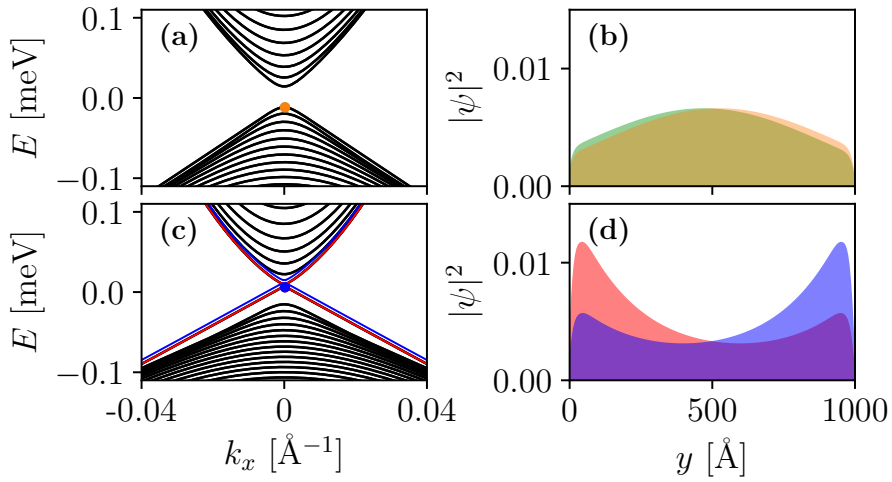

Figure 1.5: Dispersion relation (a) and probability density for the two states below the Fermi energy (b) for the BHZ model with parameters corresponding to a trivial phase for a quantum well of $d = 55$ Å (the parameters are reported in the first column of table 1.1). The ribbon has PBC in the x-direction while the y-direction is 100 nm width. In panel (c) and (d) the dispersion relation and the probability density are depicted for the topological regime, corresponding to a quantum well of $d = 70$ Å (the parameters correspond to the second column of table 1.1). The topological and degenerate bands are depicted in red and blue in panel (c); a small offset is introduced in order to improve the visibility. The states in (b) and (d) are calculated near the Dirac point at $k_x = 2 \times 10^{-4}$Å^{-1}. The energy of the states is represented in colored dots in the corresponding band dispersion.

For a Fermi energy inside the bulk gap, the topological ribbon has two conducting channels in each direction of propagation, given by the two edge states, with a total of four surface states. For each edge, the two localised states have opposite momentum and spin, since they come from the opposite subblock $h(\mathbf{k})$ or $h^*(-\mathbf{k})$. For each subblock, the spin in z is well defined and therefore the states from $h(\mathbf{k})$ are spin-up while those from $h^*(-\mathbf{k})$ are spin-down. The fact that each spin is associated with a band with a well-defined direction of propagation leads to the concept of *helicity* in the surface states. Indeed, the projection of the spin over the momentum is constant in each surface state band. The two surface states with opposite momentum and the same localisation in the edge are then called *helical partners* and they are prevented from scattering to each other by the fact that they are Kramers partners. As proved by equation (1.38), the Kramers partners are protected against

backscattering whenever TR symmetry is preserved.

On the other hand, the two surface states with the same momentum and energy are found to be localised at opposite sides of the ribbon. Thus, even if they are not prevented from hybridising by symmetry constraints, the spatial distribution minimises the overlap of the states. This leads to a quantized conductance of e^2/h associated with each set of edge states whenever the TR symmetry is conserved and the ribbon width is large enough to prevent hybridisation of the surface states from the opposite sides. By measuring the resistance signal as a function of the gate voltage, which modifies the Fermi energy, a quantized signal was measured in HgTe/CdTe wells of width $d > d_c$ [139, 219]. Theoretically, the quantized signal can be understood within the Landauer-Büttiker formalism [27] presented in appendix B.

1.3.2 3D topological insulators

The topological characterisation introduced for the 2D Chern state can be generalised to the case of 3D materials [80, 174] by including up to four topological invariants and 16 different phases. The first 3D TI observed experimentally was the semiconducting alloy $Bi_{1-x}Sb_x$ where angle-resolved photoemission spectroscopy (ARPES) imaged the surface bands [113]. A year later, the family of Bi_2Se_3 and Bi_2Te_3 was theoretically predicted [313] and experimentally demonstrated as a 3D TI [298]. Bi_2Se_3 exhibits a larger bandgap of the order of 300 meV, so the topological properties are expected to be observable at room temperature [114]. In the case of Bi_2Te_3 the gap is of the order of 165 meV [38] and a strong trigonal warping term is present in the surface state Hamiltonian.

In this thesis the 3D TIs are addressed in chapter 3 for slab geometries. The model used to describe the 3D TIs is obtained by $\mathbf{k}\cdot\mathbf{p}$ theory and by fitting of density functional theory (DFT) bands [155]. In the 3D case, similar to the 2D Chern state, the topological nature of the bands is generated by the band inversion due to spin-orbit coupling. In figure 1.6, the process of hybridisation and inversion is schematised for the case of Bi_2Se_3, starting from the atomic orbitals and considering the effect of the crystalline structure and the spin-orbit coupling. The bands underlined in the figure correspond to those found to be closest to the Fermi level, i.e. the $|P_1^+\uparrow\rangle$, $|P_2^-\downarrow\rangle$, $|P_1^+\downarrow\rangle$, $|P_2^-\uparrow\rangle$, where the superscript indicates the parity. The Hamiltonian in this basis reads as [155]

$$\mathcal{H}(\mathbf{k}) = \begin{bmatrix} h_+(\mathbf{k}) & Bk_z\sigma_y \\ Bk_z\sigma_y & h_-(\mathbf{k}) \end{bmatrix} , \tag{1.39a}$$

$$h_\pm(\mathbf{k}) = \epsilon(\mathbf{k})\mathbb{1}_2 + M(\mathbf{k})\tau_3 + Ak_x\tau_1 \pm Ak_y\tau_2 , \tag{1.39b}$$

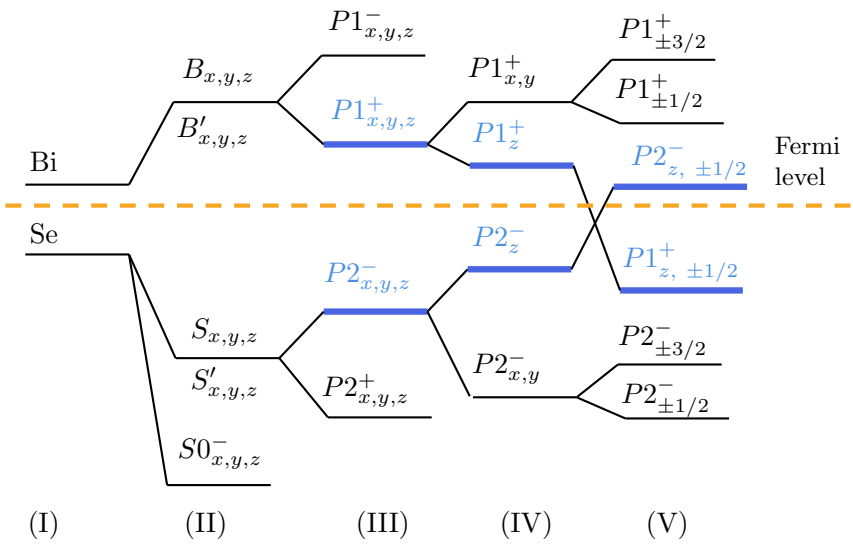

Figure 1.6: Schematic representation of the inversion process in Bi_2Se_3 bands step by step. In (I) the atomic orbitals of Bi and Se are shown. In (II) the hybridisation of the Bi and Se orbitals is included, and in (III) the formation of the bonding and anti-bonding states due to the inversion symmetry is considered. In (IV) the crystal field splitting due to the layered structure of the crystal in the z-direction is incorporated. Finally, the influence of the spin-orbit coupling is included in (V). Figure adapted from reference [155].

where the σ_i and τ_i denote the Pauli matrices acting on the spin basis and the basis of P_1^+ and P_2^- subbands, respectively. In the former expression, the following functions are defined to depend quadratically on the momentum

$$\epsilon(\mathbf{k}) = C_0 + C_1 k_z^2 + C_2 \left(k_x^2 + k_y^2\right) \ , \tag{1.39c}$$

$$M(\mathbf{k}) = M_0 - M_1 k_z^2 - M_2 \left(k_x^2 + k_y^2\right) \ . \tag{1.39d}$$

For Bi_2Se_3 the parameters of Hamiltonian (1.39a) are listed in table 1.2.

Next, the topological properties of the Hamiltonian (1.39a) are related to the Chern number defined in the previous section. Considering $\mathbf{k} = 0$, the Hamiltonian becomes

$$\mathcal{H}(\mathbf{k} = 0) = C_0 \mathbb{1}_4 + M_0 \tau_3 \otimes \sigma_0 \ , \tag{1.40}$$

such that the band edge energies can be obtained directly. The conduction (valence) band energy is $C_0 \pm M_0$, the gap is $\Delta = 2M_0$ and the centre of

Numerical values for the parameters of Bi_2Se_3		
$A = 3.33\,\text{eV Å}$	$C_0 = -0.0083\,\text{eV}$	$M_0 = -0.28\,\text{eV}$
$B = 2.26\,\text{eV Å}$	$C_1 = 5.74\,\text{eV Å}$	$M_1 = -6.86\,\text{eV Å}$
	$C_2 = 30.4\,\text{eV Å}^2$	$M_2 = -44.5\,\text{eV Å}^2$

Table 1.2: Values for the parameters of Bi_2Se_3 from reference [155]. Note that compared to reference [155] the sign of M_1 and M_2 is reversed due to the opposite sign definition in Hamiltonian (1.39a). The sign was reversed to match the sign convention employed in the modified Dirac equation.

the gap is C_0. Linearizing the Hamiltonian around the Γ point gives the following expression

$$\mathcal{H}(\mathbf{k}) \simeq Ak_x\tau_1 \otimes \sigma_0 + Ak_y\tau_2 \otimes \sigma_z + Bk_z\tau_x \otimes \sigma_y + \frac{\Delta}{2}\tau_3 \otimes \sigma_0 + C_0\mathbb{1}_4 \ . \quad (1.41)$$

The dispersion near the Γ point is then directly given by

$$E(\mathbf{k})^{\pm} \simeq C_0 \pm \sqrt{A^2(k_x^2 + k_y^2) + B^2k_z^2 + \frac{\Delta^2}{4}} \ . \quad (1.42)$$

At low energy and close to $\mathbf{k} = 0$, the dispersion resembles an anisotropic version of the gapped liner Dirac equation (1.6). Thus, as before, the relative sign of the gap with respect to the quadratic term given by M_1 and M_2 ensures the existence of topological states for the band-inverted regimes. For Bi_2Se_3 with parameters given in table 1.2 the quadratic term is negative in the three spatial directions, i.e. $M_1 < 0$ and $M_2 < 0$, as well as the gap $M_0 < 0$. Hence $M_0M_1 > 0$ and $M_0M_2 > 0$ and the topological surface states are then expected in the three spatial directions [312].

In particular, in a finite slab in z with PBC in the x and y-directions, the effective model for the surface states localised near the surface in z is given by [78, 155, 242, 313].

$$\mathcal{H}_0(k_x, k_y) = (c_0 + c_2k^2)\mathbb{1}_2 + v(k_y\sigma_x - k_x\sigma_y) + r(k_+^3 + k_-^3)\sigma_z \ , \quad (1.43)$$

where $k^2 = k_x^2 + k_y^2$ and $k_\pm = k_x \pm ik_y$. The surface state parameters are related to the bulk spectrum parameters given in table 1.2 by [155]

$$c_0 = C_0 + \alpha_3 M_0 \ , \quad (1.44a)$$
$$c_2 = C_2 - \alpha_3 M_2 \ , \quad (1.44b)$$
$$v = A_0\alpha_1 \ , \quad (1.44c)$$
$$r = R_1\alpha_1/2 \ , \quad (1.44d)$$

where $\alpha_1 = 0.99$ and $\alpha_3 = -0.15$ are defined to match the experimental values of the velocity and the position of the Dirac points [298] following the fit of reference [155].

The 3D TIs are examined in chapter 3 and the effective model for the 2D states is treated in chapters 5 and 6. In chapter 3, heterostructures of doped 3D TIs are studied under external electric fields in the growth direction. The heterostructures are formed by stacking slabs in such a way that the z-direction enters as a finite width modifying the effective gap. The surface states are studied under external fields within the Floquet formalism in chapter 6 while the effect of disorder is addressed in chapter 5. Based on an effective 2D model for the surface states, these two chapters neglect the contribution of the bulk bands.

1.3.3 Weyl and Dirac semimetals from the Chern insulator

Topological states of matter include gap and gapless systems. In particular, when the valence and conduction bands touch at a zero-measure set of points in the BZ, a TSM is obtained. In this thesis two types of TSMs are studied under the effect of external fields in chapter 2, namely the Weyl and Dirac semimetals (WSMs and DSMs). The details of these topological phases are described in the aforementioned chapter, although the topological properties are discussed in the following by deriving a minimal model from the Chern insulator.

A WSM can be constructed from the modified Dirac equation by adding an extra term that allows to change the sign of the mass term and hence the topology of the system. Starting from equation (1.14) the Hamiltonian can be rewritten as [245, 270]

$$\mathcal{H}(k_x, k_y) = vk_x\sigma_x + vk_y\sigma_y + \left[(m_0 - \alpha) - m_1(k_x^2 + k_y^2)\right]\sigma_z \ , \qquad (1.45)$$

where the mass term m was replaced in equation (1.14) by $m \to m_0 - \alpha$. For simplicity, the sign of $m_1 > 0$ and $m_0 > 0$ are fixed in the following, the other cases can be easily discussed in the same footing. Considering the sign convention, the topological phase is now given by $m_0 - \alpha > 0$, being trivial otherwise.

Turning to 3D, the role of α can be coincident with a momentum in the z-direction by $\alpha \equiv m_1 k_z^2$, so that the Hamiltonian is now given by

$$\mathcal{H}_W(k_x, k_y, k_z) = vk_x\sigma_x + vk_y\sigma_y + \left[m_0 - m_1(k_x^2 + k_y^2 + k_z^2)\right]\sigma_z \ . \quad (1.46)$$

The dispersion relation is gapless in two points of the momentum space at $\mathbf{k}_\pm = (0, 0, \pm k_W)$ with $k_W = \sqrt{m_0/m_1}$ and three different topological phases are obtained by spanning the values of k_z:

- if $k_z < -k_W$, the system is trivial;
- if $-k_W < k_z < k_W$,the system is topological and exhibits surface states in a finite-size system;
- if $k_z > k_W$, the system is again in a trivial phase.

This simple derivation is sufficient to obtain the isotropic version of the Hamiltonian for WSMs. The two points where the conduction and valence bands touch are called *Weyl points* and the surface states that appear between them form a line called *Fermi arc*. By considering k_z as a parameter, the Chern number of the bands of the Hamiltonian (1.46) can be directly related to the calculation of the 2D Chern insulator by

$$C^{\pm}(k_z) = \begin{cases} 0 & \text{if } |k_z| > k_W \ , \\ \pm 1 & \text{if } |k_z| < k_W \ , \end{cases} \tag{1.47}$$

where the superscript indicates the band, valence $(-)$ or conduction $(+)$.

The distance of the Weyl nodes in the reciprocal space gives the protection of the Weyl nodes. In fact, an external perturbation is generally written as

$$\delta\mathcal{H} = f_0\sigma_0 + \mathbf{f}\cdot\boldsymbol{\sigma} \ , \tag{1.48}$$

where $\mathbf{f} = (f_x, f_y, f_z)$. Adding this perturbation to the Weyl Hamiltonian (1.46) shifts the position of the Weyl nodes in reciprocal space. However, the Weyl nodes disappear only if the external perturbation brings the two Weyl nodes so close that they annihilate in pairs. Thus the Weyl nodes are stable to small perturbations of the Hamiltonian parameters and the distance in the reciprocal space, $2k_W$ in the model considered, quantifies the protection of the nodes.

Figure 1.7 shows the dispersion relation of a WSM nanoribbon with finite width in the y-direction and PBC in the x and z-directions. In panel (a) the dispersion relation for $k_x = 0$ is plotted as a function of k_z. The two Weyl points are obtained at $k_z = \pm k_W$ and are connected by two flat Fermi arcs. The Fermi arcs appear in pairs due to the existence of two edges in the nanoribbon, located at $y = \pm L/2$, and they are flat in the k_z-direction for this simplified particle-hole symmetric model. In the direction perpendicular to the line of nodes, i.e. the k_x-direction, the Fermi arcs are linearly dispersive, as shown in panel (b). The spatial distribution of the Fermi arc wavefunctions is peaked near the two edges as shown in orange in panel (c). On the other hand, in the trivial region of k_z, the states are extended in the bulk, as shown by the green wavefunction in panel (c).

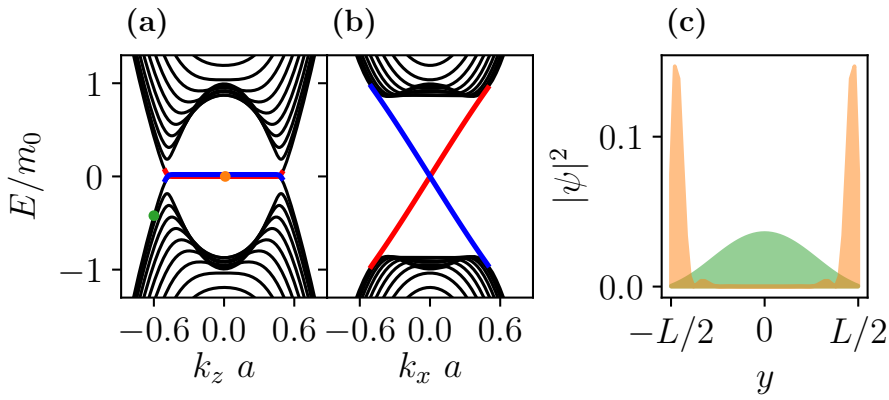

Figure 1.7: Dispersion relation for $k_x = 0$ as a function of k_z (a) and energy bands for $k_z = 0$ as a function of k_x (b). The Fermi arcs are underlined in blue and red colours, while the bulk bands are shown in black. In (c) the $|\psi|^2$ of the first state below the Fermi level is plotted for $(k_x a, k_z a) = (-0.6, 0)$ in green and $(k_x a, k_z a) = (0.01, 0)$ in orange. The corresponding energies are marked by coloured dots in panel (a). The parameters used are $L = 50a$, $m_1/(a^2 m_0) = 4$ and $v/(am_0) = 2$; a denotes the lattice constant employed in the discretization.

The TR partner of the Hamiltonian (1.46) is obtained by applying the TR operator for spinless particles (the spin of the two bands in the WSM is considered the same), given by equation (A.8). Thus the TR partner of $\mathcal{H}_W(\mathbf{k})$ is equal to $\mathcal{H}_W^*(-\mathbf{k})$, as in the case of the BHZ model.

For convenience, the WSM Hamiltonian can be re-defined by

$$\mathcal{H}_{W,\zeta}(k_x, k_y, k_z) = \zeta v k_x \sigma_x + v k_y \sigma_y + \left[(m_0 - m_1(k_x^2 + k_y^2 + k_z^2)\right] \sigma_z \ , \tag{1.49}$$

where the $\zeta = \pm 1$. In this way, the TR partner can be easily constructed by the exchange of the sign of ζ.

The sign of ζ is related to the so-called *chirality* of the Weyl nodes. The chirality is similar to the helicity in 2D and is related to the winding direction of the Berry phase. In the case of the Weyl Hamiltonian, the Berry curvature has two discontinuities in the BZ corresponding to the Weyl points due to the gap closure. The two discontinuities have opposite signs. In fact, the Weyl point at $\mathbf{k} = (0, 0, k_W)$ is found to be a source (sink) of the Berry curvature for $\zeta = +1(-1)$, while the other Weyl point has the opposite behaviour, being a sink (source) of the Berry curvature for $\zeta = +1(-1)$. Then, for a given ζ, the two Weyl points are said to have opposite chirality and the two Hamiltonians $\mathcal{H}_{W,+1}$ and $\mathcal{H}_{W,-1}$ have opposite chirality since they exchange the chirality of the Weyl points.

The chirality has a physical meaning: it relates to the two TR partners, thus interchanging the spin and the direction of propagation.

Using two TR partners, a DSM can be built in the same way that the BHZ Hamiltonian was obtained from the two Chern insulator states. If no coupling between the two Weyl sectors is included, the DSM is described by

$$\mathcal{H}_D(\mathbf{k}) = \begin{pmatrix} \mathcal{H}_{W,+1}(\mathbf{k}) & 0 \\ 0 & \mathcal{H}_{W,-1}(\mathbf{k}) \end{pmatrix} . \tag{1.50}$$

The DSM has double degenerate bands which are TR partners to each other except in the Dirac points where the degeneracy becomes fourfold. As in the case of the BHZ Hamiltonian, the total Chern number of the occupied bands is zero when counting for the two valence bands coming from the opposite Weyl blocks. However, if an additional symmetry prevents the coupling terms between the Weyl sectors, the bands are decoupled and topological. Such symmetries are the up-down parity symmetry [96, 97] or space group symmetries [84, 259, 307].

In this thesis the DSM studied is Na_3Bi. For this compoud, the up-down parity symmetry preserves the two Weyl sectors and is given by [97]:

$$U\ \mathcal{H}(-k_z)\ U^{-1} = \mathcal{H}(k_z)\ , \tag{1.51a}$$

$$U = \begin{pmatrix} \sigma_0 & 0 \\ 0 & -\sigma_0 \end{pmatrix} . \tag{1.51b}$$

The eigenstates of the parity operator correspond to bispinors with either upper or lower components coming from each pair of Weyl nodes.

In particular, to describe Na_3Bi and Cd_3As_2, a modified version of the Hamiltonian in equation (1.46) is used in the construction of the 4×4 Dirac Hamiltonian [286, 287]. The corresponding Weyl Hamiltonian is given by

$$\mathcal{H}_{W,\zeta}(\mathbf{k}) = \epsilon_0(\mathbf{k})\mathbb{1}_2 + M(\mathbf{k})\sigma_z + v(\zeta k_x\sigma_x - k_y\sigma_y)\ , \tag{1.52a}$$

$$\epsilon_0(\mathbf{k}) = c_0 + c_1k_z^2 + c_2(k_x^2 + k_y^2)\ , \tag{1.52b}$$

$$M(\mathbf{k}) = m_0 - m_1k_z^2 - m_2(k_x^2 + k_y^2)\ . \tag{1.52c}$$

$\mathbb{1}_n$ stands for the $n \times n$ unit matrix and the sign convention for k_y is reversed compared to equation (1.46) to match the usual form of the Hamiltonian in the literature [96, 97, 286, 287]. This Hamiltonian has two degeneracy points at $\mathbf{k}_D = (0, 0, \pm\sqrt{m_0/m_1})$ and generalises the minimal model (1.46) by allowing anisotropy in the z-direction and particle-hole asymmetry via $\epsilon_0(\mathbf{k})$.

The Chern number can be still obtained from the equivalent Chern insulator by considering k_z as a parameter and by calculating the Chern

number for each TR sector, i.e. for the Weyl blocks separately. The diagonal dispersive term $\epsilon_0(\mathbf{k})$ has no effect on the topology of the system. Similarly to the case of the BHZ model, the R_0 term do not enter in the computation of the Chern number in equation (1.32). The Chern number as a function of k_z is then

$$C_\zeta^\pm(k_z) = \begin{cases} 0 & \text{if } |k_z| > k_W \ , \\ \pm\zeta 1 & \text{if } |k_z| < k_W \ , \end{cases} \tag{1.53}$$

where the dependence of the chirality of the Weyl Hamiltonian is explicitly indicated by ζ. Therefore, for DSMs, between the two Dirac nodes, a pair of Fermi arcs originating from each Weyl sector connects the degeneracy points.

In particular, for Na_3Bi, the Hamiltonian (1.52a) is obtained from the DFT fitting of the low energy bands crossing near the Γ point of the $\mathbf{k}\cdot\mathbf{p}$ model. The bands involved in the crossing process come from Na-$3s$ and Bi-$6p_{x,y,z}$ orbitals. By combining the orbital states in bonding and antibonding states with definite parity and including the spin-orbit coupling, the four states closer to the gap are [287]

$$\left|S^+_{1/2}, \frac{1}{2}\right\rangle, \quad \left|P^+_{3/2}, \frac{3}{2}\right\rangle, \quad \left|S^-_{1/2}, -\frac{1}{2}\right\rangle, \quad \left|P^-_{3/2}, -\frac{3}{2}\right\rangle \ , \tag{1.54}$$

where the the superscript indicates the parity, the subscript denotes the total angular momentum J obtained from coupling the spin and the orbital angular momentum, and the projection in J_z is indicated at the right. The states are sorted according to the order of the basis in which the Hamiltonian is written (1.50), with each Weyl subblock given by equation (1.52a). The fitted parameters for Na_3Bi are listed in table 1.3. Note that $m_0 m_1 > 0$ and hence the Chern state between the Dirac nodes is non-trivial.

Numerical values for the parameters of Na_3Bi		
	$c_0 = -0.06382\,\text{eV}$	$m_0 = -0.08686\,\text{eV}$
$v = 2.4598\,\text{eVÅ}$	$c_1 = 8.7536\,\text{eVÅ}^2$	$m_1 = -10.6424\,\text{eVÅ}^2$
	$c_2 = -8.4008\,\text{eVÅ}$	$m_2 = -10.3610\,\text{eVÅ}$

Table 1.3: Values for the parameters of Na_3Bi from reference [287].

The TSMs are the main focus of chapter 2, where external electric fields are used to tune the Fermi arcs. The models addressed are the minimal model given by the Hamiltonian (1.46) and the model with dispersive diagonal terms in equation (1.52a). In the second case, the additional terms

bend the surface state bands in the direction of the nodal line. However, as already discussed, the Fermi arcs are still protected by the topology and they appear between the degeneracy points and exhibit linear dispersion in the directions perpendicular to the nodal line. In chapter 2, the analytical expression of the Fermi arcs is derived in detail. The existence conditions extracted from the algebraic solution give a complementary derivation of the conditions of existence of the topological states.

1.4 Concluding remarks

In conclusion, this chapter has been devoted to the introduction of the modified Dirac equation and the topology associated with this Hamiltonian. Starting from the linear Dirac equation in section 1.1, adding quadratic terms was proven to be indispensable to define the topology of the system. In this way the Chern number was defined in section 1.2.1, and the geometrical interpretation of the Chern number as a winding number of the Hamiltonian over the unit sphere was also discussed in section 1.2.2 for the 2D Chern insulator, which is the lattice realisation of the modified Dirac equation.

After calculating the Chern number for the Chern insulator, some representative models for the systems addressed in this thesis are briefly discussed. First, the QSH state, which is formed by two copies of Chern insulators related by time inversion, is discussed in section 1.3.1. Then the 3D TIs of the family of Bi_2Se_3 and Bi_2Te_3 are introduced as a higher dimensional generalization of the 2D Chern insulator in section 1.3.2.

Finally, the TSMs are discussed in section 1.3.3 from the idea of dynamically modifying the gap, and hence the topology of the bands, by adding a momentum in the z-direction. In this way the Chern number is still defined as a function of k_z and a topological phase coexists with a trivial phase for different momenta. The minimal model is built using the former argument, and a more complex model describing Na_3Bi and Cd_3As_2 is presented at the end of the section.

This introductory chapter provides the basic tools for understanding the topology of the systems that will be studied in this thesis. For a complete review of topology applied to condensed matter systems, the reader is referred to more extensive literature such as the references [11, 18, 42, 107, 108, 245], among many others.

2 IMPACT OF EXTERNAL FIELDS IN TOPOLOGICAL DIRAC AND WEYL SEMIMETALS

Preamble

As already discussed in section 1.3.3, the TSMs are topological 3D systems where the bands touch at isolated points in the 1BZ. In WSMs, near the Weyl node, the dispersion relation appears as a 3D analogous of graphene and it is described by an anisotropic version of the Weyl equation. The conduction and valence bands are individually non-degenerate and hence either TR or inversion symmetry is broken. The Weyl nodes are monopoles of Berry curvature and the topological charge associated with them is called chirality [11, 26]. Due to the Nielsen-Ninomiya no-go theorem [180], the Weyl nodes come in pairs and are annihilated only in pairs. As discussed in section 1.3.3, the separation of the nodes in the reciprocal space quantifies the robustness of the Weyl nodes and topological states, called Fermi arcs, connect the them. The topological nature of these nodes can be intuitively understood by comparing the 2D Chern state with the gapped states in between Weyl nodes, as presented also in section 1.3.3.

In the case of DSMs, both TR and inversion symmetry are present, and additional symmetries assure the topological protection by splitting the Dirac Hamiltonian in two Weyl sectors: a discrete symmetry called up-down parity symmetry [96, 97] or space-group symmetries [84, 259, 307]. Consequently, the Dirac points are four-fold degenerated and the net Chern number of the nodes is zero, whereas each sector is topologically non-trivial. Assuming the up-down symmetry, each Dirac point can be obtained by imposing two Weyl nodes with opposite chirality. This is the case of compounds such as A_3Bi where $A = Na, K, Rb$ and Cd_3As_2, in which ARPES experiments corroborate the existence of the Fermi arcs [159, 160, 179, 302].

The topological response of WSMs and DSMs comprises the manifestation of the chiral anomaly in a large negative magnetoresistance, in the presence of both electric and magnetic field, and in an anomalous Hall effect, due to electron transport through surface states [11, 245]. In

ultra-thin slabs of Na_3Bi a topological phase transition have been experimentally achieved by the external electric field [44]. On the other hand, in wider slabs, quantised conductance have been experimentally measured for Cd_3As_2 [181, 182, 311] and it has been interpreted as the surface transport mediated by Weyl orbits that connect the channels from opposite sides of the sample (i.e. through the bulk) in the presence of magnetic field. The understanding of the effect of external fields on the topological nature of DSMs and WSMs is of primary importance in order to interpret correctly the experimental results as well as to understand the possibilities of the semimetallic topological phases from the perspective of transport applications.

The chapter is organised as follows:

- Section 2.1 discusses the models for the TSMs that are going to be used in the subsequent calculations. The models were already presented in section 1.3.3. Here, the analytic expression for the Fermi arcs is obtained and discussed. Section 2.1.1 is devoted to the minimal toy model. This model is particle hole symmetric and isotropic in the inplane momenta and it is the minimal setting to capture the topological properties of a general WSM (DSM) by exhibiting two Weyl (Dirac) nodes aligned in the k_z-direction. The states for the Na_3Bi model are derived in section 2.1.2. In this case, the model is obtained from fitting the low-energy bands calculated by DFT. The transport properties of the Fermi arcs are discussed in section 2.1.3

- Next, in section 2.2 the effect of an external electric field perpendicular to the direction of decay of the Fermi arcs is briefly reviewed. The external field is found to reshape the Dirac cones and displace them in the reciprocal space. The results are reviewed from the perspective of the experimental realisation of a dual-gate device in reference [181] that is discussed in section 2.2.2.

- Next, section 2.3 explores the impact of the Rashba spin-orbit coupling (RSOC) on the Fermi arcs. This coupling could be induced by a substrate and tuned by an electric field and it is treated as a local interaction near the surface that is affected by the broken inversion symmetry. The RSOC couples the spin sectors of the Hamiltonian, and hence the chirality of the states, by breaking the inversion symmetry as described in section 2.3.1. By exploiting the spatial distribution of the Fermi states as well as the rotation of the spin induced by the RSOC, the spin-polarised currents can be manipulated. A spin-switching device is proposed in section 2.3.2

where transport calculation were performed in a two-leads device including point-like disorder.

- Finally, section 2.4 summarizes the main findings of the chapter and discusses the possibilities of tuning the Fermi arcs with external fields and the robustness of the topological states.

2.1 Model Hamiltonians and surface states for Dirac and Weyl semimetals

2.1.1 Minimal model for a Weyl semimetal

In this section, the effective low-energy Hamiltonians are used as a starting point for the description of the bands and the electronic states of DSMs and WSMs. The minimal model comprises two bands for each pair of Weyl nodes and four bands for the Dirac case. The minimal element needed for a Weyl node is the existence of a pair of band crossings such that the topological Chern number is defined at any point of the reciprocal space, except from the two singular points, as discussed in section 1.3.3. The typical dispersion of the WSMs near the degenerate points resembles graphene-like linear bands in the case of type I WSMs. The classification of the WSMs in type I and type II corresponds to the absence, or existence, of electron and hole pockets, being type II represented by tilted linear bands near the Weyl nodes. In this thesis only type I WSMs are considered and the minimal model that describes a pair of Weyl nodes is [93, 245]:

$$\mathcal{H}_{W,\zeta}(\mathbf{k}) = (m_0 - m_1\mathbf{k}^2)\ \sigma_z + v(\zeta k_x\sigma_x + k_y\sigma_y)\ , \tag{2.1}$$

where $\zeta = \pm 1$ denotes the chirality of the nodes and σ_i with $i = x, y, z$ are the Pauli matrices. This equation corresponds to equation (1.49) and it is reported here for completeness. This simple model has been studied extensively in the literature [93, 245], giving a valuable insight in spite of the simplicity of its formulation. The topological nature is encoded in the quadratic term and the relative sign of its coefficient m_1 with respect to the gap m_0, as argued in equation (1.53).

The bulk dispersion of the minimal model is given by

$$E_b = \pm\sqrt{(m_0 - m_1\mathbf{k}^2)^2 + v^2(k_x^2 + k_y^2)}\ , \tag{2.2}$$

and it is shown in figure 2.1. The Weyl points are located at $\pm\mathbf{k}_W = \pm(0, 0, R)$ with $R = \sqrt{m_0/m_1}$.

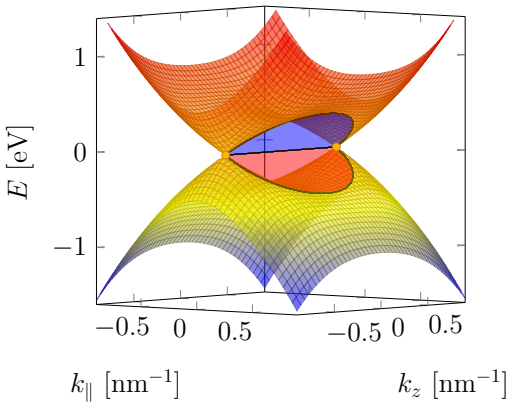

Figure 2.1: Dispersion relation as a function of the absolute value of the inplane momentum $k_\parallel = \sqrt{k_x^2 + k_y^2}$. Bulk states [see equation (2.2)] are plotted in meshed, surface states [see equation (2.8)] in opaque red and blue for $\zeta = -1$ and $\zeta = 1$, respectively. The two Weyl points are marked by dots. The parameters are $m_0 = 0.35\,\mathrm{eV}$, $m_1 = 1.0\,\mathrm{eV nm^2}$, and $v = 1.0\,\mathrm{eV\,nm}$.

As already discussed in section 1.3.3, from the Weyl Hamiltonian in equation (2.1), a minimal Dirac model can be written by gathering two Weyl pairs with opposite chirality. In the absence of coupling between both chiralities, the Hamiltonian for a DSM can be written as two blocks, which are TR partners of 2×2 Weyl Hamiltonians. Hence, a minimal model for a DSM protected by up-down symmetry is given by:

$$\mathcal{H}_D(\mathbf{k}) = \begin{pmatrix} \mathcal{H}_{W,+1}(\mathbf{k}) & 0 \\ 0 & \mathcal{H}_{W,-1}(\mathbf{k}) \end{pmatrix} . \tag{2.3}$$

In the following, the Fermi arcs are obtained for a slab with a finite width in the perpendicular direction to the line of nodes, i.e. in the x-y plane. The geometry considered for the analytic derivation is a semi-infinite slab with a single surface located at $y = y_0$ and extended in the half-plane $y > y_0$, as shown in figure 2.2. In the other spatial directions, the slab is infinite assuring that k_x and k_z are good quantum numbers.

The surface states obtained fulfil Dirichlet boundary conditions by imposing $\psi|_{y=y_0} = 0$. Employing the *ansatz* $\psi_s \sim e^{ik_x x} e^{ik_z z} e^{-\lambda(y-y_0)} \Phi$, where Φ is a constant and normalised spinor, the solution obtained depends on the chirality ζ and it reads as

$$\psi_{s,\zeta} = A_s \left[e^{-\lambda_1 (y-y_0)} - e^{-\lambda_2 (y-y_0)} \right] \Phi_\zeta \ , \tag{2.4}$$

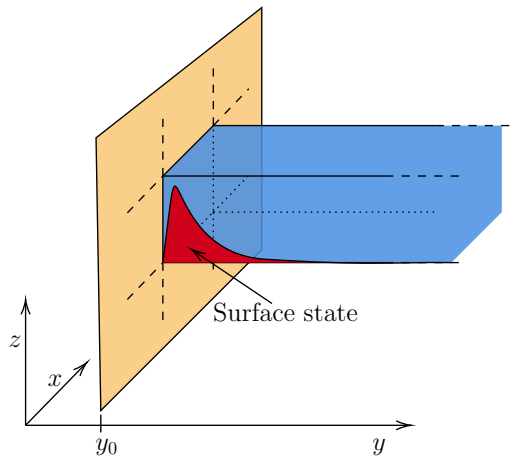

Figure 2.2: Schematic representation of the geometrical arrangement of the semi-infinite slab. The probability density is sketched in the direction of decay. The slab is inifinte in the x and z-directions and semiinfinite in y with a single surface at $y = y_0$.

where $\zeta = \pm 1$ and A_s is a normalization constant. λ_1 and λ_2 describe the decay and oscillations of the state, and they are real or complex valued depending on the parameters:

$$\lambda_1 = \Delta + \sqrt{F} \ , \qquad \lambda_2 = \Delta - \sqrt{F} \ , \tag{2.5}$$

where the following quantities are defined

$$\Delta \equiv \frac{v}{2m_1} \ , \qquad F \equiv F(k_x, k_z) = k_x^2 + k_z^2 - R^2 + \Delta^2 \ . \tag{2.6}$$

The number of surface states depends on the model. The WSM in equation (2.1) has only one state with spinorial part $\Phi = (1, \kappa)^t$. For the Dirac Hamiltonian (2.3) two solutions are obtained with different Φ, depending on the chirality of the Weyl blocks, leading to

$$\Phi^{\mathrm{D}}_{\zeta=+1} = A_\Phi (1, \kappa, 0, 0)^t, \quad \Phi^{\mathrm{D}}_{\zeta=-1} = A_\Phi (0, 0, 1, \kappa)^t, \tag{2.7}$$

where $A_\Phi^{-1} = \sqrt{1 + |\kappa|^2}$ is a normalization constant and t indicates the transpose. For the minimal model $\kappa = 1$.

The dispersion relation of the surface states is obtained by solving the Hamiltonian (2.1) with the states in equation (2.4):

$$E_{s,\zeta} = \zeta v k_x \ , \tag{2.8}$$

where the direction of propagation depends on the chirality. For DSMs, this implies the two linearly independent solutions are counterpropagating modes, one the TR partner of the other.

To have localised states, the condition of $\Re(\lambda_{1,2}) > 0$ is checked on the decay lengths. The former condition leads to $F < \Delta^2$ and it imposes a radius for the existence of the surface states in the reciprocal space given by

$$k_x^2 + k_z^2 < R^2 \ . \tag{2.9}$$

The radius of existence corresponds to the merging point of the linearly dispersive bands of the surface states with the quadratic bulk bands. The surface states decrease their spatial localisation by increasing $k_{\parallel} = \sqrt{k_x^2 + k_z^2}$ due to the contribution of $F(k_x, k_z)$ in equation (2.5), until they become completely delocalised and touch the bulk bands at $k_{\parallel} = R$.

The condition of existence of the surface state is related to the definition of the Chern number as a function of k_z discussed in section 1.3.3. A non-trivial Chern number is obtained for $|k_z| < R$ as along as the bulk gap is open. This leads to $|C| = 1$ for the momenta that fulfil equation (2.9).

Finally, according to the nature of decay of the surface states, two types can be distinguished: The oscillatory decay (i.e. $\lambda_i \in \mathbb{C}$) and the purely exponential decay (i.e. $\lambda_i \in \mathbb{R}$). In the following they are denote by type A and type B surface states, respectively. Type A surface states lead to smaller penetration lengths and oscillatory decays, whereas type B are related to longer and purely exponential decays [17, 93]. In figure 2.3 the surface states for type A and B are plotted for two sets of model parameters. Depending on the model parameters, the previously presented models host only type B or both type A and type B surface states, for higher momenta. The condition for oscillatory states is that $|\Im(\lambda_{1,2})| > 0$, which implies the more restrictive condition $F < 0$. Hence, an exponential with oscillations appears for the momenta that fulfils $F < 0$ and a purely exponential decay corresponds to the states with $0 < F < \Delta^2$, as exemplified in figure 2.3(a).

2.1.2 Model Hamiltonian for Na_3Bi and Cd_3As_2

In the following, a specific model is introduced to describe DSMs of the family of A_3Bi ($A = Na, K, Rb$) [287] and Cd_3As_2 [48, 286]. These compounds have a single band inversion occurring near the Γ point that has been observed by ARPES measurements [159, 160, 179, 302]. The bands obtained from DFT calculations show particle-hole asymmetry and anisotropic dispersion in the reciprocal space. The low-energy fitting of the DFT bands results in a four-band model [286, 287] provides a DSM

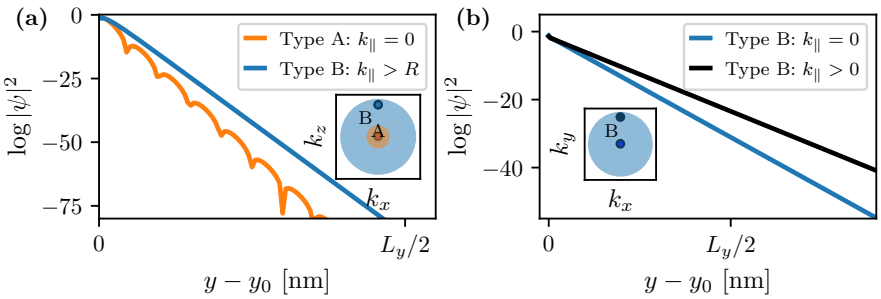

Figure 2.3: Surface states of type A and type B for the minimal model, numerically obtained by solving the Hamiltonian in equation (2.1) in a system of $L_y = 200\,\text{nm}$ with PBC in x and z-directions. The parameters are $m_0 = 0.35\,\text{eV}$, $m_1 = 1\,\text{eVnm}^2$ and $v = 1\,\text{eV nm}$ in (a) and $v = 2.5\,\text{eV nm}$ in (b). The parameters in (a) show both type A and B states depending on the momenta, while the slab in (b) only exhibits type B states. The insets show the regions of existence in reciprocal space defined by equations (2.9) and the condition for type A surface states of $F < 0$.

protected by up-down symmetry [96, 97]. For the sake of concreteness, the analysis is restricted to the case of Na_3Bi. If no coupling terms between chiralities are considered, the Dirac Hamiltonian has the block-diagonal form of equation (2.3) where the WSM blocks are replaced by

$$\mathcal{H}_{W,\zeta}(\mathbf{k}) = \epsilon_0(\mathbf{k})\mathbb{1}_2 + M(\mathbf{k})\sigma_z + v(\zeta k_x\sigma_x - k_y\sigma_y)\ , \tag{2.10a}$$

$$\epsilon_0(\mathbf{k}) = c_0 + c_1k_z^2 + c_2(k_x^2 + k_y^2)\ , \tag{2.10b}$$

$$M(\mathbf{k}) = m_0 - m_1k_z^2 - m_2(k_x^2 + k_y^2)\ . \tag{2.10c}$$

$\mathbb{1}_n$ stands for the $n \times n$ identity matrix. This Hamiltonian was already reported in equation (1.52a) and it is written in the basis of the orbitals given by expression (1.54). The bulk dispersion of the Hamiltonian (2.10a) is

$$E_b = \epsilon_0(\mathbf{k}) \pm \sqrt{M(\mathbf{k})^2 + v^2(k_x^2 + k_y^2)}\ , \tag{2.11}$$

and it is plotted in figure 2.4.

The surface states of the model are discussed in detail in reference [17] in a single-surface approximation and in a slab configuration with two parallel surfaces. In the case of the semi-infinite slab with a single surface at $y = y_0$ plotted in figure 2.2, the surface states obtained has the form of equation (2.4) with decay lengths given by equation (2.5), replacing F and Δ by the following expressions:

$$F_\zeta(k_x, k_z) \equiv (k_x + \zeta k_{x,0})^2 + \frac{m_1}{m_2}\,k_z^2 + \Delta^2 - R^2\ , \quad \Delta \equiv \frac{v}{2\sqrt{m_2^2 - c_2^2}}\ , \tag{2.12}$$

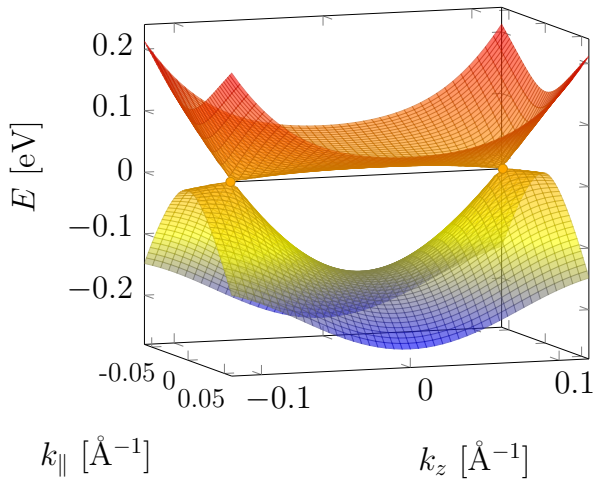

Figure 2.4: Dispersion relation of the bulk bands near the Γ point for the Hamiltonian (2.10a) with parameters corresponding to Na_3Bi, listed in table 1.3. In the axis, $k_\parallel = \sqrt{k_x^2 + k_y^2}$. The Dirac points are marked with two dots and connected by a Fermi arc.

where $k_{x,0} \equiv c_2\Delta/m_2$ and $R^2 \equiv m_0/m_2 + \Delta^2 (c_2/m_2)^2$. The spinor component in equation (2.7) is $\kappa = \sqrt{(m_2 - c_2)/(m_2 + c_2)}$.

In this case, by imposing $\mathcal{R}(\lambda_{1,2}) > 0$ to ensure the spatial decay of the states, an elliptic and chiral condition is obtained for the states in the $k_x - k_z$ plane due to the chiral dependence of F_ζ. The dispersion of the states is linear in the x-direction and it shows non-flat bands along the z-direction due to the diagonal term $\epsilon_0(\mathbf{k})\mathbb{1}_4$:

$$E_{s,\zeta} = \varepsilon(k_z) + \zeta v C_3 k_x \ , \tag{2.13}$$

where the non-flat band contribution is

$$\varepsilon(k_z) = C_1 + C_2 k_z^2 \ . \tag{2.14}$$

In the last equations C_1, C_2 and C_3 are combinations of the Hamiltonian parameters given by

$$C_1 = c_0 + c_2 m_0/m_2 \ , \tag{2.15a}$$
$$C_2 = c_1 - c_2 m_1/m_2 \ , \tag{2.15b}$$
$$C_3 = \sqrt{m_2^2 - c_2^2}/m_2 \ . \tag{2.15c}$$

The numerical values of the parameters for Na_3Bi are listed in table 1.3. According to the parameters, Na_3Bi exhibits only type B surface states and hence a purely exponential decay.

2.1.3 Transport signatures of the Fermi arcs

The Fermi arcs of the TSMs constitute electronic protected channels with a well defined direction of propagation for each chirality. The dispersion relation is linear [see equations (2.8) and (2.13)] and chiral-dependent. In the case of the WSMs, only one direction of propagation is allowed. On the other hand, in DSMs, two couter-propagating modes with opposite chirality are localised at each surface. Due to TR symmetry, if there are no extra coupling terms between the two Weyl sectors of the DSM, the scattering between states with opposite chirality is prohibited, allowing for two perfectly quantised channels in both directions. In the following the transport properties of the Fermi arcs are calculated for a Hall bar by applying the Landauer-Büttiker formalism in an analytic toy model and, later, by numerical calculations in a finite system employing `Kwant` [102].

The setup considered is a Hall bar elongated in the x-direction and with a finite section of area $L_y \times L_z$. For an injecting energy inside the gap, the conductance is expected to be driven by the Fermi arc states. Hence, a simple toy model can be constructed considering only the Fermi arcs in the T-matrix of the system. For that, the following points have to be taken into account:

- The Fermi arcs decay in the y-direction and they constitute the two conducting channels, inside the gap, that surround the Hall bar in clockwise (counter-clockwise) direction for $\zeta = +1$ (-1).
- Due to the topological protection of the states, each channel is expected to contribute with a transmission of $|T| = 1$ in the x-direction, see figure 2.5. The sign depends on the direction of propagation and the chirality (see the following points).
- The transmission coefficient of the chiral states from a lead i to its neighbour terminal j in the clockwise direction is $T_{i,j}^{\zeta} = \zeta$, where $\zeta = \pm 1$ is the chirality of the state.
- Conversely, for the counter-clockwise direction, between leads i and j, the sign is reversed $T_{i,j}^{\zeta} = -\zeta$.

In conclusion, the transmission coefficient is:

$$T_{i,j}^{\zeta} = \begin{cases} \zeta & \text{if the } i \text{ and } j \text{ are adjacent } \textit{clockwise} \text{ leads ,} \\ -\zeta & \text{if the } i \text{ and } j \text{ are adjacent } \textit{counterclockwise} \text{ leads ,} \\ 0 & \text{otherwise .} \end{cases} \tag{2.16}$$

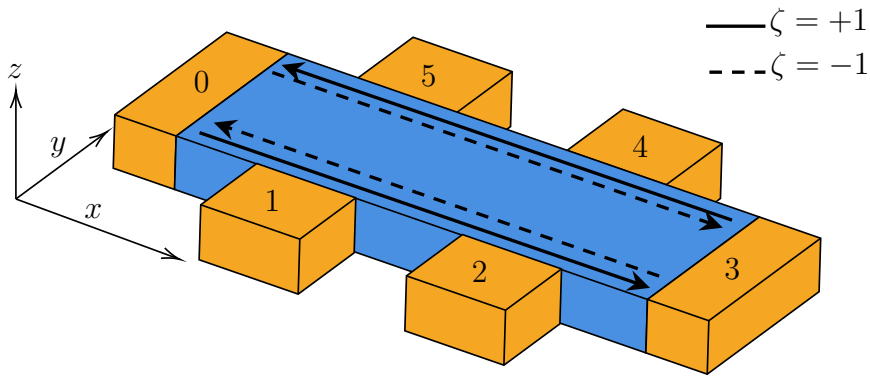

Figure 2.5: Sketch of the Hall bar and schematic representation of the topological channels in a DSM slab. The leads are marked in orange and numbered in counter-clockwise order starting from the lead aligned in the x-direction. The topological surface states are represented by arrows pointing in the direcion of propagation. Different lines are employed depending on the chirality of the state, as indicated in the legend.

Specifically, the Hall bar is formed by six terminals, arranges as sketched in figure 2.5. By applying the Landauer-Büttiker formalism discussed in appendix B, the T-matrix involved in the calculations can be factorised according to the chirality of the modes. In this way, the conductance from the incoming to the outcoming lead from equation (B.5b) is split in the following contributions

$$G = G_{++} + G_{--} + G_{+-} + G_{-+} \ , \tag{2.17}$$

where the subscripts indicate the chirality $\zeta = \pm 1$ of the incoming and outcoming modes.

In the approximation of considering only the Fermi arcs, due to their topological protection, no scattering is expected between the two chiral sectors leading to $G_{+-} = G_{-+} = 0$. By defining the chiral currents as

$$I_p^{\zeta} = \sum_q G_{\zeta\zeta}[V_p - V_q] \ , \tag{2.18}$$

the total intensity at terminal I can be obtained as the sum of the currents with $\zeta = +1$ and $\zeta = -1$:

$$I_i = {I_i}^{\zeta=+1} + {I_i}^{\zeta=-1} = \frac{e^2}{h} \sum_{j \neq i} \sum_{\zeta=\pm 1} ({T_{ij}}^{\zeta} V_j - {T_{ji}}^{\zeta} V_i) \ . \tag{2.19}$$

The former expression is written in matrix form by replacing the transmission in equation (2.16) and it reads as:

$$\begin{pmatrix} I_0^{\zeta=+1} \\ I_1^{\zeta=+1} \\ I_2^{\zeta=+1} \\ I_3^{\zeta=+1} \\ I_4^{\zeta=+1} \\ I_5^{\zeta=+1} \end{pmatrix} = \frac{e^2}{h} \begin{pmatrix} -1 & 1 & 0 & 0 & 0 & 0 \\ 0 & -1 & 1 & 0 & 0 & 0 \\ 0 & 0 & -1 & 1 & 0 & 0 \\ 0 & 0 & 0 & -1 & 1 & 0 \\ 0 & 0 & 0 & 0 & -1 & 1 \\ 1 & 0 & 0 & 0 & 0 & -1 \end{pmatrix} \begin{pmatrix} V_0 \\ V_1 \\ V_2 \\ V_3 \\ V_4 \\ V_5 \end{pmatrix} , \tag{2.20a}$$

and

$$\begin{pmatrix} I_0^{\zeta=-1} \\ I_1^{\zeta=-1} \\ I_2^{\zeta=-1} \\ I_3^{\zeta=-1} \\ I_4^{\zeta=-1} \\ I_5^{\zeta=-1} \end{pmatrix} = \frac{e^2}{h} \begin{pmatrix} -1 & 0 & 0 & 0 & 0 & 1 \\ 1 & -1 & 0 & 0 & 0 & 0 \\ 0 & 1 & -1 & 0 & 0 & 0 \\ 0 & 0 & 1 & -1 & 0 & 0 \\ 0 & 0 & 0 & 1 & -1 & 0 \\ 0 & 0 & 0 & 0 & 1 & -1 \end{pmatrix} \begin{pmatrix} V_0 \\ V_1 \\ V_2 \\ V_3 \\ V_4 \\ V_5 \end{pmatrix} . \tag{2.20b}$$

Given an infinitesimal current flow between a pair of leads, the system of equations (2.20a) and (2.20b) have to be solved following the steps discussed in appendix B.1. In this way, the voltage drop is determined and the resistance reads as

$$R_{ij;kl} = (V_i - V_j)/(I_k - I_l) , \tag{2.21}$$

where the subscripts $ij;kl$ indicated the leads where the voltage and the current are measured.

The measure of $R_{ij;kl}$ for some specific current-voltage configurations in a Hall bar elucidate the direction, localisation and chirality of the Fermi arcs. For example, by considering a current probe between the two leads in the x-direction, i.e. the leads 0 and 3 according to figure 2.5, it is possible to prove the localisation of the states of the Fermi arcs in the external surfaces of the slab located $y = \pm L_y/2$. For the positive chirality $\zeta = +1$, for a current $I_0 = -I_3 = \tilde{I}$, the voltages are found to be:

$$V_0 = V_4 = 0 , \quad V_1 = V_2 = V_3 = \tilde{I}\frac{h}{e^2} . \tag{2.22}$$

With this voltage drop, a quantized resistance is obtained in the transverse leads connected to the surface at $L_y/2$, i.e. leads 1, 2 and 3 according to figure 2.5. The resistance is then

$$R_{i0;03}^{\zeta=+1} = \frac{h}{e^2} , \text{ where } i = 1, 2, 3 . \tag{2.23}$$

Similarly, for the opposite chirality $\zeta = -1$, the voltages obtained for the same current configuration are:

$$V_0 = V_1 = V_2 = -i\frac{h}{e^2} \ , \quad V_3 = V_4 = 0 \ , \tag{2.24}$$

that leads to

$$R_{i0;03}^{\zeta=-1} = \frac{h}{e^2} \ , \text{ where } i = 3, 4, 5 \ , \tag{2.25}$$

which correspond to the current driven by the Fermi arc peaked at $-L_y/2$. By reversing the current direction to $I_3 = -I_0 = \tilde{I}$, the results for $\zeta = +1$ are reversed to $\zeta = -1$ and viceversa. These results are in perfect agreement with the chiral channels shown in figure 2.5. The WSM case is obtained by considering only one of the chiralities in the derivation presented here for a DSM.

Finally, the resistance obtained from the previous formalism, based on the assumption of considering the Fermi arcs only, is compared with the transport calculations in a wire of Na_3Bi of $300 \times 50 \times 50$ Å^3 with leads of width 50×50 Å^2 in the six-terminal Hall bar configuration shown in figure 2.5. The results are plotted in figure 2.6 (b), together with the band structure of the leads in (a). The predicted quantised channels appear for the Fermi energies within the bulk gap. At $E_F \sim 0.6\,\text{eV}$, the bulk bands increase the number of available channels and break the quantised plateau. For energies inside the gap, the resistance obtained follows equation (2.23), and $R_{40;03}^{\zeta=+1}$ vanishes. Due to the symmetry of the system, the numerically calculated $R_{i0;03}^{\zeta=-1}$ are equivalent to their spatially mirror-symmetric counterparts with $\zeta = +1$. This implies that $R_{i0;03}^{\zeta=+1} = R_{n_l-i,0;03}^{\zeta=-1}$ where $n_l = 6$ is the number of leads in the Hall bar. Hence equation (2.25) is also fulfilled for the injection energies inside the gap.

2.2 Control of the Fermi arcs through an external electric field

The effect of the external electric field on the surface states of WSMs and DSMs have been addressed in my master thesis and the subsequent publication [14]. However, the main results are briefly summarised in this section to be compared with the experimental realisation of a dual-gated device of Cd_3As_2 in a recent work by Nishihaya *et al.*[181]. This work provides an experimental evidence of the phenomena described by the theoretical model in a slab with both electric and magnetic fields.

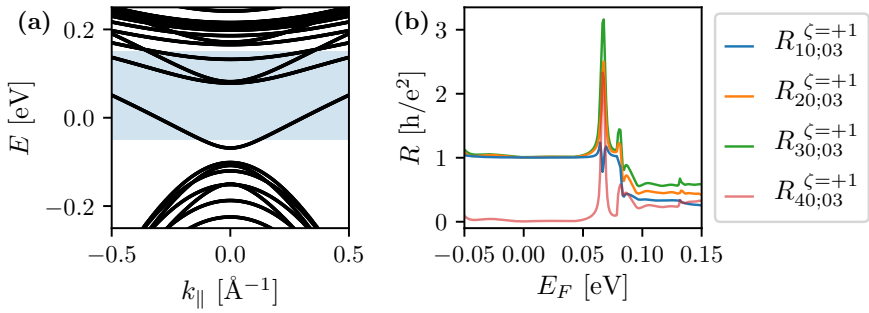

Figure 2.6: (a) Dispersion relation of the leads in the Hall bar of Na_3Bi with section 50×50Å^2 as a function of the momentum. (b) Resistance as a function of the Fermi energy, for the $\zeta = +1$ channels for a current flow between the horizontal leads. The shaded area in (a) corresponds to the energies used in the resistance calculations in (b). The dispersion relation in (a) shows a small gap due to the hybridisation of the surface states of the opposite sides of the slab as a consequence of the finite size in the direction of decay of the Fermi arcs. The linearly dispersive bands within the gap correspond to the Fermi arcs as elucidated by the transport results.

2.2.1 Impact of the external electric field on the Fermi arcs

In the theoretical approach, the effect of an electric field in the direction of decay of the states, i.e. in the y-direction, is studied by including an external potential of the form

$$\mathcal{H}_f = efy\mathbb{1}_2 \ , \tag{2.26}$$

where e is the elementary electric charge and f is the strength of the external electric field. The effect of the field is studied in the perturbative and non-perturbative regime focussing on the effect on the surface states. Three main effects are identified: the shifting of the momenta of the Dirac cones crossings near the Fermi energy, the displacement in energy of the Dirac nodes and the renormalization of the velocity by the reshaping of the Dirac cone. Figure 2.7 shows the evolution of these three quantities as a function of the electric field for slabs of width of hundreds of Å.

The electric field is a diagonal term in the orbital basis [see equation (2.26)]. Therefore, it does not mix chiralities, but it breaks the spatial inversion symmetry, leading to a splitting of the two cones of the opposite surfaces in a slab geometry. By considering the Hamiltonian (2.26) as a perturbation, the correction to the energy of the states up to first order in f is proportional to the expectation value of the position operator in

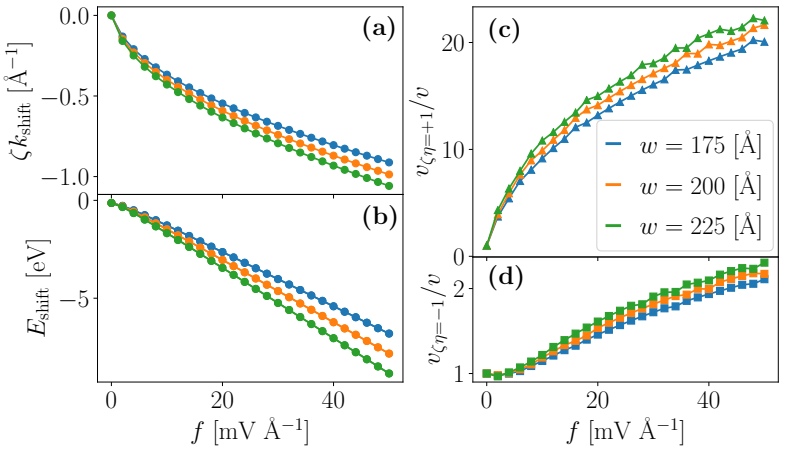

Figure 2.7: (a) k_{shift}, (b) E_{shift} and (c)-(d) velocity as a function of the external electric field for three different widths of a Na_3Bi slab. The spatial width of the slabs is $2w$.

the direction of the decay:

$$\delta E^1 = \langle \psi^0 | \mathcal{H}_f | \psi^0 \rangle = ef \langle \psi^0 | y | \psi^0 \rangle \ , \tag{2.27}$$

where ψ^0 indicates the states of the unperturbed Hamiltonian. In the case of the surface states, that are peaked near the edges of the slab, $\langle y \rangle \simeq -\eta w$ where $\eta = \pm 1$ is the index that distinguishes the two surfaces of the slab located at $y = \eta w$. The correction is then roughly $\delta E \simeq -ef\eta w$ and the surface states are displaced up and down in energy depending on their edge. In a DSM slab, each surface hosts two states with opposite chirality ζ, and consequently opposite directions of propagation, that conform a Dirac cone in the k_x-direction. By including the electric field, the cone of each surface is displaced up and down depending on its edge and the intersection of the two surface states of the same chirality and opposite surface localisation generates a new band crossings near the Fermi energy. The energy of this band crossing defines E_{shift} depicted in figure 2.7(b). Figure 2.8 shows the evolution of the dispersion for a Na_3Bi slab as a function of the electric field for $k_x = 0$ and $k_z = 0$ in the upper and lower panels, respectively. In the $k_z = 0$ dispersion relation, the shifting of the cones is visible as well as the merging of the bulk bands due to the electric field.

Figure 2.8 shows that the electric field not only displaces the cones but also reshapes them by modifying the Fermi velocity. In reference [14] the perturbative corrections are analytically obtained as well as the first order

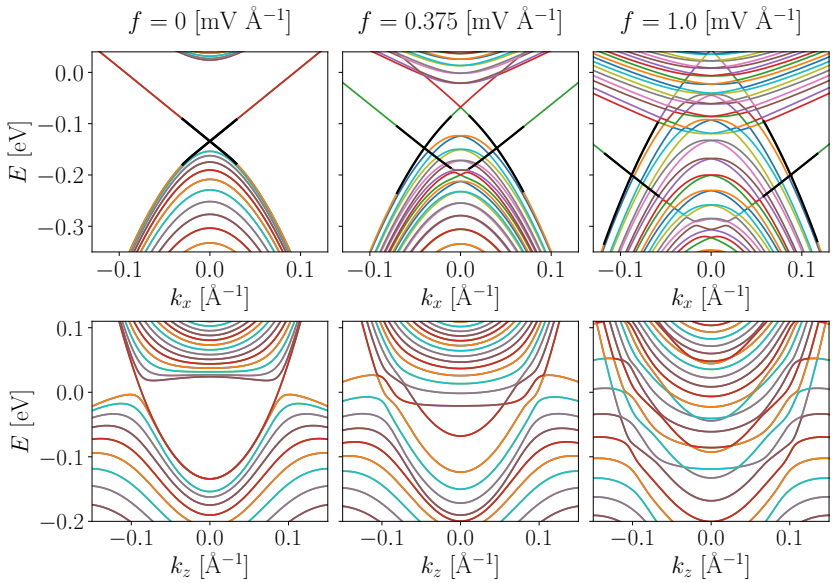

Figure 2.8: Change of the dispersion relation with the electric field f in a slab of $w = 200$ Å and setting $\zeta = +1$. In the upper panels, the shifting of the cones is utterly visible in the dispersion as a function of k_x (at $k_z = 0$). In the bottom panels, the coalescence of the bands in the dispersion as a function of k_z (at $k_x = 0$) is plotted. To improve visibility, the crossing of the surface energy branches is underlined in a black line.

corrections for the Fermi velocity of the surface states proving that the modification of the Fermi velocity depends on both the surface index η and the chirality ζ of the Weyl block. Hence, the surface states bands near the Fermi energy show a strongly chiral dependent velocity as well as a nonzero momentum k_{shift} at the Fermi energy, as reported in figure 2.7(c) and (d).

Since the surface state type (A or B) depends on the interplay of the momenta and the model parameters such as the Fermi velocity, the electric field may induce a transition between the different spatial decays. For the range of the fields considered, no type transition is found in Na_3Bi. Even though, for other parameters, the type transition can be achieved from an oscillatory type A to a purely exponential decay of type B, as shown in figure 2.9.

In summary, the electric field reshapes the dispersion of the Dirac surface states by displacing the cones as well as by modifying the Fermi velocity and the curvature of the bands depending on the chirality. Note that the screening could also renormalise the Dirac velocity, as has already

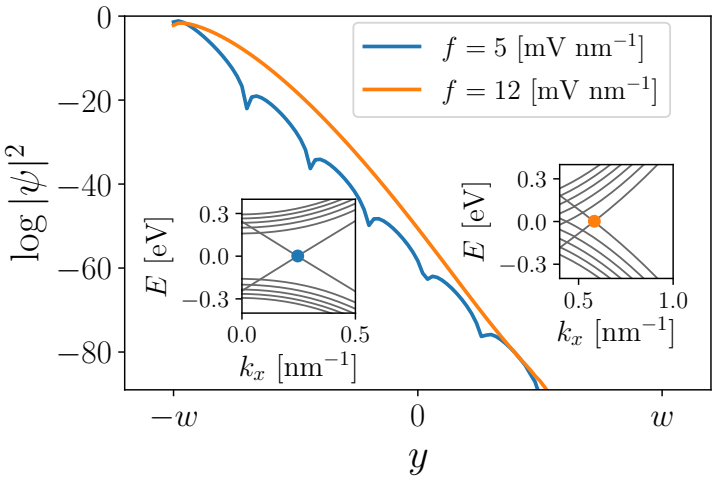

Figure 2.9: Type transition between type A and type B surface states for a system with parameters $w = 50$ nm, $m_0 = 0.35\,\text{eV}$, $m_1 = 1.0\,\text{eVnm}^2$, $v = 1.0\,\text{eV nm}$ and $\zeta = +1$ described by the Hamiltonian (2.3) with $\mathcal{H}_{W,\zeta}$ from equation (2.1). The main panel shows the wavefunctions and the insets show the first ten bands of the dispersion relation in the plane $k_x = 0$. The left (right) inset corresponds to $f = 5$ (12) mVnm^{-1}, the colored dots mark the energy and momentum of the wavefunctions plotted. The cone is shifted but the oscillatory decay is preserved for the smaller field whereas for the higher field the decay becomes purely exponential, showing the type transition.

been shown for graphene, where a renormalisation of 17% was found at the GW level [267]. This could be studied in the future in a self-consistent approach for the Dirac cones of the Fermi arcs in semimetals.

2.2.2 Experimental measurements of the quantum Hall state in Cd_3As_2

In the experimental setup studied in reference [181], a Cd_3As_2 slab of 750 Å is controlled by a dual-gate with top and back gate voltages V_T and V_B. In this way, the voltage drop across the sample generates an electric field $f = (V_T - V_B)/L$, while each gate controls the electron density of the back and top surfaces. The experiment is focused in probing the nature of the quantum Hall state in DSMs. In fact, even if the QHE is generally acknowledged as a 2D phenomenon, at high magnetic field, DSMs slabs show a quantised conductance equivalent to the QHE in 2D systems [158, 236, 272, 309, 310].

The quantum Hall plateaus are related to the Fermi arcs of the DSM, even though the nature of surface states causing the quantum Hall states

was unclear. Two physical processes were proposed:

- A TI-like surface orbit in each side of the slab that appears if the topological protection is lost by a perturbation as proved in reference [126].

- A more complex state comprising opposite surfaces that is connected by a Landau level (LL). This state was named *Weyl orbit* and it appears when the topology of the DSM bands is preserved. If the magnetic field is perpendicular to the direction of the line connecting the Dirac points, a Weyl orbit is formed by two Fermi arcs from the two Weyl points of opposite surfaces and a chiral LL through the bulk. The Weyl orbit forms a closed loop by joining the states from opposite surfaces and generates a stable quantum Hall channel.

Figures 2.10 (a) and (c) show a schematic representation of both states: on the top and bottom surfaces the Fermi arcs connecting two Weyl points are represented in momentum space while the vertical lines along the real y-axis indicate the bulk chiral LLs in (c); in (a) the TI-like surface states are independently localised at each surface.

The first experimental proposals showed a phase shift of the quantum Hall plateaus when the bulk thickness was modulated [202, 311, 316], pointing out that the Weyl orbit process was generating the Hall signal. Even though, this is not a completely conclusive result due to the inhomogeneity of the carrier density that is induced when varying the thickness [182]. Therefore, the experiment of reference [181] was proposed to control each surface electron density independently and elucidate the contributions of each surface separately. Depending on which process drives the Hall signal the following results were expected:

- If the QHE is generated by two separate TI-like surface states, the modulation of V_B and V_T independently increases the number of LLs that contribute to the QHE state and hence a chessboard pattern is expected, as depicted in figure 2.10 (b) [43].

- On the other hand, if the Weyl orbits were driven the QHE, the electron density of both surfaces could be modulated by top and/or back gating. Hence, a stripe pattern is expected along the constant density lines as a function of V_B and V_T, as schematised in figure 2.10 (d).

In the case of the [112] slab of Cd_3As_2 of 75 nm thickness studied in reference [181], the Hall measurements show a stripe pattern as a function

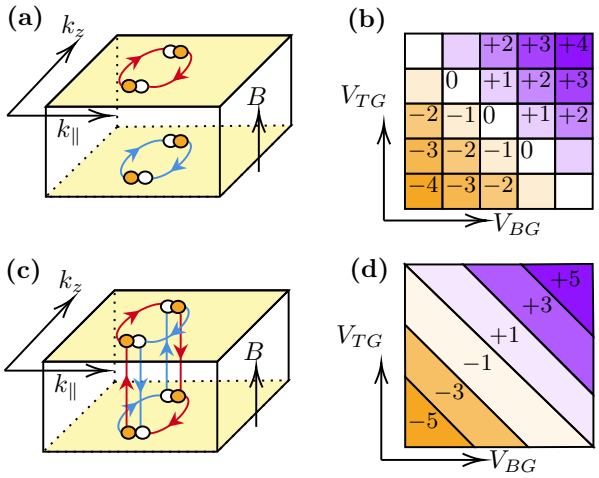

Figure 2.10: Sketch of the TI-like surface states in (a) and the Weyl orbits in (c). The figure mixes the representation in the reciprocal space and the real space. In the top and bottom surfaces, the Fermi arcs are depicted in the reciprocal space. On the other hand, the Weyl orbits in (c) are connected through the slab, in the real space representation via the LLs. Note that such chiral LLs exist everywhere in the real space even though only one is exemplified here. In (b) and (d) the expected Hall conductance is plotted qualitatively as a function of the top and bottom gate in the colorscale indicated. Figure adapted from reference [181].

of the two gates, resembling the model in figure 2.10(d) and proving the existence of the Weyl orbits. The stripe pattern corresponds to quantised values of odd integer values of the quantum Hall filling factor ν, obtained from $\nu = n_{2D}h/eB$ where n_{2D} is the electron sheet density, B the magnetic field and h and e are the Planck constant and the elementary charge, respectively.

Together with the odd integer values expected in the Weyl orbit case, even integers such as $\nu = 6$ and $\nu = 8$ appear, as shown in figure 2.11. This discordance from the expected results is explained by the splitting effect driven by the electric field discussed in section 2.2. In fact, the dual gate setup generates an electric field in the direction of growth of the slab. Due to the electric field, the pairs of Weyl nodes shift oppositely in energy and momentum directions and the two Weyl orbits with opposite chirality lift the double degeneracy. By applying the magnetic field, the two Weyl orbits with opposite chirality split and cross with each other leading to a deviation from the odd-integers occupation ν for higher electric fields. In the appendix of reference [181], the configuration of the electric field is

modified showing that indeed the even integers plateaus depends on the field. Hence, the experiment in reference [181] can be considered an experimental validation of the effects discussed in section 2.2 and published in reference [14].

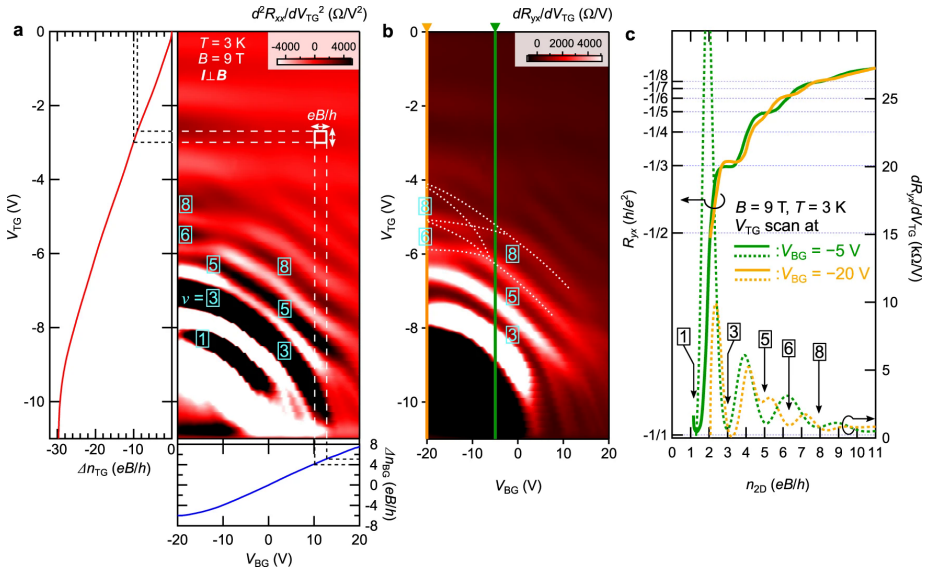

Figure 2.11: The second derivative of the longitudinal resistance R_{xx} (a) and first derivative of the Hall resistance R_{xy} with respect to V_{TG}(b) are mapped as a function of the top V_{T} and bottom gate V_{B}. The darker regions in (a) correspond to the minima in between the peaks that separates the plateaus transitions, as expected in a R_{xx} signal of a QHE; in (b) the first derivative of R_{xy} is minimum in a plateau and it is also marked in a darker colorscale. In (c) the R_{yx} is represented in a solid line together with its first derivative (dashed line) along the vertical lines of $V_{BG} = -5\,\mathrm{V}$ and $V_{BG} = -20\,\mathrm{V}$ marked in (b). The figure corresponds to figure 3 in reference [181].

2.3 Rashba spin-orbit coupling in slabs

The second part of the chapter is devoted to the effect of external fields that couple the chirality and that are related to a symmetry breaking. More specifically, in this section, the coupling of both chiral sectors due to the breaking of the symmetry at the surface is described by a Rashba spin-orbit term. In general, due to the inversion symmetry breaking, spin-orbit coupling terms can arise in the absence of external magnetic fields such as the bulk and surface inversion asymmetry. The bulk inversion

asymmetry emerges from the lack of a center of inversion symmetry in the crystal itself [62]. This is the case of the zinc blende structure of III-VI and II-VI compounds like InSb and $Hg_xCd_{1-x}Te$. The lowest correction is given by the Dresselhaus coupling that is a third order term in the momentum, i.e. of the form k^3.

On the other hand, in nanostructures, the spin degeneracy can be lifted by the lack of structure inversion in the confining potential. The electric field that arises in this case is related to the variation of the band edge in asymmetric nanostructures and it is referred to as structural inversion asymmetry. More specifically, the lowest linear contribution is given by the Rashba term [168, 294]:

$$\mathcal{H}_R = \alpha_R \, \boldsymbol{\sigma} \cdot \mathbf{k} \times \boldsymbol{f} \ , \tag{2.28}$$

where $\boldsymbol{f}$ is the electric field, $\boldsymbol{\sigma}$ is a vector of Pauli matrices and α_R parametrises the strength of the coupling. Hence, by cutting a surface, the RSOC term arises and it could be enhanced by the interaction with the substrate and controlled by an external electric field. This capability has already been experimentally demonstrated in InGaAs/InAlAs heterostructures [183] and HgTe quantum wells [235].

The RSOC impacts on the charge carriers similarly to a momentum-dependent effective magnetic field and generates a spin-dependent velocity correction and a geometric phase. These features are particularly attractive for device applications based on the spin polarization of charge currents. In fact, many spintronics devices are based on the RSOC, after the pioneering proposal by Datta and Das of a spin field effect transistor [50].

Upon the discovery of the QSH in TIs, new possibilities for spintronics applications have emerged [19, 124, 165]. As discussed in section 1.3.1, in a 2D QSH state the states at the edges counterpropagate and show opposite spin polarization and wave numbers at each boundary, forming Kramers pairs[1]. These states are helical edge states due to the connection between spin and propagation direction and TR symmetry prohibits elastic backscattering from one state to its Kramers companion. The helical edge states are the only ones accessible inside the gap, leading to a quantised conductance at low enough temperatures, as observed in the first experiments in TIs [139]. Despite that, the observed quantised signal deviates from the expected values for longer edges [98, 104, 145]. The loss of quantization is explained by multiple processes related to the inelastic backscattering driven by phonons, e-e interactions [232, 295, 301], electron-phonon interaction [25] or by scattering with localised spins such

[1] See appendix A.3 for a detailed discussion of the properties of the Kramers pairs.

as magnetic impurities [164, 166, 260]. The spin precession generated by the RSOC is another processes that modifies the spin-polarised currents, even if the edge channels remain Kramers pairs [193, 194, 220, 221].

In this section, the RSOC is studied in TSMs, where the Fermi arcs replace the edge states of the TIs by exhibiting an equivalent helical-like behaviour related to the chirality. The Fermi arcs are two chiral channels localised at opposite sides of a slab that propagate in opposite directions for a fixed chirality, see section 1.3.3. In these 3D materials, the intrinsic effect due to the broken inversion symmetry at the surface appears similarly to the 2D TIs in the region near the surface cut. The RSOC, although it exists by symmetry considerations, is probably small and has not been observed experimentally. However, a carefully designed sample with a slab of TSM on a substrate of heavy atoms should induce a strong RSOC, which, due to its spatial localisation near the surface, mainly affects the Fermi arcs. This section focuses on the possibility of tuning the Fermi arcs and their topological transport signal within this scenario. The effect of the RSOC on the surface of TSMs is studied in a few work: the paper [15] related to the content of this chapter, and in the 2D ultrathin film limit studied in reference [2].

2.3.1 Impact of the RSOC on the surface states

This section is devoted to the impact of the RSOC interaction on the Fermi arcs in the approximation of a single decoupled surface given by equation (2.4) and discussed in section 2.1. In the 3D system, the RSOC is approximated as a local interaction near the surface that impacts the states localised in that region. The 2D RSOC term given by equation (2.28) is employed to model the interaction near the substrate with an effective electric field in the direction of decay of the states given by $\mathbf{f} = f\hat{\mathbf{y}}$. By considering only the coupling between the electron bands, in the basis of the Hamiltonian (2.3), the term for the Rashba coupling has the following form [2, 221]

$$\mathcal{H}_R = f_R(y) \begin{pmatrix} 0 & 0 & -iR_0k_- & 0 \\ 0 & 0 & 0 & 0 \\ iR_0k_+ & 0 & 0 & 0 \\ 0 & 0 & 0 & 0 \end{pmatrix}, \tag{2.29}$$

where $k_\pm \equiv k_z \pm ik_x$ and $f_R(y)$ is the function that encodes the spatial dependence of the coupling in the direction of decay of the Fermi arcs. The parameter R_0 quantifies the strength of the interaction, which usually relates to an external or internal electric field depending on the material. Reference [2] provides a derivation of the Rashba term for Na_3Bi thin films.

In the single layer case, reference [2] reports a value of $R_0 \approx 0.654\,\text{eV Å}$ for an electric field $f = 0.1\,\text{eV/Å}$ from DFT calculations. In this section, the slabs considered are formed by multiple layers of Na_3Bi, even though, the given value for a single layer is a reference for the magnitude of the external fields and its effect on RSOC. The exact strength of the coupling can be only computed with detailed self-consistent methods by taking into account the properties of the substrate in the slab configuration considered and it is outside the scope of this thesis.

The Rashba term $\mathcal{H}_R$ in equation (2.29) couples the electron bands but not the hole bands in the basis of the effective model (1.54). The particle-hole asymmetry is a general effect since Rashba terms for electrons depends linearly on k while hole terms are cubic in momentum [293] and the higher order terms are not considered here. By the addition of the $\mathcal{H}_R$, the two chiral sectors in the Hamiltonian (2.3) are coupled. Hence, due to the breaking of the axial symmetry, the chiral surface states (CSSs) turn into states with a more generic and intriguing spin structure than merely having opposite and constant spin orientations independently of energy. TR symmetry still dictates that the two counterpropagating Kramers partners have orthogonal spinors, but it does not require equal spinors at different energies. These states were named general surface states (GSSs) in contrast to the CSSs obtained without RSOC [193].

The GSS are analytically studied here starting from the basis of the CSS and neglecting the contribution of the bulk bands. This is equivalent to considering that the GSS are a linear combinations of the CSS. The approximation is consistent because the Rashba interaction is local, and the surface states have a negligible overlap with the bulk states due to their localisation near the surface. In this approximation, the localisation function in equation (2.29) is chosen as $f_R(y) = 1$ such that the spatial dependence of the coupling in the direction of decay of the states is considered trivial. In the basis of the Fermi arcs, the localisation of the surface states themself naturally set a cut-off in the spatial depth of the Rashba coupling and hence the constant $f_R(y)$ is consistent with the level of approximation. For the sake of simplifying the notation, from now on the subindex s which denotes the surface states is omitted and the states are labelled by their momenta $\boldsymbol{k}$ and chirality ζ. In this way, the effective Hamiltonian in the CSS basis reads as

$$\mathcal{H}_{\text{eff}} = \sum_{\boldsymbol{k}\zeta} E_{k\zeta} c^\dagger_{\boldsymbol{k}\zeta} c_{\boldsymbol{k}\zeta} + \sum_{\boldsymbol{k}\boldsymbol{k}'} \sum_{\zeta\zeta'} \langle \psi_{\boldsymbol{k}\zeta} | \mathcal{H}_R | \psi_{\boldsymbol{k}'\zeta'} \rangle c^\dagger_{\boldsymbol{k}\zeta} c_{\boldsymbol{k}'\zeta'} \,, \tag{2.30}$$

where $E_{\boldsymbol{k}\zeta}$ is the energy of the CSS given by equation (2.8) and (2.13) for the minimal model and the Na_3Bi model, respectively. The operator $c^\dagger_{\boldsymbol{k}\zeta}$ ($c_{\boldsymbol{k}\zeta}$) creates (annihilates) a particle in the CSS $\psi_{\boldsymbol{k}\zeta}$, which is referred in

the following as $\psi_{\boldsymbol{k}\uparrow}$ and $\psi_{\boldsymbol{k}\downarrow}$, where the up and down arrows correspond to the chiral index $\zeta = 1$ and $\zeta = -1$, respectively. Explicitly, the effective Hamiltonian as a function of the model parameters reads as

$$\mathcal{H}_{\text{eff}} = \sum_{\boldsymbol{k}} \left(c^{\dagger}_{\boldsymbol{k}\uparrow}, c^{\dagger}_{\boldsymbol{k}\downarrow}\right) \begin{pmatrix} E_{\boldsymbol{k}\uparrow} & -iR_0 g_{\mathbf{k}} k_- \\ iR_0 g_{\mathbf{k}} k_+ & E_{\boldsymbol{k}\downarrow} \end{pmatrix} \begin{pmatrix} c_{\boldsymbol{k}\uparrow} \\ c_{\boldsymbol{k}\downarrow} \end{pmatrix} , \tag{2.31}$$

where $k_\pm = k_z \pm ik_x$. $E_{\boldsymbol{k}\uparrow(\downarrow)}$ is the energy of the CSS without the RSOC and the off-diagonal part is written as a function of a term that depends on the momentum, $g_{\mathbf{k}}$, for convenience. The latter is obtained from the second term of equation (2.30) as $g_{\mathbf{k}} \equiv i\langle\psi_{\boldsymbol{k}\uparrow}|\mathcal{H}_R|\psi_{\boldsymbol{k}\downarrow}\rangle/R_0 k_-$. By performing the integration and using the states reported in equation (2.4), the following expression is obtained

$$g_{\mathbf{k}} = \frac{16|A_\Phi|^2\Delta^2\sqrt{\Delta^2 - F_\downarrow}\sqrt{\Delta^2 - F_\uparrow}}{16\Delta^4 - 8\Delta^2(F_\downarrow + F_\uparrow) + (F_\downarrow - F_\uparrow)^2} , \tag{2.32}$$

where Δ, A_Φ and $F_{\uparrow,\downarrow} \equiv F_{\zeta=\pm1}$, are defined previously for both models in equations (2.6) and (2.12). By diagonalizing $\mathcal{H}_{\text{eff}}$ the dispersion relation for the GSS with Rashba interaction reads as

$$E^{\text{RSOC}}_{\pm}(\boldsymbol{k}) = \varepsilon(k_z) \pm v_{\boldsymbol{k}} C_3 k_x , \tag{2.33}$$

with the modified velocity

$$v_{\boldsymbol{k}} \equiv \sqrt{v^2 + \frac{g^2_{\mathbf{k}} {R_0}^2 (k_x^2 + k_z^2)}{{C_3}^2 {k_x}^2}} . \tag{2.34}$$

In the former expressions, C_3 depends on the model parameters and it is defined in equation (2.15c) together with the non-flat band contribution $\varepsilon(k_z)$ given by equation (2.14). Note that $C_3 \neq 0$ as it is expressed as a function of m_2 in equation (2.15c) and $m_2 \neq 0$ is non-zero for topologically protected Weyl nodes. For the range of positive k_x, the eigenstates, that are the GSS, can be written as

$$\psi_{\boldsymbol{k}+} = \frac{1}{\sqrt{2v_{\boldsymbol{k}}(v + v_{\boldsymbol{k}})}} \begin{pmatrix} v + v_{\boldsymbol{k}} \\ ig_{\mathbf{k}} R_0 k_+ / C_3 k_x \end{pmatrix} , \tag{2.35a}$$

$$\psi_{\boldsymbol{k}-} = \frac{1}{\sqrt{2v_{\boldsymbol{k}}(v + v_{\boldsymbol{k}})}} \begin{pmatrix} ig_{\mathbf{k}} R_0 k_- / C_3 k_x \\ v + v_{\boldsymbol{k}} \end{pmatrix} . \tag{2.35b}$$

For $R_0 = 0$ the velocity resembles $v_{\boldsymbol{k}} = v$ and the expected correspondence between GSS and CSS is recovered, namely $\psi_{\boldsymbol{k}+} = \psi_{\boldsymbol{k}\uparrow}$ and $\psi_{\boldsymbol{k}-} = \psi_{\boldsymbol{k}\downarrow}$ for $C_3 > 0$. If $C_3 < 0$ then $\psi_{\boldsymbol{k}-} = \psi_{\boldsymbol{k}\uparrow}$ and $\psi_{\boldsymbol{k}+} = \psi_{\boldsymbol{k}\downarrow}$.

The connection between CSS and GSS becomes clearer by writing down the effective Hamiltonian (2.31) in the following form

$$\mathcal{H}_{\text{eff}} = \sum_{\mathbf{k}} \left(c^{\dagger}_{\boldsymbol{k}\uparrow}, c^{\dagger}_{\boldsymbol{k}\downarrow} \right) \left(\varepsilon(k_z) \mathbb{1}_2 + \boldsymbol{h} \cdot \boldsymbol{\sigma} \right) \begin{pmatrix} c_{\boldsymbol{k}\uparrow} \\ c_{\boldsymbol{k}\downarrow} \end{pmatrix} , \tag{2.36a}$$

$$\boldsymbol{h} = -|C_3| k_x v_k \left(\sin\theta\cos\phi, \sin\theta\sin\phi, \cos\theta \right) . \tag{2.36b}$$

The angles that define the Pauli vector components are momentum-dependent

$$\theta = \cos^{-1}\left[-\text{sign}(C_3) v / v_{\boldsymbol{k}} \right] , \qquad \phi = \tan^{-1}(-k_z/k_x) . \tag{2.37}$$

Within this formulation, the eigenvectors given by equation (2.35) can be written as

$$\psi_{\boldsymbol{k}\pm} = \begin{pmatrix} \sin(\theta/2) \\ -e^{i\phi}\cos(\theta/2) \end{pmatrix} , \qquad \psi_{\boldsymbol{k}\mp} = \begin{pmatrix} e^{-i\phi}\cos(\theta/2) \\ \sin(\theta/2) \end{pmatrix} . \tag{2.38}$$

In the former expression, it is apparent that the pair of GSSs still have orthogonal spinors, however they exhibit a more complex spin structure. The spin projection of the states is described by the two momentum-dependent angles θ and ϕ.

Minimal model

Next, the results are particularised for the minimal model discussed in section 2.1.1. In this model, $\varepsilon = 0$, $C_3 = 1$, $\kappa = 1$ and F does not depend on chirality. Therefore, $g_{\mathbf{k}} = 1/2$ and the modified velocity as well as the GSSs have an utterly simplified form. Due to the absence of momentum dependence in $g_{\mathbf{k}}$, the GSSs are obtained by rotating the CSSs and, with a redefinition of the spin bases, the states are still chiral states. Consistently, by writing down the dispersion of the effective model, an anisotropic version of a 2D Dirac equation with an R_0-dependent velocity is obtained from equation (2.33)

$$E^{\text{RSOC}}_{\pm}(\boldsymbol{k}) = \pm \sqrt{ \left(v^2 + \frac{R_0^2}{4} \right) k_x^2 + \frac{R_0^2}{4} k_z^2 } . \tag{2.39}$$

Na_3Bi

The case of Na_3Bi has some more subtleties due to the non-flat bands. In this model, $C_3 = \sqrt{m_2^2 - c_2^2}/m_2$ and $g_{\mathbf{k}}$ is momentum-dependent and it is given by

$$g_{\mathbf{k}} = -\frac{\text{sign}(m_2) c_{2+} \sqrt{ c_2^2 k_x^2 v^2 / c_{2\pm}^2 + \left(k_x^2 m_2 + k_z^2 m_1 - m_0 \right)^2 }}{2\left(k_z^2 m_1 m_2 - c_{2\pm}^2 k_x^2 - m_0 m_2 \right)} , \tag{2.40}$$

where $c_{2\pm} = c_2 \pm m_2$ and $c_{2\pm}^2 = c_2^2 - m_2^2$. For small momenta, a parabolic function approximates $g_{\mathbf{k}}$ as

$$g_{\mathbf{k}} = g_0 + g_1 k_x^2 + g_2 k_z^2 + \mathcal{O}(k_x^2, k_z^2) \ , \tag{2.41}$$

where g_i with $i = 0, 1, 2$ are constants given by the model parameters. In particular, $g_0 = c_+/2m_2$ resembles the momentum-independent contribution of the minimal model.

By adding the quadratic terms in the onsite energy, the GSSs become more complex and gain a non-trivial spin-mixing. Figure 2.12 shows the squared absolute value of the upper and lower component of $\psi_{\boldsymbol{k}+}$ as a function of R_0. The components of $\psi_{\boldsymbol{k}+}$ evolve in a more mixed state by increasing R_0 and the strength of the evolution rises for states with higher k_z.

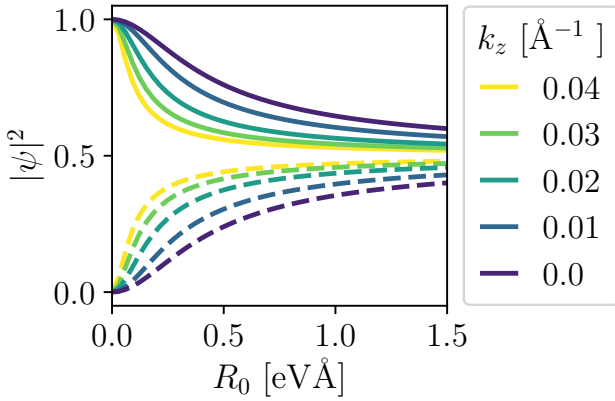

Figure 2.12: Squared absolute value of the upper (solid line) and lower (dotted line) component of $\psi_{\boldsymbol{k}+}$ for Na_3Bi as a function of R_0 and k_z at fixed $k_x = 0.01\,\text{Å}^{-1}$. The GSSs are represented in the basis of the CSSs. Hence, the limit of $|\psi|_i^2 \to 0.5$ corresponds to a state with fully mixed chirality.

2.3.2 Effect of the RSOC on electron transport in a finite slab setup

The RSOC induces a spin precession that could generate spin-switching processes as well as a non-trivial spin texture of the scattering states. To study the effect of RSOC interaction on the conductance, transport calculations are performed within the Landauer-Büttiker formalism[2] at zero-temperature with the toolkit `Kwant` [102]. The proposed setup is a

[2] See appendix B for a more detailed discussion of this formalism.

finite slab system, with 2D metallic leads, represented schematically in figure 2.13 (a). The choice of this setup aims at measuring the transport properties of the surface states only, as already studied in reference [40]. The metallic 2D leads maximize the overlap with the surface states, which are localised near the surfaces, and they minimize the contribution of the bulk states, which are expected to be extended in the scattering region.

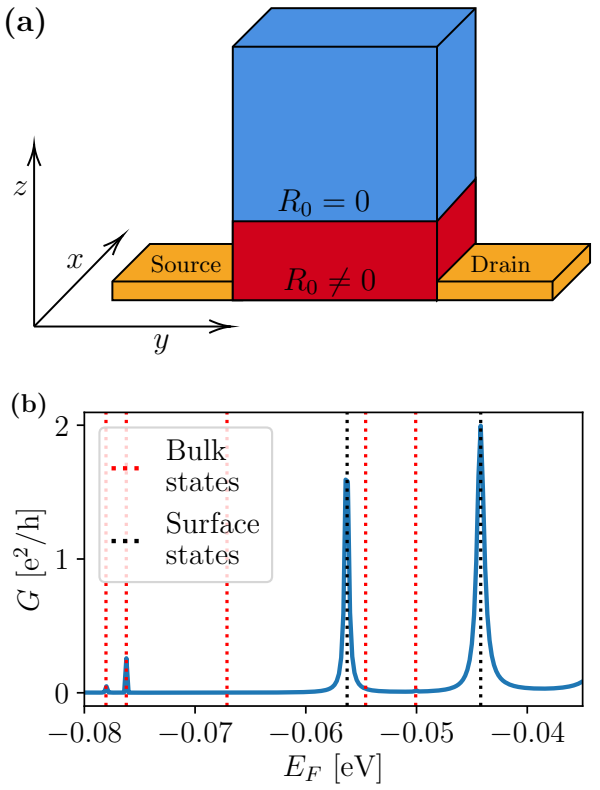

Figure 2.13: (a) Schematic view of the device. The metallic leads are represented in orange with the source and drain indicated. The red color marks the part where the RSOC is considered whereas the blue part indicates the pure DSM without coupling. (b) Conductance as a function of the Fermi energy; the eigenenegies of the system are marked with black (red) vertical lines for surface (bulk) states. The setup consideres is a slab of Na_3Bi with $R_0 = 0$ and size $150 \times 250 \times 40$ Å^3.

The slab has dimensions $L_x \times L_y \times L_z$ with 2D leads attached in the plane $y = 0$ at the two ends of the sample. The discretization length is set to 5 Å in the following. The metallic leads are semi-infinite in the

x-direction and they intersect the scattering region at the edge extended along z. The leads are described by a conventional metallic Hamiltonian

$$\mathcal{H}_{\text{leads}} = (A\mathbf{k}^2 + B)\mathbb{1}_4 \ , \tag{2.42}$$

where A and B are chosen to connect efficiently with the sample and to reach the quantised conductance without RSOC. The scattering region is described by the following Hamiltonian:

$$\mathcal{H}_{\text{scat}} = \mathcal{H}_D + \mathcal{H}_R \ , \tag{2.43}$$

where $\mathcal{H}_D$ is the pristine Dirac semimetal Hamiltonian from equation (2.3) and $\mathcal{H}_R$ is the Rashba perturbation in equation (2.29).

Figure 2.13 (b) shows the conductance as a function of the Fermi energy for a slab without RSOC. The system reaches the quantised conductance only for the surface states while the conductance is practically zero for the bulk states except for sharp resonances.

Note that, in the metallic leads, the RSOC is not included and hence, the spin is conserved. In systems with a conserved quantity in the leads, the conductance can be factorised by the contributions of the modes that have the same eigenvalue for such operator. In the basis of Na_3Bi Hamiltonian (1.54), the chirality operator is

$$\Gamma_\zeta = \sigma_z \otimes \mathbb{1}_2 \ ,$$

where σ_z is the Pauli matrix in the basis of the Weyl sectors and the identity $\mathbb{1}_2$ correspond to the S and P orbitals basis. Due to the form of the basis reported in equation (1.54), the chiral sectors match the spin, being the states with $\zeta = +1$ also the $s^z = +1/2$ and the $\zeta = -1$ the one with $s^z = -1/2$. Hence, there is a correspondence between spin and chirality in this model. The spin operator conmutes with the Hamiltonian of the metallic leads and the DSM Hamiltonian if $R_0 = 0$.

Considering the decomposition in spin-modes, the total conductance G_{tot} is calculated from equation (B.5b) by summing up the following contributions

$$G_{\text{tot}} = G_{++} + G_{--} + G_{+-} + G_{-+} \ , \tag{2.44}$$

where the subscripts indicate the spin-polarization of the incoming and outcoming modes in the leads. $G_{\pm\pm}$ corresponds to the conductance of modes with the same spin/chirality, while $G_{\pm\mp}$ is the conductance of modes with opposite spin/chirality in the incoming and outgoing channels. Due to TR symmetry, the transmissions with opposite direction

and chirality are equivalent. Hence, the following equalities hold for this system

$$G_{++} = G_{--} \ , \quad G_{+-} = G_{-+} \ , \tag{2.45}$$

implying that the four terms in equation (2.44) are reduced to two contributions.

Finally, it is important to point out some aspects related to the finite-size effects. Due to the finite size, the surface states exist at discrete energies and the quantisation of k_x, k_y and k_z leads to multiple surface states. The Fermi energy of the sample is set to the fundamental mode without RSOC and the evolution of the conductance G is studied as a function of R_0. This configuration is close to an experimental realisation: The aim is to set the Fermi energy of the sample to the maximum value of the transmission for $R_0 = 0$, which corresponds to the fundamental mode. Then the RSOC term is implemented by turning on an electric field in the substrate. The analysis is restricted to this mode, which is nodeless in all spatial directions. This state is chosen for the sake of concreteness, but equivalent results are obtained for the other surface state modes. In Na_3Bi hybrid bulk-surface states arise at higher energies due to the quadratic terms in the Hamiltonian. Therefore, the conductance is not perfectly quantized even without RSOC. These states show a strong size dependence, but their contributions can be avoided by an appropriate choice of Fermi energy, as shown in figure 2.13 (b). In the presented results, the Fermi energy is fixed as this would provide a simpler setting for actual experiments.

In the following, the results for the minimal model and for Na_3Bi are discussed. As expected, the non-trivial mixing in Na_3Bi have important consequences in the transport properties compared to the minimal model.

Spin-switcher

As already discussed in section 2.1.3, the Fermi arcs form two channels that, without external perturbations, amounts for a contribution of e^2/h to the conductance for each state. In the setup shown in figure 2.13 (a), one spin channel surrounds the cuboid while the other propagates in the plane $y = 0$. Hence, in a two-leads device, the conductance for $R_0 = 0$ is expected to be $G = 2e^2/h$ from the contribution of the two surface states. This was checked in figure 2.13(b). When the RSOC is included in the bottom part of the structure, a spin-rotation effect can arise in the $y = 0$ plane and, due to the mixing induced by RSOC, the spin-flip conductance $G_{\pm\mp}$ becomes nonzero, allowing for spin-switching. The quantization is then lost.

In figure 2.14 the spin polarised conductance is shown along with the total conductance for a slab of Na_3Bi. The conductance is factorised according to the spin polarization of the modes in the leads by equation (2.45). In the regime of $R_0 \gtrsim 0.5\,\mathrm{eV\,Å}$, the spin-switch conductance $G_{\pm\mp}$ becomes dominant compared to the spin-conserved conductance $G_{\pm\pm}$. Note that, even if the quantization is lost, the total conductance does not decrease for this specific configuration. The device is then a spin-switcher and the switching effect is controlled by the strength of R_0, which in turns can be tuned by an electric field.

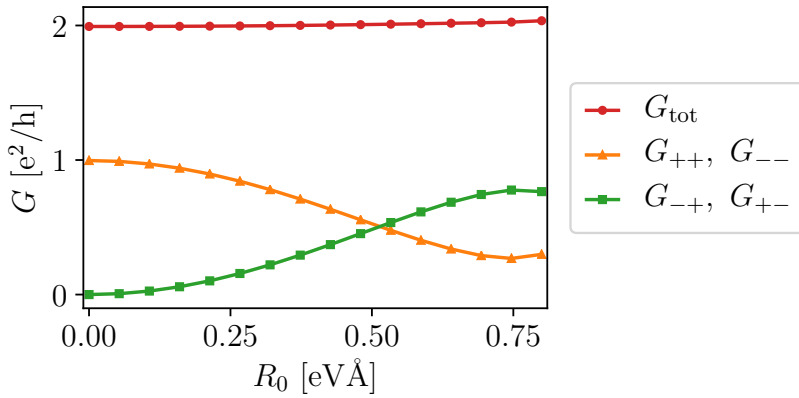

Figure 2.14: Total conductance G_{tot} and polarised spin conductance G_{ij} with $i, j = \pm$ as a function of R_0. The system is a slab of Na_3Bi with dimensions $150 \times 150 \times 100$ Å^3 and $L_{\mathrm{RSOC}} = 50$ Å.

In the former calculation, the RSOC term is implemented by equation (2.29) using a step function that reads as

$$f_R(y) = \theta(y - L_{\mathrm{RSOC}}) \,, \tag{2.46}$$

where θ denotes the usual Heaviside step function. Smoother functions were tested without significant deviations from the presented results due to the highly peaked shape of the surface states near the interface. The value of L_{RSOC} can be related to the charge accumulation near the surface that breaks the symmetry. In the system considered, the charge accumulation is mostly given by the surface states and their decay. Therefore, L_{RSOC} is estimated to be of the order of the surface states decay length. This assumption yields to $L_{\mathrm{RSOC}} \sim 50$ Å for the model parameters considered here.

An accurate determination of the length L_{RSOC} is only possible via DFT methods that are outside the scope of this work. However, it is found that the value of L_{RSOC} is not critical, as long as is it of the order of

the decay length of the surface states. Figure 2.15 shows the conductance for a range of values of L_{RSOC} as a function of R_0. If L_{RSOC} is much smaller than the decay length of the surface states, the switching effect is minimised. However, the conductance quickly converges to the result for $L_{\mathrm{RSOC}} = 50$ Å. Note that in figure 2.15 the details of the shape of the conductance curve as a function of R_0 are modified for $L_{\mathrm{RSOC}} = 20\,$Å and $L_{\mathrm{RSOC}} = 50\,$Å. A larger L_{RSOC} affects the bulk modes of the slab and thus changes the spectrum, especially for higher values of R_0. The results are consistent for $R_0 \lesssim 0.6\,$eV and L_{RSOC} which exceeds the localisation length of the surface states.

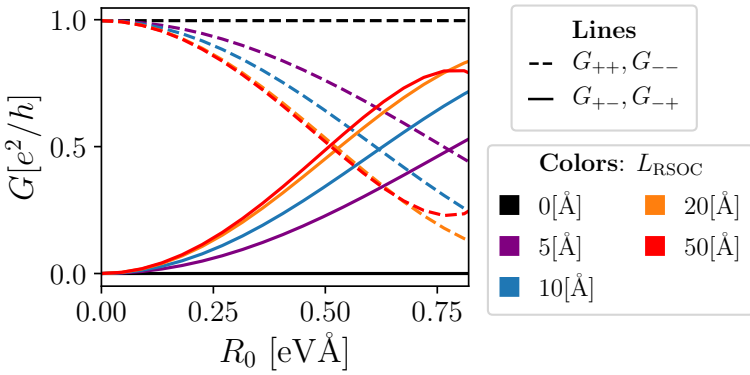

Figure 2.15: Polarised spin conductance $G_{\pm\pm}$ (in dashed line) and $G_{\pm\mp}$ (in solid line) for a range of L_{RSOC} highlighted with the colors defined in the legend. The legend $L_{\mathrm{RSOC}} = 0\,$Å corresponds to the case with no Rashba coupling. The system is a slab of Na_3Bi with dimensions $150 \times 150 \times 100$ Å^3.

Effect of the quadratic terms and remarks on the system size

Next, the main ingredients of the spin-switching effect are investigated finding that the non-trivial dispersion of the surface states in the z-direction has an important role in this effect. The absence of quadratic terms in the Hamiltonian leads to a trivial rotation of the spin-chiral basis without spin-flip effects. In figure 2.16(a), the conductance without quadratic terms is reported showing $G_{\pm\mp} = 0$ independently of R_0.

In the absence of dispersion in the z-direction, the analytic calculations of section 2.3.1 have shown that the effect of RSOC is a trivial rotation of the spin basis. In the transport calculations, the basis rotates with increasing R_0 and the injected current becomes non-polarised within the

new spin basis due to the basis mismatch. No spin-switching arises and the spin-polarised current as well as the total current lowers by increasing R_0, due to the growing mismatch of the basis.

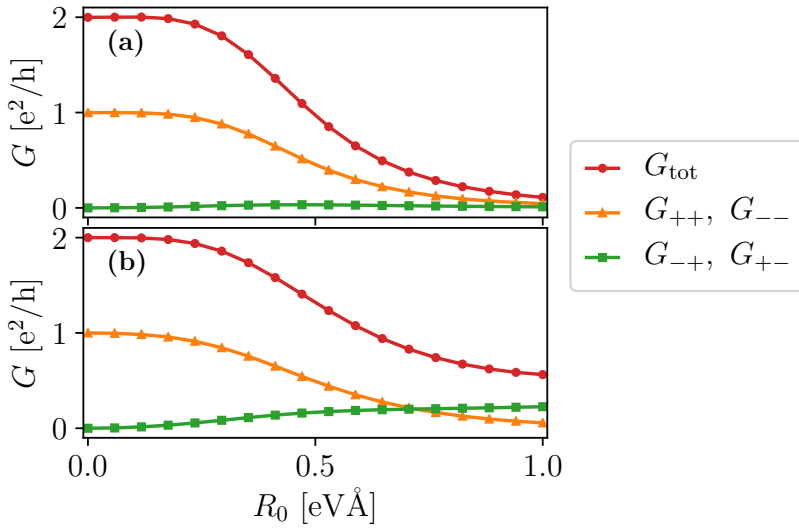

Figure 2.16: Total conductance G_{tot} and polarised spin conductance G_{ij} $(i, j = \pm)$ as a function of the RSOC coupling constant R_0. (a) Slab of DSM with the same parameters as Na_3Bi but setting the quadratic terms to zero, i.e. with $c_0 = c_1 = c_2 = 0$. The dimensions are $150 \times 150 \times 100$ Å^3. (b) Na_3Bi sample of size $80 \times 150 \times 40$ Å^3 and $L_{\text{RSOC}} = 50$ Å.

On the other hand, the magnitude of the spin-switching effect depends also on the particular geometric shape of the device. Thinner slabs typically show lower values for the total conductance. The reason for this lies in the multiplicity of the surface states that appear in the scattering region. Due to the finite size of the samples, the slab shows multiple surface modes from the quantization of the momenta, as discussed in figure 2.13 (b). In bigger samples, the energy distance between the surface states diminishes and many surface modes overlap for a given energy of injection, thus leading to higher vales of the conductance. On the other hand, in smaller samples, the spin-flip effect is also noticeable, but the conductance is lowered as long as the next surface mode is separated in energy and not accessible at a fixed injection energy, as exemplifies in figure 2.16 (b). A careful adjustment of the Fermi energy for each value of R_0 would prevent the conductance reduction.

2.3.3 Effect of impurity disorder

Finally, the robustness of the spin-switch effect is checked against point-like disorder. The point defects are placed randomly in the scattering region and the disorder is modelled by non-magnetic point-like impurities with an equal weight in the four orbitals of the basis of the Hamiltonian (2.3). For that, the onsite energy is replaced by W_0 in a fraction of sites of the grid used in the numerical calculation of the transport problem, choosing the sites randomly. The strength of the impurity potential W_0 is comparable to the intra-band hopping in order to have an impact on the electron states. Specifically, $W_0 = 0.5$ eV in the calculations and the spin polarised conductance is averaged over 250 realisations of disorder.

Figure 2.17 shows the average conductance for the same parameters of figure 2.14 when the impurity density is as large as $n_{\text{imp}} = 4 \times 10^{19}$ cm^{-3}. Error bars indicate the standard deviation calculated by:

$$\delta\langle G\rangle = \sqrt{\frac{1}{N_R}\sum_i |G_i - \langle G\rangle|^2}\,, \tag{2.47}$$

where the sum runs over the disorder realisations, N_R is the total number of realisations and $\langle G\rangle$ is the mean value of the conductance.

By adding disorder, the only noticeable effects are an overall reduction of the conductivity, as expected, and a slight shift of the crossing point towards higher values of R_0. However, the spin-flip effect is still clearly revealed. Hence, the effect is robust against disorder, even at such large impurity density.

2.4 Conclusions

In this chapter, the impact of the external electric field and the RSOC on the surface Fermi arcs of DSMs and WSMs is analysed. Two models for describing the TSMs are studied, namely a minimal model that describes two isotropic cones with totally flat Fermi arcs and a DFT fitting model with dispersive terms, describing the low-energy physics of materials like Na_3Bi and Cd_3As_2.

The effect of the electric field is briefly addressed in section 2.2 and it was compared with the experimental Hall measurements of reference [181]. Even if the main scope of the experiment was to prove the existence of the Weyl orbits, the experimental results show clear evidence of theoretical predictions. The setup manipulates the voltage gate in each surface of the slab separately and an external electric field results from the voltage drop in the slab. The dependence of the LLs on the voltage configuration

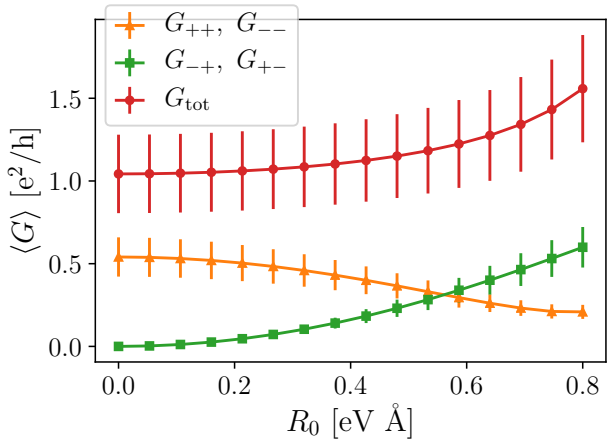

Figure 2.17: Average conductance in the presence of point-like impurities of strength $W_0 = 0.5\,\text{eV}$ and density $n_{\text{imp}} = 4 \times 10^{19}\ \text{cm}^{-3}$. The rest of parameters are the same as in figure 2.14. Results are averaged over 250 realisations of disorder and error bars correspond to the standard deviation (2.47).

is evidence of the modification of the Dirac cones due to the electric field. According to the theoretical calculations, together with a renormalization of the Fermi velocity, the Dirac cones of the Fermi arcs are displaced by the electric field in opposite directions in energy and momentum depending on the chirality. This impacts the crossings of the LLs of the system when a magnetic field is introduced in the slab, resulting in filling factors that are modified according to the electric field configuration.

On the other hand, the coupling between chiral sectors is analysed through the RSOC in section 2.3. This coupling is obtained when the spatial inversion asymmetry is broken in a nanostructure and it could be tuned with an external electric field in the substrate. The impact of the RSOC on the Fermi arcs is addressed analytically in section 2.3.1 through an effective model that captures the rotation of the spin of the surface states and the mixing of the chiralities as a function of the electron's momentum and the coupling strength. The Fermi arcs of DSMs have definite chirality when RSOC terms are absent and their spin orientation keeps constant for each energy branch. Once the RSOC is taken into account, the spinors of counter-propagating surface states are still orthogonal but develop a non-trivial spin structure.

This impacts on the transport properties of the states that are studied through transport calculations in bars of DSM connected to 2D metallic leads in one of the surfaces. When the chiralities are decoupled, the

conductance is quantised with equal contribution from both spins and without signatures of spin-flip conductance due to the electron transport in the topological channels. On the other hand, by including the RSOC, depending on the magnitude of the quadratic terms in the Hamiltonian, the spin-flip conductance may become dominant, thus showing the potential of the system for spintronic applications. The effect of the disorder is also quantitatively addressed to prove the robustness of the spin-switcher. This effect withstands a relatively high density of point-like disorder, as discussed in section 2.3.3. By increasing the impurity density, the total conductance is suppressed and the crossing point of the oppositely polarised conductances are displaced in R_0, without destroying the spin-flip for relatively high impurity densities, being a promising prediction for an experimental realisation of this device.

3 HIGH CHERN NUMBER QUANTUM ANOMALOUS HALL HETEROSTRUCTURES

Preamble

This chapter deals with topological gapped phases of matter, namely TIs. Due to the topological properties of the band structure, these materials exhibit protected edge or surface states between regions of gap inversion, as already discussed in section 1.3.1. Gap inversion could occur at the interface of the TI slab with the vacuum, as well as by stacking different insulators with trivial and inverted gaps. Exploiting the possibilities of quantum well configurations created by stacking was the basis for the first experimentally observed QSH insulator in HgTe/CdTe quantum wells predicted in 2006 [19] and measured one year later [139]. A trivial state is obtained when the thickness is below the critical value, while a pair of helical channels appears for wider wells, see section 1.3.1. The physical process leading to the topological transition is the band inversion in the HgTe region together with quantum confinement, which shifts the energy levels into a non-inverted regime. The edge states that arise for the non-trivial width contribute to two perfect channels, each with a quantised conductance of e^2/h. The conductance experiments in HgTe/CdTe samples showed the signature of the QSH in two-lead devices [139] and in non-local Hall bar configurations [219].

In the QSH effect, the spins propagate in opposite directions and the total conductance vanishes. To obtain a single channel and a non-zero total conductance, the degeneracy of the Kramers partners of the QSH state needs to be removed by breaking the TR symmetry. Then, a QAH state is obtained, in which only one spin sector hosts the topological channels while the other has trivial states. In the late 1980s, Haldane proposed the first model for a QAH state [105] in a honeycomb lattice with a periodic magnetic flux that breaks TR symmetry. Despite the zero net magnetic flux, the periodic magnetic field introduces a phase in the second-neighbour hopping of the model and drives the electrons to form a conducting edge state without external fields [105]. This model was a breakthrough in the starting field of topology applied to condensed matter systems. However, it has only been realised in ultracold atom lattices [120].

Despite the difficulties in realising the QAH, new prospects have emerged

since the discovery of 2D and 3D TIs. Intuitively, by introducing magnetic order to break the TR symmetry in QSH materials, a single chiral edge state could be obtained [205]. Following this prescription, HgTe wells doped with Mn impurities were first proposed as QAH platforms [154]. Due to the paramagnetism of the doped HgTe, an external magnetic field of 70 mT was required to drive the system into the quantised regime [24]. A similar approach in 3D TIs of $(Bi/Sb)_2(Se/Te)_3$ family was proposed soon after [204, 308] and successfully realised in Cr−doped $(Bi, Sb)_2Te_3$ films in 2013 [34] without including magnetic fields. Since then, doped 3D TIs have been extensively studied [33, 172, 195]. The magnetic TIs are not the only platforms where the QAH state has been achieved. In fact, intrinsically magnetic TIs such as $MnBi_2Te_4$ [39], moiré materials such as graphene-based heterostructures [241, 243] and transition metal dichalcogenides [148] were proven to host QAH states. The reader is referred to several reviews [35, 41, 110, 156, 265, 291] for a more detailed state of the art.

A new development of the QAH effect has been achieved in heterostructures made of TI layers with varying magnetic doping. Depending on the number of layers, the Chern number C that gives the number of edge states is controlled at will [69, 281]. In the heterostructures, the doped layers play a dual role: they break the TR symmetry in the nearest TI, and they act as trivial insulators, where the thickness is a control parameter to connect the neighbouring topological states. For thin magnetically doped layers the heterostructure exhibits a single $C = 1$ state, while for thicker layers the sample shows a higher C number. Chern numbers as high as $C = 5$ have been measured experimentally in devices based on multilayered heterostructures [319].

As already discussed in chapter 2, the external electromagnetic fields can manipulate the topological properties of materials. In the case of high-Chern number magnetic insulators, it would certainly be desirable to tune the topological properties in the device by means of electric fields. In fact, an external electric field could be of use in different types of electronic devices where a fast change in the amount of current or the effective electrical resistance is required.

The chapter is organised as follows:

- The models for describing a QAH state are introduced in section 3.1, starting from a minimal model and progressing to more realistic Hamiltonians in three steps:
  - First, in section 3.1.1 the QAH state is achieved in 2D systems by Zeeman splitting generated by magnetic doping.
  - Then, in section 3.2.1, the surface states of a 3D TI are used

to build an effective model where the results of section 3.1.1 are generalised.

– Finally, the heterostructures of layered TIs with varying doping concentrations are discussed in section 3.1.3. In these heterostructures, higher Chern number can be achieved due to the multiple topological bands resulting from the layered interfaces.

- In section 3.2 the heterostructure of layered magnetic TI is studied when subject to an external electric field in the growth direction. First, the case of a single magnetically doped slab is addressed in section 3.2.1. Then, in section 3.2.2 the Chern number is calculated for the heterostructure with external field as well as the effect of the electric field on transport.

3.1 Models for a QAH insulator

This section is devoted to the discussion of the model for the QAH insulator used in section 3.2.2. The model is derived theoretically from the breaking of TR symmetry in TIs by magnetic doping. The model is presented in three steps:

- First, a minimal model for a QAH state is obtained from the QSH state. In this 2D system, the effect of the QAH state can be understood from the band inversion in a simple cartoon plotted in figure 3.1.

- Next, the former reasoning is extended to 3D were an effective model for the surface states in a slab is derived. This model is cast in a similar form to the previous section such that a (more complicated) band inversion process is obtained, as shown in figure 3.2.

- Finally the model for the slabs of doped Bi_2Se_3 is discussed in section 3.1.3.

3.1.1 Minimal model for a QAH: 2D TI with magnetic doping

In this section a minimal model for a QAH state is derived from the BHZ model, discussed in section 1.3.1. The magnetically doped 2D TI is presented here at the level of theory, although not experimentally achievable. In fact, HgTe/CdTe quantum wells have been proved antiferromagnetic, thus preventing them from showing the QAH effect [24]. The case of

InAs/GaSb was also proposed theoretically [283] but not yet experimentally realised due to the limitation of sample quality resulted from the small bandgap, generated by the weaker spin-orbit coupling in III-V semiconductors. The derivation of the QAH state is specially clear for the 2D system and hence it is presented here as a valuable example.

Near the Γ point, the BHZ model can be cast in two separate TR partners in the basis of $|E_1\uparrow\rangle, |H_1\uparrow\rangle, |E_1\downarrow\rangle, |H_1\downarrow\rangle$ [19]

$$\mathcal{H}_{\mathrm{BHZ}}(\mathbf{k}) = \begin{pmatrix} h(\mathbf{k}) & 0 \\ 0 & h^*(-\mathbf{k}) \end{pmatrix} . \tag{3.1}$$

If inversion symmetry and axial symmetry around the growth axis are preserved, the interblock elements vanish[1]. The form of $h(\mathbf{k})$ is then:

$$h(\mathbf{k}) = R_0(\mathbf{k}) + \mathbf{R}(\mathbf{k})\boldsymbol{\sigma} , \tag{3.2}$$

with

$$R_x(\mathbf{k}) \pm iR_y(\mathbf{k}) = vk_\pm , \tag{3.3a}$$
$$R_z(\mathbf{k}) = m_0 - m_1(k_x^2 + k_y^2) , \tag{3.3b}$$
$$R_0(\mathbf{k}) = c_0 - c_1(k_x^2 + k_y^2) . \tag{3.3c}$$

Here $k_\pm = k_x \pm ik_y$ and all the other quantities are constants obtained by fitting of DFT calculations or experimental ARPES measurements. As already discussed in section 1.3.1, the topological nature of this model is encoded in the relative sign of the mass term, being non-trivial for $m_0 m_1 > 0$.

To achieve a QAH state TR symmetry has to be broken. The magnetic doping was first proposed as a suitable method for this end [154]. To model it, a phenomenological term describing the induced spin splitting is introduced. The spin splitting resembles two contributions, depending on the nature of the bands: g_{E} for the electron subbands and g_{H} for the heavy-hole subbands. In the aforementioned basis, it has the following form:

$$\mathcal{H}_{\mathrm{Z}} = \begin{pmatrix} g_{\mathrm{E}} & 0 & 0 & 0 \\ 0 & g_{\mathrm{H}} & 0 & 0 \\ 0 & 0 & -g_{\mathrm{E}} & 0 \\ 0 & 0 & 0 & -g_{\mathrm{H}} \end{pmatrix} . \tag{3.4}$$

The system with magnetic doping is then described by the two contributions

$$\mathcal{H}_{\mathrm{tot}} = \mathcal{H}_{\mathrm{BHZ}} + \mathcal{H}_{\mathrm{Z}} , \tag{3.5}$$

[1] See section 1.3.1 for a more detailed discussion of BHZ model.

where $\mathcal{H}_{\mathrm{BHZ}}$ is given by equation (3.1) and $\mathcal{H}_{\mathrm{Z}}$ by expression (3.4).

In the pristine BHZ model the total Chern number cancels. In fact, the two subblocks lead to degenerate bands with opposite sign in the Chern number $C^{(n)}$, as already discussed in section 1.3.1. However, by including the Zeeman term the two bands are not degenerated, the two spin blocks are no longer one the TR partner of the other. The Chern number no longer cancels exactly in pairs. The Zeeman term in equation (3.4) can be interpreted as an effective mass for each one of the blocks separately, leading to a gap in the upper and lower spin sectors of

$$\Delta^{\uparrow} = 2m_0 + (g_{\mathrm{E}} - g_{\mathrm{H}}) \ , \tag{3.6a}$$

$$\Delta^{\downarrow} = 2m_0 - (g_{\mathrm{E}} - g_{\mathrm{H}}) \ . \tag{3.6b}$$

In order to obtain a QAH state the unbalance between the subblocks is required. In other words, the following conditions must be met:

- One block must be in a trivial insulator phase ($\Delta^i m_1 < 0$) and the other block in a topological phase ($\Delta^j m_1 > 0$), for $i \neq j$ where $i = \uparrow, \downarrow$ and $j = \uparrow, \downarrow$. This implies that $\Delta^{\uparrow}\Delta^{\downarrow} < 0$.
- The entire system should still be in the insulating phase with a full bulk gap. In this case, this condition translates to $(2m_0 + g_{\mathrm{E}} + g_{\mathrm{H}})(2m_0 - g_{\mathrm{E}} - g_{\mathrm{H}}) < 0$.

In order to fulfil both conditions, the Zeeman splitting of the opposite subbands must have opposite sign, i.e. $g_{\mathrm{E}} g_{\mathrm{H}} < 0$

These conditions can be understood intuitively as follows. The effect of the mass modification on the surface states is to push the surface states of one of the spin sectors towards delocalisation in the bulk, due to the decrease of the gap, until the bands merge and become trivial. However, the opposite spin sector continues to be topological. Hence, it holds surface states without Kramers partners that lead to the QAH state.

The QAH derived from the QSH is then associated with a band inversion process. Figure 3.1 shows the evolution of the bands resulting in the QAH phase.

3.1.2 Effective surface state model for a magnetically doped 3D TI

In 3D TIs of the tetradymite semiconductors Bi_2Te_3, Bi_2Se3, and Sb_2Te_3, the QAH have been predicted since 2010 from the seminal work by Yu *et al.* [308]. There, from first principle calculations, magnetically ordered insulators were obtained by the doping of transition metals such as Cr and Fe.

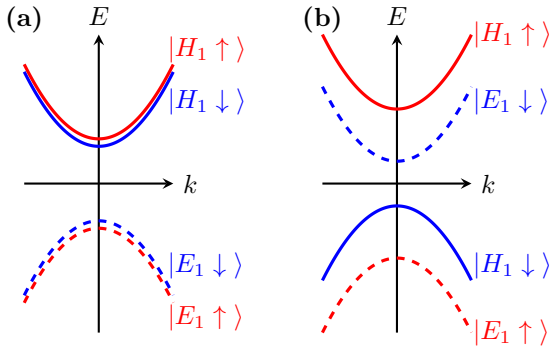

Figure 3.1: Schematic representation of the subband evolution by increasing the exchange field. In (a) the initial (inverted) subbands are plotted. The degeneracy of the bands is lifted to improve the visibility. In (b) by increasing the exchange field with $g_{\mathrm{E}} < 0$ and $g_{\mathrm{H}} > 0$, the $|E_1\rangle$ and $|H_1\rangle$ states enter the trivial regime whereas the spin up bands stay topological and increase their gap.

The low-energy model for the 3D TIs was presented in section 1.3.2. The basis of the four-band model is given by the bonding and anti-bonding p_z orbitals ordered as $|P_1^+\uparrow\rangle$, $|P_2^-\downarrow\rangle$, $|P_1^+\downarrow\rangle$, $|P_2^-\uparrow\rangle$, where the superscripts $\pm$ stand for even and odd parity, and $\uparrow,\downarrow$ represent spin-up and spin-down states. In this basis, and considering a non-periodic system in the z spatial direction, the Hamiltonian (1.39a) reads as [155]

$$\mathcal{H}_{3\mathrm{D}}(z,k_\parallel) = \begin{bmatrix} h_+(z,k_\parallel) & -iB\partial_z\sigma_y \\ -iB\partial_z\sigma_y & h_-(z,k_\parallel) \end{bmatrix} , \tag{3.7a}$$

where $h_\pm(z,k_\parallel)$ describes two blocks of size 2×2 with opposite chirality, hybridised by the terms proportional to B, which are linear in the spatial derivative in the z-direction. $h_\pm(z,k_\parallel)$ is given by the following expression

$$h_\pm(z,k_\parallel) = \epsilon(k_\parallel,z)\mathbb{1}_2 + M(z,k_\parallel)\tau_3 + Ak_x\tau_1 \pm Ak_y\tau_2 , \tag{3.7b}$$

with $\mathbb{1}_n$ the $n\times n$ unit matrix and $k_\parallel = \sqrt{k_x^2+k_y^2}$ the absolute value of the inplane momentum. In equations (3.7a) and (3.7b), σ_i and τ_i denote the Pauli matrices acting on the spin basis and the orbital basis. The on-site term and the mass term are

$$\epsilon(z,k_\parallel) = C_0 - C_1\partial_z^2 + C_2k_\parallel^2 , \tag{3.7c}$$

$$M(z,k_\parallel) = M_0 + M_1\partial_z^2 - M_2k_\parallel^2 . \tag{3.7d}$$

The topology of the Hamiltonian is given by the sign of the mass parameters: if $M_0 M_1 > 0$ and $M_0 M_2 > 0$, the system is in the inverted regime. The diagonal term $\epsilon(z, k_\parallel)$ accounts for the particle-hole asymmetry and has no impact on the topology of the bands.

In figure 3.2, the bulk bands dispersion is plotted together with the spin texture for the parameters of Bi_2Se_3 listed in table 1.2. As shown in the figure, the system is gapped and the spin of the bands is inverted due to the non-trivial topology for such parameters.

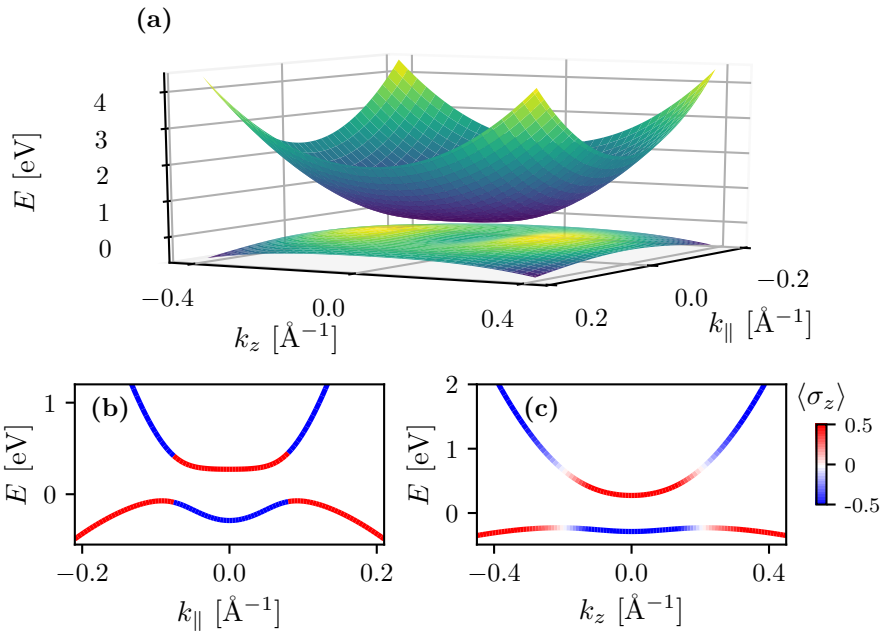

Figure 3.2: Dispersion relation of the bulk bands of the Hamiltonian (3.7a) for Bi_2Se_3 using the parameters given in reference [154]. Due to the rotational symmetry in the x-y plane the spectrum depends only on $k_\parallel$ and k_z. Panel (a) shows the spectrum as a function of the inplane momentum $k_\parallel$ and k_z. Panel (b) and (c) show, respectively, the spectrum for $k_z = 0$ and $k_\parallel = 0$ with the colormap indicating the expectation value $\langle\sigma_z\rangle$ over the states.

Due to the non-trivial topology of the bulk bands, in a 2D thin film, Dirac-like surface states appear on the top and bottom surfaces. As a first approach, the discussion is focused on the effective low-energy Hamiltonian for these states. Considering a minimal basis formed by the surface states give by $|t\uparrow\rangle$, $|t\downarrow\rangle$, $|b\uparrow\rangle$, $|b\downarrow\rangle$, where t (b) represents the surface state sitting on the top (bottom) surface and $\uparrow$ and $\downarrow$ stand for

the spin, a Dirac-type Hamiltonian is obtained

$$\mathcal{H}_{\mathrm{sf}}(k_x,k_y)=\begin{pmatrix} 0 & iv_{\mathrm{F}}k_- & m(k_x,k_y) & 0 \\ -iv_{\mathrm{F}}k_+ & 0 & 0 & m(k_x,k_y) \\ m(k_x,k_y) & 0 & 0 & -iv_{\mathrm{F}}k_- \\ 0 & m(k_x,k_y) & iv_{\mathrm{F}}k_+ & 0 \end{pmatrix} , \quad (3.8)$$

where v_{F} is the Fermi velocity and $m(k_x,k_y)=m_0-m_1(k_x^2+k_y^2)$ takes into account the tunneling effect between the top and bottom surface. The constants v_{F}, m_0 and m_1 are determined by the projection of the Hamiltonian (3.7a) over the surface states basis, and they depend on the width of the slab.

In the presence of magnetically doped impurities, the effect of the magnetization has to be included as a perturbation to the Hamiltonian (3.8) by an exchange field in the z-direction. As a first approximation, the system can be considered invariant under spatial inversion in z, so that both surfaces are equivalent and all parameters defined on the upper surface are equal to the lower one. The minimal model for the exchange field is then given by a spin-dependent Zeeman interaction that reads as

$$\mathcal{H}_{\mathrm{Z}}=\begin{pmatrix} g & 0 & 0 & 0 \\ 0 & -g & 0 & 0 \\ 0 & 0 & g & 0 \\ 0 & 0 & 0 & -g \end{pmatrix} , \quad (3.9)$$

with the alternating sign given by the ordering of the spin in the basis considered. The effective Hamiltonian for the surface states with the magnetic doping is then described by

$$\mathcal{H}_{\mathrm{tot}}=\mathcal{H}_{\mathrm{surf}}+\mathcal{H}_{\mathrm{Z}} , \quad (3.10)$$

where $\mathcal{H}_{\mathrm{surf}}$ is given by equation (3.8) and $\mathcal{H}_{\mathrm{Z}}$ by the perturbation in (3.9).

In order to apply the same reasoning of the BHZ model described in the previous section, it is particularly convenient to cast this model in a BHZ-like form by defining the symmetric and antisymmetric combination of the surface states [308]:

$$|\pm\uparrow\rangle=\frac{|t\uparrow\rangle\pm|b\uparrow\rangle}{\sqrt{2}} ,$$
$$|\pm\downarrow\rangle=\frac{|t\downarrow\rangle\pm|b\downarrow\rangle}{\sqrt{2}} .$$

By ordering the basis as $|+\uparrow\rangle$, $|-\downarrow\rangle$, $|+\downarrow\rangle$, $|-\uparrow\rangle$ and by including the Zeeman term, the resulting Hamiltonian $\mathcal{H}_{\text{eff}}$ is

$$\mathcal{H}_{\text{eff}}(k_x, k_y) = \begin{pmatrix} h(k_x, k_y) + g\sigma_z & 0 \\ 0 & h^*(-k_x, -k_y) - g\sigma_z \end{pmatrix} , \tag{3.11}$$

where

$$h(k) = m(k_x, k_y)\sigma_z + v_{\text{F}}(k_y\sigma_x - k_x\sigma_y) . \tag{3.12}$$

In this BHZ-like form, the procedure of the previous section can be applied similarly. However, unlike the 2D TIs, now the exchange field is described by a σ_z term. Hence, no matter whether the two subbands with opposite parity are inverted or not, a strong enough exchange field g induces the QAH state:

- If the subbands are inverted from the beginning, the gap term of the upper block grows with the exchange field, and *viceversa* for the lower block, until the upper block becomes trivial.
- On the other hand, starting from trivial subbands, the lower block decreases its gap until both bands invert and become non trivial.

Figure 3.3 illustrates the process in a more pictorial approach. In conclusion, in 3D TIs, a strong Zeeman coupling makes the surface states transition to a QAH state regardless of whether the initial state was topological or not.

3.1.3 Magnetically doped 3D TI

So far, the only states considered were the surface states in a slab configuration. However, a complete derivation of the subbands considering also the contribution of bulk bands can be obtained from the 3D Hamiltonian (3.7a) as demonstrated by Wang *et al.* [281].

Up to a first order, the magnetic doping is described in equation (3.7a) by replacing M_0 by a modified mass term M_0^{Cr} which varies as a function of the doping, and by adding a Zeeman splitting [308]

$$\mathcal{H}_{\text{Z}} = \begin{pmatrix} g\sigma_z & 0 \\ 0 & -g\sigma_z \end{pmatrix} , \tag{3.13}$$

where $g > 0$ is the strength of the exchange field. The Hamiltonian for the magnetically doped slab is then given by

$$\mathcal{H}_{\text{tot}} = \mathcal{H}_{\text{3D}} + \mathcal{H}_{\text{Z}} , \tag{3.14}$$

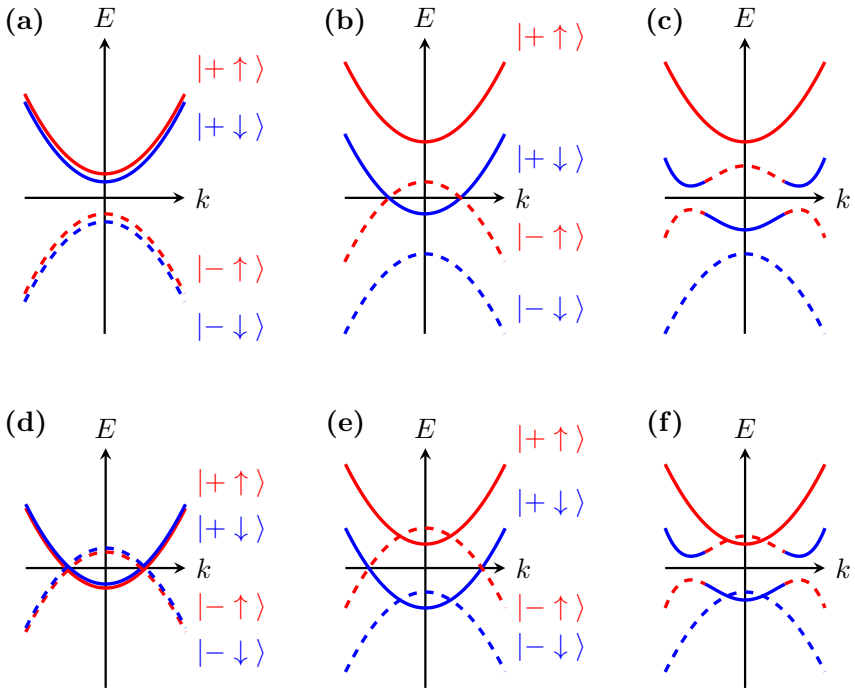

Figure 3.3: Schematic representation of the subband evolution by increasing the exchange field. In (a) the initial subbands are not inverted. By increasing the exchange field in (b) the $|+\downarrow\rangle$ and $|-\uparrow\rangle$ coalesce and become non-trivial. If a spin-orbit coupling term is included in (c), the degeneracy points gap. In the lower panels the evolution of initially inverted subbands is plotted (d) by adding the exchange field (e) and by including exchange field and spin-orbit coupling (f). Figure adapted from reference [308].

where $\mathcal{H}_{3D}$ is defined in equation (3.7a) and $\mathcal{H}_Z$ is given by (3.13).

The former Zeeman term is obtained by setting an equal splitting in both orbitals with sign depending on the spin. It resembles the form of the Zeeman splitting for the effective model for the surface states in equation (3.9). By increasing the doping, M_0^{Cr} grows as well as the Zeeman splitting g [314].

The Chern number of the slabs can be determined either by numerical calculations or by methods based on obtaining the effective mass term for the subbands. This second method has been proposed in reference [281] in Cr-doped slabs by the decoupling of the two chiral sectors and by Fourier transforming the Hamiltonian. More precisely, the procedure is to set the coupling term $B = 0$ and write the Hamiltonian in the basis of the

quantum well states

$$\varphi_n(z) = \sqrt{\frac{2}{L_z}} \sin\left(\frac{n\pi z}{L_z} + \frac{n\pi z}{2}\right) , \tag{3.15}$$

where L_z is the width of the slab and n an integer. In this way, N effective subbands with quantised $k_z = n\pi/L_z$ are obtained and the effective mass of the n-th subband is given by

$$m_{\pm}(n) = M_0 - M_1(n\pi/L_z)^2 - M_2(k_x^2 + k_y^2) \mp g \ . \tag{3.16}$$

The Chern number of the n-th subband is

$$C^{(n)} = \begin{cases} +1 & \text{if } m_+(n) < 0 \ , \\ -1 & \text{if } m_-(n) < 0 \ , \\ 0 & \text{otherwise} \ . \end{cases} \tag{3.17}$$

The Chern number of the slab is computed by summing up all the contributions of the bands up to the Fermi level by

$$C = \sum_{\text{occupied}} C^{(n)}. \tag{3.18}$$

Considering equation (3.17), the Chern number is given by the following expression

$$C = N_+ - N_- \ , \tag{3.19}$$

where $N_\pm$ is the number of bands with $m_\pm(n) < 0$ below the Fermi energy.

The expression (3.19) gives conveniently the Chern number of the heterostructure by counting the number of inverted subbands. However, this approximation is valid only for $B = 0$. When including the coupling, the phase diagram calculated without the coupling must be adiabatically modified to obtain the new Chern map, see reference [285] for more details on this procedure.

The Chern number of the finite slab in the z-direction corresponds to the number of topological surface states that appear when cutting the system in the $x - y$ plane. For example, in a slab of width L_z, height L_y and PBC in the x-direction, C surface state appear inside the gap and below the Fermi energy, with C being the Chern number calculated by equation (3.19) for a system with finite L_z and PBC in x and y.

In figure 3.4 the case of a slab of width $L_z = 30\,\text{Å}$ and $L_y = 200\,\text{Å}$ is addressed. In this case, $C = 1$ for a $E_F = 0$. The dispersion relation is plotted in panel (e) showing two linear bands corresponding to the surface states near the Fermi energy. The probability density of the states is represented in panels (a)-(d). The surface states are plotted in panels (b) and (c) while the bulk conductance and valence band are depicted in (a) and (d), respectively.

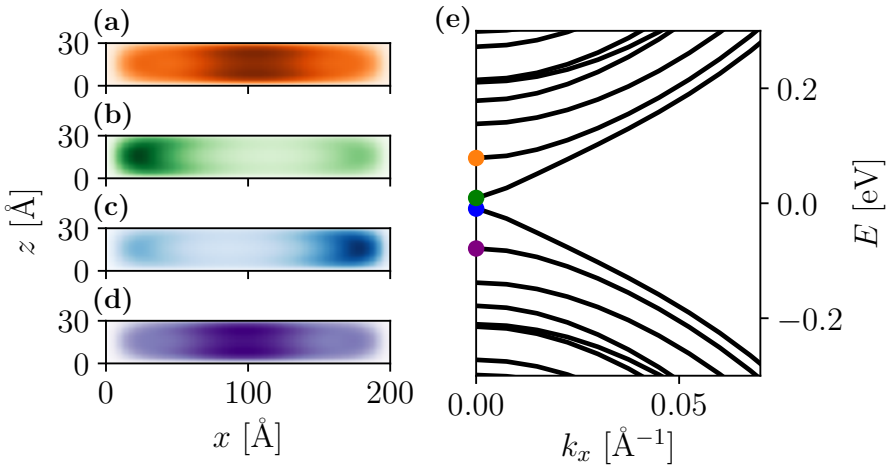

Figure 3.4: Spectrum and states for a slab with $L_z = 30$ Å and $L_y = 200$ Å. The parameters used correspond to Bi_2Se_3 in table 1.2 with $g = 0.1$ eV, $M_0^{\mathrm{Cr}} = -0.1$ eV and onsite energy $\epsilon(z, k_\parallel) = 0$, i.e. $C_0 = C_1 = C_2 = 0$. Panels (a)-(d) show $|\psi|^2$ at $k_x = 0$ corresponding to the eigenstates of the nearest band to the Fermi energy for the valence (a) and conductance (d) bulk bands and the topological surface states inside the gap (b) and (c). The right panel (e) shows the dispersion relation as a function of the momentum k_x. The colored dots in (e) indicate the energy of the states plotted in (a)-(d).

3.2 Manipulating the QAH state with external fields

Once the QAH state is achieved, it would certainly be desirable to tune the topological properties of the samples by means of an external field. As already discussed in chapter 2, external electromagnetic fields can be used to manipulate the topological properties of materials. In the case of magnetic TIs, the electric field was proposed in the first place to reduce the exchange coupling strength [65, 282]. In this way, a topological phase transition was achieved in samples close to the critical point where the electric field induces the paramagnetic trivial state [310].

In recent experiments, the width and the doping of a heterostructure consisting of alternating magnetically doped and undoped TI layers were proposed [285] and experimentally realised as a new platform for controlling the number of Chern states in the sample [319]. In this section, based on the published work [13], a tuning method for controlling those states with an external electric field is investigated in doped Bi_2Se_3 starting from a single slab in section 3.2.1 and discussing the case of the heterostructures in section 3.2.2.

3.2.1 Effect of the electric field in a Cr-doped slab

In this section, the effect of the electric field on a doped 3D TI slab is briefly introduced through the case of a magnetically doped slab of $L_z = 30$ Å. Without external fields, the system is described by the Hamiltonian (3.14). The electric field in the direction of growth is introduced by adding a linear potential

$$\mathcal{H}_{\mathrm{f}} = efz\mathbb{1}_4 \ , \tag{3.20}$$

where e is the elementary electric charge and f is the external electric field. The Hamiltonian of the system is then given by

$$\mathcal{H}_{\mathrm{tot}} = \mathcal{H}_{\mathrm{3D}} + \mathcal{H}_Z + \mathcal{H}_{\mathrm{f}} \ , \tag{3.21}$$

where $\mathcal{H}_{\mathrm{3D}}$ is given by equation (3.7a), $\mathcal{H}_Z$ from equation (3.13) gives the Zeeman splitting and $\mathcal{H}_{\mathrm{f}}$ was defined in equation (3.20) above. As already discussed in section 3.1.3, up to a first approximation, the magnetic doping changes the gap M_0^{Cr} and the Zeeman term g, hence these two parameters are employed for the phase maps represented in figure 3.5.

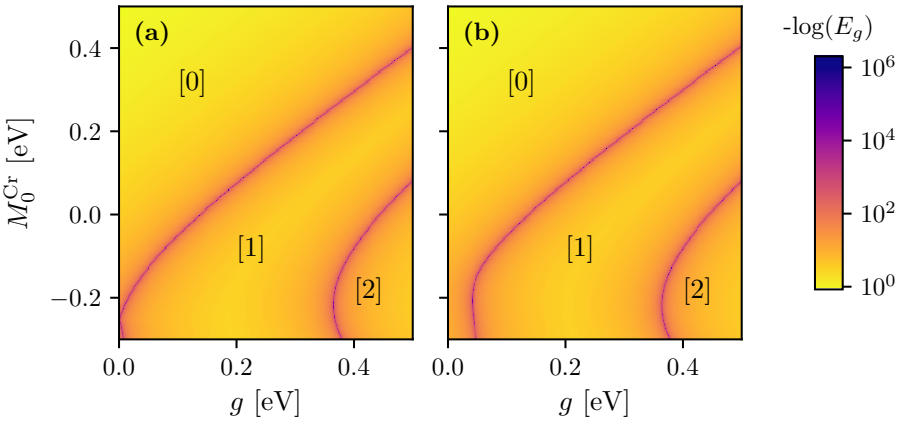

Figure 3.5: Phase diagram for a slab of width 30 Å as a function of the mass parameter M_0^{Cr} and the Zeeman splitting g. Panel (a) corresponds to the phase map in the absence of electric field while in panel (b) $f = 5\,\mathrm{meV/Å}$.

In figure 3.5 (a) the phase diagram for a slab of width 30 Å is presented as a function of the mass parameter M_0^{Cr} and the Zeeman splitting g. The phase diagrams are plotted as a function of both g and M_0^{Cr} as independent parameters. However, the doping concentration modifies both quantities [308, 314] in a correlated way. The complete phase diagram is

not accessible experimentally as long as multiple samples must be grown to change the doping concentration. Due to this issue, an external field that changes dynamically the properties of a given device is a remarkable alternative to tune the Chern number.

The electric field in the growth direction does not break the translation symmetry of the system in x and y-directions and the Chern number can still be computed. Nevertheless, when the term in equation (3.20) is introduced, the quantum well basis (3.15) is not a good approximation for the states in z and numerical methods are required. In the results presented, the `Z2Pack` [100, 254] is employed, based on hybrid Wannier functions, to compute the Chern number numerically in the gapped regions for a half-filled spectrum, i.e. setting $E_F = 0$ in our model.

In figure 3.5 (b) the phase map of a slab is plotted for an electric field of 5 meV/Å. Compared to panel (a), the trivial insulator region is enlarged by the coalescence of the lower topological bands due to the Stark effect. However, due to the strong confinement in the z-direction, the electric field slightly shifts the Chern number regions in the phase diagram without substantial changes. Larger electric fields, together with wider samples, are required to obtain more pronounced modifications of the topology. In fact, in the slab configuration, the finite width effects are essential in the system, since the gap is related to the width of the sample [72, 77].

3.2.2 Heterostructure of magnetically doped TI

Minimal model for magnetic doping in the heterostructure

As already introduced in the previous sections, the heterostructure of stacked layers of magnetically doped and undoped TIs was recently proved as an attractive platform to achieve high Chern number QAH states [319]. Experimentally, Chern states up to $C = 5$ have been measured in these devices, see figure 3.6. The number of topological states is controlled by the doping [see panel (a)] and the thickness of the layers [see panel (b)], as well as by the amount of layers in the heterostructure.

From the perspective of the models, the heterostructures are described, up to a first approximation, by the Hamiltonian (3.7a) with a spatial dependent mass term $M_0(z)$ and a non-zero Zeeman splitting only in the doped layers [285]:

$$M_0(z) = \begin{cases} M_0 & (z \in \text{undoped layer}) \,, \\ M_0^{\text{Cr}} & (z \in \text{Cr-doped layer}) \,. \end{cases} \tag{3.22}$$

The Zeeman splitting is given by equation (3.13) with the constant g

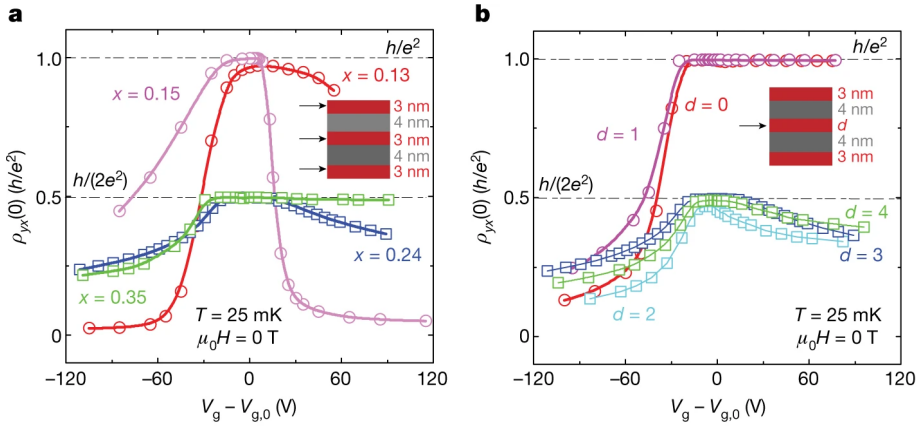

Figure 3.6: Experimental results from reference [319]. Dependence of the transversal resistivity ρ_{xy} on the gate voltage for the sample schematised in the inset. Panel (a) shows different curves by varying Cr-doping concentration x. The $C = 2$ is achieved for $x \geq 0.2$ while $C = 1$ for lower doping concentrations. In panel (b) the width d of the central magnetically doped layer is changed. A Chern state $C = 2$ appears only for $d \geq 2\,\text{nm}$.

replaced by the step-like function

$$g(z) = \begin{cases} 0 & (z \in \text{undoped layer}) \,, \\ g & (z \in \text{Cr-doped layer}) \,. \end{cases} \tag{3.23}$$

For concreteness, we focus on the heterostructure reported in reference [319] and shown schematically in figure 3.7. The layered structure under consideration consists of three films of three quintuple layers of $(\text{Bi},\text{Sb})_{2-x}\text{Cr}_x\text{Te}_3$ with two films of four quintuple layers of $(\text{Bi},\text{Sb})_2\text{Te}_3$ in between. The Cr-doped layers are 30 Å width and the pristine TI layers are 40 Å width.

The configuration is highly symmetric and enables to get high Chern numbers states up to 4 without the electric field. Figure 3.8(a) shows the phase diagram as a function of M_0^{Cr} and g. The Chern number is computed numerically employing `Z2pack` for a system with stacking configuration in z reported in figure 3.7 and PBC in x and y-directions. The phase diagram in panel (a) comprises wide regions where $C = 1$, 2 and 4 and a small region of $C = 3$. The region of $C = 4$ is inconsistent with the results presented in reference [319], as already pointed out by Wang *et al.* [285]. However, a small region with $C = 3$ is obtained between those with $C = 2$ and $C = 4$, in contrast to reference [285]. The inversion symmetry in the z-direction assures that the states come in pairs, except

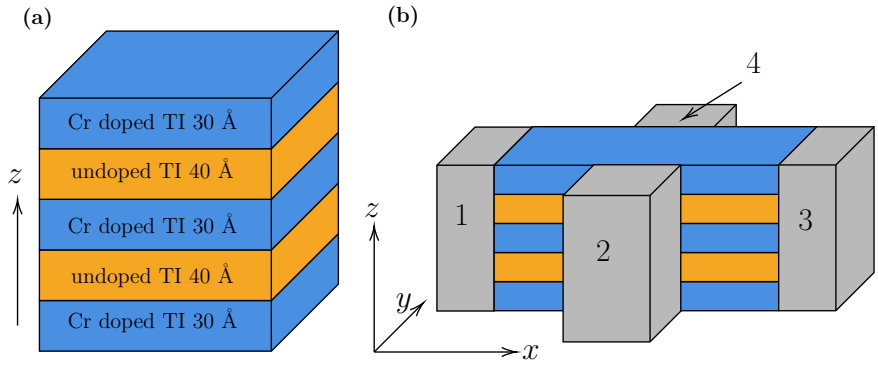

Figure 3.7: (a) Schematic representation along the stacking direction z of alternated Cr-doped (30 Å) and undoped films (40 Å) of the TI heterostructure. (b) Sketch of the Hall bar for the conductance calculations. The size is $L_x = 300$ Å and $L_y = 180$ Å. In the stacking direction z, the sample resembles the same geometry shown in figure 3.7.

for the fully interlayer-connected $C = 1$ state. Due to finite-size effect and the subsequent discretization of levels, the $C = 3$ region pops out in tight-binding models in a small area. In the results shown, the parameters correspond to the binary compound Bi_2Se_3 from reference [155], collected in table 1.2. The diagonal term $\epsilon(z, k_{\|})$ has no impact on the topological nature of the bands, and it has been set to zero without loss of generality. As already proved in reference [319] by computing the phase maps for Sb_2Te_3, no qualitative modifications are expected for the Sb binary compound or the ternary compound that resembles the experimental reference. Hence, for concreteness the results presented in the following are computed for the parameters of Bi_2Se_3, collected in table 1.2.

Effect of the electric field in the direction of stacking

The electric field (3.20) breaks the translation symmetry along the z-direction, but it does not break the particle-hole symmetry, since it contributes equally in all the orbitals. Therefore, the spectrum is particle-hole symmetric, and the degenerate branches diverge when they acquire a non-zero expectation value $\langle z \rangle$. The electric field acts as a confining potential on the states due to the Stark effect and tends to close the gap by the coalescence of particle and hole bands with opposite spatial distribution.

A simple picture of the band modification due to the electric field can be obtained from perturbation theory. By considering the term $\mathcal{H}_{\mathrm{f}}$ of equa-

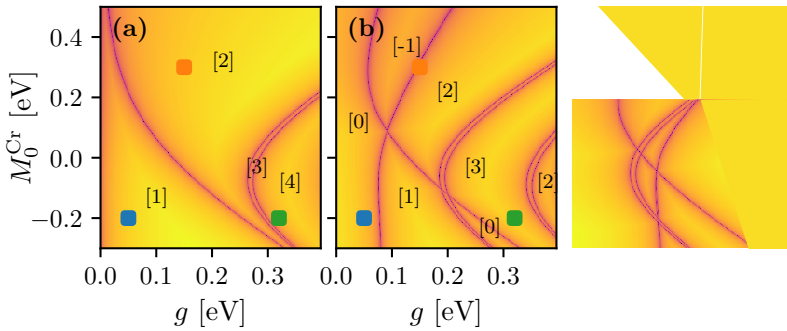

Figure 3.8: Phase diagram of the energy gap, in logarithmic scale, and the Chern numbers of the system indicated between the regions of gap closing and inside brackets. Panels (a), (b) and (c) correspond to electric fields of 0 meV/Å, 1 meV/Å and 2 meV/Å, respectively. The blue, orange and green squares correspond to the calculated points in figure 3.14. The system is finite in the z-direction following the stacking represented in figure 3.7. PBC are imposed in the x and y-directions.

tion (3.20) as a perturbation of the Hamiltonian given by equation (3.7a), the first order correction in the energy is

$$\delta E^{(1)} = \langle \psi^0_{n,\mathbf{k}} | \mathcal{H}_\mathrm{f} | \psi^0_{n,\mathbf{k}} \rangle \ , \tag{3.24}$$

where $\psi^0_{n,\mathbf{k}}$ is the unperturbed state of the n-th Bloch band. Considering the linear potential in equation (3.20), the first order correction is an energy shift proportional to the expectation value of z

$$\delta E^{(1)} = ef \langle \psi^0_{n,\mathbf{k}} | z | \psi^0_{n,\mathbf{k}} \rangle \ . \tag{3.25}$$

Therefore, the states with $\langle z \rangle$ positive (negative) increase (decrease) their energy. Inside the gap, this implies the coalescence of hole and electron bands with opposite sign of $\langle z \rangle$. The energy shift affects mostly the states peaked in the interfaces between layers due to their localisation. On the other hand, the bulk states remain almost unchanged.

The physical mechanism inducing the topology in the bands of the heterostructure is the same as the one discussed in the previous sections: an induced band inversion process. However, in the heterostructure the situation is more complex due to the multiple subbands arising from the different layers. The identification of the inverted subbands becomes more challenging. Figure 3.9 shows a typical dispersion for a heterostructure with $C = 4$ without external fields. The inversion symmetry in z induces doubly degenerated states with $\langle z \rangle = 0$. The spin texture of the bands is non-trivial, and the inverted bands can be hinted near the Fermi

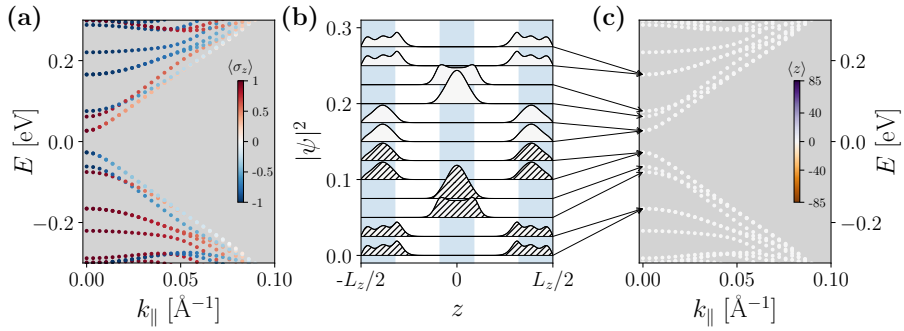

Figure 3.9: Energy dispersion and states for a $C = 4$ state for $f = 0$. The system is finite only in the z-direction [see figure 3.7] and PBC are implemented in the x and y-directions. The parameters are $M_0^{\mathrm{Cr}} = -0.2\,\mathrm{eV}$ and $g = 0.32\,\mathrm{eV}$. The energy dispersions show the projection of σ_z and $\langle z\rangle$ in (a) and (c) panels, respectively. Due to the symmetry of the structure, the expectation value of z is zero for all the states. In panel (b), the probability density $|\psi|^2$ is plotted for the indicated states at $k_\parallel = 0$. The states below the Fermi energy are hatched.

energy. Even if counterintuitive, the spatial localisation of the wave functions along the z-direction is not a definite signature of the bands topology [285].

In figure 3.10 the states of the system in figure 3.9 are plotted in the presence of an electric field of 1 meV/Å. By comparing it with the case of $f = 0$ reported in figure 3.9, the external field breaks the inversion symmetry and localizes the states on one of the sides of the slab, lifting the degeneracy between levels with $\langle z\rangle \neq 0$. Therefore, after the addition of an electric field, even if the Chern number is still given by the crossing between levels, the localisation plays an indirect role giving the direction and strength of the displacement of the bands.

As argued in section 3.1.3, the total Chern number of the heterostructure can be obtained via the sum in equation (3.19) where the topology of the bands is encoded in the effective mass $m_\pm(n)$ in expression (3.16). From the perspective of the subbands, adding the electric field has a double effect:

- The subbands are rigidly displaced in energy. Up to a first approximation, the displacement is given by expression (3.25), that relates to the spatial localisation of the states.

- The subbands states are modified such that the replacement $k_z \to n\pi/L_z$ in equation (3.16) and the quantum well states (3.15) are

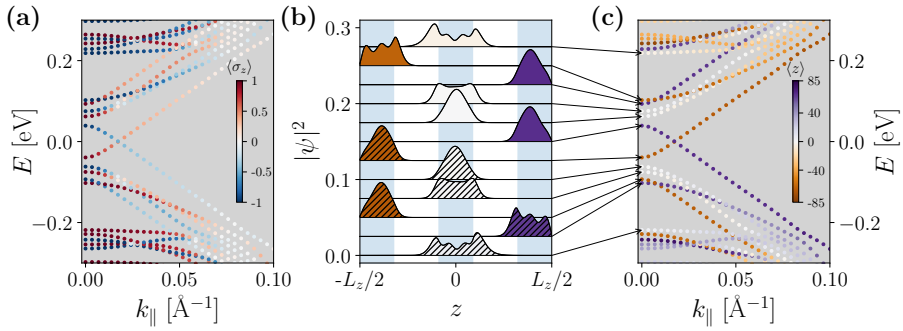

Figure 3.10: Energy dispersion and states for a $C = 3$ state at $f = 1\,\text{meV/Å}$ in a one-dimensional chain in the z-direction [see figure 3.7]. The parameters are $M_0^{\text{Cr}} = -0.2\,\text{eV}$ and $g = 0.32\,\text{eV}$. The energy dispersions show the projection of σ_z and $\langle z\rangle$ in (a) and (c) panels, respectively. Panel (b) shows the probability density $|\psi|^2$ for the indicated states at $k_\parallel = 0$. The states below the Fermi energy are hatched. The parameters correspond to a $C = 4$ state in the absence of electric field (see figure 3.9 for comparison with the case at $f = 0$).

no longer a correct approximation. This implies that the effective mass of each one of the subbands is modified by the external field.

The first point was already checked in figures 3.9 and 3.10 and discussed in the former paragraphs finding that indeed the external field shifts the bands by the usual Stark effect. To check the second aspect, in figure 3.11, the expectation value of k_z^2 is plotted for the $2N$ bands below the Fermi level in a multilayered system of N sites with parameters corresponding to a $C = 4$ state without the electric field. The $\langle k_z^2\rangle$ decreases by approaching the gap, but it is not modified by the external electric field. The expectation value of the momentum is computed by projecting the states in the basis defined in equation (3.15). The lower panel shows, for each band, the difference between the expectation values in the presence of the electric field and in the pristine case, proving that the modification of $\langle k_z^2\rangle$ is almost negligible.

This results are consistent with the calculations in the single slab reported in section 3.2.1. In fact, only strong electric fields are capable of modifying the localisation, and consequently the Chern number, of the thin slab. In conclusion, the change of the effective mass in equation (3.16) by the varying of momentum does not play a significant role in the modification of the Chern number by the external field.

The previous calculations were performed in heterostructures with finite L_z and PBC in the x and y-directions. By the bulk-boundary cor-

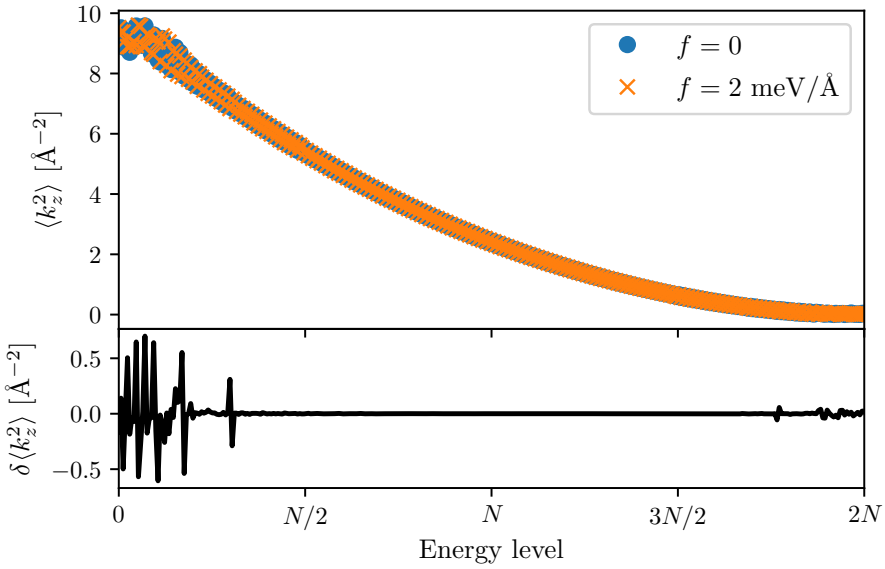

Figure 3.11: Expectation value of k_z^2 for a multilayered system with parameters $M_0^{\mathrm{Cr}} = -0.2\,\mathrm{eV}$ and $g = 0.32\,\mathrm{eV}$. The system is finite in the z-direction following the stacking represented in figure 3.7. PBC are implemented in the x and y-directions.

respondence theorem, the Chern number gives to the number of surface states appearing when a finite system is studied. Hence, in a slab with finite L_y and z-stacking represented in figure 3.7, the topological states appear inside the gap, and they are identified by their localisation in the y-direction, being linearly dispersive as a function of k_x.

In order to quantify the localisation of the states the participation ratio (PR) is defined in the basis of the spatial coordinates as follows

$$\mathrm{PR} = \frac{\left(\sum_{i=1}^{N} p_i\right)^2}{\sum_{i=1}^{N} p_i^2} \,, \tag{3.26}$$

where N is the number of sites in the system and p_i is the probability density at site i, i.e. $|\psi_i|^2$. With this definition, the maximum values of PR is N for a completely delocalised state and 1 for a state localised in only one site. Although the spatial localisation is not a sufficient condition for establishing the topological properties of electron states, the topological states are by their own nature localised at the edges of the sample. Therefore, the PR value is an indicative quantity to track the evolution of the states with the electric field. In finite-size slabs the states evolve continuously with the electric field and they lose the topological localisation in a

continuous way, in contrast with the calculated abrupt transitions in the semi-infinite Chern number results represented in figure 3.8.

Figures 3.12 and 3.13 show the spectrum as a function of the electric field for two representative cases in a finite slab in the y and z-directions. In figure 3.12, a $C = 1$ state turns trivial due to the hybridisation of the bands at $f \sim 0.7\,\mathrm{eV/Å}$, while in figure 3.13, a $C = 2$ state turns into $C = -1$. In the former case, the topological transition is driven by both the hybridisation of the topological bands and by the crossing of a new level coming from the upper part of the energy spectrum.

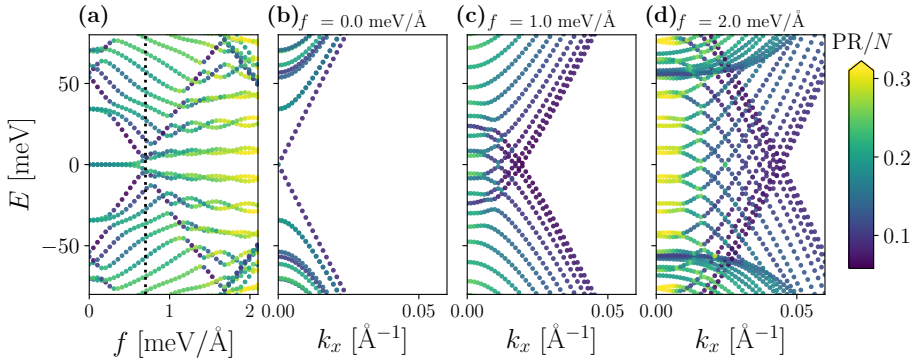

Figure 3.12: Energy levels at zero momentum as a function of the electric field (a) and energy dispersion for $f = 0, 1, 2$ meV/Å, in panels (b), (c) and (d) in a 2D slab with $L_y = 400\,\text{Å}$ and z stacking corresponding to figure 3.7. The parameters are $M_0^{\mathrm{Cr}} = -0.2\,\mathrm{eV}$ and $g = 0.05\,\mathrm{eV}$, corresponding to a $C = 1$ in the absence of electric field. The system becomes trivial at $f \sim 0.7\,\mathrm{eV/Å}$, indicated by a dashed vertical line in panel (a). The dispersions also show the PR/N as an indicator of the localisation of the state. The PR is calculated by equation (3.26).

Lastly, it is important to emphasise the role of the stacking configuration in generating topological transitions. Comparing the phase map 3.8 with the previous one for the slab shown in figure 3.5, it is clear that the electric field has a much larger effect in the case of the heterostructure. In fact, as discussed earlier, the modification of the phase diagram with the applied electric field is mostly induced by the crossing of the subbands rather than by the change of the effective Hamiltonian parameters due to the electric field. Thus, the multiband heterostructure is affected by multiple crossings, which are prevented in the ultrathin slab by the quantum confinement.

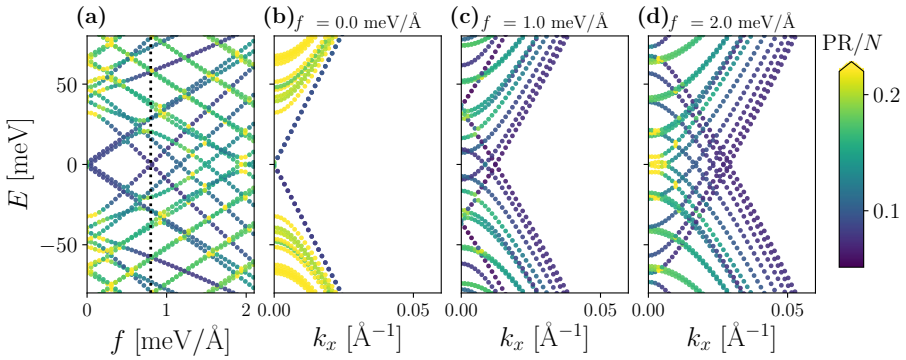

Figure 3.13: (a) Energy levels at zero momentum as a function of the electric field and energy dispersion for (b) $f = 0\,\text{meV/Å}$, (c) $f = 1\,\text{meV/Å}$ and (d) $f = 2\,\text{meV/Å}$ in a 2D slab with $L_y = 400\,\text{Å}$ and z stacking corresponding to figure 3.7. The PR projection is plotted in the scale indicated on the right side of the plots. The parameters are $M_0^{\text{Cr}} = 0.3\,\text{eV}$ and $g = 0.1\,\text{eV}$, corresponding to a $C = 2$ state that shifts to $C = -1$ at $f \sim 0.8\,\text{eV/Å}$. The value of $f = 0.8\,\text{eV/Å}$ is indicated in a dashed vertical line in panel (a).

Impact of the electric field on transport

This section addresses the problem of measuring topological phase transitions in a transport setup. An experimentally feasible scenario is a Hall bar with four terminals, where the presence of transverse conductance is a key signature of the topological states. Figure 3.7 (b) shows a schematic view of the device. The system consists of the multilayered sample connected to four leads with the same structure in the stacking direction. The electric field is applied only in the scattering region, excluding the leads, and an Anderson-like disorder is added to account for defects and other imperfections in the sample. The Anderson perturbation is introduced into the Hamiltonian by adding the following term

$$\mathcal{H}_{\text{A}} = w(x, y, z)\ \mathbb{1}_4\ , \tag{3.27}$$

where $w(x, y, z)$ is a function that at each site gives the onsite random energy, uniformly distributed in the range $[-W/2, W/2]$, with the disorder strength W. The Hamiltonian for the scattering region is then given by

$$\mathcal{H}_{\text{scat}} = \mathcal{H}_{\text{3D}} + \mathcal{H}_{\text{f}} + \mathcal{H}_{\text{A}}\ , \tag{3.28a}$$

while in the leads

$$\mathcal{H}_{\text{leads}} = \mathcal{H}_{\text{3D}}\ . \tag{3.28b}$$

In the former expressions $\mathcal{H}_{\text{3D}}$ is given by equation (3.7a) with $M_0(z)$ from (3.22), the Zeeman term has the form of (3.13) with $g(z)$ from (3.23),

the electric field potential is expressed in equation (3.20) and the Anderson disorder is defined in equation (3.27).

The transport calculations were performed using `Kwant` [102] within the Landauer-Büttiker formalism in a slab of $300 \times 180 \times 170\,\text{Å}$, see appendix B. The injection energy is set to the Fermi energy with a small positive shift to exceed the finite-size gap. The conductances reported are obtained from the transmission between transverse leads as discussed in appendix B. Due to the breaking of TR symmetry with the addition of the Zeeman splitting, the current of the anomalous Hall channels flows in a preferential direction. By numbering the leads as in figure 3.7 and denoting the conductance direction by the order of the subscript in equation (B.5b), G_{12} is the conductance in the direction of the topological states, while G_{21} is mediated by the contributions of trivial currents. Hence, the measure of G_{12} and G_{21} is related to the evolution of the topological and trivial states, respectively.

If the transverse conductance is given only by Chern numbers of filled bands, it fulfils the following relation [291]:

$$G_{12}^{\text{Chern}} = \frac{e^2}{h} \sum_n C^{(n)} \,, \tag{3.29}$$

where the sum runs over the Chern numbers $C(n)$ of the occupied bands, i.e. the states below the Fermi energy.

Figure 3.14 shows the conductance for three different sets of parameters as a function of the electric field. The average conductance is plotted together with the standard deviation of the disorder realisations for an Anderson disorder with strength $W = 4E_g$, where E_g is the energy of the first mode above the Chern states at $f = 0$, and it is a measure of the effective finite-size gap. The squared variance was previously defined in equation (2.47).

In figure 3.14, the values of the Hall conductance from the Chern states [see equation (3.29)] are indicated by crosses. Two regimes are obtained for G_{12}, depicted in a solid line in the figure, depending on the electric field:

- At small electric fields, before the first gap closing, the conductance G_{12} shows a perfect quantization even in the presence of disorder. This proves that, for this regime, the electrons are driven by the topological states. In fact, the disorder would had a significant impact on the trivial states.

- At the first gap closing, two situations are obtained depending on the Chern number after the gap closing. If $C \neq 0$ the conductance G_{12} starts to decrease smoothly and the disorder affects the

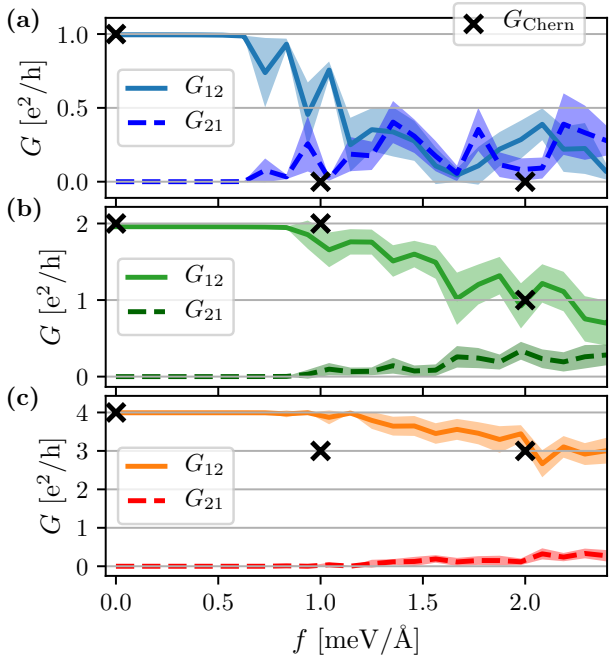

Figure 3.14: Conductance as a function of the electric field in a Hall bar with four terminals. Lines indicate the average transverse conductance while shadowed areas correspond to the squared variance for 100 disorder realisations from equation (2.47). Solid lines indicate the conductance G_{12} while dotted lines are the conductance in reversed direction G_{21}. Crosses are the transverse conductance given by the Chern number from equation (3.29). The parameters correspond to the coloured squares in the phase diagram plotted in figure 3.8: $g = 0.05\,\text{eV}$ and $M_0^{\text{Cr}} = -0.2\,\text{eV}$ (blue), $g = 0.15\,\text{eV}$ and $M_0^{\text{Cr}} = 0.3\,\text{eV}$ (green), $g = 0.32\,\text{eV}$ and $M_0^{\text{Cr}} = -0.2\,\text{eV}$ (orange).

transmission of the trivial states, yielding to a higher variance, see panels 3.14(b) and (c). However, the average conductance G_{12} still exceeds the values of the G_{12}^{Chern} and hence both topological and trivial states contribute. The trivial states come from the bulk states bands that appear at the Fermi energy when the electric field closes the gap.

- On the other hand, if $C = 0$ after the gap closing, the states become trivial and the conductance is dominated by the effect of the disorder, see panel 3.14(a).

The measure of the conductance in the opposite direction of the topological currents, G_{21}, gives a complementary criterion to establish the

robustness of the topological states with the electric field. G_{21} gives the order of magnitude of the current driven by the trivial channels and hence it can be compared with the magnitude of G_{12} to have an estimation of the contribution of the trivial states:

- In a topological state, even if the conductance G_{21} becomes non-zero with the electric field, its value is always reduced in comparison with the G_{12}. This is the case of panels (b) and (c) in figure 3.14.
- On the other hand, when a trivial phase is induced by the field $G_{21} \approx G_{12}$. This is the case of panel (a) in figure 3.14.

Finally, it is important to stress that in the Hall bar, due to finite-size effects, a soft transition between topological states is obtained. In this is way, in figure 3.14, the conductance G_{12} decreases smoothly between two different Chern numbers as a function of f, in contrast to the sharp step of the G^{Chern}. This effect is specially apparent in panels (b) and (c).

3.3 Conclusions

In this chapter, the effect of the external electric field on the topology of the QAH states in magnetically doped TIs is discussed. In particular, two configurations have been considered: thin slabs of TIs and heterostructures of topologically doped and undoped TIs. The Chern number was the main quantity computed to study the modification of the topological properties with the external fields, together with the conductance in a Hall transport setup. The results prove that the tuning of the Chern number in ultra-thin slabs is prevented due to the quantum confinement. However, the case of the ultra-thin slab is a valuable example to understand the effect, being this configuration easier to interpret due to the concurrence of fewer subbands.

In the case of the heterostructure, the multiple subbands generated by the stacking of alternating Cr-doped and undoped layers enable the occurrence of several inverted bands and, employing this mechanism, multiple Chern states are achieved. In the presence of an electric field in the stacking direction, the bands coalesce and hybridise, generating new inverted bands and collapsing the previously inverted ones. In this way, the number of Chern states is tuned externally in the sample, without modifying the number and width of the layers or the doping level. However, due to the multiple band crossing possibilities, the topological transitions are difficult to predict, and the phase diagrams are complex and intricate. The level of complexity increases by finite-size effects in a slab, where

the finite width of the sample enhances the hybridisation of edge states located at the opposite surfaces.

In all this phenomenology, the general trend is to decrease the number of inverted bands due to the electric field by the approaching of the bands. This effect is detected by the variation of the transverse conductance as a function of the electric field at constant injection energy at the Fermi level. In the transport calculations, defects and other imperfections of the device are included by an Anderson-like disorder model, which allows a better visualisation of the topological features by reducing the contribution of the trivial bulk states. At the same time, the topological states are robust to disorder and generate a persistent channel for electric transport.

4 ELECTRONIC TRANSPORT IN GRAPHENE NANORIBBONS

Preamble

This chapter is dedicated to graphene-based systems. Since its discovery in 2004, graphene has completely revolutionised condensed matter theory and experiments as the first 2D material obtained in a monolayer. Graphene exhibits astonishing properties, especially those related to electronic transport, see reference [178] for a comprehensive review on the topic. The linear dispersion of the electrons near the Fermi energy is one of the most striking properties of graphene sheets, together with the high quality of the samples, which allows ballistic transport and easy observation of the quantum Hall since the first experimental measurements [186, 187, 317].

Since graphene was not covered in the introductory chapter 1, a comprehensive introduction to graphene systems is provided in section 4.1. The structure of the chapter is the following:

- The electronic properties of graphene are reviewed in section 4.1. This section is split into several subsections that address the general questions related to the degrees of freedom dealt with in sections 4.2 and 4.3.
  - In subsection 4.1.1, the main symmetries are discussed: valley and sublattice symmetries arising from the hexagonal lattice, as well as TR symmetry. The low-energy Hamiltonian is employed to gain more insight into the different symmetry operators. Various mass terms that break the aforementioned symmetries are also covered in this section.
  - Subsection 4.1.2 is devoted to the Kane-Mele model. This model corresponds to a Chern insulator in a hexagonal lattice. In this subsection, the bulk dispersion is discussed.
  - In subsection 4.1.3, graphene nanoribbons are studied. The modification of the dispersion relation due to confinement is discussed for the two prototypical edges, the armchair and the zigzag. Both trivial nanoribbons and topological Kane-Mele nanoribbons are addressed.

Once the main models and symmetries are introduced, more specific problems are treated in the following sections.

- Section 4.2 is focused on the e-e interaction in graphene nanoribbons. The interaction is treated at the level of mean-field by the Hubbard model via a self-consistent algorithm, which is explained in detail in the text. The effect on transport of monovacancies at the edge of the nanoribbon is studied within this formalism for trivial and Kane-Mele nanoribbons.

- Section 4.3 is dedicated to non-local resistance calculations in graphene nanoribbons with broken sublattice symmetry due to the hBN substrate. The aim of the study is to understand the experimental data from the Nanotechnology Group in Salamanca reported in figure 4.10.

- Finally, section 4.4 concludes the chapter by reviewing the main results.

4.1 Electronic properties of graphene

The main feature of the electronic bands of graphene sheets is the linearity of the bands near the Fermi level. The carbon atoms in graphene are in a honeycomb arrangement formed by two triangular sublattices, so that each unit cell contains two atoms, labelled A and B. In reciprocal space, the 1BZ is a hexagon whose corners are labelled as $\mathbf{K}$ and $\mathbf{K}'$. The linear dispersion relation in graphene was predicted in the late 1940s [280] and it is generated by the band crossing at $\mathbf{K}$ and $\mathbf{K}'$ points in the 1BZ. Figure 4.1 shows the lattice vectors, that read as

$$\mathbf{a}_1 = \frac{a_{CC}}{2}(3, \sqrt{3}) \ , \quad \mathbf{a}_2 = \frac{a_{CC}}{2}(3, -\sqrt{3}) \ , \tag{4.1}$$

where $a_{CC} \simeq 1.42\,\text{Å}$ is the distance between nearest carbon atoms such that B atoms are at $\boldsymbol{\delta} = (-a_{CC}, 0)$ away from the A atoms.

The hexagonal lattice in graphene is created by the hybrid sp^2 covalent bonds formed by three of the four outer electrons of the carbon atom, that form strong σ bonds. The fourth remaining outer electron corresponds to the perpendicular p_z orbital. Due to symmetry, p_z orbitals do not overlap with s, p_x and p_y orbitals and can then be approximated as independent π bonds. The carbon atoms are distinguished in two site types, named as A and B. Within the π band basis and one orbital in each atomic site, a two-band model describes the low energy dispersion of graphene for each

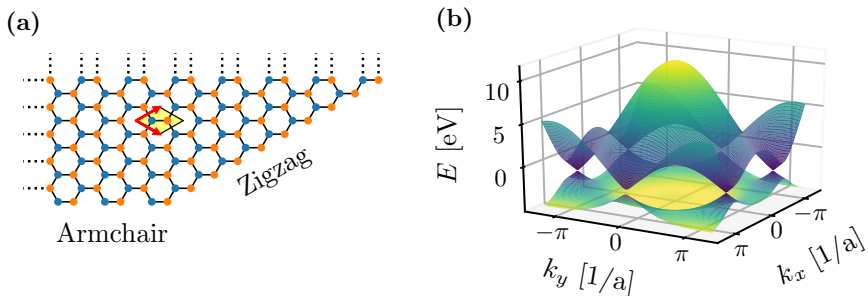

Figure 4.1: (a) Graphene honeycomb lattice with unit cell underlined in yellow and the lattice unit vectors plotted in red. The two main edges in graphene are indicated in figure. (b) Dispersion relation (4.3a) for $t_2 = 0.2t$ and $t_1 = 2.7\,\mathrm{eV}$.

spin. The tight-binding Hamiltonian takes into account that electrons can tunnel to the neighbouring atoms up to order l and it reads as

$$\mathcal{H} = \sum_i \epsilon_i c_i^\dagger c_i - \sum_l \sum_{\{\langle i,j\rangle\}_l} t_l c_i^\dagger c_j + \text{h.c.}\ , \tag{4.2}$$

where $c_i^\dagger$ (c_i) creates an electron on site i and orbital A or B, l indicates the sum over the neighbours orders with hopping parameter given by t_l and ϵ_i represents the onsite energy.

The dispersion relation of this model, by considering tunnel process up to second-nearest neighbours is [178, 266, 280]:

$$E(\mathbf{k}) = \pm t_1 \sqrt{3 + f(\mathbf{k})} - t_2 f(\mathbf{k})\ , \tag{4.3a}$$

$$f(\mathbf{k}) = 2\cos(k_y a) + 4\cos(k_y a/2)\cos\left(\sqrt{3}k_x a/2\right)\ , \tag{4.3b}$$

where the lattice constant is $a = \sqrt{3}a_{\mathrm{CC}}$ and the onsite energy ϵ is set to zero for simplicity. The bands are plotted in figure 4.1(b).

4.1.1 Valleys in graphene, time-reversal symmetry and sublattice symmetry

The bands given by equation (4.3a) are linear up to second order in the momentum near the gapless points of the spectrum $\mathbf{K}$ and $\mathbf{K}'$ such that the dispersion is

$$E_\pm(\mathbf{q}) = \pm\hbar v_{\mathrm{F}}|\mathbf{q}| + \mathcal{O}\left[(q/K)^2\right]\ , \tag{4.4}$$

where $\mathbf{q} = \mathbf{K}^{(\prime)} - \mathbf{k}$ is the vector relative to the degeneracy point and the Fermi velocity is $v_{\mathrm{F}} = 3t_1 a/(2\hbar)$. Even if the bands have the same

slope in both $\mathbf{K}$ and $\mathbf{K}'$ points, the low-energy Hamiltonian around each is different and relates to the other by a TR symmetry operation. In fact, in the basis of $\{\phi_K^A, \phi_K^B, \phi_{K'}^A, \phi_{K'}^B\}$, the linear expansion gives [127, 266]

$$\mathcal{H}(\mathbf{q}) = \begin{pmatrix} \epsilon_A(\mathbf{q}) & \hbar v_F q_- & 0 & 0 \\ \hbar v_F q_+ & \epsilon_B(\mathbf{q}) & 0 & 0 \\ 0 & 0 & \epsilon_A(\mathbf{q}) & -\hbar v_F q_- \\ 0 & 0 & -\hbar v_F q_+ & \epsilon_B(\mathbf{q}) \end{pmatrix} , \tag{4.5}$$

where $q_\pm = q_x \pm i q_y$ and $\epsilon_{A(B)}$ is the onsite energy at A (B). In the former Hamiltonian (4.5), the momentum $\mathbf{q}$ measures the deviation from $\mathbf{K}$ in the upper part, while in the lower sector $\mathbf{q}$ corresponds to the distance to $\mathbf{K}'$. The $\mathbf{K}$ and $\mathbf{K}'$ intended in this way, as two degrees of freedom of the low-energy Hamiltonian, are called *valleys*. The $\mathbf{K}$ valley is then described by

$$\mathcal{H}_{\mathbf{K}}(\mathbf{q}) = \epsilon_A \sigma_0 + (\epsilon_B - \epsilon_A)\sigma_z + \hbar v_F (q_x \sigma_x + q_y \sigma_y) , \tag{4.6}$$

conversely, near the $\mathbf{K}'$ the Hamiltonian is given by

$$\mathcal{H}_{\mathbf{K}'}(\mathbf{q}) = \epsilon_A \sigma_0 + (\epsilon_B - \epsilon_A)\sigma_z + \hbar v_F (-q_x \sigma_x + q_y \sigma_y) . \tag{4.7}$$

In the former expressions σ_i with $i = x, y$ are the Pauli matrices in orbital space. The spin is neglected in the models presented so far.

In the following sections important symmetries are discussed starting from the low energy continuum Hamiltonian of graphene (4.5). To distinguish the operations in the different degrees of freedom, the Pauli matrices in the valley representation are denoted by τ_i, in the sublattice by σ_i and for the spin by s_i, where $i = 0,\ x,\ y$ and z. The matrix representation of the Pauli matrices is distinguished by the hat $\hat{\sigma}_i$.

In a spinless system, the TR operator is given by complex conjugation in real space, see section A, which in the Bloch Hamiltonians corresponds to

$$\mathcal{H}(\mathbf{k}) = \mathcal{H}^*(-\mathbf{k}) . \tag{4.8}$$

For the Hamiltonian (4.5), the TR symmetry exchanges both valleys by changing the sign of the momenta. Due to the different definition of $\mathbf{q}$ in each of the sectors, the exchange of the valleys must be implemented explicitly. This leads to the following condition for the Bloch Hamiltonian (4.5):

$$\mathcal{H}(\mathbf{q}) = \tau_x \mathcal{H}^*(-\mathbf{q})\tau_x , \tag{4.9}$$

where τ_x is the Pauli matrix x in the valley basis, i.e. $\tau_x = \hat{\sigma}_x \otimes \hat{\sigma}_0$.

The gapless dispersion in equation (4.4) is obtained from equation (4.5) only if $\epsilon_B = \epsilon_A$. The onsite energy mismatch between sublattices, called

Semenoff mass [239], has the following form for the continuum Hamiltonian [122]:

$$V_s = m_s \sigma_z \ , \tag{4.10}$$

where σ_z is expressed in the basis of the sublattices and $m_s = \epsilon_B - \epsilon_A$. The Semenoff mass is TR invariant as $V_s = \tau_x V_s^* \tau_x$, if $m_s \in \mathcal{R}$. However, m_s breaks the inversion symmetry by distinguishing the two sublattices.

Inversion symmetry is implemented by reversing the direction of the momentum and the coordinates in real space. In the case of graphene, this implies changing A atoms by B atoms and reversing the spatial coordinates. In reciprocal space this leads to the exchange of the sublattice together with the change of the sign of the momentum:

$$\mathcal{P} : \ c_k \to \sigma_x c_{-k} \ , \tag{4.11}$$

For the Hamiltonian (4.5) consisting of the two valleys, the effect of the inversion symmetry also reverses the valleys by exchanging the momentum coordinate of the Dirac points, and not only the $\mathbf{q}$ relative to $\mathbf{K}$ and $\mathbf{K}'$. The condition over the Bloch Hamiltonian is then

$$\tau_x \sigma_x \mathcal{H}(\mathbf{q}) \sigma_x \tau_x = \mathcal{H}(-\mathbf{q}) \ . \tag{4.12}$$

where τ_x comes from the inversion of the two valleys and σ_x from the inversion of the subbands, the inversion of the relative momenta is given by the sign change to $-k$. The Semenoff mass (4.10) is forbidden by sublattice symmetry as $V_s = -\tau_x \sigma_x V_s \sigma_x \tau_x$.

In pristine graphene, atoms A and B are indistinguishable and therefore sublattice symmetry forbids the Semenoff mass term. In other hexagonal materials, such as hexagonal boron nitride (hBN), the broken symmetry generates a non-zero mass term due to the different atoms in each sublattice. Due to its structural similarity to graphene and its large band gap of $6 - 7\,\text{eV}$ [20, 217, 289], hBN is extensively used to encapsulate graphene to achieve flat samples with high mobility. The encapsulated graphene shows a breaking of the sublattice symmetry due to the interaction with hBN [63, 122, 173]. In section 4.3, the effect of the Semenoff mass and the valley as a new degree of freedom in graphene nanostructures is addressed by non-local resistance measurements in graphene Hall bars.

4.1.2 Lifting the degeneracy at the Dirac points: the Kane-Mele model

Even if sublattice symmetry forbids the Semenoff mass, this symmetry does not suffice to guarantee the stability of Dirac points in general. In

fact, a mass term that is inversion symmetric was proposed by Haldane in 1988 [105] leading to the first example of a topological Chern insulator. The Haldane mass has the form

$$V_H = m\tau_z\sigma_z \ , \tag{4.13}$$

and it breaks TR symmetry, allowing for a QAH effect in honeycomb lattices. Unfortunately, the Haldane model was only achieved in optical lattices [120] and not in graphene-based systems.

In 2005, graphene was again a starting point for the investigation of new topological properties through the Kane-Mele (KM) model, which was proposed as a platform for the QSH state [123, 124]. The mass term theorised in this case is generated by an intrinsic spin-orbit coupling, and it respects both inversion and TR symmetry. The general form of the KM mass is

$$V_{\mathrm{KM}} = \lambda_{\mathrm{SO}}\sigma_z\tau_z s_z \ , \tag{4.14}$$

where s_z is the spin Pauli matrix in z. Unfortunately, this term in graphene is of the order of 10^{-3} meV [171, 305] and hence almost negligible. The subsequent application of the same term to heavier atoms with stronger spin-orbit interactions like bismuth bilayer [175] and HgTe/CdTe heterostructures [19] ended up in the experimental realisation of the QSH effect, discussed in more detail in section 1.3.1.

The tight-binding model for the KM graphene is given by

$$\mathcal{H}_{\mathrm{KM}} = -t\sum_{\langle ij\rangle}\sum_{\alpha} c^{\dagger}_{i\alpha}c_{j\alpha} + i\lambda_{\mathrm{SO}}\sum_{\langle\langle ij\rangle\rangle}\sum_{\alpha\beta}\nu_{ij}s^{z}_{\alpha\beta}c^{\dagger}_{i\alpha}c_{j\beta} + \lambda_v\sigma_z\sum_{i} c^{\dagger}_{i}c_{i} \ , \tag{4.15}$$

where $c_{i\alpha}(c^{\dagger}_{i\alpha})$ annihilates (creates) an electron with spin $\alpha = \uparrow, \downarrow$ at the i-th site of the lattice, and the sum in the first term runs over the nearest-neighbors. The second term gives the hopping between the second nearest neighbours by summing over $\langle\langle ij\rangle\rangle$. This term allows spin-flip events due to the third Pauli matrix s^z, which acts on the spin space and has a chiral nature thanks to the factor ν_{ij}. Depending on the direction of hoping, the intrinsic spin-orbit coupling has a factor of -1 $(+1)$ when (counter-)clockwise neighbours are considered. The strength of the spin-orbit coupling is given by λ_{SO}. The third term is a staggered sublattice potential λ_v, which is included to describe the transition between the QSH phase and the trivial insulator. The staggered potential breaks the inversion symmetry with an energy difference between the two sublattices of $2\lambda_v$.

The bulk spectrum of the KM model is gapped with magnitude

$$\Delta E = |6\sqrt{3}\lambda_{\mathrm{SO}} - 2\lambda_v| \ . \tag{4.16}$$

The two parameters compete then to generate an insulating system: if $\lambda_v > 3\sqrt{3}\lambda_{SO}$ the system is trivial while for $\lambda_v < 3\sqrt{3}\lambda_{SO}$ a QSH state is obtained. The transition between the two regimes is achieved through the gap closing. The $\mathbb{Z}_2$ number describes the topological properties of the Hamiltonian, as shown by Kane and Mele in reference [124].

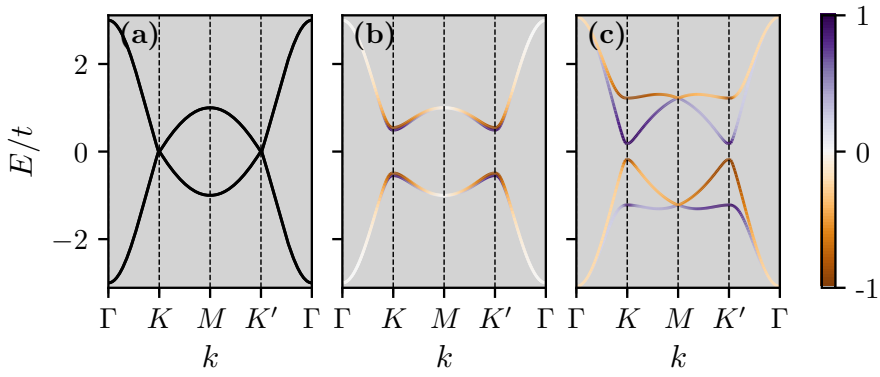

Figure 4.2: Bulk dispersion through the BZ for a graphene sheet with first nearest neighbours (a), a KM model in the QSH regime with parameter $\lambda_{SO} = 0.1t$ and $\lambda_v = 0$ (b) and a KM model in the insulator regime with $\lambda_{SO} = 0.1t$ and $\lambda_v = 0.7t$ in (c). In panel (a) the states are equally distributed in both sublattices and the bands are colored in black to improve the visibility. In (b) the bands are degenerated and each of them is distributed in one of the sublattices; a small vertical shift has been introduced in the energy to show the degenerate band located in A. The colormap indicates as $+1$ (-1) a full A (B) state and corresponds to the expectation value of τ_z over the eigenstates.

Figure 4.2 shows the bulk spectrum in the two regimes. The colour map represents the occupation of the sublattice given by $\langle \tau_z \rangle$, where +1 (-1) is a full A (B) state. The occupation shifts between the two regimes: in the QSH state both valleys are occupied in both sublattices, while in the insulating regime the valley occupation is A-type in the conduction band and B-type in the valence band for the bands closer to the Fermi level. The two regimes exhibit different edge states in nanoribbons, as addressed in the following section.

4.1.3 Graphene nanoribbons

Finite graphene systems exhibit characteristic states due to the special symmetries of the lattice. Two prototypal edges are obtained by cutting

the graphene sheets in certain directions, namely the armchair and the zigzag terminations, shown in figure 4.1 (a). For the zigzag case, the edge is parallel to $\mathbf{a}_z = \mathbf{a}_1$ (or $\mathbf{a}_2$), while for the armchair case the edge follows the linear combination of the two unit vectors $\mathbf{a}_a = \mathbf{a}_1 + \mathbf{a}_2$.

More specifically, if a strip of graphene is cut along the same edge on both sides, a nanoribbon with a simple unit cell is obtained. Nanoribbons with both edges of the same type are named armchair graphene nanoribbons (aGNR) or zigzag graphene nanoribbons (zGNR), depending on the termination. From a theoretical point of view, the simplicity of the ribbon unit cell in these two cases facilitates the calculation of the spectrum and wave functions. Recently, experimental efforts to grow samples with clean edges down to the atomic level have been successful in synthesising such samples using a novel technique based on the surface-assisted coupling of molecular precursors into linear polyphenylenes [28, 47, 177]. However, in a more general case, such clean edge cuts are not experimentally achievable, and a mixed edge is expected [87, 161, 214], resulting in important modifications of the nanoribbon transport properties [10, 103].

Nevertheless, the two prototypal nanoribbons are an indispensable starting point for the theoretical investigation of transport properties. A derivation of the dispersion is given below for the simplest case of a nearest-neighbour graphene model, i.e. equation (4.2) with $l = 1$. Figure 4.3 shows the unit cell for aGNR and zGNR as well as the convention of counting based on the number of dimers across the ribbon width.

When periodicity is considered, the electron operators in equation (4.2) are expressed as a Fourier transform. Taking the direction of the periodicity in x and the open boundary conditions in y, the electron operators reads as

$$c^\dagger_{x,y} = \frac{1}{\sqrt{N}} \sum_k e^{ikx} c^\dagger_{k,y} \ , \quad c_{x,y} = \frac{1}{\sqrt{N}} \sum_k e^{-ikx} c_{k,y} \ , \tag{4.17}$$

where N is the number of sites in the y-direction and k is the wavenumber.

In aGNR, the x axis is defined in the direction of $\mathbf{a}_a$, the length of the translational vector is $a_a = 3a_{\mathrm{CC}}$, and the Hamiltonian for a N-dimer nanoribbon is expressed as a function of the dimensionless wavevector $k = 3a_{\mathrm{CC}}k_x$ as:

$$\mathcal{H}(k) = t_1 \phi^\dagger_k \begin{pmatrix} 0 & g_k & 0 & 1 & 0 & 0 & \dots \\ g_k^* & 0 & 1 & 0 & 0 & 0 & \dots \\ 0 & 1 & 0 & g_k & 0 & 1 & \dots \\ 1 & 0 & g_k^* & 0 & 1 & 0 & \dots \\ 0 & 0 & 0 & 1 & 0 & g_k & \dots \\ 0 & 0 & 1 & 0 & g_k^* & 0 & \dots \\ \dots & \dots & \dots & \dots & \dots & \dots & \dots \end{pmatrix} \phi_k \ , \tag{4.18}$$

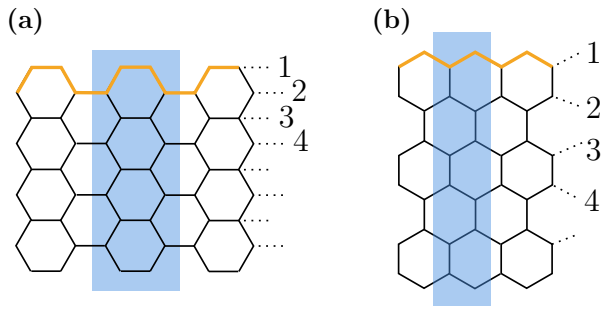

Figure 4.3: Ribbon counting for aGNRs and zGNRs in (a) and (b) panels, respectively. The unit cell is plotted in a shadowed blued and the edge is underlined in orange.

where $g_k = e^{ika_a/2}$ and $\phi_k = \{c_k^{1A}, c_k^{1B}, ...c_k^{NA}, c_k^{NB}, \}$. By diagonalizing this Hamiltonian, the spectrum is found to be [49, 81, 279]:

$$E_\pm = \pm\sqrt{3 + 4\cos(k_\perp)\cos(k/2) + 2\cos(2k_\perp)}\ , \tag{4.19a}$$

where the transverse wavenumber $k_\perp$ is given by:

$$k_\perp = \frac{2\pi n}{N+1}\ , \quad n = 1, 2, ..N\ . \tag{4.19b}$$

The energy gap closes for $k = 0$ when $N = 3n - 1$, which is the condition for the metallic aGNR. Comparing the former expression with equation (4.3a) for $t_2 = 0$, the aGNR dispersion is simply a sum of slices across graphene band structure at N equidistant $k_y = 2k_\perp/a$ values.

In zGNRs, the x periodic direction is $\mathbf{a}_1$, with a translational vector length of $a_z = \sqrt{3}a_{\mathrm{CC}}$. In this case, the Hamiltonian takes the form:

$$\mathcal{H}(k) = t_1\phi_k^\dagger \begin{pmatrix} 0 & g_k & 0 & 0 & 0 & ... \\ g_k & 0 & 1 & 0 & 0 & ... \\ 0 & 1 & 0 & g_k & 0 & ... \\ 0 & 0 & g_k & 0 & 1 & ... \\ 0 & 0 & 0 & 1 & 0 & ... \\ ... & ... & ... & ... & ... & ... \end{pmatrix} \phi_k\ , \tag{4.20}$$

where $g_k = 2\cos(ka_z/2)$ and $\phi_k = \{c_k^{1A}, c_k^{1B}, \ldots c_k^{NA}, c_k^{NB}, \}$.

By diagonalizing the Hamiltonian, the dispersion is more complex than in the case of aGNRs, and it reads as

$$E = \pm\sqrt{1 + g_k^2 + 2g_k\cos(k_\perp)}\ , \tag{4.21a}$$

$$\sin(k_\perp N) + g_k\sin[(k_\perp(N+1))] = 0\ . \tag{4.21b}$$

In this case, $k_\perp$ from equation (4.21b) depends on k. Hence, the dispersion is not only the slicing of bulk graphene, but an extra state appears, corresponding to the zigzag edge state[1].

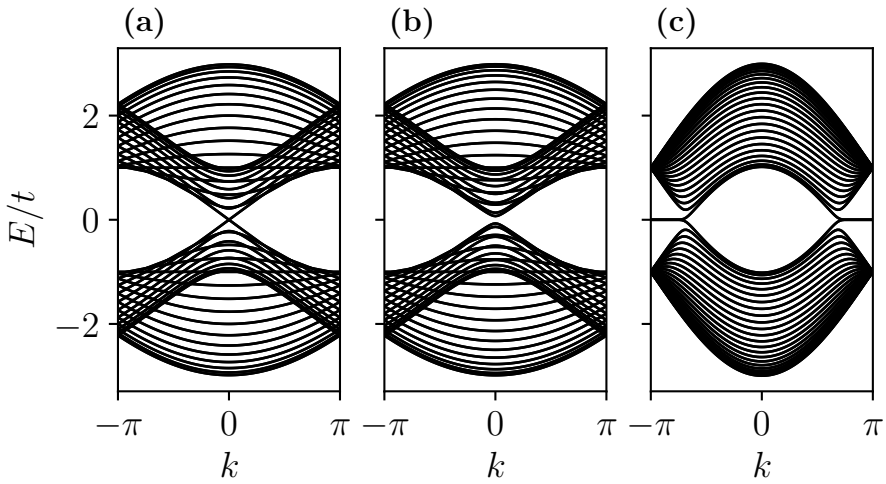

Figure 4.4: Dispersion relation for 11-aGNR (a), 13-aGNR (b) and 23-zGNR considering only first nearest neighbours in the Hamiltonian (4.2).

Figure 4.4 shows the dispersion for the three main types of graphene nanoribbons described above: the metallic aGNR, the insulating aGNR and the zGNR. Although both metallic aGNR and zGNR are gapless systems, the states at zero energy are of a very different nature. In the case of metallic aGNR the states are delocalised and dispersive, while in zGNR the states are localised at the edges and show non-dispersive flat bands, when considering a first nearest-neighbour model. The edge state in zGNR connects the projection of the two valleys $\mathbf{K}$ and $\mathbf{K}'$, and thus interesting topological properties arise depending on the termination of the edges by distinguishing whether they are from the same or the opposite sublattice[2]. The edge states correspond to the flat band in panel 4.4(c).

In gapped systems, such as the KM model described by the Hamiltonian (4.15), adding a mass term has important consequences in zGNRs. This is due to the survival of the valleys $\mathbf{K}$ and $\mathbf{K}'$ in the nanoribbon dispersion. As previously discussed in section 4.1.2, the KM model shows two different phases depending on the competition of λ_v and λ_{SO} in the generation of the gap. When the gap is mainly generated by the spin-

[1] The appendix of reference [279] provides more details about the derivation of the dispersion relation (4.21a).

[2] For a detailed discussion of the topology of edge terminations in zGNR see chapter 7.5 of reference [18].

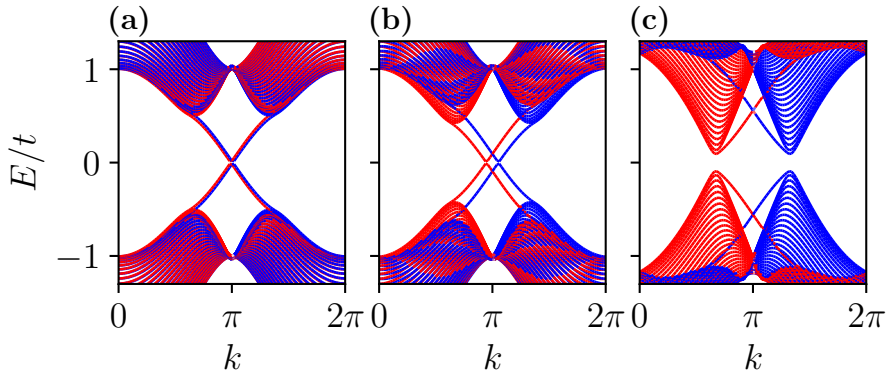

Figure 4.5: Dispersion for a zGNR of width $40a_{CC}$ and parameters $\lambda_{SO} = 0.1t$ in all the three panels. The staggered potential is $\lambda_v = 0$ (a), $\lambda_v = 0.1t$ (b) and $\lambda_v = 0.6t$ (c). In panel (a) a small shift in the spectrum have been introduced in order to visualize the two degenerate spin bands. The color code is red por spin up and blue for spin down states.

orbit coupling, the system is in a topological phase described with a $\mathbb{Z}_2$ invariant [124] and zGNRs show two edge states connecting the upper and lower bulk bands with the same spin and opposite valleys, as illustrated in figure 4.5(a). On the other hand, if the gap is mainly caused by the staggered potential, the two valleys are connected without traversing the gap, see panel (c) of figure 4.5. The intermediate regime, in panel 4.5 (b), is a QSH with broken inversion symmetry. In this case, due to the contribution of the staggered potential, a spin-dependent shift of the valleys leads to a crossing of the edge states for $k = \pi$ at non-zero energy. In between the two different topological phases, the bulk gap closes, allowing the edge states to switch between the two configurations.

In the following, two main problems concerning graphene-based systems are addressed. First, the effect of impurities and electron-electron (e-e) interaction is studied by means of the Hubbard model in the mean-field Hartree-Fock approximation in section 4.2. Second, the role of hBN and the sublattice symmetry breaking is analysed in non-local resistance measurements in section 4.3.

4.2 Electron-electron interactions in graphene: mean-field Hubbard model

Many-body problems are particularly challenging due to the difficult trade-off between approximations based on a wide range of scales. In

graphene, many-body effects have attracted much interest due to the important symmetry breaking generated in the Dirac spectrum [142]. Moreover, recent theoretical [185] and experimental studies [128] have shown that many-body effects in graphene-based systems play a crucial role in describing and tuning the electron motion. Reference [128] shows that e-e interactions in graphene can be modulated by proximity screening.

In this section the Hubbard model is used as a starting point for describing the e-e interaction. The Hubbard model accounts for the interaction by including only the largest contribution to the Coulomb integral, which is expected to come from two electrons in the same atom. According to the Pauli exclusion principle, the two electrons must differ in spin, and with this constraint the Hubbard term is given by the interaction of pairs of opposite spins in the same site:

$$\mathcal{H}_{\mathrm{U}} = U \sum_i c^\dagger_{i\uparrow} c_{i\uparrow} c^\dagger_{i\downarrow} c_{i\downarrow} \ , \tag{4.22}$$

where $c_{i\alpha}(c^\dagger_{i\alpha})$ annihilates (creates) an electron with spin $\alpha = \uparrow, \downarrow$ at the i-th site of the lattice. By defining the number operator $n_{i\alpha} = c^\dagger_{i\alpha} c_{i\alpha}$ the Hubbard term is written in a more compact form as:

$$\mathcal{H}_{\mathrm{U}} = U \sum_i n_{i\uparrow} n_{i\downarrow} \ . \tag{4.23}$$

The exclusion of the long-range Coulomb interactions from this model has led to a debate about its validity [142], except when restricted to systems where a strong screening effect arises from the substrate or through the dynamical screening effects of graphene itself [208]. However, in the specific case of graphene, previous works have shown that mean-field theory is a valuable first approach to the many-body problem, especially when applied to magnetic properties. The mean-field Hubbard has been compared finding a qualitative good agreement with quantum Monte Carlo simulations in nanoribbons [71, 207] as well as DFT calculations [73, 146] and it was applied to study the effect of vacancies in graphene [29, 36, 152, 185, 196].

This section describes the implementation of a general algorithm for the determination of e-e interactions in graphene within an unrestricted Hubbard model. The unrestricted Hubbard model is obtained from the Hartree-Fock mean-field method by including any possible spin-flip event, which permits spontaneous magnetic ordering even when non-magnetic disorder is considered. In fact, disorder such as impurities at the edges, when surrounded by interacting electrons, can generate a local magnetisation leading to the backscattering of electrons at these sites by breaking the symmetries of the topological protection [152, 185]. The quantization

of the conductance is broken, and thus experimental results for quantum wells [139] and atomically thin crystals [296] are reproduced. The self-consistent method exposed here has been implemented by Irián Sánchez-Ramírez for graphene nanoribbons with an impurity at the edge to control the thermoelectric properties of graphene nanoribbons in reference [228].

4.2.1 Unrestricted Hartree-Fock approximation

The exact solution of the problem with the Hubbard term, as described by equation (4.23), is still not feasible in large systems. In addition, a one-particle Hamiltonian would be more suitable for transport calculations. To obtain the effective Hamiltonian, a mean-field theory is a convenient approximation that allows a smaller basis set.

The basic idea of mean-field theory is to replace the interaction between all particles with an average single-particle potential by expanding the interaction as fluctuations around the mean value of the field. The correlations are then included only on average, and one-electron operators are a proper basis for the Hamiltonian. The Hartree-Fock approximation considers fluctuations around the mean value of the number operator $\langle n_{i,\alpha}\rangle$. By replacing the number operator with

$$n_{i,\alpha} = \langle n_{i,\alpha}\rangle + \delta n_{i,\alpha} \ , \tag{4.24}$$

the Hubbard term in equation (4.23) reads as:

$$\begin{aligned} n_{i,\uparrow}n_{i,\downarrow} &= \langle n_{i,\uparrow}\rangle\langle n_{i,\downarrow}\rangle + \delta n_{i,\uparrow}\langle n_{i,\downarrow}\rangle + \langle n_{i,\uparrow}\rangle\delta n_{i,\downarrow} + \delta n_{i,\uparrow}\delta n_{i,\downarrow} \\ &\approx n_{i,\uparrow}\langle n_{i,\downarrow}\rangle + \langle n_{i,\uparrow}\rangle n_{i,\downarrow} - \langle n_{i,\uparrow}\rangle\langle n_{i,\downarrow}\rangle \ , \end{aligned} \tag{4.25}$$

where the second order term in $\delta n_{i,\alpha}$ is neglected in the last step. With a single number operator in each term, the resulting term is naturally a one-particle expression, where the effect of the e-e interaction is only taken into account as an onsite term that depends on the occupation of the opposite spin at each site. The average occupation of site i is in fact given by the electron density in the site:

$$\langle n_{i,\alpha}\rangle = \sum_j f(E_{j,\alpha}) \left|\phi_{i,\alpha}^{(j)}\right|^2 \ , \tag{4.26}$$

where $f(E)$ is the Fermi-Dirac distribution and $\phi_{i,\alpha}^{(j)}$ is the $j-$component of the eigenfunction $\phi_{i,\alpha}$ with eigenvalue $E_{j,\alpha}$.

In this way, the mean-field Hamiltonian with the Hubbard term (4.25) is obtained by solving the ground state of the system such that the mean-field occupations are extracted from the electron density. Usually self-consistent routines are implemented to find the ground state: starting

from an initial guess for the occupations, the system is diagonalised and a new value for the occupation is calculated until two successive iterations produce the same output.

If the system has no spin-flipping terms, the former mean-field theory forbids any spin-switching process. In fact, within the Hartree approximation, the e-e interaction is approximated by interactions of electrons with the same spin: as shown in equation (4.25), all contributions come from number operators defined over a site and a well-defined spin. In order to study the spontaneous polarisation in a non-magnetic system, an extended version of the Hartree-Fock method has to be applied, taking into account the spin-flipping processes. This method is referred to in the literature as unrestricted Hartree-Fock [277–279]. Within this approximation, the fluctuations at the level of the creation-annihilation pairs are evaluated as

$$\begin{aligned} n_{i,\alpha}n_{j,\beta} &= c^\dagger_{i,\alpha}c_{i,\alpha}c^\dagger_{j,\beta}c_{j,\beta} \\ &\approx c^\dagger_{i,\alpha}c_{i,\alpha}\langle c^\dagger_{j,\beta}c_{j,\beta}\rangle + \langle c^\dagger_{i,\alpha}c_{i,\alpha}\rangle c^\dagger_{j,\beta}c_{j,\beta} - \langle c^\dagger_{i,\alpha}c_{i,\alpha}c^\dagger_{j,\beta}c_{j,\beta}\rangle \ . \end{aligned} \tag{4.27}$$

Due to Wick's theorem, considering all pairs of operators, from equation (4.27) is obtained:

$$\begin{aligned} n_{i,\uparrow}n_{i,\downarrow} \approx{}& \langle c^\dagger_{i,\uparrow}c_{i,\uparrow}\rangle c^\dagger_{i,\downarrow}c_{i,\downarrow} + c^\dagger_{i,\uparrow}c_{i,\uparrow}\langle c^\dagger_{i,\downarrow}c_{i,\downarrow}\rangle - \langle c^\dagger_{i,\uparrow}c_{i,\uparrow}\rangle\langle c^\dagger_{i,\downarrow}c_{i,\downarrow}\rangle \\ &- \langle c^\dagger_{i,\uparrow}c_{i,\downarrow}\rangle c^\dagger_{i,\downarrow}c_{i,\uparrow} - c^\dagger_{i,\uparrow}c_{i,\downarrow}\langle c^\dagger_{i,\downarrow}c_{i,\uparrow}\rangle + \langle c^\dagger_{i,\uparrow}c_{i,\uparrow}\rangle\langle c^\dagger_{i,\downarrow}c_{i,\uparrow}\rangle \ . \end{aligned} \tag{4.28}$$

After rearranging the terms of equation (4.28), and defining $S^+_i = c^\dagger_{i,\uparrow}c_{i,\downarrow}$ and $S^-_i = c^\dagger_{i,\downarrow}c_{i,\uparrow}$, the Hubbard Hamiltonian (4.23) is expressed as

$$\begin{aligned} \mathcal{H}_{\mathrm{U}} \approx{}& U\sum_i \left(\langle n_{i\downarrow}\rangle n_{i\uparrow} + \langle n_{i\uparrow}\rangle n_{i\downarrow} - \langle n_{i\uparrow}\rangle\langle n_{i\downarrow}\rangle\right) \\ &- U\sum_i \left(\langle S^+_i\rangle c^\dagger_{i\downarrow}c_{i\uparrow} + \langle S^-_i\rangle c^\dagger_{i\uparrow}c_{i\downarrow} - \langle S^+_i\rangle\langle S^-_i\rangle\right) \ . \end{aligned} \tag{4.29}$$

In the following, the application of the self-consistent algorithm is particularised for the KM-Hubbard model in the unrestricted Hartree-Fock approximation. The choice of the KM model is motivated by its adaptability, which describes a QSH state as well as graphene with first-nearest neighbours by setting $\lambda_{\mathrm{SO}} = 0$. The Hamiltonian of the system in the mean-field approximation is given by

$$\mathcal{H}_{\mathrm{MF}} = \mathcal{H}_{\mathrm{KM}} + \mathcal{H}_{\mathrm{U}} \ , \tag{4.30}$$

where the non-interacting KM contribution is given by the Hamiltonian (4.15) and the Hubbard term in the mean-field approximation corresponds to equation (4.29).

In $\mathcal{H}_{\mathrm{U}}$, the meanfield values for the inplane spin $\langle S_i^{\pm}\rangle$ and the occupation of both spin projections $\langle n_{i,\uparrow/\downarrow}\rangle$ have to be obtained self-consistently for the system considered by applying the algorithm from reference [71]. In the basis of the lattice sites and orbitals sorted as

$$\{1_{\uparrow}^{A}, 1_{\downarrow}^{A}, 1_{\uparrow}^{B}, 1_{\downarrow}^{B}, 2_{\uparrow}^{A}, \cdots, (N/2)_{\downarrow}^{B}\} \ ,$$

where N is the number of sites of the lattice and A and B are the two sublattices of the honeycomb lattice, the algorithm is implemented in the following steps:

1. Generate a random set of 4 vectors of length N for the initial values of the inplane spin and spin occupations:

$$\mathcal{V}_0 = \{\langle S_i^{+}\rangle, \langle S_i^{-}\rangle, \langle n_{i,\uparrow}\rangle, \langle n_{i,\downarrow}\rangle\}_{i=1}^{N} \ . \tag{4.31}$$

   Selecting a random set first may slow down convergence. However, it helps to avoid magnetic frustration.

2. Diagonalise the Hamiltonian of the scattering region and obtain $2N$ eigenvalues $\{E_v\}_{v=1}^{2N}$ and $2N$ eigenvectors ϕ_v, where v is the band index. The i-th component of each eigenvector is expressed by the spinor at each site

$$\phi_{v,i} = \begin{bmatrix} \phi_{v,i}^{\uparrow} \\ \phi_{v,i}^{\downarrow} \end{bmatrix} . \tag{4.32}$$

3. From the eigenvectors and eigenvalues of step 2, calculate a new set $\mathcal{V}_1$ analogous to the one of equation (4.31) by computing over each spinor

$$\langle \mathbf{m}_i\rangle^{(1)} = \sum_{v=1}^{N_e} \phi_{v,i}^{(0)\,\dagger}\ \boldsymbol{\sigma}\ \phi_{v,i}^{(0)} \ , \tag{4.33a}$$

$$\langle n_{i,\uparrow}\rangle^{(1)} = \sum_{v=1}^{N_e} \phi_{v,i}^{(0)\,\dagger} \begin{pmatrix} 1 & 0 \\ 0 & 0 \end{pmatrix} \phi_{v,i}^{(0)} \ , \tag{4.33b}$$

$$\langle n_{i,\downarrow}\rangle^{(1)} = \sum_{v=1}^{N_e} \phi_{v,i}^{(0)\,\dagger} \begin{pmatrix} 0 & 0 \\ 0 & 1 \end{pmatrix} \phi_{v,i}^{(0)} \ , \tag{4.33c}$$

$$\langle S_i^{\pm}\rangle^{(1)} = \frac{\langle m_x\rangle^{(1)} \pm i\langle m_y\rangle^{(1)}}{2} \ , \tag{4.33d}$$

   where $\boldsymbol{\sigma}$ is a three-component vector formed by the Pauli matrices and $\langle \mathbf{m}_i\rangle$ is the magnetic moment of the i-th site. The expectation

values are calculated over the set of N_e lowest states of the system. This is equivalent to fixing the number of electrons in the system to N_e. The chemical potential is then extracted from the value of the highest energy considered $E_{N_e} = \mu$.

The above expressions introduce the superscripts (0) and (1) to label the iteration step.

4. Using the new set $\mathcal{V}_1$ build a new scattering region and repeat steps 2 and 3 iteratively until convergence. The convergence criteria is

$$\{\mathcal{V}_k^{(n)}(i)\}_{n=1}^4 - \{\mathcal{V}_{k-1}^{(n)}(i)\}_{n=1}^4 \leq \text{tol} \ , \forall i \ , \tag{4.34}$$

where tol is the tolerance, i the lattice site and n the component of $\mathcal{V}_k$. To improve convergence and avoid stagnation, a variable-weight method is implemented that uses information from iteration $k-1$ and $k-2$ for iteration k as follows

$$\begin{aligned}\{\mathcal{V}_k^{(n)}(i)\}_{n=1}^4 = &\left(1 - \frac{k}{k^{1.5}+1}\right) \\ &\times \{\mathcal{V}_{k-2}^{(n)}(i)\}_{n=1}^4 + \frac{k}{k^{1.5}+1}\{\mathcal{V}_{k-1}^{(n)}(i)\}_{n=1}^4 \ ,\end{aligned} \tag{4.35}$$

where it was imposed that $k/\left(k^{1.5}+1\right) \geq \text{tol}$.

The algorithm is implemented for a finite Hilbert space of size $2N \times 2N$. When applied to a nanoribbon, some precautions must be taken. First, a finite scattering region must be considered, and hence the nanoribbon must be finite in both directions. To suppress the contribution of the edges in the longitudinal direction, PBC are applied and the states in equation (4.33a) are calculated for zero momenta.

If the system is not translationally invariant, e.g. due to edge roughness or the presence of impurities in the scattering region, the scattering region must be enlarged to ensure a correct description of both the impurity or edge distortion and the absence of edges in the sides connected to the leads.

Finally, note that the number of electrons is a parameter of the mean-field model and takes discrete values by filling the levels. The chemical potential is then extracted from the self-consistent calculations for each filling factor. However, when performing transport calculations by changing the voltage gate, the chemical potential is continuously shifted so that the filling factors obtained may be fractional. The presented algorithm, based on discrete band fillings, prevents the region between each integer filling factor from being consistently defined.

To overcome this problem, the Fermi energy is recalculated for each filling factor in the windows of the considered gate voltages. Since E_F^N is the Fermi energy obtained for $N_e = N$ occupied states and E_F^{N+1} is the Fermi energy for $N_e = N + 1$, the transport calculations for a voltage gate within this energy window $V_g \in (E_F^N, E_F^{N+1})$ are computed using the effective parameters extracted for $N_e = N$. When the injection energy exceeds E_F^{N+1}, the effective model is recalculated for one more filling factor, and a new energy window is established for the transport calculations. This process is referred in the following as the *Fermi energy recalculation algorithm*.

In the calculations reported, the tolerance for the Fermi energy recalculation is set to $2.1 \times 10^{-3}t$. This corresponds to 25 K for $t = 1$ eV. In pristine graphene, where $t = 2.7$ eV, the tolerance is equivalent to $T = 67.5$ K.

4.2.2 Zigzag graphene nanoribbons with a monovacancy

The first system to be addressed is a zGNR with a monovacancy in one of the edges. In zGNRs, the edge states are not topologically protected and there are two spin channels at each edge. This implies that backscattering is possible even between states with opposite spin polarisation. By introducing the vacancy at the edge and computing the mean-field state for a given occupancy, spin-polarised states around the vacancy are obtained. Numerically it has been checked that the main contribution comes from the m_x and m_y components, while the m_z component is almost negligible. Figure 4.6 shows an example of the self-consistent values obtained for a zGNR of $L = 30a_{CC}$ and $W = 20a_{CC}$. The vacancy is located in the lower centre of the nanoribbon and generates the inplane magnetization of the states localised in the lower part.

Once the self-consistent values for $\langle S_i^{\pm} \rangle$ and $\langle n_{i,\uparrow/\downarrow} \rangle$ are obtained according to the previously presented algorithm, a scattering setup is built that includes a nanoribbon with two longitudinal leads. The scattering region is constructed using the tight-binding KM from equation (4.30) expressed in the single-particle orbitals. The mean-field calculation provides the $\langle S_i^{\pm} \rangle$ and $\langle n_{i,\uparrow/\downarrow} \rangle$ of the Hubbard term (4.29). Then, the conductance is calculated within the Landauer-Büttiker formalism as implemented in `Kwant` [102]. Note that the self-consistent values are calculated for a fixed Fermi energy, corresponding to a number of electrons N_e. To calculate the conductance as a function of the Fermi energy, the self-consistent values for $\langle S_i^{\pm} \rangle$ and $\langle n_{i,\uparrow/\downarrow} \rangle$ are recalculated according to the Fermi energy recalculation algorithm previously explained. In the Landauer-Büttiker formalism, detailed in appendix B, the conductance at energy E for a two-

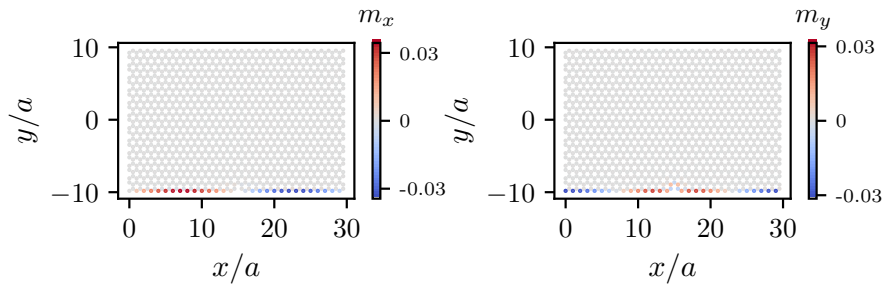

Figure 4.6: Values of m_x and m_y from equation (4.33a) obtained for a zGNR with only first neighbours hoppings and $U = 0.5t$. The size of the ribbon is $L = 30a_{CC}$ and $W = 20a_{CC}$. The Fermi energy is set to $E_F = 0.086t$.

lead device with spin-polarised leads can be factorised by the following contributions

$$G(E) = G_{\uparrow\uparrow}(E) + G_{\downarrow\downarrow}(E) + G_{\uparrow\downarrow}(E) + G_{\downarrow\uparrow}(E) \ , \tag{4.36}$$

where the subscripts indicate the spin polarization of the incoming and outcoming modes.

The transport setup is built by adding 2D semi-infinite leads to the scattering region where the self-consistent mean-field Hamiltonian has been calculated in advance. The leads are described by $\mathcal{H}_{\mathrm{KM}}$ from equation (4.15) by setting $\lambda_{\mathrm{SO}} = \lambda_v = 0$. An onsite energy of $\epsilon_i = U$ is included in all sites of the lead to avoid scattering processes at the boundary between the leads and the systems due to the onsite energy mismatch.

In a pristine zGNR with translational symmetry and no vacancies, the electronic transport is given by the number of channels available at that energy. When a vacancy is introduced, the perfect quantisation is lost due to scattering and reflections. However, the small roughness of the edge does not dramatically affect the quantisation in the absence of e-e interaction, as shown in the $U = 0$ curve of panel (a) of figure 4.7. When the e-e interaction is included, the impurity creates a scattering centre near the edge, thus breaking the quantisation due to the effective magnetization. In a zGNR there is no topological protection and there are two edge states that propagate in both directions in the same side of the nanoribbon at low energies. The vacancy equally affects the two channels localised in the edge of the monovacancy.

Panel (b) of the same figure shows the reflected conductance for spin-polarised current for different interaction strengths U. When the monovacancy is encountered, the current reflects in the channel with the same

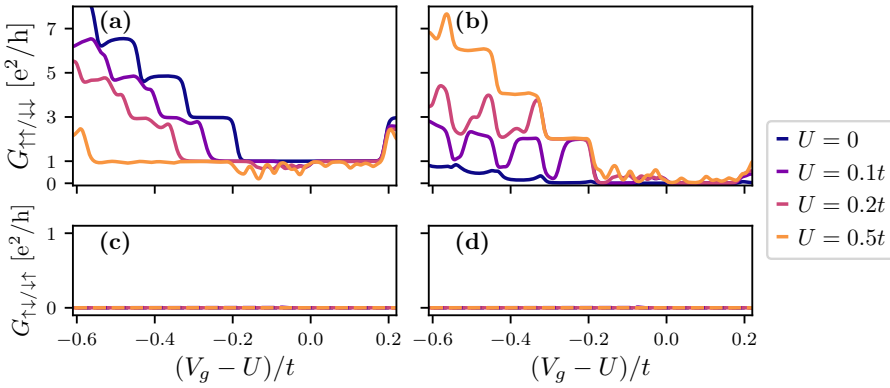

Figure 4.7: Spin-polarised conductance as a function of voltage gate V_g for a zGNR. Panels (a) and (c) show the conductance from left to right for the spin-conserved (a) and spin-flip (c) signals. The right panels depict the reflected signal for spin-conserved (b) and spin-flip (d). The nanoribbon has zigzag edges on both sides and a width of $20a_{CC}$. The spin-polarised conductance is the same for both spin channels, i.e. $G_{\uparrow\uparrow} = G_{\downarrow\downarrow}$ as well as the spin-flip conductance $G_{\uparrow\downarrow} = G_{\downarrow\uparrow}$.

spin but with the opposite direction of propagation. This is evident from the decrease in the spin-conserved conductance from left to right, which is exactly equal to the reflected contribution.

Consistently, no spin-flip processes are observed. In panels (c) and (d), the spin-flip conductance is plotted for the transmitted case (i.e., from left to right lead) and the reflected conductance (i.e., from when injection and collection leads are the same), respectively. The zero spin-flip conductances imply that there are no scattering processes involving the flipping of s_z. The current is simply reflected by the monovacancy, and such effect is enhanced by adding the e-e interaction.

In the transport calculations, the nanoribbon under consideration has a width of $20a_{CC}$. In the leads, the onsite energy was set to U without performing any self-consistent calculation. The choice of this value is made to avoid scattering due to the mismatch between the leads and the scattering region. Depending on the value of the onsite energy, the mismatch between the lead bands and the scattering region produces a shift of the quantised steps shown in figure 4.7 (b). However, the one-mode region, in this case the $V_g - U \in (-0.2t, 0.2t)$, is not significantly modified by the choice of onsite energy, as along as propagating modes are available in the leads at this energy range.

4.2.3 Kane-Mele zigzag graphene nanoribbon with an edge monovacancy

In this section, the case of a zigzag KM nanoribbon is addressed. The intrinsic spin-orbit coupling in graphene is very weak and the QSH phase is not expected. However, a strong in-plane magnetic field favours the appearance of a spin-polarised QSH phase, as discussed in reference [306], and the KM coupling term correctly describes this scenario. In the following, the spin-orbit term is set to $\lambda_{SO} = 0.1t$.

In the KM nanoribbon, due to the helicity of the Hamiltonian (4.15), there is a single spin channel per edge for each direction of propagation. In other words, each edge hosts two channels with opposite spin and direction of propagation following the usual form of the QSH channels. If a monovacancy is placed in one of the edges, it generates a magnetic scattering point that is localised near the edge. However, at this edge, the only other channel available has the opposite direction of propagation and opposite spin. Therefore, when the monovacancy is encountered, the quantisation of the conductance is lost only for the channel propagating in that direction, which corresponds to a spin channel.

In the absence of e-e interaction, the topological protection of the edge states is ensured by TR invariance, and the quantisation of the topological state remains intact even in the presence of the vacancy. However, the out-of-plane spin may not be conserved due to multiple perturbations, such as a Rashba interaction generated from broken mirror symmetry due to the substrate $V = \lambda_R \hat{z} \cdot (\mathbf{S} \times \mathbf{p})$, a multiband effect $V \propto \mathbf{L} \cdot \mathbf{S}$ or by the e-e interactions studied here.

In the context of the e-e interaction modeled by the unrestricted Hatree-Fock, the TR invariance is broken locally in the system. In fact, when the e-e interaction is included, the vacancy generates an effective local magnetic field [185]. By breaking TR symmetry, in the absence of any topological protection against spin flip, the spin-polarised current will be reflected upon encountering the vacancy by a spin-flipping process. A sketch of this mechanism is shown in figure 4.8(c). In panels (a) and (b) the scattering wavefunctions for the propagating modes from left to right (a) and in the opposite direction (b) are plotted together with the spin projection for $U = t$ and $V_g = 0.2t$.

In figure 4.9 the transmitted and reflected conductances for a zKM nanoribbon are plotted as a function of gate voltage. In the case in figure 4.9, the spin-down channel propagates from left to right along the edge with the monovacancy, hence the spin-down is the only channel affected by the monovacancy, while the other spin-polarised state remains unaltered. The two transmitted spin channels are different, i.e. $G_{\uparrow\uparrow} \neq$

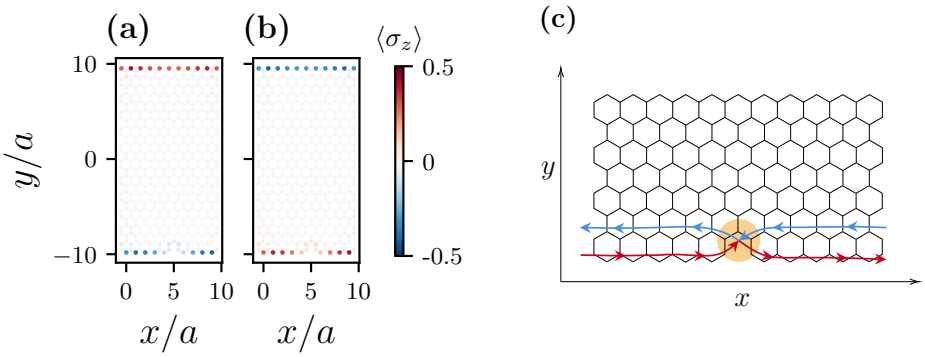

Figure 4.8: Scattering wavefunction for the propagating modes from left to right (a) and in the opposite direction (b) for a zKM nanoribbon of $20a_{CC}$ width and $V_g = 0.2t$. The expectation value of the spin in the z-direction is plotted in the colorscale indicated in the colour bar. In the panel (c) a schematic sketch of the scattering process of the spin-polarised currents due to the vacancy is included. The helical edge channels are plotted in red and blue and the monovacancy is underlined in orange. Due to the interaction-induced magnetism, the helical states scatter into each other near the monovacancy.

$G_{\downarrow\downarrow}$ in panel (a) and the spin-flipped $G_{\uparrow\downarrow} \neq G_{\downarrow\uparrow}$ in panel (d).

In the transport calculations presented here, the width of the KM nanoribbons is $20a$ and the leads are pristine graphene nanoribbons with zigzag edges, i.e. setting $\lambda_{S0} = 0$ and $U = 0$. In this way the topological part of the system is limited to the scattering region, while the matching of the leads and the scattering region is ensured by the first neighbour hopping. Trivial graphene leads are employed to permit counterpropagating modes (in the leads) with both spins in both edges, so that the spin-flip conductances can be measured for all spin and propagation configurations. The bands of the leads are responsible for the structure of the reflected conductance plotted in figure 4.9 (b), where the steps of the conductance mainly correspond to the bulk modes of the zGNR that are reflected when the topological scattering region is encountered. Similar to the previous case, the region of interest, which coincides with $V_g \in (0, 0.2t)$, is not qualitatively affected by the choice of the parameters of the leads, as long as the connection between the leads and the scattering region is adequate and propagating modes (with both spin orientations) are available at this energy.

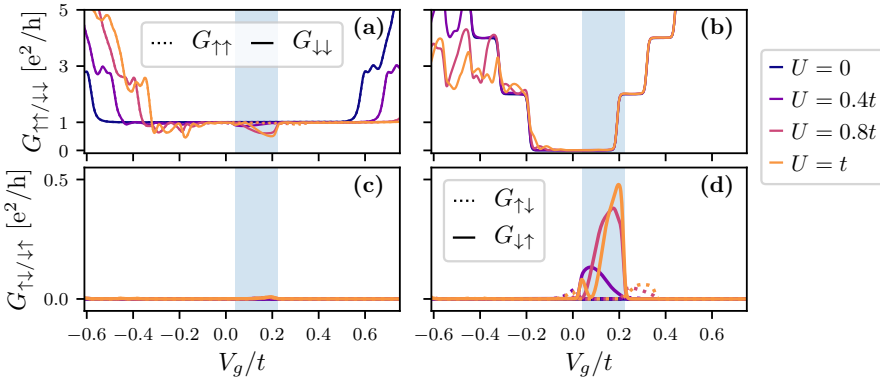

Figure 4.9: Spin-polarised conductance as a function of the voltage gate V_g for a zGNR. Panels (a) and (c) show the conductance from left to right leads for spin-conserved (a) and spin-flip (c) signal. Right panels represent the reflected signal for spin-conserved (b) and spin-flip (d) conductance. The nanoribbon has zigzag edges in both sides and a width of $20a$. To improve visibility, the shadowed area marks the region where the $G_{\uparrow\downarrow/\downarrow\uparrow} > 0.1\ e^2/h$.

4.3 Graphene and hBN

The hBN is extensively used to grow graphene-hBN heterostructures due to the structural solidity it brings to graphene-based devices, such as ripple reduction and higher mobility by reducing disorder [52, 53, 303]. The hBN has the same structure as graphene with a lattice constant stretched by 1.8% and exhibits a wide bandgap of 5.97 eV due to the breaking of the inversion symmetry between the boron and nitrogen sublattices [20, 289]. Although the bandgap almost prevents the tunneling of carriers between graphene and hBN, the effect of moiré patterns, which arise due to the lattice mismatch even in perfectly aligned sheets, affects the electronic dispersion of graphene. Several phenomena are proposed for twisted systems, such as a gap opening at the Dirac point [7, 85, 130, 255] and the appearance of secondary Dirac cones in holes and conduction band [201] with reduced Fermi velocity [304]. In the case of single or doubly aligned graphene and hBN heterojunctions, the hBN still affects the graphene sheet by inducing inversion symmetry breaking. It has been proposed that doubly aligned hBN/graphene generates a super-moiré pattern [288] with non-uniform spatially localised band gaps [5, 215].

Based on the pioneering experimental work of Abanin *et al.* [1], the measurement of non-local currents in graphene provides a platform to study the more subtle interactions in graphene. The non-local setup

consists of measuring the potential drop between contacts that do not correspond to the injection and collection of the current flow. In general, for an ohmic conductor, the non-local signal is expected to be non-zero by the van der Pauw relation [1]. In the case of a nanowire of width w, the voltage drop at a distance L from the source and drain is given by the following relation in the regime of $L \gg w$:

$$R_{\mathrm{NL}} \simeq 4\pi\rho_{xx} \exp(-\pi L/w) \ . \tag{4.37}$$

Hence, the non-local resistance is expected to decrease exponentially with the distance from the contacts. However, in graphene heterostructures with hBN, the non-local signal measured exceeds the ohmnic contribution [1, 4, 95, 138, 213].

This signal could be produced by a variety of interactions and many mechanisms have been proposed to explain the experimental observations. The first hypothesis by Abanin *et al.* was the magnetic field induces a spin/valley effective splitting and creates an imbalance in the net Hall voltage, similar to the QSH, yet in the absence of a spin-orbit interaction [1]. However, subsequent measurements have shown a non-local signal even without a magnetic field [95]. This suggests that the non-local signal should be generated by processes related to the system itself, without the requirement of external fields.

On the other hand, the measurement of strong non-local signals is related to the appearance of an anomalous velocity induced by the accumulation of Berry curvature due to a bulk gap. This is explained by the following toy model for a gapped Dirac system. At low energies, the dispersion of a gapped graphene near $\mathbf{K}$ and $\mathbf{K}'$ is expressed by rewriting the Hamiltonian (4.5) as

$$\mathcal{H}(\mathbf{q}) = \mathbf{R}(\mathbf{q}) \cdot \boldsymbol{\sigma} \ , \tag{4.38a}$$

$$\mathbf{R}(\mathbf{q}) = (\tau_z \hbar v_F q_x, \hbar v_F q_y, m_s) \ , \tag{4.38b}$$

where $\boldsymbol{\sigma} = (\sigma_x, \sigma_y, \sigma_z)$ is the vector of Pauli matrices, $\epsilon_A = 0$ for simplicity and τ_z distinguishes the two valleys $\mathbf{K}$ and $\mathbf{K}'$.

The Berry curvature for the conduction band of the Hamiltonian (4.38) is given by [300]

$$\boldsymbol{\Omega}(\mathbf{q}) = -\tau_z \, \frac{(\hbar v_F)^2 m_s}{8(m_s^2 + (\hbar v_F |\mathbf{q}|)^2)^{3/2}} \, \hat{z} \ . \tag{4.39}$$

The former expression is obtained by applying equation (1.23b) rewritten as

$$\boldsymbol{\Omega}(\mathbf{k}) = -\boldsymbol{\nabla}_{\mathbf{k}} \times \langle u(\mathbf{k}) | i \boldsymbol{\nabla}_{\mathbf{k}} | u(\mathbf{k}) \rangle \ , \tag{4.40}$$

to the conduction eigenstates

$$u(\mathbf{k}) = A_u \begin{pmatrix} R_z(\mathbf{k}) + |\mathbf{R}(\mathbf{k})| \\ R_x(\mathbf{k}) + iR_y(\mathbf{k}) \end{pmatrix} , \tag{4.41}$$

with A_u a normalization constant.

In the presence of an external field, it has been shown semiclassically that the states acquire a group velocity given by [299]:

$$\mathbf{v}_n(\mathbf{k}) = \frac{1}{\hbar} \left[\boldsymbol{\nabla}_{\mathbf{k}} E_n(\mathbf{k}) + e\mathbf{A} \times \boldsymbol{\Omega}(\mathbf{k}) \right] , \tag{4.42}$$

where $\mathbf{A}$ is the vector potential of the external field and $E_n(\mathbf{k})$ is the energy dispersion of the band n.

The anomalous velocity is given by the second term of the former equation and thus generates a current perpendicular to the external field due to the cross product. The sign of τ_z in equation (4.39) implies that each valley generates a current in an opposite direction, leading to the valley Hall effect. However, when both valleys are considered, the total charge current vanishes due to the equal contribution of the two valley currents in opposite directions.

Recently, the valley Hall effect was reinterpreted using the orbital magnetic moments instead of the valley indices [21]. By employing the orbital magnetic moment, a physical quantity substitutes the non-measurable valley degrees of freedom. Furthermore, the orbital magnetic moment is defined in the full 1BZ, and this simplifies the formalism by removing the cutoffs in the regions of reciprocal space where the valleys are defined.

Following the ideas of the toy model in equation (4.38), the models to describe the non-local signals are based on the valley asymmetry by breaking the spatial symmetry in graphene sheets due to the hBN substrate. This removes the degeneracy of the valleys and allows the carriers from the two valleys to propagate in opposite directions when a current is applied along the sample. Recently it has been proposed that for aligned hBN/graphene heterostructures the moiré pattern generates a spatially non-uniform gap profile that guides the valley Hall currents [215]. Similarly, dispersive edge states with non-local signals and chiral behaviour are observed in the models based on long-range hopping due to the interaction with the substrate [169].

Besides the debate on nomenclature, our aim was to develop a model that correctly describes the recent experimental work of the Nanotechnology Group at the University of Salamanca. The experimental results are discussed below in section 4.3.1, while the theoretical model and transport calculations are discussed in section 4.3.2.

4.3.1 Experimental results for non-local currents

Recent experimental measurements of non-local currents in encapsulated graphene nanoribbons elucidate the effect of the hBN in generating chiral currents [227]. The experimental setup is a hBN/graphene/hBN heterostructure aligned along the exfoliated straight edges, where the twist angles along the vertical structure are expected to be multiples of 30°. Due to the absence of the secondary satellite Dirac peaks, as well as the estimated gap of $\lesssim 10\,\text{meV}$, the predicted orientation is $\pm 30°$.

The experimental setup comprises a structure consisting of a graphite back gate of 15 nm thickness and the monolayer graphene encapsulated by two hBN layers. The thickness of the hBN layers is 10 nm and 50 nm for the top and bottom layers, respectively. The multi-terminal Hall bar has a width of $W = 1.5\,\mu\text{m}$, the total length is $L \approx 11\,\mu\text{m}$ and the distance between the contacts is $\Delta x = 2.5\,\mu\text{m}$. The measurements were performed at 1.5 K and with an excitation current of $10 - 20\,\text{nA}$.

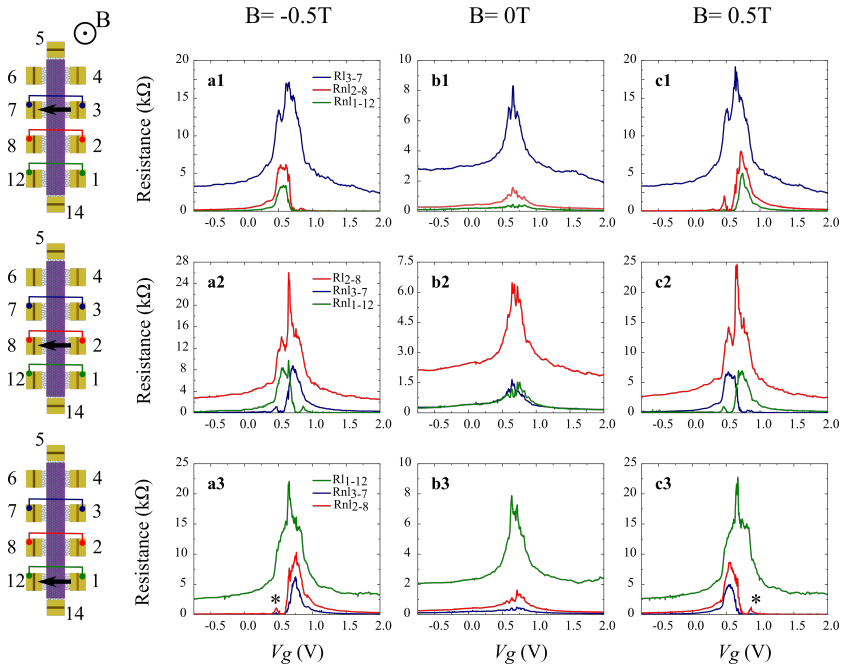

Figure 4.10: Local (R_L) and non-local (R_NL) resistances as a function of the backgate voltage for three different configurations of the injection-collection terminals. The left column includes schematically the corresponding configuration for each row of graphs. Each column corresponds to a different value of the magnetic field, in the out-of-plane direction. Figure adapted from reference [227].

Figure 4.10 shows the local and non-local resistances for three different

injection and collection configurations. The main feature of the experimental results are listed in the following.

- The quality and homogeneity of the sample is evidenced by the mirror symmetric arrangements, such as panels (a1) and (c3) or (a3) and (c1), with similar values of resistance.

- The non-local signal is orders of magnitude higher than expected and therefore not primarily generated by ohmic contributions. In the panels of rows (1) and (3), the two pairs of non-local leads are at two different distances from the injector and collector contacts. In the device, the distance between adjacent leads is $\Delta x = 2.5\,\mu\text{m}$, therefore in panels (1) and (3) the resistances are measured at $\Delta x_1 = 2.5\,\mu\text{m}$ and $\Delta x_2 = 5\,\mu\text{m}$. The ratio of the resistance response is $R_{\text{NL}}(\Delta x_1)/R_{\text{NL}}(\Delta x_2) \sim 0.3$ for the measured values, see reference [227] for a more detailed analysis. However, by applying equation (4.37), a value of $R_{\text{NL}}(\Delta x_1)/R_{\text{NL}}(\Delta x_2) \sim 0.005$ is expected for the ohmic contribution.

- The presented experimental results show a clear chiral behaviour in the non-local signal by permutations of the injection-collection leads and magnetic field directions. With the addition of the magnetic field, the charge neutrality point (CNP) is not displaced, i.e. it is located at $V_g \sim 0.6\,\text{eV}$, while the non-local signal shows a sharp increase, especially near the CNP. When $B \neq 0$, the peak of the CNP splits into two contributions from the electron and hole sectors, and each sector contributes depending on the relative orientation of the contacts where the non-local signal is measured with respect to the injection-collection leads.

- For the symmetric configuration shown in row (2) of figure 4.10, the sign of the field reverses the hole and electron sectors, which are the dominant contribution for each of the non-local contact pairs, depending on the spatial orientation.

- On the other hand, when the current is injected and collected in one of the side leads, as in the panels of rows (1) and (3), the contribution of holes and electron sectors depends on both the direction of the magnetic field and the orientation of the non-local contacts. Thus, the hole peak in (a1) is exchanged for electrons in (c1) by reversing the sign of the field; and the hole sector in (a1) is exchanged for electrons in (a3) by preserving the sign of the field and reversing the position of the contacts.

The effect of the magnetic field is further investigated in reference [227] by including an inplane contribution $B_{\parallel}$ while preserving the perpendicular $B_{\perp} = 0.5\,\mathrm{T}$. The inplane field reduces the local and non-local resistances and induces a symmetrical signal with respect to the CNP. This proves that the chiral non-local currents observed for $B_{\parallel} = 0$ are not related to a spin dependent effect.

4.3.2 Theoretical model and transport results

This section is devoted to the discussion of the model employed. The main characteristics of the effective model are the following. On the one hand, to describe the experimental hole and electron peaks appearing in the non-local signals, a gapped model with hole and electron pockets is required. Apart from including two type of carriers, another important property of the observed resistances is the chirality with respect to the spatial directions and the magnetic field. As discussed in the toy model (4.38), the valley degree of freedom causes the current to drift in opposite directions, see equation (4.42). Therefore, an asymmetric valley model will capture this feature. Besides, the magnetic field should unbalance the electron and hole pockets so that the non-local signal is not cancelled out by the contribution of the two valleys.

In terms of the degrees of freedom of the system, the valley plays an important role, consistent with previous work on graphene and hBN heterostructures. On the other hand, the spin is excluded from the study due to the resistance measurements as a function of in-plane magnetic fields. A spin-polarised current generates a non-local resistance that oscillates as a function of the field [225, 226], instead of the monotonous decrease observed.

In the work of Marmolejo-Tejada *et al.* [169], the effect of the hBN substrate is studied in an alternate stacking of carbon atoms and boron and nitrogen atoms with a rotation of 60° with respect to the carbon atom located on top of the boron atom, such that the second unit cell carbon is located at the centre of the hBN hexagon. This configuration was demonstrated by DFT to be the most energetically stable for an aligned sample when the moiré pattern is neglected [85]. Although the geometrical arrangement of the sheets does not resemble the experimental configuration, the results for the non-local signal as a function of magnetic field agree with the observed measurements. Therefore, the model of Marmolejo-Tejada [169] is used as a first approximation to understand the importance of the different contributions to the non-local signal.

The tight-binding presented in reference [169] shows up to the fifth nearest-neighbour hoppings and it is expressed in terms of a single p_z

Parameters for the tight-biding Hamiltonian		
$t_1 = 266.72\,\text{meV}$	$t_{5A} = 41.6\,\text{meV}$	$\epsilon_A = \epsilon_0$
$t_2 = 208.3\,\text{meV}$	$t_{5B} = 42.8\,\text{meV}$	$\epsilon_B = \epsilon_0 + 5\,\text{meV}$
$t_3 = 200\,\text{meV}$	$t_{5L} = 41.6\,\text{meV}$	$\epsilon_L = -150\,\text{meV}$
$t_4 = -180\,\text{meV}$		$\delta = 85.5\,\text{meV}$

Table 4.1: Parameters used in the calculations. Numerical values are adapted from table A2 in reference [169]. All values are reported from the reference execpt for $\epsilon_B - \epsilon_A$, that is increased up to 5 meV instead of the fitted 2.5 meV. This is done to increase the gap and hence improve the non-local signal. For the specificity of the transport calculations, the armchair leads have an energy offset of ϵ_L to assure that many modes are available at the injection energy. Finally, the energy offset ϵ_0 locates the gap near the zero-energy and it is set for convenience. The value of ϵ_0 is specified in the different scenarios considered.

orbital in each carbon site. The parameters are determined by DFT fitting [169]. From the Hamiltonian (4.2), the fifth nearest-neighbour model is recovered by particularizing for $l = 5$. For zGNRs, it leads to

$$H = \sum_i \left(\epsilon_i a_i^\dagger a_i + \epsilon_i b_i^\dagger b_i\right) - \sum_{l=1,3,4} \sum_{\{\langle i,j\rangle\}_l} t_{ij}^{(l)} \left(a_i^\dagger b_j + \text{h.c.}\right) \tag{4.43}$$
$$- \sum_{\{\langle i,j\rangle\}_2} t_{ij}^{(2)} \left(a_i^\dagger a_j + b_i^\dagger b_j + \text{h.c.}\right) - \sum_{\{\langle i,j\rangle\}_5} \left(t_{ij}^{(5\text{A})} a_i^\dagger a_j + t_{ij}^{(5\text{B})} b_i^\dagger b_j + \text{h.c.}\right) ,$$

where a (b) indicates the annihilation operator for an electron in the site of type A (B). In the former expression, the onsite energy depends on the position and it follows the three cases

$$\epsilon_i = \begin{cases} \epsilon_A + \delta(i) & \text{if } i \in \text{A site in the scattering region} , \\ \epsilon_B + \delta(i) & \text{if } i \in \text{B site in the scattering region} , \\ \epsilon_L + \delta(i) & \text{if } i \in \text{the leads} , \end{cases} \tag{4.44}$$

where $\delta(i) = \delta$ if the site is located in the zigzag edges, otherwise $\delta(i) = 0$. The numerical values for the constants are reported in table 4.1. An energy offset between the two lattices of 5 meV is introduced to account for the breaking of the inversion due to the hBN.

The quantum transport calculations are carried out within the Landauer-Büttiker formalism[3] in `Kwant` in a Hall bar with six transverse armchair leads and two longitudinal zigzag leads. The system is shown in figure 4.11 where the details of the transport calculations setup are reported. The spacing between the leads fulfils that $L_v/W > 10$, so the non-local signal

[3] See appendix B for more details on the Landauer-Büttiker formalism.

obtained is consistent with a robust drifting of the current which propagates over a long distance. In fact, in geometries with $L_v \ll W$ a non-local signal is obtained by evanescent modes that propagate, due to the short distance, from the first to the second crossbar through the gap [169, 269].

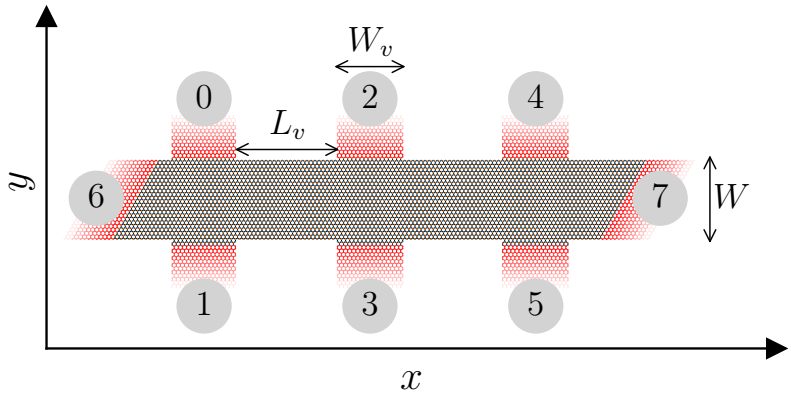

Figure 4.11: Schematic representation of the device: the nanoribbon has zigzag edges and a width of $W = 13.28\,\text{nm}$. The leads in the transverse direction are separated by $L_v = 157\,\text{nm}$ and they have a width in x of $W_v = 13.5\,\text{nm}$.

The non-local current is achieved by transport through the edge states. In fact, if the zigzag states are not dispersive, the non-local signal is absent. This is shown in figure 4.12, where the dispersion relation for a zGNR with PBC conditions in the x-direction is compared for three different models:

- in panels (a) and (d), the nearest neighbour graphene is obtained by setting $t_l = 0$ for $l = 2, 3, 4, 5$ and $\delta = 0$;
- in (b) and (e), the model by equation (4.43) with $\delta = 0$ is considered;
- the complete model from equation (4.43) with parameters in table 4.1 corresponds to panels (c) and (f).

For the system with nearest-neighbour hoppings only, zero non-local signal is obtained even if the inversion symmetry is broken, see panel 4.12(d). On the other hand, the curvature of the edge bands in the long-range hopping models produces the highest non-local signal, see panels 4.12(e) and (f). In these panels, the resistance decreases with the distance from the leads, so that $R_{23;01} \gg R_{45;01}$.

Once the importance of long-range hopping in generating the non-local signal is established, the next step is to check the symmetries of the resistance as a function of the voltage gate V_g and the sign of the magnetic

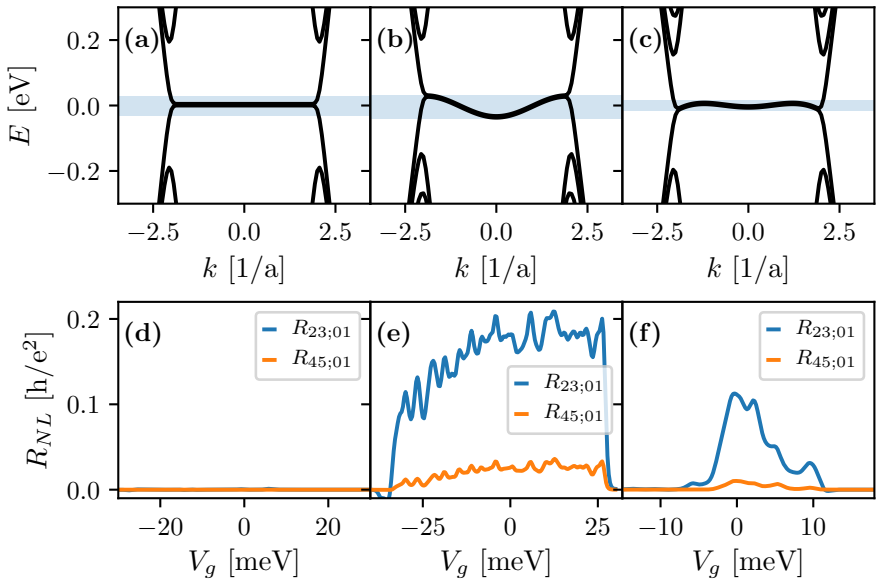

Figure 4.12: Dispersion for a zGNR of $W = 13.28\,\text{nm}$ for three different models: nearest-neighbours only (a), up to five nearest neighbours with values from table 4.1 and $\delta = 0$ (b) and complete model from table 4.1. The lower panels (d)-(f) represent the non-local resistance as a function of the injection energy V_g in correspondence to the upper panels nanoribbons. The setup for the transport calculations is depicted in figure 4.11. In order to locate the Dirac points near the zero energy, $\epsilon_0 = 0$ in (a) and (d); $\epsilon_0 = 400\,\text{meV}$ in (b) and (e); and $\epsilon_0 = 350\,\text{meV}$ in (c) and (f). The temperature is set to $T = 5\,\text{K}$ as detailed in appendix D.

field. The magnetic field is included by the minimal substitution of the vector potential in the tight-binding hoppings of equation (4.43). Appendix C gives a more detailed derivation of the magnetic field phase in tight-binding models.

The magnetic field has to be scaled to match the experimental regime and the reduced width of the simulated nanoribbons. The experimental magnetic fields are $B = 0.5\,\text{T}$, corresponding to a magnetic length of $l_B = \sqrt{\hbar/B_T} \sim 36\,\text{nm}$. The characteristic width of the experimental samples is of the order of µm in both width and contact spacing. The lengths of the system are then about 30 times the magnetic length l_B. In the calculations, the system is scaled down for numerical feasibility, and the magnetic field is proportionally increased. The magnetic length chosen for the transport calculations is $l_B = 4.7\,\text{nm}$, which corresponds to a magnetic field of 30 T. Compared to the characteristic lengths of the

system, the distance between the contacts is $L_v \sim 33 l_B$, while the width is an order of magnitude smaller, $W \sim 3 l_B$. Enlarging the width of the nanoribbon shifts the location of the bulk bands, which are not involved in the low-energy transport that generates the non-local currents, while the separation of the edge channels from the opposite sides of the nanoribbon is already fulfilled for the setup considered. On the other hand, the condition $L_v \gg W$, which ensures the non-local transport mediated by non-trivial evanescent modes, imposes a compromise on the system size in the transport calculations. To focus on the non-local transport results, the distance between the leads is chosen as the reference length for the calculations to match the experimental regime.

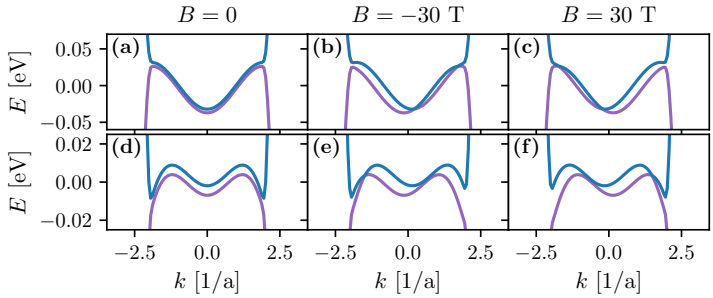

Figure 4.13: Dispersion relation for a zGNR of $W = 13.28\,\text{nm}$ as a function of the magnetic field. Panels (a)-(c) correspond to the model in equation (4.43) with $\delta = 0$; in (d)-(f) the complete model with the onsite edge correction δ given by the Hamiltonian (4.43) and the numerical values in table 4.1 is considered.

In figure 4.13 the dispersion relation for the fifth nearest-neighbour Hamiltonian (4.43) is plotted for the case without edge correction, i.e. $\delta = 0$, and for the full model. Both models show electron and hole pockets. In the case of $\delta \neq 0$ the pockets are on opposite sides of the 1BZ, while for $\delta = 0$ the pocket is centred around $k = 0$. By including the magnetic field, the $\delta \neq 0$ model shows a valley coupling with the magnetic field, which closes the gap for each of the pockets depending on the direction of the field. This valley coupling with the carrier type follows the experimental results. On the other hand, for $\delta = 0$ the dispersion does not display the correct symmetry exchange as a function of the magnetic field direction.

Finally, the non-local signal is computed in the same configuration of the experiment for the zGNR with on-site edge correction. The results are shown in figure 4.14 with colours and labels corresponding to the experimental data in figure 4.10. The non-local resistance peaks show a chiral behaviour with respect to the direction of the magnetic field, the measurement leads and the type of carrier. This is particularly apparent in panels

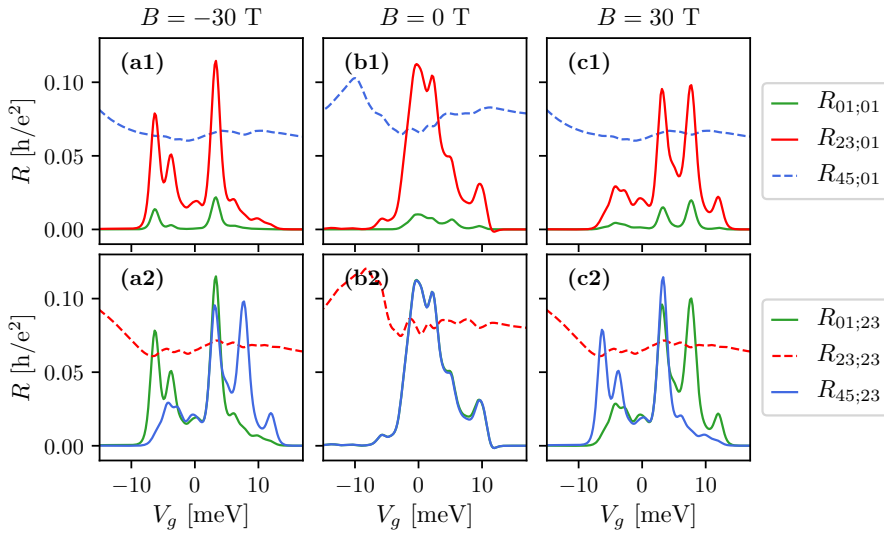

Figure 4.14: Calculated non-local resistance for the Hall bar depicted in figure 4.11 for magnetic fields $B = \pm 30\,\mathrm{T}$ and for $B = 0$. The colors and the labels match the experimental figure 4.10. The local signal R_{23} in the upper panels and R_{01} in the lower panels are multiplied by 0.05. Due to the spatial symmetry of the structure, the case of $R_{ij;45}$ is obtained by mirroring the first row of the figure, therefore it is not included in the plots. Temperature is set to $T = 5\,\mathrm{K}$.

(a2)-(c2), where the carrier type is inverted either by the magnetic field or by the relative direction of the measurement leads with respect to the current injector-collector axis. Although the model resembles the main symmetry features of the non-local signal measured experimentally, it is important to stress that the agreement is only qualitative. For example, a secondary peak near $V_g \simeq 3\,\mathrm{meV}$, resulting from the gap created by the staggered potential, is present in the calculations, while the experimental resistances show broader peaks. Indeed, a more accurate model that takes into account the details of the geometry of the double hBN is needed for a more quantitative result. Nevertheless, the presented results give a valuable insight in determining the minimal elements to correctly explain the non-local measurements in graphene nanoribbons.

4.4 Conclusions

In this chapter, graphene systems are introduced from the perspective of transport calculations in two main regimes: the e-e interaction problems

related to spin transport and the non-local signals in graphene encapsulated in hBN. The effect of the e-e interaction is treated by an unrestricted Hartree-Fock approximation, which allows the rotation of the spin. The mean-field approximation can be used to calculate the effective one-particle Hamiltonian for later implementation in transport calculations. In fact, the section mainly focuses on describing the application of an algorithm that calculates the mean-field contributions in a scattering region, taking into account the effect of the e-e interactions.

The zGNRs with first nearest neighbours graphene and the Kane-Mele-Hubbard model are studied in the presence of a monovacancy within the mean-field approximation. The transport results elucidate the effect of the non-magnetic vacancies in the spin-polarised current. Indeed, in the case of the Kane-Mele nanoribbon, the vacancy generates a local magnetic field that affects the spin transport by locally breaking TR symmetry. In this way, the spin-flipped conductance depends on the spin of the incoming current and the direction of propagation.

The second part of the chapter deals with the experimental measurements of reference [227] in graphene nanoribbons encapsulated between two hBN layers. The breaking of the inversion symmetry due to the hBN generates an anomalous velocity that leads to non-local peaks in the resistance. In addition, the signals show chiral behaviour as a function of the relative direction of the measurement leads with respect to the injector-collector leads and to the direction of the out-of-plane magnetic field. In this way, the nature of the charge carriers, holes or electrons, changes depending on these two elements.

Section 4.3 focuses on the correct modelling of the non-local signals by identifying the main symmetry properties to model the electron-hole pocket exchange as a function of the magnetic field. The non-local currents are obtained through the channels of the zigzag edges, which are dispersive for the long-range hopping Hamiltonian. The results qualitatively capture the symmetry properties of the experimental signals. The model used does not take into account the precise geometry of the double hBN layers. However, the transport calculations provide a valuable approximation to determine the main elements for understanding the measured non-local chiral currents.

5 IMPURITIES AND DISORDER IN TOPOLOGICAL INSULATORS

Preamble

The study of the effects of disorder is of primary importance in understanding the optical and transport properties of real solids beyond the ideal and periodic model Hamiltonians. In fact, in addition to interactions, realistic models should include disorder since real samples contain vacancies, impurities and other defects, so that the systems are not strictly periodic. In normal metals, strong disorder produces Anderson localisation, which turns the metal into an insulator. This was first demonstrated by Anderson's pioneering work on the absence of diffusion in random lattices [8]. Since then, different models of disorder have played a major role in understanding the transport properties of real solids with point defects.

In particular, the advent of topological and 2D Dirac materials has led to renewed interest in this topic. Disordered topological materials involve a new phenomenology due to the robustness provided by the topological protection, as well as by the linear dispersion. In general, in TIs the disorder drives a topological transition and renders the system trivial for magnetic [163] and non-magnetic impurities [190, 203, 318]. The role of disorder have been systematically addressed in experimental setups in TIs [37], finding hints of the crossover from diffusive transport to the Anderson localisation in slabs of $(Bi_{1-x}Sb_2)_2Te_3$ [150].

This chapter deals with the effect of a random distribution of non-magnetic impurities on the states formed at the surface of a TI described by a linear Dirac Hamiltonian. The interaction of the electrons with the impurities is accounted for by a separable pseudopotential method, which allows to obtain closed expressions for the density of states [58, 59, 88, 92, 136, 162, 251, 322]. The separable pseudopotential model allows us to obtain closed analytical expressions for the average Green's function. In particular, short-range potentials approaching the δ function limit, often used in previous work [22, 83, 133, 247], can be considered as limiting cases of the separable pseudo-potential model. The spectral properties of the surface states are evaluated by the Green's function averaged over disorder realisations [67, 91].

Apart from a first review of the methods and approximations employed

to compute the average Green's functions in disordered systems, the main point of the chapter is to compare two different self-consistent methods. These methods are the self-consistent Born approximation (SCBA) and the coherent potential approximation (CPA). The CPA is often considered to be the best single-site theory for studying the spectral properties of disordered systems [91, 290]. However, although numerous works use the SCBA to analyze the many-impurity scattering on the surface of a topological material and graphene-based systems [83, 101, 121, 133, 144, 184, 200, 229, 257], the CPA studies on the same problem are scarce in the literature [211, 212, 258], especially in the context of surface states of TIs. In this chapter, based on the published work [111], the SCBA and CPA are compared for a binary disorder in the effective model for the Dirac surface states of a 3D TI.

The chapter is organised as follows:

- In section 5.1 the formalism to describe the disorder is set up by defining a general Hamiltonian with a pseudo-separable potential. The problem is posed by using the retarded Green's functions of the averaged system considering different approximations.

- The first approximation to be introduced is the CPA in section 5.1.2. This approximation is obtained by imposing certain restrictions on the T-matrix of the effective medium.

- Next, section 5.1.3 derives more generally the Feynman rules for the averaged Green's function for the binary on-site disorder. The self-energy is presented in this section and it facilitates the definition of the different approximations by its diagrammatic representation. The self-energy enters the Green's function as a complex magnitude and gives a shift and a broadening of the spectral function as well as a modification of the poles of the Green's function.

- In the next sections other approximations are presented, such as the virtual crystal approximation (VCA) in section 5.1.4 and the SCBA in section 5.1.5. Both are defined by the Feynman diagrams at the level of the self-energy.

- Section 5.2 applies the formalism derived in section 5.1 to obtain the effective Green's function for a 2D Dirac linear spectrum corresponding to the surface states of a TI. The spectral properties are obtained in SCBA and CPA using the single-particle Green's function, and the two methods are compared in section 5.2.5.

- Finally, section 5.3 summarizes the main results of the chapter.

5.1 Effective models for disordered systems

In the following, the problem of describing a disordered system by an effective medium with the appropriate average Green's functions is formulated. An overview of the main approximations used in the literature is given and Feynman diagrams are introduced to illustrate the differences between the approximations.

5.1.1 General definitions

The Hamiltonian of a disordered system is generically expressed as

$$\mathcal{H} = \mathcal{H}_0 + \mathcal{V} \ , \tag{5.1}$$

where the term $\mathcal{H}_0$ describes the Hamiltonian in the absence of impurities and $\mathcal{V}$ is the potential due to the random distribution of point defects. For simplicity the potential is considered separable, such that the pseudopotential operator can be cast in the form [251, 322]

$$\mathcal{V} = \sum_n \mathcal{V}_n \ , \qquad \mathcal{V}_n = \mid \omega_n \rangle \lambda_n \langle \omega_n \mid \ , \tag{5.2}$$

where the index n runs over all sites $\boldsymbol{R}_n$ of the square lattice of impurities with lattice constant a. The $\omega(\boldsymbol{r} - \boldsymbol{R}_n) = \langle \boldsymbol{r} \mid \omega_n \rangle$ will be referred to as *shape function* and λ_n is the coupling constant. The lattice constant a do not correspond to the crystalline lattice. In fact, the lattice is related to the distribution of the impurities in the surface.

The Hamiltonian in equation (5.1) is expressed as the sum of the Hamiltonian $\mathcal{H}_0$ corresponding to the translationally invariant system and the impurities contribution given by the potential $\mathcal{V}$. The retarded Green's function operator for $\mathcal{H}_0$ is generally known, and it is given by

$$\mathcal{G}^0(z) = (z - \mathcal{H}_0)^{-1} \ , \tag{5.3}$$

where $z = E + i0^+$. On the other hand, the Green's function for the complete problem is defined by

$$\mathcal{G}(z) = (z - \mathcal{H})^{-1} \ . \tag{5.4}$$

By replacing the Hamiltonian (5.1) in the previous equation, a Dyson-like expression is obtained for the Green's function of the system with impurities:

$$\mathcal{G}(z) = \mathcal{G}^0(z) + \mathcal{G}^0(z) \ \mathcal{V} \ \mathcal{G}(z) \ , \tag{5.5}$$

which is equivalently written as a series expansion as

$$\mathcal{G}(z) = \mathcal{G}^0(z) + \mathcal{G}^0(z)\ \mathcal{V}\ \mathcal{G}^0(z) + \mathcal{G}^0(z)\ \mathcal{V}\ \mathcal{G}^0(z)\ \mathcal{V}\ \mathcal{G}^0(z) + \dots\ , \tag{5.6}$$

or as function of the T-matrix by

$$\mathcal{T}(z) \equiv \mathcal{V}\left[1 - \mathcal{G}^0(z)\ \mathcal{V}\right]^{-1}\ , \tag{5.7a}$$

$$\mathcal{G}(z) = \mathcal{G}^0(z) + \mathcal{G}^0(z)\ \mathcal{T}(z)\ \mathcal{G}^0(z)\ . \tag{5.7b}$$

By comparing equations (5.5) and (5.7b), $\mathcal{T}(z)$ is associated to the operation

$$\mathcal{T}(z)\ \mathcal{G}^0(z) = \mathcal{V}\ \mathcal{G}(z)\ . \tag{5.8}$$

In this way, by using equation (5.5), a Dyson-like equation is obtained for the T-matrix

$$\mathcal{T}(z) = \mathcal{V} + \mathcal{V}\ \mathcal{G}^0(z)\ \mathcal{T}(z)\ . \tag{5.9}$$

In the specific case of a separable potential (5.2), the T-matrix is written as a sum of the contributions from each site as

$$\mathcal{T}(z) = \sum \mathcal{V}_n\left[1 + \mathcal{G}^0(z)\mathcal{T}(z)\right] = \sum_n \mathcal{Q}_n(z)\ . \tag{5.10}$$

The terms $\mathcal{Q}_n$ do not correspond to the single site T-matrix, denoted by t_n. In $\mathcal{Q}_n$, multiple scattering events which in turns concern the same site are taken into account. In fact, the single site T-matrix is

$$t_n(z) = \mathcal{V}_n\left[1 - \mathcal{G}^0(z)\ \mathcal{V}_n\right]^{-1}\ . \tag{5.11}$$

The scattering operator $\mathcal{Q}_n$ is related to the single site t_n by [30]

$$\mathcal{Q}_n(z) = t_n(z)\left[1 + \mathcal{G}^0(z)\sum_{m\neq n}\mathcal{Q}_m(z)\right]\ . \tag{5.12}$$

Up to this point, a system with a given impurity distribution has been characterised. However, the purpose of this section is to describe the ensemble average system with impurities by means of effective models. Indeed, ensemble averaging is a powerful tool to describe the behaviour of perturbed systems by restoring translation invariance on average. The following section discusses an approximation for constructing the effective model from the T-matrix called CPA. After that, section 5.1.3 derives the Feynman rules for the averaged Green's function up to all orders. In this way, the other levels of approximation, such as the VCA and the SCBA, are derived from the diagrammatic contributions.

5.1.2 Coherent potential approximation

The CPA dates back to 1960s and has proved to be a successful mean-field theory for the study of various elementary excitations (electrons, phonons, excitons, magnons) in disordered systems [192, 256, 261, 276]. The CPA arises naturally from the previously introduced definitions by imposing the average conditions on the T-matrix combining two basic ideas. On the one hand, the averaged Green's function of the disordered system is calculated by introducing a periodic (translation invariant) effective medium. On the other hand, this effective medium is determined by requiring that the fluctuations of the Green's function average out to zero, leading to a self-consistency condition [67].

Firstly, the effective Hamiltonian in the separable pseudo-potential model is introduced by [88, 251]

$$\mathcal{H}_{\text{eff}} = \mathcal{H}_0 + \sum_n |\, \omega_n \,\rangle \lambda_{\text{CPA}}(z) \langle\, \omega_n \,|\ , \tag{5.13}$$

where $\lambda_{\text{CPA}}(z)$ is in general complex. The determination of the $\lambda_{\text{CPA}}(z)$ by self-consistent methods is the central problem in the CPA formalism.

The resolvent of the effective Hamiltonian is given by the Green's function of the effective medium that is a function of $\lambda_{\text{CPA}}(z)$ and it reads as

$$\mathcal{G}^{\text{eff}}(z) = (z - \mathcal{H}_{\text{eff}})^{-1}\ . \tag{5.14}$$

Note that, in contrast to the Hamiltonian of the disordered system (5.1) with $\mathcal{V}$ given by equation (5.2), the effective Hamiltonian $\mathcal{H}_{\text{eff}}$ has the full symmetry of the impurity lattice since $\lambda_{\text{CPA}}(z)$ is taken to be independent of the site. Therefore, the translation-invariance is restored in the effective Hamiltonian.

Next, the problem is expressed as a function of the difference between the translational invariant contribution (the effective Hamiltonian) and the complete problem including the impurities distribution such that

$$\mathcal{H} - \mathcal{H}_{\text{eff}} = \sum_n \mathcal{W}_n\ , \tag{5.15}$$

with

$$\mathcal{W}_n = |\, \omega_n \,\rangle \left[\lambda_n - \lambda_{\text{CPA}}(z)\right] \langle\, \omega_n \,|\ \ . \tag{5.16}$$

By formulating the problem over the difference in $\mathcal{W}_n$ and due to the translational invariance of $\mathcal{H}_{\text{eff}}$, the free propagator $\mathcal{G}^0$ can be replaced by the $\mathcal{G}^{\text{eff}}$ in equation (5.7b) leading to

$$\mathcal{G}(z) = \mathcal{G}^{\text{eff}}(z) + \mathcal{G}^{\text{eff}}(z)\ \mathcal{T}'(z)\ \mathcal{G}^{\text{eff}}(z)\ . \tag{5.17}$$

$\mathcal{T}'(z)$ is the operator $\mathcal{T}(z)$ for the potential associated to $\sum_n \mathcal{W}_n$.

$\mathcal{G}^{\text{eff}}(z)$ does not depend on the disorder configuration and it is not affected by the average. Hence, by taking the average of the previous expression and by demanding that the effective Green's function matches the averaged one, i.e. that $\langle \mathcal{G}(z) \rangle_{\text{av}} = \mathcal{G}^{\text{eff}}(z)$, the condition that the averaged value of the T-matrix cancels is obtained

$$\left\langle \mathcal{T}'(z) \right\rangle_{\text{av}} = 0 \ . \tag{5.18a}$$

From equations (5.10) and (5.12), we conclude that the T-matrix is a function of the t-matrix operator of a single site. The central assumption of the CPA is that the condition (5.18a) is equivalent to

$$\left\langle \mathcal{T}'(z) \right\rangle_{\text{av}} = 0 \overset{\text{CPA}}{\Longrightarrow} \langle t'_n(z) \rangle_{\text{av}} = 0 \ . \tag{5.18b}$$

The single-site t_n-matrix is obtained for $\mathcal{W}_n$ from equation (5.11) as

$$\begin{aligned} t'_n(z) &= \left[1 - \mathcal{W}_n \, \mathcal{G}^{\text{eff}}(z) \right]^{-1} \mathcal{W}_n = \sum_{m=0}^{\infty} \left[\mathcal{W}_n \, \mathcal{G}^{\text{eff}}(z) \right]^m \mathcal{W}_n \\ &= \frac{| \, \omega_n \, \rangle \, [\lambda_n - \lambda_{\text{CPA}}(z)] \, \langle \, \omega_n \, |}{1 - [\lambda_n - \lambda_{\text{CPA}}(z)] \, \langle \, \omega_n \, | \, \mathcal{G}^{\text{eff}}(z) \, | \, \omega_n \, \rangle} \ , \end{aligned} \tag{5.18c}$$

such that the CPA condition reads as [67, 91, 119]

$$\left\langle \frac{\lambda_n - \lambda_{\text{CPA}}(z)}{1 - [\lambda_n - \lambda_{\text{CPA}}(z)] \, \langle \, \omega_n \, | \, \mathcal{G}^{\text{eff}}(z) \, | \, \omega_n \, \rangle} \right\rangle_{\text{av}} = 0 \ . \tag{5.19}$$

The only approximation in CPA is the assumption in equation (5.18b). By averaging equation (5.10) and using the relation of $\mathcal{Q}_n$ in equation (5.12), this approximation is equivalent to neglecting the averaged term in the square brackets of equation (5.12). Physically, this is interpreted as disregarding the rescattering correction given by the subsequent scattering of an electron in the same impurity.

Finally, it is important to stress that the CPA condition (5.19) is an implicit equation for the λ_{CPA} due to the dependence of $\mathcal{G}^{\text{eff}}(z)$ on the coupling constant λ_{CPA}, in the denominator of (5.19).

5.1.3 Binary disorder: towards the Feynman rules for the average system of random impurities

In this section, the Feynman rules for the averaged Green's function are derived to relate the different approximations by diagrammatic representations. In order to write the expressions in a more compact way, it is

appropriate to consider a particular type of disorder. The case of onsite binary disorder is studied in this chapter. Binary disorder involves two different types of impurities, A and B, located in a lattice of constant a. In a 2D system, a square lattice is considered such that a given site is occupied by an impurity A with probability c or by an impurity B with probability $1-c$. The coupling constant λ_n takes two values, λ_A and λ_B, depending on the site. Again, the lattice with constant a is only related to the distribution of impurities on the surface. The probability distribution in this model is

$$\mathcal{P}(\lambda_n) = c\delta(\lambda_n - \lambda_A) + (1-c)\delta(\lambda_n - \lambda_B) \ . \tag{5.20}$$

λ_B acts as an energy offset. Therefore, the only significant magnitude is the energy difference between the two types of impurities given by

$$\Delta \equiv \lambda_A - \lambda_B \ . \tag{5.21}$$

Without loss of generality, in the following $\lambda_B = 0$ and the disorder is described by N_i impurities of type A with coupling constant Δ located at random lattice positions $\mathbf{R}_j$, where $j = 1 \dots N_i$. The number of impurities is related to the fraction c by

$$N_i = cN \ , \tag{5.22}$$

where N is the total number of sites in the lattice.

As already mentioned, it is very convenient to use the plane waves basis to formulate the problem. This is due to the translational invariance which is restored on average in the effective system and that is intrinsic to the system without impurities. In this basis, the Green's function of the pristine system is expressed as

$$\langle \mathbf{k}|\mathcal{G}^0(z)|\mathbf{k}'\rangle \equiv \mathcal{G}^0_{\mathbf{k}}(z)\delta_{\mathbf{k},\mathbf{k}'} = (z - E_{\mathbf{k}})^{-1}\delta_{\mathbf{k},\mathbf{k}'} \ , \tag{5.23}$$

where $E_{\mathbf{k}}$ denotes the energy of the state with momentum $\mathbf{k}$.

The Green's function of the disordered Hamiltonian, given by equation (5.6), is also written for convenience as a function of the momenta and in orders n of the scattering potential as [23]

$$\mathcal{G}_{\mathbf{k},\mathbf{k}'}(z) = \sum_{n=0}^{\infty} \mathcal{G}^{(n)}_{\mathbf{k},\mathbf{k}'}(z) \ , \tag{5.24}$$

where the n-th order is

$$\begin{aligned} \mathcal{G}^{(n)}_{\mathbf{k},\mathbf{k}'}(z) &\equiv \langle \mathbf{k}|\mathcal{G}^0(z)\left[\mathcal{V}\mathcal{G}^0(z)\right]^n|\mathbf{k}'\rangle \\ &= \sum_{q_1,\dots q_{n-1}} \langle \mathbf{k}|\mathcal{G}^0(z)|\mathbf{q}_{n-1}\rangle\langle \mathbf{q}_{n-1}|\mathcal{V}|\mathbf{q}_{n-2}\rangle \dots \langle \mathbf{q}_1|\mathcal{G}^0(z)|\mathbf{k}'\rangle \ . \end{aligned} \tag{5.25}$$

By considering that all type A impurities are described by the same coupling and shape function, the impurity potential (5.2) is given by the following non-local potential in the plane wave basis

$$\langle \mathbf{k}|\mathcal{V}|\mathbf{k}'\rangle = \Delta \sum_{j=1}^{N_i} \langle \mathbf{k}|\omega_j\rangle\langle\omega_j|\mathbf{k}'\rangle = \frac{\Delta}{V}\sum_{j=1}^{N_i} \omega(\mathbf{k})\omega^*(\mathbf{k}')e^{-i(\mathbf{k}-\mathbf{k}')\mathbf{R}_j} \ , \quad (5.26)$$

where the coupling constant is set to Δ and the sum is over the impurity sites.

To obtain equation (5.26), the following expression was employed

$$\langle \mathbf{k}|\omega_n\rangle = \frac{1}{\sqrt{V}}\,\omega(\mathbf{k})e^{-i\mathbf{k}\mathbf{R}_n} \ , \quad (5.27)$$

with $\omega(\mathbf{k})$ the Fourier transform of the function $\omega(\mathbf{r})$ and V the volume of the system.

Equation (5.25) can be then rewritten as

$$\mathcal{G}^{(n)}_{\mathbf{k},\mathbf{k}'}(z) = \frac{1}{V^n}\sum_{q_1,\dots q_{n-1}} \rho_{\mathbf{k}-\mathbf{q}_{n-1}}\cdots\rho_{\mathbf{q}_2-\mathbf{q}_1}\ \rho_{\mathbf{q}_1-\mathbf{k}'} \times \mathcal{G}^0_{\mathbf{k}}(z)U_{\mathbf{k},\mathbf{q}_{n-1}}\mathcal{G}^0_{\mathbf{q}_{n-1}}(z)\dots U_{\mathbf{q}_2,\mathbf{q}_1}\mathcal{G}^0_{\mathbf{q}_1}(z)U_{\mathbf{q}_1,\mathbf{k}'}\mathcal{G}^0_{\mathbf{k}'}(z) \ , \quad (5.28)$$

where the form factor is

$$U_{\mathbf{k},\mathbf{k}'} = \Delta\omega(\mathbf{k})\omega^*(\mathbf{k}') \ , \quad (5.29)$$

and the structure factor is $\rho_{\mathbf{k}} = \sum_{j=1}^{N_i} e^{-i\mathbf{k}\mathbf{R}_j}$. Note that each factor $\rho_{\mathbf{k}_i-\mathbf{k}_{i-1}}$ has an implicit internal sum over the impurities from its definition. The former expression can be interpreted as describing a propagating electron with incoming momentum $\mathbf{k}'$ having n scattering events given by $\rho_{\mathbf{q}}U_{\mathbf{q},\mathbf{q}'}$ until it leaves the system with momentum $\mathbf{k}$. Between the scattering events the electron propagates with the free propagator $\mathcal{G}^0(z)$ with momentum dictated by the conservation of momentum.

So far, the formalism has been developed for a particular configuration of impurities located at random positions of the impurity lattice. Hence, the averaging must be performed to obtain the results for the effective disordered system. In the specific case of the binary alloy described by the distribution (5.20) such that N_i impurities are located at the random sites $\{\mathbf{R}_\mathbf{j}\}_{j=1\dots N_j}$, the n-th order Green's function in equation (5.28) is averaged over the disorder realisations to extract the Feynman rules. The only term that depends on the position of the impurities is $\rho_{\mathbf{k}}$ and

equation (5.28) is averaged by

$$\left\langle \mathcal{G}^{(n)}_{\mathbf{k},\mathbf{k}'}(z) \right\rangle_{\mathrm{av}} = \frac{1}{V^n} \sum_{q_1,\dots q_{n-1}} \left\langle \rho_{\mathbf{k}-\mathbf{q}_{n-1}} \cdots \rho_{\mathbf{q}_2-\mathbf{q}_1} \rho_{\mathbf{q}_1-\mathbf{k}'} \right\rangle_{\mathrm{av}} \times \mathcal{G}^0_{\mathbf{k}}(z) U_{\mathbf{k},\mathbf{q}_{n-1}} \mathcal{G}^0_{\mathbf{q}_{n-1}}(z) \dots U_{\mathbf{q}_2,\mathbf{q}_1} \mathcal{G}^0_{\mathbf{q}_1}(z) U_{\mathbf{q}_1,\mathbf{k}'} \mathcal{G}^0_{\mathbf{k}'}(z) \ . \quad (5.30)$$

The averaging of the form factors is explicitly done in appendix E and leads to a conservation rule that dictates that the sum of all scattering momenta on the same impurity must be zero. In this way, the Feynman rules for the effective system are calculated and listed in table 5.1 in the approximation of $N_i \gg 1$. Averaging restores translation invariance, so the effective Green's function is diagonal in $\mathbf{k}$:

$$\left\langle \mathcal{G}_{\mathbf{k},\mathbf{k}'}(z) \right\rangle_{\mathrm{av}} = \delta_{\mathbf{k},\mathbf{k}'} \ \mathcal{G}^{\mathrm{av}}_{\mathbf{k}}(z) \ . \quad (5.31)$$

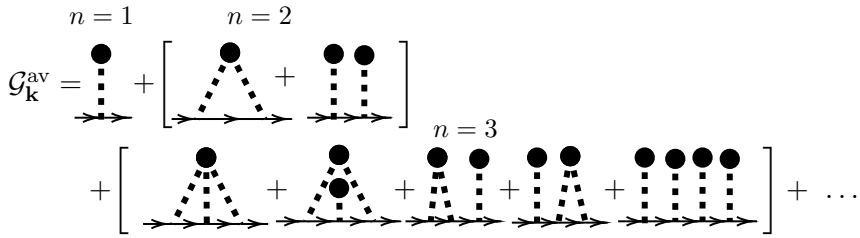

Figure 5.1: Diagrammatic representation of $\mathcal{G}^{\mathrm{av}}_{\mathbf{k}}$ up to $n = 3$.

The former derivation is valid for any shape function and it is therefore suitable for the study of finite-range impurity potentials. However, particularly simple expressions are found for point-like impurities located in a lattice with constant a. In this case, $\omega(\mathbf{k})$ becomes independent of $\mathbf{k}$. Since the resulting integral is divergent at large momenta, a momentum cutoff k_{c} is imposed (or, equivalently, a finite bandwidth is introduced) leading to

$$\omega(\mathbf{k}) = \omega(k) = a\Theta(k_{\mathrm{c}} - k) \ , \quad (5.32)$$

where Θ is the Heaviside step function, and the impurity lattice constant a is introduced for convenience.

The assumption of point impurities, although approximated, is widely used in the context of continuous models. It should be emphasised, however, that the pseudo-potential model employed in this chapter does not require this assumption, and more structured electron-impurity potentials can be treated on the same footing. In particular, lattice distortion around the impurity site can be accounted for by setting a finite-range function $\omega(\boldsymbol{r})$.

Diagram elements:

- ▪▪▪▪▪ $= U_{\mathbf{q},\mathbf{q}'}$ denotes the scattering amplitude (i.e. the magnitude of the disorder)
- ● $= n_i\ \delta_{0,\mathbf{q}}$ denotes the vertex of the momentum-conserved interaction with the impurity, with $n_i = N_i/V$ and V the volume of the system
- ⟶ $= \mathcal{G}^0_{\mathbf{q}}(z)$ denotes the free propagator
- ⟹ $= \mathcal{G}^{\text{av}}_{\mathbf{q}}(z)$ denotes the averaged effective propagator

Feynman rules for constructing the n-th order averaged propagator

1. Draw p impurities, being $1 \leq p \leq n$.
2. Draw n scattering lines such that the p impurities are connected in all inequivalent combinations.
3. Connect the n lines by $n-1$ integral propagators $\mathcal{G}^0_{\mathbf{q}}$ such that $\mathbf{q}$ is an internal momentum that fulfils momentum conservation in each impurity. Perform the sum $\frac{1}{V}\sum_{\mathbf{q}_j}$ over the internal momenta $\mathbf{q_j}$.
4. Add the external propagators $\mathcal{G}^0_{\mathbf{k}}$ and $\mathcal{G}^0_{\mathbf{k}'}$.

Table 5.1: Feynman rules for the effective Green's functions for constructing the n-th order averaged propagator.

Definition of the self-energy

Figure 5.1 shows the diagrams for $n \leq 3$ for $\mathcal{G}^{\text{av}}$. The treatment of the whole $\mathcal{G}^{\text{av}}$ up to all orders is a complex problem due to the intricate nesting that occurs for higher n, as shown in the selected diagrams in figure 5.1. This problem is shortened by defining the self-energy Σ, which contains only the irreducible diagrams without the external propagators in $\mathcal{G}^{\text{av}}$. The irreducible diagrams are defined such that they cannot be obtained by cutting an internal line. In the diagrammatic representation,

the self-energy is defined as

$$\Sigma_{\mathbf{k}}(z) =$$ 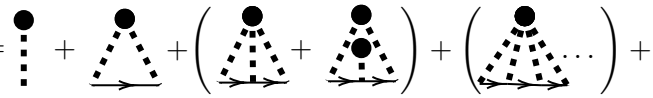 $$+ \ \ldots \ .$$ (5.33)

The self-energy is related to $\mathcal{G}^{\text{av}}$ by

$$\mathcal{G}^{\text{av}}_{\mathbf{k}}(z) = \mathcal{G}^{0}_{\mathbf{k}}(z) + \mathcal{G}^{0}_{\mathbf{k}}(z)\ \Sigma_{\mathbf{k}}(z)\ \mathcal{G}^{\text{av}}_{\mathbf{k}}(z)\ , \tag{5.34}$$

which is the Dyson equation as a function of $\Sigma_{\mathbf{k}}(z)$. The former expression is readily solved by

$$\mathcal{G}^{\text{av}}_{\mathbf{k}}(z) = \frac{1}{(\mathcal{G}^{0}_{\mathbf{k}}(z))^{-1} - \Sigma_{\mathbf{k}}(z)} = \frac{1}{z - E_{\mathbf{k}} - \Sigma_{\mathbf{k}}(z)}\ . \tag{5.35}$$

By the definition of $\mathcal{G}^{0}$, the average Green's function reads as

$$\mathcal{G}^{\text{av}}_{\mathbf{k}}(z) = \mathcal{G}^{0}_{\mathbf{k}}(z - \Sigma_{\mathbf{k}})\ . \tag{5.36}$$

Thus the problem of solving the averaged propagator $\mathcal{G}^{\text{av}}(z)$ is reduced to the calculation of the self-energy $\Sigma_{\mathbf{k}}(z)$.

From equation (5.36), the self-energy can be considered as an additive correction to the unperturbed energy $E_{\mathbf{k}}$. The self-energy is complex valued: the real part accounts for an energy shift and the imaginary part can be interpreted as the inverse of the lifetime of the quasiparticles given by the scattering. The imaginary part of the self-energy is inversely proportional to the level broadening of the spectral functions from a standard delta shape for the free electrons to a Lorentzian.

Although the self-energy simplifies the diagrammatic representation of the averaged propagator by including all irreducible diagrams, it cannot be calculated exactly, and various approximations of different degrees of sophistication are employed. Such approximations are usually defined either at the level of the diagrammatic scattering contributions or by imposing a self-consistent condition on the T-matrix, such as the CPA discussed earlier.

By comparing equation (5.36) with the Green's function for the effective Hamiltonian within CPA (5.14) and following the same steps of equation (5.35), the coupling constant obtained within CPA can be related to the self-energy by projecting onto the plane waves basis:

$$\Sigma^{\text{CPA}}_{\mathbf{k}}(z) = \lambda_{\text{CPA}}(z)\ \frac{|\omega(\mathbf{k})|^2}{a^2}\ . \tag{5.37}$$

In this way, the coupling constant of the CPA is proportional to the corresponding self-energy and has the same physical interpretation in terms of the energy shift and level broadening.

In the following sections, the VCA and the SCBA are introduced from their definition within the self-energy contributions in the diagrammatic description.

5.1.4 Virtual crystal approximation

The lowest order of the self-energy defined in equation (5.33) is given by the single scattering line with one impurity and it is known in the literature as VCA. The self-energy is given by

$$\Sigma_{\mathbf{k}}^{\mathrm{VCA}} = \quad = n_i U_{\mathbf{k},\mathbf{k}} \ , \tag{5.38}$$

where $n_i = N/V$ with $V = Na^2$ the volume of the system, i.e. the area in the case of a 2D system. The area is determined by the size of the unit cell a^2 times the number of sites in the system, this leads to $n_i = c/a^2$. The zero momentum exchange in the previous expression is due to the conservation of momentum in the single scattering point. The self-energy in the VCA is energy independent, so the self-energy only shifts the energy levels. In fact, replacing the results in (5.34), the effective propagator can be solved by

$$\mathcal{G}_{\mathbf{k}}^{\mathrm{VCA}}(z) = \frac{1}{z - (E_{\mathbf{k}} + \Sigma_{\mathbf{k}}^{\mathrm{VCA}})} \ . \tag{5.39}$$

where $E_{\mathbf{k}}$ are the energies of $\mathcal{H}_0$.

For the binary disorder model given by the distribution (5.20), the VCA is obtained by

$$\Sigma_{\mathbf{k}}^{\mathrm{VCA}} = c\Delta \ \frac{|\omega(\mathbf{k})|^2}{a^2} \ . \tag{5.40}$$

The VCA is equivalently derived by averaging at the level of the coupling constants, leading to

$$\lambda_{\mathrm{VCA}} \equiv \langle \lambda_n \rangle_{\mathrm{av}} = c\Delta \ . \tag{5.41a}$$

The VCA self-energy is then

$$\Sigma_{\mathbf{k}}^{\mathrm{VCA}} = \lambda_{\mathrm{VCA}} \ \frac{|\omega(\mathbf{k})|^2}{a^2} \ . \tag{5.41b}$$

The VCA is a reasonably good description only if $c \to 0$ and $\lambda_{\mathrm{A}} \simeq \lambda_{\mathrm{B}}$. More elaborated, self-consistent methods have a much wider range of validity. Within these methods, the VCA appears usually as a first constant term in the expansion of the Green's function.

5.1.5 Self-consistent Born approximation

The SCBA considers single and double scattering with one impurity. The approximation is self-consistent because the propagator between the two scattering events is the effective $\mathcal{G}^{\text{eff}}(z)$ instead of the unperturbed $\mathcal{G}^{0}(z)$. Diagramatically, the SCBA reads as

$\Sigma^{\text{SCBA}}_{\mathbf{k}}(z) =$  . (5.42)

From the Feynman rules, the analytic expression for the self-energy in the basis of the plane waves is given by the diagonal contribution

$$\Sigma^{\text{SCBA}}_{\mathbf{k}}(z) = \Sigma^{\text{VCA}}_{\mathbf{k}} + n_i \frac{1}{V} \sum_{\mathbf{q}} U_{\mathbf{k},\mathbf{q}} \mathcal{G}^{\text{eff}}_{\mathbf{q}}(z) U_{\mathbf{q},\mathbf{k}} \ . \tag{5.43}$$

The contribution of the self-energy enters in the Green's function operator of the effective medium as

$$\mathcal{G}^{\text{eff}}_{\mathbf{k}}(z) = \mathcal{G}^{0}_{\mathbf{k}} \left[z - \Sigma^{\text{SCBA}}_{\mathbf{k}}(z) \right] \ . \tag{5.44}$$

In this way, equation (5.43) is a self-consistent expression for the determination of the self-energy. In the case of the separable pseudo-potential model with the binary disorder (5.20) it reads as

$$\begin{aligned} \Sigma^{\text{SCBA}}_{\mathbf{k}}(z) = & \frac{|\omega(\mathbf{k})|^2}{a^2} \lambda_{\text{VCA}} \\ & + \int \frac{\mathrm{d}^2\mathbf{q}}{4\pi^2} \, c\Delta^2 \frac{|\omega(\mathbf{k})\,\omega(\mathbf{q})|^2}{a^2} \, \mathcal{G}^{0}_{\mathbf{q}}\big[z - \Sigma^{\text{SCBA}}_{\mathbf{q}}(z) \big] \ . \end{aligned} \tag{5.45}$$

For convenience, the self-energy is defined as the product of an effective coupling constant $\lambda_{\text{SCBA}}(z)$ and the shape function $\omega(\mathbf{k})$ as follows

$$\Sigma^{\text{SCBA}}_{\mathbf{k}}(z) = \lambda_{\text{SCBA}}(z) \, \frac{|\omega(\mathbf{k})|^2}{a^2} \ . \tag{5.46a}$$

Therefore, equation (5.45) is written for the effective coupling constant as

$$\begin{aligned} \lambda_{\text{SCBA}}(z) = & \lambda_{\text{VCA}} \\ & + c\Delta^2 \int \frac{\mathrm{d}^2\mathbf{k}}{4\pi^2} \, |\omega(\mathbf{k})|^2 \, \mathcal{G}^{0}_{\mathbf{k}} \left[z - \lambda_{\text{SCBA}}(z) \frac{|\omega(\mathbf{k})|^2}{a^2} \right] \ . \end{aligned} \tag{5.46b}$$

5.2 Disorder in the surface states of a TI

5.2.1 Theoretical model

In this section, the SCBA and CPA formalism are applied to the 2D surface states of a 3D TI. The pristine Hamiltonian of the system is denoted as $\mathcal{H}_0$ and it is diagonal in the basis of plane waves

$$\langle \mathbf{k} \mid \mathcal{H}_0 \mid \mathbf{k}' \rangle = \mathcal{H}_0(\mathbf{k})\, \delta_{\mathbf{k},\mathbf{k}'} \ , \tag{5.47a}$$

with

$$\mathcal{H}_0(\mathbf{k}) = \hbar v \left(\sigma_x k_y - \sigma_y k_x\right) \ , \tag{5.47b}$$

where σ_x and σ_y are Pauli matrices and $\mathbf{k} = (k_x, k_y)$ is the in-plane momentum. This Hamiltonian is obtained by considering only the linear Dirac cone in expression (1.43). v is a matrix element having dimensions of velocity and it is related to the bulk spectrum parameters by equation (1.44c). For example, $v = 4 \times 10^5\,\mathrm{m/s}$ for Bi_2Te_3 [38] and $v = 5 \times 10^5\,\mathrm{m/s}$ for Bi_2Se_3 [298].

The bands of $\mathcal{H}_0$ are the Dirac cone given by $E_{\mathbf{k}} = \pm\hbar v|\mathbf{k}|$. Note that this two-band model is restricted to the study of a single Dirac cone and neglects intervalley scattering as well as the contribution of non-linear terms in momentum. The bulk bands are not included and the regime studied is limited to the case of disorder that modifies the spectrum but does not collapse the bulk gap. The results shown are valid as long as the 2D effective model holds. Although the model is introduced to describe the surface states of a TI, it is important to stress that the results shown here can be easily extended to any 2D material where the electron dynamics is described by the massless Dirac equation, such as graphene.

In addition to the continuum model of the Dirac cone, the impurities are introduced on the surface of the TI and they are described within the formalism of the previous section. The impurities are assumed to be on a regular square lattice of parameter a, which does not depend on the size of the unit cell of the crystal structure of the TI, but on the spatial distribution of the disorder. In fact, the electrons do not *see* the crystal structure, since a continuous approximation is used for the Hamiltonian (5.47b). The disorder studied is of the binary type with a probability distribution given by equation (5.20).

For the Dirac model, the retarded Green's function operator for $\mathcal{H}_0$ is

$$\langle \mathbf{k} \mid \mathcal{G}^0(z) \mid \mathbf{k}' \rangle = \mathcal{G}^0_{\mathbf{k}}(z)\, \delta_{\mathbf{k},\mathbf{k}'} \ , \tag{5.48a}$$

with

$$\mathcal{G}^0_{\mathbf{k}}(z) = \frac{1}{z - \mathcal{H}_0(\mathbf{k})} = \frac{z + \mathcal{H}_0(\mathbf{k})}{z^2 - \hbar^2 v^2 k^2} \ . \tag{5.48b}$$

Density of states

As mentioned in the previous section, the main point of this chapter is to calculate the ensemble average of the Green's function operator in the disordered medium, i.e. $\mathcal{G}^{\text{av}}$. The conceptually simplest way to find an approximation to $\mathcal{G}^{\text{av}}$ is to introduce an effective translation invariant medium represented by a Green's function operator $\mathcal{G}^{\text{eff}}$ such that $\mathcal{G}^{\text{eff}} = \mathcal{G}^{\text{av}}$ up to a certain approximation.

Once the effective Green's function is determined, important physical quantities can be calculated. In particular, the average DOS per unit area can be easily obtained from the following expression

$$\rho(E) = -\frac{1}{\pi S}\,\text{Im}\left[\,\text{Tr}\left(\mathcal{G}^{\text{eff}}(E + i0^{+})\right)\right] , \tag{5.49}$$

where the trace is performed over the states and Im denotes the imaginary part. For simplicity $S = 1$ and $\rho(E)$ is referred as the DOS hereafter.

In the case of the 2D effective Hamiltonian (5.47b), this expression is written as

$$\rho(E) = -\frac{1}{\pi}\,\text{Im}\sum_{\tau=\pm1}\int \frac{\mathrm{d}^2\mathbf{k}}{4\pi^2}\,\frac{1}{E + i0^{+} - \tau\hbar v k - \Sigma_{\mathbf{k}}(E)} , \tag{5.50}$$

where $\Sigma_{\mathbf{k}}$ is the self-energy calculated within a given approximation. The summation over $\tau = \pm 1$ comes from the two bands of the dispersion relation.

For the binary disorder model with $\omega(\mathbf{k})$ given by equation (5.32) and the three approximations considered, i.e. VCA, SCBA and CPA, the self-energy is proportional to the effective coupling constant by

$$\Sigma_{\mathbf{k}}(z) = \lambda(z)\,\frac{|\omega(\mathbf{k})|^2}{a^2} , \tag{5.51}$$

where Σ refers either to Σ_{VCA}, Σ_{SCBA} or Σ_{CPA} as well as the λ refers to λ_{VCA}, λ_{SCBA} or λ_{CPA}. Next, it is interesting to express the effective coupling constant in its real and imaginary parts and evaluate it by substituting $z \to E + i0^{+}$

$$\lambda(E) = \alpha(E) - i\Gamma(E) , \tag{5.52}$$

where $\alpha(E)$ and $\Gamma(E)$ are real. Due to the proportionality of the coupling constant and the self-energy (5.51), the physical states with a finite lifetime correspond to the solutions of the coupling constant with negative imaginary part, i.e. with $\Gamma(E) > 0$. By writing the energy in units of

$\hbar v_F/a$ and using the definitions in equation (5.52), the DOS reads as

$$\rho(E) = \frac{1}{4\pi^2}\Bigg\{\Gamma \ln\big[M(E)\big] + 2(E-\alpha)\Bigg[\arctan\left(\frac{E_c+\alpha-E}{\Gamma}\right) - \arctan\left(\frac{E_c-\alpha+E}{\Gamma}\right) + 2\arctan\left(\frac{E-\alpha}{\Gamma}\right)\Bigg]\Bigg\} + \frac{1}{2\pi}E\big[\Theta(E-E_c)+\Theta(E+E_c)-1\big]\ , \tag{5.53a}$$

where

$$M(E) = \frac{\left[(E_c-\alpha+E)^2+\Gamma^2\right]\left[(E_c+\alpha-E)^2+\Gamma^2\right]}{\left[\Gamma^2+(\alpha-E)^2\right]^2}\ . \tag{5.53b}$$

For the sake of simplicity, in the former expression, the dependence on E in $\alpha \equiv \alpha(E)$ and $\Gamma \equiv \Gamma(E)$ was omitted. The cut-off in energy is related to the momentum cut-off k_c as

$$E_c \equiv \hbar v k_c\ . \tag{5.54}$$

Thus, by determining the effective coupling constant within the different approximations, the self-energy and the DOS are calculated directly by equations (5.51) and (5.53a), respectively.

5.2.2 VCA in the linear Dirac model

The VCA takes into account an energy shift by averaging at the level of the coupling constant. The λ_{VCA} is then given by equation (5.41a) for all models, independently of the Hamiltonian of the pristine system. The coupling constant has no imaginary part in the VCA and the DOS at low energy corresponds to the pristine Dirac cone upon an energy shift:

$$\rho(\overline{E}) = \frac{1}{2\pi}|\overline{E}|\ , \tag{5.55}$$

where the shifted energy is defined as

$$\overline{E} \equiv E - \lambda_{\mathrm{VCA}}\ . \tag{5.56}$$

5.2.3 SCBA in the linear Dirac model

The SCBA is determined by the self-consistent equation (5.46b). In this expression, the propagator in the integral over the internal momenta is

given by the effective Green's function within the SCBA. The effective Green's function is related to the pristine Green's function $\mathcal{G}^0$ by the self-energy correction (5.36). However, since $\mathcal{H}_0(\mathbf{k})$ in the numerator of $\mathcal{G}^0$ in the Dirac model (5.48b) is an odd function of the momentum, the corresponding integration vanishes, leading to

$$\frac{\overline{\lambda}_{\mathrm{SCBA}}(\overline{z})}{c\Delta^2} = \mathcal{F}\left[\overline{z} - \overline{\lambda}_{\mathrm{SCBA}}(\overline{z})\right] \ , \tag{5.57a}$$

where the function $\mathcal{F}$ is particularised for the Dirac Hamiltonian as

$$\mathcal{F}(z) = \frac{a^2}{4\pi}\int_0^{k_c} \mathrm{d}k\, k \left(\frac{1}{z+\hbar v k} + \frac{1}{z-\hbar v k}\right) \ . \tag{5.57b}$$

In the former expressions the energy and coupling constant are expressed in terms of the λ_{VCA} (5.41a). This way the shifted coupling constant in SCBA is $\overline{\lambda}_{\mathrm{SCBA}}(\overline{z}) \equiv \lambda_{\mathrm{SCBA}}(z) - \lambda_{\mathrm{VCA}}$ and $\overline{z} \equiv z - \lambda_{\mathrm{VCA}}$.

In the SCBA equation (5.57a), apart from the λ_{VCA} included in the shifted energy and coupling constant, the SCBA depends on a single parameter related to the disorder, namely $c\Delta^2$. It is therefore convenient to express the SCBA condition as a function of a *disorder parameter* β, defined as follows

$$\beta \equiv \frac{c\Delta^2 a^2}{4\pi(\hbar v)^2} \ . \tag{5.58}$$

By expressing the energies in units of $\hbar v/a$, equation (5.57a) can be cast as a function of the dimensionless disorder parameter β and the energy cut-off E_c (5.54) as

$$\overline{\lambda}_{\mathrm{SCBA}} = \beta\ (\overline{E} - \overline{\lambda}_{\mathrm{SCBA}}) \ln\left[\frac{(\overline{E} - \overline{\lambda}_{\mathrm{SCBA}})^2}{(\overline{E} - \overline{\lambda}_{\mathrm{SCBA}})^2 - E_c^2}\right] \ , \tag{5.59}$$

where it is understood that $\overline{\lambda}_{\mathrm{SCBA}} \equiv \overline{\lambda}_{\mathrm{SCBA}}(\overline{E})$.

Next, it is interesting to discuss the symmetry properties of this equation by explicitly separating the real and imaginary parts of the effective coupling constant:

$$\overline{\lambda}(\overline{E}) \equiv \overline{\alpha}(\overline{E}) - i\Gamma(\overline{E}) \ , \tag{5.60}$$

where $\overline{\alpha} \equiv \alpha - \lambda_{\mathrm{VCA}}$ while Γ is the same of equation (5.52). Due to the properties of the complex logarithm, equation (5.59) is invariant under the exchange $(\overline{\alpha}, \Gamma, \overline{E}) \to (-\overline{\alpha}, \Gamma, -\overline{E})$. Hence, the real part of the effective coupling constant is an odd function of the shifted energy, $\overline{\alpha}_{\mathrm{SCBA}}(\overline{E}) = -\overline{\alpha}_{\mathrm{SCBA}}(-\overline{E})$, while the imaginary part is an even function, $\Gamma_{\mathrm{SCBA}}(\overline{E}) = \Gamma_{\mathrm{SCBA}}(-\overline{E})$.

Considering the symmetry properties of the equation, the SCBA equation (5.59) can be solved explicitly in the case of $\overline{E} = 0$. The real

part of the coupling constant must vanish at $\overline{E} = 0$ and by replacing $\overline{\lambda}_{\mathrm{SCBA}} \to -i\Gamma_{\mathrm{SCBA}}$, the self-consistent condition reduces to

$$-\frac{1}{\beta} = \ln\left[\frac{\Gamma^2_{\mathrm{SCBA}}(\overline{E}=0)}{E_c^2 + \Gamma^2_{\mathrm{SCBA}}(\overline{E}=0)}\right] , \tag{5.61}$$

whose solution leads to the coupling constant for $\overline{E} = 0$ given by

$$\overline{\alpha}_{\mathrm{SCBA}}(\overline{E}=0) = 0 , \qquad \Gamma_{\mathrm{SCBA}}(\overline{E}=0) = E_c \exp\left(\frac{1}{2} - \frac{1}{2\beta}\right) . \tag{5.62}$$

This exponential behaviour is opposite to the case of single-node WSMs studied in reference [133], where a critical point signals a disorder-induced phase transition. In the Dirac-like Hamiltonian (5.47b), no critical behaviour is observed as a function of the magnitude of disorder, as discussed later.

The SCBA self-consistent equation can be solved analytically also in the limit of $|\overline{E}| \ll E_c$ and small disorder $\beta \ll 1$. In this case, the coupling constant fulfils $|\overline{\lambda}_{\mathrm{SCBA}}(\overline{E})| \ll E_c$. Therefore, the SCBA equation (5.57a) is expanded as

$$\overline{\lambda}_{\mathrm{SCBA}} \simeq \beta(\overline{E} - \overline{\lambda}_{\mathrm{SCBA}}) \ln\left[-\frac{(\overline{E} - \overline{\lambda}_{\mathrm{SCBA}})^2}{E_c^2}\right] , \tag{5.63}$$

where $\overline{\lambda}_{\mathrm{SCBA}} \equiv \overline{\lambda}_{\mathrm{SCBA}}(\overline{E})$. Considering solutions with $\mathrm{Im}(\overline{\lambda}_{\mathrm{SCBA}}) < 0$, the following expression is obtained

$$\overline{\lambda}_{\mathrm{SCBA}}(\overline{E}) \simeq \overline{E}\left\{1 - \frac{1}{2\beta}\left[\mathcal{W}\left(-i\,\frac{\overline{E}}{2\beta E_c}\, e^{1/(2\beta)}\right)\right]^{-1}\right\} , \tag{5.64}$$

where $\mathcal{W}(x)$ is the Lambert-W function [46]. This approximate solution resembles the exact case at $\overline{E} = 0$ for small β, as expected.

5.2.4 CPA in the linear Dirac model

The CPA formulated in section 5.1.2 leads to expression (5.19) for the determination of the λ_{CPA} of the effective model. However, the equation is general and the term $\langle \omega_n \,|\, \mathcal{G}^{\mathrm{eff}}(z)|\, \omega_n\rangle$ in the denominator has to be specified for the shape function employed. The derivation of this term for the shape function given by equation (5.32) is discussed in appendix F leading to

$$\langle \omega_n \,|\, \mathcal{G}^{\mathrm{eff}}(z)|\, \omega_n\rangle = \int \frac{\mathrm{d}^2\mathbf{k}}{4\pi^2} |\omega(\mathbf{k})|^2\, \mathcal{G}^0_{\mathbf{k}}\left[z - \lambda_{\mathrm{CPA}}(z)|\omega(\mathbf{k})|^2/a^2\right] . \tag{5.65}$$

It is worth mentioning that $\langle \omega_n \mid \mathcal{G}^{\text{eff}}(z) \mid \omega_n \rangle$ becomes site independent since the effective medium in translationally invariant. Thus, the ensemble average for the binary disorder (5.20) poses no problem and (5.19) is averaged by

$$\frac{c}{\lambda_{\text{B}} - \lambda_{\text{CPA}}(z)} + \frac{1-c}{\lambda_{\text{A}} - \lambda_{\text{CPA}}(z)} = \int \frac{\mathrm{d}^2\mathbf{k}}{4\pi^2} |\omega(\mathbf{k})|^2 \, \mathcal{G}^0_{\mathbf{k}} \left[z - \lambda_{\text{CPA}}(z) |\omega(\mathbf{k})|^2 / a^2 \right] . \quad (5.66)$$

The above expression is valid for any shape function. In particular, in the case of point-like impurities (5.32), it is obtained

$$\frac{c}{\lambda_{\text{B}} - \lambda_{\text{CPA}}(z)} + \frac{1-c}{\lambda_{\text{A}} - \lambda_{\text{CPA}}(z)} = \mathcal{F}\left[z - \lambda_{\text{CPA}}(z) \right] , \quad (5.67)$$

where $\mathcal{F}(z)$ is defined in (5.57b). Once more, it is more convenient to express the left-hand side of equation (5.67) in terms of the coupling constant obtained within the VCA (5.41a) by defining

$$\overline{\lambda}_{\text{CPA}}(\overline{z}) \equiv \lambda_{\text{CPA}}(z) - \lambda_{\text{VCA}} , \quad (5.68)$$

whence

$$\frac{\overline{\lambda}_{\text{CPA}}(\overline{z})}{\left[c\Delta + \overline{\lambda}_{\text{CPA}}(\overline{z}) \right] \left[(1-c)\Delta - \overline{\lambda}_{\text{CPA}}(\overline{z}) \right]} = \mathcal{F}\left[\overline{z} - \overline{\lambda}_{\text{CPA}}(\overline{z}) \right] , \quad (5.69)$$

where $\Delta = \lambda_{\text{A}} - \lambda_{\text{B}}$, as previously defined.

By writing the coupling constant as real and imaginary parts, see equation (5.52), the self-consistent CPA equation (5.69) is invariant under the exchange $(\overline{\alpha}, \Gamma, \overline{E}, c) \to (-\overline{\alpha}, \Gamma, -\overline{E}, 1-c)$ and $(\Delta, c) \to (-\Delta, 1-c)$. Therefore, the parameter space can be restricted to $\Delta > 0$ and $0 \leq c < 0.5$, since all the other scenarios are derived from the first parameter sets.

Finally, note that the SCBA is obtained by expanding the self-consistent CPA equation given by (5.69). This can be achieved by solving for $\overline{\lambda}_{\text{CPA}}(\overline{z})$ and expanding the result in a Taylor series for small c and Δ up to the third order

$$\overline{\lambda}_{\text{CPA}}(\overline{z}) = c\Delta^2 \mathcal{F}\left[\overline{z} - \overline{\lambda}_{\text{CPA}}(\overline{z}) \right] + \mathcal{O}(c^2, \Delta^3) . \quad (5.70)$$

Therefore, the SCBA equation (5.57a) is obtained from the truncation of the CPA series. This is further clarified in the diagrammatic formalism with Feynman rules. On the one hand, the SCBA takes into account the two irreducible diagrams in equation (5.42). The first diagram is the constant VCA term, while the second describes the double scattering

from a single impurity with a dressed internal propagator. On the other hand, the CPA sums all diagrams with any number of scattering events on the same impurity. These diagrams are called wigwams because of their tent-like appearance, and after a proper re-summation [68] they give the self-consistent equation (5.69). Therefore, the CPA self-energy is expressed diagrammatically as

$$\Sigma_{\mathbf{k}}^{\mathrm{CPA}}(z) =$$ 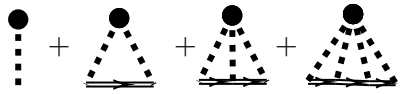 $$+ \dots ,$$ (5.71)

where the first two contributions match the SCBA.

5.2.5 Comparison between SCBA and CPA

In this section, the results of the two self-consistent approximations are compared. First, the comparison is presented at the level of the self-energies and later for the resulting DOS.

Self-energy comparison

As already discussed in sections 5.2.3 and 5.2.4, the SCBA equation (5.59) and the CPA equation (5.69) have specific symmetry properties related to the disorder parameters c and Δ and the energy $\overline{E}$. However, the symmetry properties of the two self-consistent equations are not the same. This is due to the truncation of the series expansion of the CPA to obtain the SCBA, which is visually clear in the Feynman diagrams in equations (5.42) and (5.71).

When considering $\lambda_{\mathrm{B}} = 0$, the symmetry $(\Delta, c) \to (-\Delta, 1-c)$ is a physical consequence of the particle-hole symmetrical spectrum due to the swapping of the roles of the impurity sites A and B. However, in SCBA the symmetry $(\Delta, c) \to (-\Delta, 1-c)$ is lost as soon as the higher order terms in c are neglected when taking the limit of $c \to 0$. In fact, to study the range $c \geq 0.5$, the expansion of CPA to obtain SCBA in equation (5.70) must be performed around $1-c$ instead of c. Therefore, the SCBA expression in equation (5.57a) can only be used for $0 \leq c < 0.5$.

Closely related to this issue is the reduction of disorder parameters in the SCBA. As already mentioned, the SCBA can be written as a function of a single β disorder parameter defined in equation (5.58). The CPA, on the other hand, requires both c and Δ separately and this ensures the correct behaviour in the limit of the exchange of sites A and B.

Due to the truncation shown in equation (5.70), an artificial symmetry in energy is generated in the SCBA self-energy, resulting in a symmetric

DOS. This symmetry, already reported in the literature [83, 115, 249], is due to the presence of a single type of diagrams besides the VCA term in the self-energy, as explained in more detail in the diagrammatic approach introduced in equation (5.42). In the CPA, odd terms in Δ are considered in the expansion of the self-energy, leading to an asymmetric DOS. This asymmetry is consistent with purely numerical results in Dirac-like systems [199, 252].

In the weak disorder limit, i.e. $\beta \ll 1$, the approximate analytical solution for the SCBA (5.64) is expected to agree with the numerical solution of the full SCBA. Moreover, in this regime the SCBA is also expected to approximate the CPA results, as predicted from the series expansion of the CPA at small disorder (5.70). Figure 5.2 shows a comparison of the analytical expression for the coupling constant with the numerically solved SCBA equation as a function of energy for weak disorder. The approximated solution is in excellent agreement with the numerics as long as the range of parameters considered satisfies all the conditions for the approximation to be valid. For the sake of completeness, the CPA results are also plotted in solid lines in figure 5.2. It is worth noting that the CPA and SCBA results are in very good agreement for small magnitude of disorder and low concentration of impurities.

Comparison of the DOS

Figure 5.2(c) shows the DOS in the limit of $\beta \ll 1$. Although both approximations agree in this regime, the asymmetry in the DOS obtained from the CPA is already noticeable at higher energies.

Thanks to the analytical limit of the SCBA, the limit of $\overline{E} \to 0$ is particularly suitable for extracting tendencies. As already mentioned, the SCBA predicts an exponential-like broadening given by equation (5.62), which for small disorder parameters resembles a purely exponential decay, approximated as

$$\Gamma_{\mathrm{SCBA}}(\overline{E}=0) \simeq E_c\, e^{-1/(2\beta)} \ . \tag{5.72}$$

The above expression allows to write explicitly the DOS in the zero-energy limit within the SCBA as

$$\rho_{\mathrm{SCBA}}(\overline{E}=0) = \frac{E_c}{2\pi^2\beta\sqrt{e^{1/\beta}-1}} \simeq \frac{E_c}{2\pi^2\beta}\, e^{-1/(2\beta)} \ . \tag{5.73}$$

Figure 5.3 shows a comparison of the analytical limit and the results of the numerically solved $\Gamma(\overline{E})$ and DOS as a function of the disorder parameter β within the SCBA. The absence of a disorder induced phase transition is apparent and it is a crucial difference between the 2D and 3D

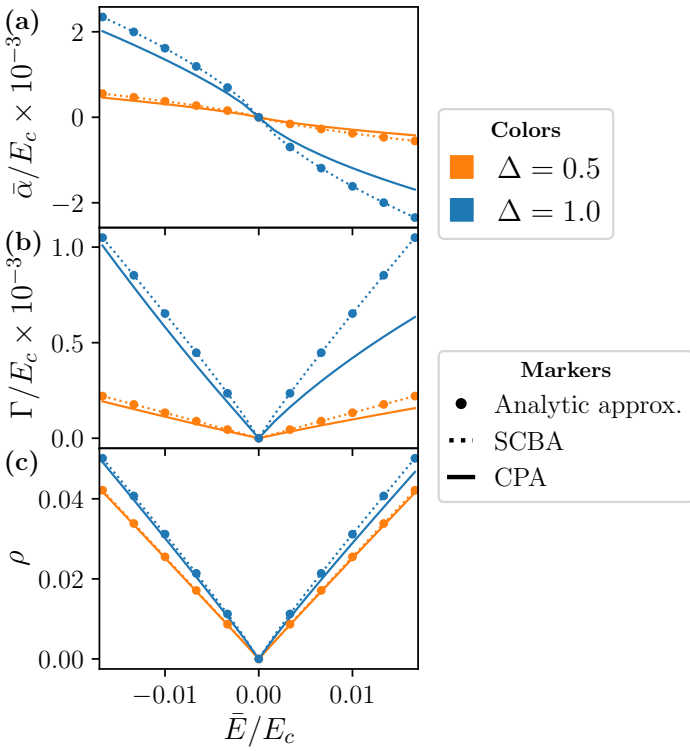

Figure 5.2: Real part of the coupling constant $\overline{\alpha}$ (a), imaginary part Γ (b) and DOS ρ (c) plotted as a function of the shifted energy. Panels compare the results for fixed $c = 0.2$ and two values of $\Delta = [0.5, 1.0]$, shown in orange and blue, respectively. Three approaches are compared: the analytical solution given by equation (5.64), the SCBA and the CPA. Δ is expressed in units of $\hbar v/a$ and $E_c = 15$ in the same units.

cases. In 3D WSMs, the phase transition is well established from analytical and numerical methods [74, 75, 137, 191, 230], while in 2D Dirac-like materials the phase transition is not observed. In graphene, Dirac-like approaches and tight-binding approximations lead to the exponential behaviour shown in equation (5.72) and reported in the literature [60, 115, 249]. On the other hand, 2D models with mass terms such as the BHZ model show more complex phase diagrams [143, 147, 218].

The absence of a phase transition is also observed in the CPA results. In fact, the DOS at zero energy $\overline{E}$ shows a smooth dependence on the magnitude of disorder Δ and impurity fraction c, as shown in figure 5.4. This figure shows another important aspect of the predictions of both methods, namely the overestimation of the SCBA compared to the CPA. The disagreement becomes more pronounced as the perturbation magni-

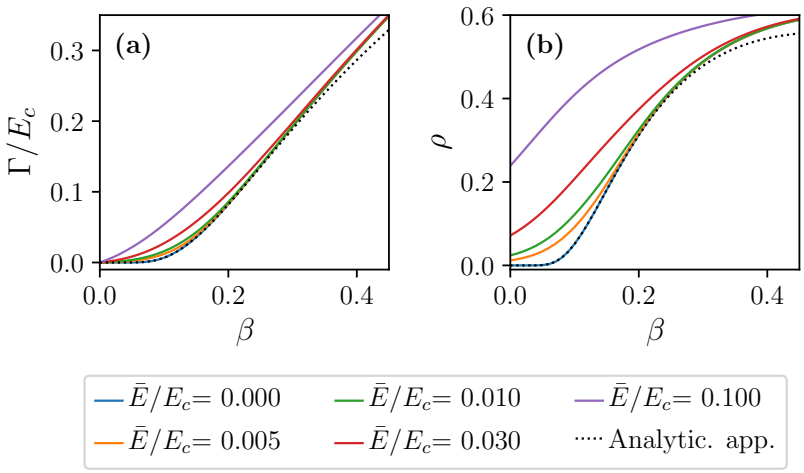

Figure 5.3: Imaginary part of the effective coupling constant (a) and DOS (b) within the SCBA as a function of the disorder parameter β. Dotted lines correspond to equations (5.72) and (5.73) while solid lines show the results from self-consistent calculations. Energy is expressed in units of $\hbar v/a$ and $E_c = 15$.

tude increases, as shown in figure 5.5, which compares the DOS of both methods as a function of c and Δ.

Figure 5.6 shows in more detail the range of equivalence of the two approximations. For small c and Δ ($c \lesssim 0.2$ and $\Delta \lesssim 0.5$ in the figure), SCBA and CPA are in agreement, while for higher values of disorder the overestimation of the SCBA becomes noticeable. Note that in the range of weak disorder, the analytical limit given by equation (5.73) is accurate and the DOS follows the exponential trend $-1/\ln\left[\rho(\overline{E})\right] \sim c\Delta^2$. In a wider range of magnitude of disorder Δ and impurity fraction c the disagreement becomes apparent, leading to an excess of DOS of the order of the value itself, as shown in figure 5.4.

The SCBA predicts a threshold for non-zero DOS lower than that obtained by the CPA, as shown in figure 5.5 (b). In this panel, the DOS is plotted as a function of the magnitude of disorder Δ.

For non-zero energy, the tendency remains the same and the SCBA results is an overestimation of the effect of impurities. Due to the strictly non-zero DOS for $|\overline{E}| > 0$, the relative error is a measure of the disagreement between the two methods and it is defined as

$$\delta\rho(\overline{E}) = 2\,\frac{\rho_{\mathrm{SCBA}}(\overline{E}) - \rho_{\mathrm{CPA}}(\overline{E})}{\rho_{\mathrm{SCBA}}(\overline{E}) + \rho_{\mathrm{CPA}}(\overline{E})}\ . \tag{5.74}$$

Figure 5.7 shows the relative error at a given energy as a function of Δ

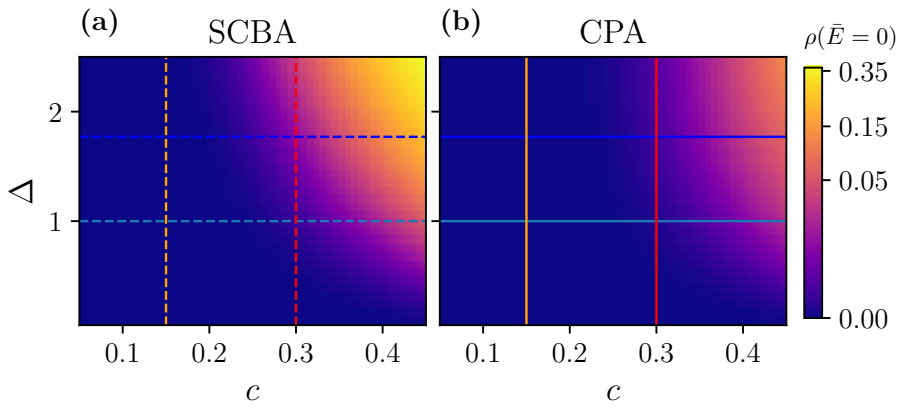

Figure 5.4: The colour map displays the DOS at zero shifted energy as a function of the magnitude of disorder Δ and the impurity fraction c in SCBA (a) and CPA (b). The solid vertical and horizontal lines correspond to the profiles plotted in figure 5.5. The cut-off energy is set to $E_c = 15$, the energy and Δ are expressed in units of $\hbar v/a$.

and c. The difference increases with the energy, as previously observed in the DOS plots, see figure 5.2.

Finally, the range of validity of the CPA is further discussed. The CPA has been shown to be reliable in obtaining the self-energy for a wide range of scenarios. It gives the correct result in the weak scattering limit (where it coincides with the SCBA), in the strong limit and in the dilute limit [23, 68]. In fact, the only approximation assumed in the CPA condition is that if the averaged single-site t_n-matrix is zero, then the averaged T-matrix of the effective system is zero, see equation (5.18b). This approximation is correct whenever the spatial correlation of the disorder is negligible. The single-site CPA incorrectly treats multiple scattering terms associated with clusters of a fixed number of neighbouring sites [67]. Diagrammatically this corresponds to the self-energy in CPA not including wigwam diagrams with crossing lines, whose contribution is negligible as long as the scattering length of the impurity potential is less than a [23]. Therefore, if the impurities are dilute and there is no short-range order, CPA results are accurate. In particular, for the results obtained in this chapter for the 2D Dirac materials, the CPA is an appropriate method to describe the disorder if the bulk gap is maintained.

After a trivial rotation, the Hamiltonian (5.47b) is basically the same as that of a low energy bands in graphene. Therefore, the results are of interest for the description of graphene with non-magnetic impurities [252]. Starting from the seminal work of Noro *et al.* [249], disordered

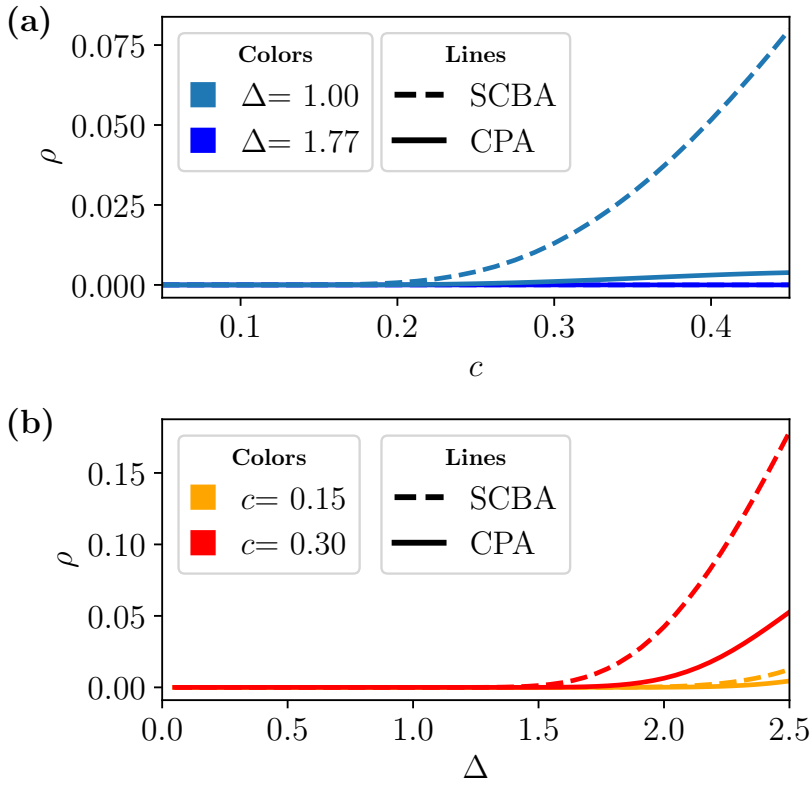

Figure 5.5: DOS at $\overline{E} = 0$ as a function of c (a) and Δ (b) within SCBA and CPA. Colours and line style match the solid vertical and horizontal lines in (a) and (b) of figure 5.4. The cut-off energy is set to $E_c = 15$; energy and Δ are expressed in units of $\hbar v/a$.

graphene sheets have been extensively studied within the SCBA approximation [115, 184], showing a significant effect of the disorder present in the samples. The numerical results in graphene match the behaviour presented here for the DOS [297]. Furthermore, proposals were made in the literature to determine the averaged DOS of these systems by measuring the quantum capacitance [149].

5.3 Conclusions

This chapter is devoted to the description of disordered systems by deriving effective models based on averaging techniques. Within different approximations, the effective models are constructed in such a way that

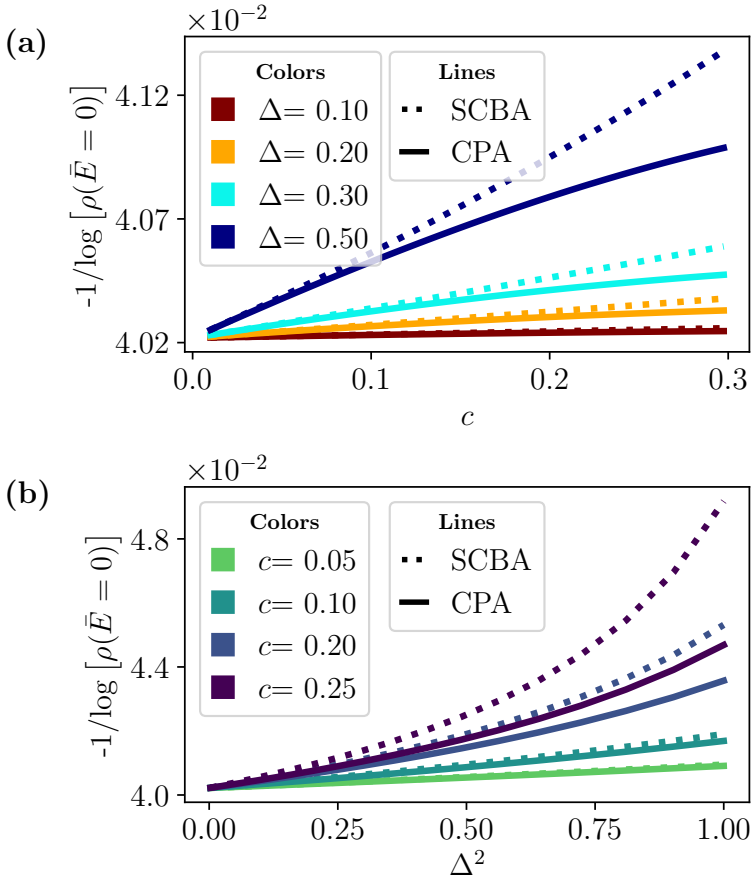

Figure 5.6: DOS for small disorder and low type A impurity concentration. The reported magnitude is the inverse of the logarithm of ρ at zero energy as a function of c and Δ^2. The cut-off is set to $E_c = 15$ in the numerical calculations. Energy and Δ are expressed in units of $\hbar v/a$.

they replace the disordered system by a translationally invariant effective system. In particular, two self-consistent methods, namely the SCBA and the CPA, are discussed and applied to the case of many impurities on a 2D surface of a TI.

The aim of the chapter is to analyse in detail the differences, weaknesses and strengths of both methods. On the one hand, the simplicity of SCBA allows the determination of the analytical trends, giving almost exact results for small perturbations and low impurity concentrations, without requiring the numerical solution of the self-consistency conditions. On the other hand, CPA provides an exact solution for any number of single impurity scattering events, providing reliable results even in the

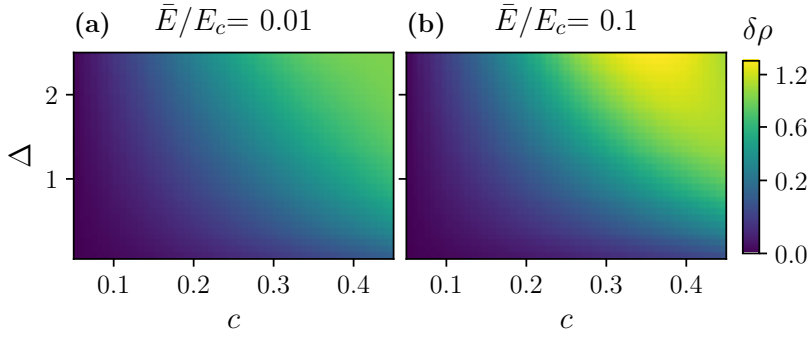

Figure 5.7: Relative error for the DOS computed from equation (5.74) at two different energies for $E_c = 15$. Energy and Δ are expressed in units of $\hbar v/a$. Note that from equation (5.74), $\delta\rho > 1$ implies that $\rho_{\mathrm{SCBA}} - \rho_{\mathrm{CPA}}$ exceeds the mean value of ρ_{SCBA} and ρ_{CPA}.

non-perturbative limit. Also, as expected from the correspondence between SCBA and CPA for weak disorder, both approximations agree in the range of dilute and weak impurity potential.

The comparison is based on the self-energy or equivalently the effective coupling constant. A reliable determination of the effective coupling constant is crucial to calculate physically relevant quantities such as the DOS, which is given by the effective single-particle Green's function. To achieve this, it is necessary to use an appropriate method that suits the regime of concentration and disorder strength.

In particular, in the case of the 2D linear Dirac Hamiltonian, the SCBA is found to overestimate the effect of disorder, especially in the DOS, and to introduce artificial symmetries in the effective medium. In conclusion, the results not only suggest a revision of current theories based on the SCBA, but also provide a reliable implementation of the CPA for the study of impurity scattering in 2D Dirac matter.

6 DIRAC SYSTEMS AND FLOQUET DRIVING

Preamble

External time-dependent electromagnetic fields have proven to be a fruitful tool for controlling quantum materials [9, 16]. The idea of controlling a quantum lattice system by a strong periodic external field dates back to the proposal of Dunlap and Kenkre in 1986 [64]. In their seminal work, a charged particle in a 1D tight-binding model was studied under the effect of a sinusoidal driving. The external field delocalizes the state, although a localised phase could be induced by varying the magnitude and frequency of the external electric field [64]. This tuning possibility was called *dynamical localisation*, and this effect was first observed in Bose-Einstein condensates in a shaken optical lattice [151, 250], where an equivalent mechanism suppresses tunneling for large frequencies.

The idea of control by the external field introduced in Dunlap's paper led to the concept of *Floquet engineering* [16, 189, 222], where the effective renormalization of the parameters of a quantum system are tuned by the external drivings, especially in the high-frequency regime. Floquet engineering has been successfully implemented in ultracold atoms, where the modulation is introduced by shaking the underlying optical lattice [66, 89]. The realisation of the Floquet technique in solid state systems is a challenging but fruitful area [167, 170, 284]. In this case, the modulation is performed by external electromagnetic radiation, and to achieve the high driving amplitudes required, ultrashort laser pulses are used. This leads to short-lived Floquet phases and difficulties in their detection.

Recently, the field of Floquet condensed matter was revisited in the search of controlling the topological properties of the systems. A topological phase can be in fact induced by applying a circularly polarised light to graphene, leading to a quantum Hall insulator [132, 170, 188, 189]. Similarly, a Floquet topological insulator was proposed in semiconductor quantum wells where the topological phase can be tuned by a frequency greater than the bandgap [90, 153]. Experimentally, these phases were achieved in optical lattices by a synthetic topological gauge [89] while the light-induced QAH effect was first measured in graphene in reference [170].

On the other hand, time-resolved ARPES measurements allowed the

imaging of the Floquet-Bloch states in the surface states of Bi_2Se_3 [167, 284]. In the first experiments, an intense ultrashort mid-infrared pulse with energy below the bulk band gap dresses the Bloch states by creating gaps due to the hybridisation of the bands [284]. Indeed, together with the accompanying replicas of the original bands, avoided crossings in the momentum space appear due to the breaking of symmetries by the driving, as predicted by the theory [70, 153].

This chapter focuses on the modulation of the surface state bands by electromagnetic pulses. In particular, it is of interest to understand the effect of the finite width of the pulse and the lack of time periodicity when interpreting the results within a Floquet-based formalism called $t - t'$ [61, 112]. This formalism considers two time scales: the envelope time scale and the period related to the frequency, which must be shorter than the envelope time scale. In this way, the driving pulse is described by an instantaneous Floquet basis, with the pulse amplitude as a decoupled parameter. The formalism has been shown to successfully describe strong pulses [116] in two level systems matching the experimental results in WSe_2 monolayers [271].

Thanks to the striking time resolution of the recent ARPES measurements [117, 209, 210, 231], the formation of sidebands in the surface states of the TIs was observed with subcycle precision [117]. The experimental observation of the bands within one cycle prompts naturally the question of how the Floquet structure is actually built up from a theoretical counterpart. This chapter aims to answer this question by analyzing the case of non-periodical drivings and extending the Floquet formalism to the *t-t'* formulation for the case of Dirac Hamiltonians.

The chapter is organised as follows:

- In section 6.1, the standard Floquet formalism for periodic driving is briefly reviewed. The formalism is introduced from two perspectives: on the one hand, section 6.1.2 presents the Fourier decomposition by expansion of the Hilbert space. On the other hand, section 6.1.3 interprets the dynamics within the Floquet picture by separating the contributions of the stroboscopic and micromotion evolution operators. The observables of interest, such as the time-averaged density of states and the photoelectron spectrum, are discussed in section 6.1.4. The 2D linear Dirac Hamiltonian is used as an illustration.

- In section 6.2, the Floquet formalism is extended to the non-periodic driving regime. First, observables such as Floquet fidelity and time-dependent occupancy are introduced in section 6.2.1. These observables are related to the definition of a reference Floquet basis.

However, this is not the case for the short pulses, where no reference frame can be consistently defined due to the limited time duration. To overcome this limitation, the $t - t'$ formalism is derived in section 6.2.2, where the reference basis can be defined in a time-dependent form.

- Section 6.3 is devoted to the study of the surface states of Bi_2Se_3. The topological states are described in this material by a Dirac Hamiltonian with trigonal warping, and they are investigated both under the driving of a periodic external field and in the regime of a short pulse, in sections 6.3.1 and 6.3.2, respectively.

- While the rest of the chapter establishes the notation for the Floquet formalism and reproduces already known results in the literature for Dirac cones, the application of $t - t'$ to the modified Dirac cone in section 6.3.2 is the central result of the chapter as well as the main original contribution.

- Finally, section 6.4 summarizes the main results of the chapter and discusses the limitations of the methods employed.

6.1 Floquet theory for periodic drivings

6.1.1 Floquet formalism

Floquet theory deals with time periodic Hamiltonians that can be expressed as

$$\mathcal{H}(t) = \mathcal{H}_0 + V(t) \ , \tag{6.1}$$

such that $V(t) = V(t+T)$. T is the period and it is related to the driving frequency ω by the usual expression $\omega = 2\pi/T$.

The goal is to solve the time-dependent Schrödinger equation (TDSE)

$$i\hbar \frac{d}{dt} \ |\psi(t)\rangle = \mathcal{H}(t) \ |\psi(t)\rangle \ , \tag{6.2}$$

where $|\psi(t)\rangle$ denotes the state and $\mathcal{H}(t)$ is given by equation (6.1). Due to the periodicity of $V(t)$, the TDSE is solved in a convenient basis, called the Floquet basis, such that the states are expressed as the product of a periodic function and a non-periodic phase. This factorization is given by the Floquet theorem [248], which is an analogue of the Bloch theorem, albeit with periodicity in time instead of the spatially periodic potential treated by the Bloch formalism.

The solution of the TDSE is then expressed as a linear combination of the Floquet basis by

$$|\psi(t)\rangle = \sum_b f_b \, |\phi_b^F(t)\rangle \ , \tag{6.3}$$

where f_b are complex constants, the summation is carried over the bands and the Floquet functions are defined by

$$|\phi_b^F(t)\rangle = e^{-i\xi_b t/\hbar} \, |u_b(t)\rangle \ . \tag{6.4a}$$

In the former expression $u_b(t+T) = u_b(t)$ is a periodic function, while the non-periodic part is given by the so-called Floquet *quasi-energy* ξ_b. Note that, due to the breaking of the invariance in time, the energy is not a conserved quantity of the system. However, the periodicity creates a discrete invariance, which translates into a conservation of the quasi-energy modulo the driving frequency. This can be directly derived from equation (6.4a), that can be re-written as

$$|\phi_b^F(t)\rangle = e^{-i(\xi_b/\hbar + l\omega)t} e^{il\omega t} \, |u_b(t)\rangle \ , \tag{6.4b}$$

where l is an arbitrary integer. Thanks to its periodicity, it is possible to re-define

$$|u_{b,l}(t)\rangle \ \equiv e^{il\omega t} \, |u_b(t)\rangle \ , \tag{6.5}$$

such that the quasi-energy for the state is now given by

$$\xi_{b,l} \ \equiv \xi_b + l\hbar\omega \ . \tag{6.6}$$

If the phase in equation (6.5) is global (i.e. it adds to all the Floquet functions of the basis), it is not a measurable quantity and hence the factorization by the Floquet theorem can determine the quasienergy only modulo $\hbar\omega$.

For the same reason, all Floquet solutions to the TDSE can be shifted to quasi-energies that fall within the same interval of width $\hbar\omega$. This defines the *Floquet-Brillouin zone* (FBZ) such that the first FBZ contains all the quasi-energies in the interval $-\hbar\omega/2 < \xi^{1\mathrm{FBZ}} < \hbar\omega/2$. The FBZs are a convenient solution for restricting the multivalued ξ_b, but they lack a physical interpretation unless combined with the spectral weighting of replicas introduced in section 6.1.4.

Finally, it is interesting to further comment on f_b in equation (6.3). The coefficients f_b are independent of the time evolution for a periodic driving. They are defined as the projection of the states over the Floquet functions

$$f_b = \langle \phi_b^F(t) | \psi(t) \rangle \ . \tag{6.7}$$

In the case of knowing the initial conditions of the problem, the coefficients f_b can be computed at $t = 0$. Then, for a periodic driving, the time evolution is dictated by equation (6.3) and the dynamics is encoded in the basis itself, so that the coefficients f_b remain constants.

6.1.2 Floquet Hamiltonian

As long as the expansion coefficients f_b are determined by the projection over the basis and the driving frequency ω is a known quantity, the solution of the TDSE (6.2) is reduced to the determination of the Floquet states $|u_b(t)\rangle$ and the quasi-energies ξ_b.

A common strategy for this is to exploit the periodic properties of $|u_b(t)\rangle$ and perform a discrete Fourier series decomposition in terms of the harmonics of the driving frequency as

$$|u_b(t)\rangle = \sum_{m=-\infty}^{\infty} e^{-im\omega t} \, |u_b^{(m)}\rangle \, , \tag{6.8}$$

where $|u_b^{(m)}\rangle$ is the m-th Fourier coefficient. Using equation (6.3) as an *ansatz* of the TDSE (6.2), the following expression is obtained as a function of the Fourier coefficients

$$\xi_b \, |u_b^{(m)}\rangle = \sum_n \left[\frac{1}{T} \int_0^T dt \, \mathcal{H}(t) e^{i(m-n)\omega t} - m\hbar\omega\delta_{m,n} \right] |u_b^{(n)}\rangle \, , \tag{6.9}$$

where the delta function is defined as $\delta_{m,n} = (1/T) \int_0^T dt \; e^{i(m-n)\omega t}$. The former expression can be interpreted as an eigenvalue equation in the Fourier space as [86]

$$\xi_b \, |u_b^{(m)}\rangle = \sum_n H^{\mathrm{F}}_{mn} \, |u_b^{(n)}\rangle \, , \tag{6.10}$$

where H^{F}_{mn} corresponds to the effective Floquet Hamiltonian defined by the quantity inside square brackets in equation (6.9). There is no time dependence in the effective Floquet Hamiltonian due to the integration over one period.

By writing the effective Hamiltonian in matrix form, H^{F} is represented by an infinite matrix of $d \times d$ blocks, where d is the size of the Hilbert space of $\mathcal{H}(t)$. In this matrix notation, the diagonal blocks are given by $\mathcal{H}_0$ with a shift of $-m\hbar\omega$, while the upper and lower diagonal blocks are the Fourier transform coefficients of $V(t)$.

Although the Fourier series considers an infinite number of modes, the fact that each $|u_b^{(m)}\rangle$ has a support on a limited range of Fourier modes

allows the truncation of H^{F} to a finite number of Fourier harmonics. The accuracy of the truncation depends on the Fourier transform of $V(t)$ as well as on the localisation of the states in Fourier space. However, by increasing the size of the Fourier space, it is possible to obtain an accurate result. It should be noted, however, that the truncation distorts the eigenvectors and eigenvalues of the harmonic boundaries, so that only the central results of the diagonalisation should be considered. On the other hand, the convergence of the harmonic series should be checked by increasing the size of the basis and verifying that the central results remain invariant.

6.1.3 Time-evolution operators in the Floquet formalism

Next, the evolution dictated by the periodic Hamiltonian is solved by the time-evolution propagator $U(t, t_0)$. The Floquet states are related to this operator, and the derivation of the Floquet formalism from this point of view allows a direct interpretation of the basis in terms of the time evolution.

In general, the evolution of an initial state $|\psi(t_0)\rangle$ is expressed as a function of the time-evolution operator by the well known expression

$$|\psi(t)\rangle = U(t, t_0)|\psi(t_0)\rangle \ , \tag{6.11}$$

where $U(t, t_0)$ encodes all the dynamic of the system, and it is obtained formally by integrating the TDSE (6.2) as

$$U(t, t_0) = \mathcal{T} \exp\left[-\frac{i}{\hbar}\int_{t_0}^{t} \mathcal{H}(t)dt\right] \ , \tag{6.12}$$

where $\mathcal{T}$ denotes the time-ordering operator. Note that $U(t, t_0)$ is unitary and has the following semigroup property

$$U(t_1 + t_2, t_0) = U(t_1 + t_2, t_1)\ U(t_1, t_0) \ . \tag{6.13}$$

In particular, for periodic Hamiltonians, this property implies that the time-evolution operator is factorised into two contributions [112]

$$U(t + nT, t_0) = U(t, t_0)\,[U(t_0 + T, t_0)]^n \ , \tag{6.14}$$

which is a particular formulation of the Floquet theorem. Thus, by solving the evolution operator within one period, the dynamics is calculated at any time.

Of particular interest is the one-period evolution operator, denoted for brevity as $U_T \equiv U(t_0 + T, t_0)$. Due to the characteristics of unitary

operators, it can be written as

$$U_T = \exp\left[-\frac{i}{\hbar}F_{t_0}T\right] \ , \tag{6.15}$$

where F_{t_0} is a time-independent hermitian operator that depends parametrically on the initial time t_0.

Being U_T unitary, it has a spectrum that generates a complete set of eigenvectors expressed by

$$U_T \ |v_b(t_0)\rangle = e^{-i\theta_b T/\hbar} \ |v_b(t_0)\rangle \ , \tag{6.16}$$

where $|v_b(t_0)\rangle$ denotes the eigenvector and $\theta_b \in \mathbb{R}$ ensures the eigenvalues to have norm 1. From equation (6.15), the following expression is obtained

$$F_{t_0}|v_b(t_0)\rangle = \theta_b|v_b(t_0)\rangle \ . \tag{6.17}$$

The set of eigenstates $|v_b(t_0)\rangle$ constitute a convenient basis to decompose the states. In fact, the time evolution of such states is expressed by the evolution operator as

$$U(t,t_0) \equiv P(t,t_0)\exp\left[-\frac{i}{\hbar}F_{t_0}\cdot(t-t_0)\right] \ , \tag{6.18}$$

The $P(t,t_0)$ operator is T-periodic, $P(t,t_0) = P(t+T,t_0)$. Due to the properties of the evolution operator and the definition of F_{t_0}, it also fulfills $P(t_0+nT,t_0) = 1$. By replacing the evolution operator in equation (6.18), the evolution for the $|v_b(t_0)\rangle$ is given by

$$U(t,t_0) \ |v_b(t_0)\rangle = e^{-i\theta_b(t-t_0)/\hbar} \ |v_b(t)\rangle \ , \tag{6.19}$$

where

$$|v_b(t)\rangle \equiv P(t,t_0) \ |v_b(t_0)\rangle \ , \tag{6.20}$$

and it is T-periodic. A general state is then expressed by

$$|\psi(t)\rangle = \sum_b d_b \ e^{-i\theta_b(t-t_0)/\hbar} \ |v_b(t)\rangle \ , \tag{6.21}$$

where d_b is determined by the initial conditions from $d_b = \langle v_b(t_0)|\psi(t_0)\rangle$.

Comparing equation (6.21) with the Floquet evolution in (6.3), the agreement with the definition of the Floquet states in section 6.1.1 is clear. Thus, by setting the initial time $t_0 = 0$, the following quantities are identified

$$|v_b(t)\rangle \equiv |u_b(t)\rangle \ , \quad \theta_b \equiv \xi_b \ , \quad d_b \equiv f_b \ . \tag{6.22}$$

The evolution operator then relates to the Floquet states by

$$U(t,t_0) = \sum_b |\phi_b^F(t)\rangle\langle\phi_b^F(t_0)| \ , \tag{6.23}$$

where the sum runs over the bands of $\mathcal{H}_0(t)$.

In conclusion, the derivation in this section leads to the same definition of the Floquet basis of section 6.1.1. Nevertheless, the introduction of the evolution operators brings a new interpretation of the Floquet formalism by separating the time evolution (6.15) into two contributions. On the one hand, the fast motion operator $P(t)$ yields the micromotion within one period; on the other hand, the slow dynamics (stroboscopic motion) is governed by F_{t_0}. The Floquet modes are related to the micromotion within one period, while the evolution at stroboscopic times, i.e. whenever $t = t_0 + nT$, is given by the Floquet Hamiltonian F_{t_0}, which ensures the non-periodic phase.

Although the computational cost is less convenient than calculating the effective Hamiltonian for the Fourier replicas from equation (6.10), the Floquet evolution can be obtained by the evolution operator. The one-period propagator U_T can be computed by integrating the TDSE for some fixed initial conditions. Then, F_{t_0} is determined by its definition (6.15) and by diagonalising it the quasi-energies and the Floquet modes are extracted.

6.1.4 Floquet observables: the case of the linear Dirac Hamiltonian

In interpreting the physics behind the Floquet theory, some observables are counterparts to related quantities of the non-driven systems. In particular, the time-averaged spectral function is a useful tool to visualize the distribution of replica weights. As proved in reference [273], a positive spectral density analogue to equilibrium is obtained by averaging over a period T the Green's function, expressed with respect to the time $\bar{t} = (t + t')/2$. Thus, the averaged DOS is defined similarly to the DOS (5.49) introduced in section 5.2.1 by

$$\overline{\rho}(E) = -\frac{1}{\pi S} \operatorname{Im}\left[\operatorname{Tr}\left(\overline{\mathcal{G}}_0(E + i0^+)\right)\right] \ , \tag{6.24}$$

where $\overline{\mathcal{G}}_0$ is the retarded single-particle Green's function after time averaging. After Fourier transform and making the substitution $E \to E + i0^+$, the following expression is obtained, see references [188, 320] for a detailed derivation

$$\overline{\rho}(E) = \sum_{b,m} A_b^{(m)} \ \delta(\xi_b + m\hbar\omega - E) \ , \tag{6.25}$$

where $A_b^{(m)} = \langle u_b^{(m)} | u_b^{(m)} \rangle$ are the Fourier components of the Floquet function given by equation (6.8). The term $A_b^{(m)}$ captures the spectral weight of the m-th harmonic sideband corresponding to the b-th Floquet function $|\phi_b^F(t)\rangle$.

The experimental imaging of the Floquet spectra is obtained by time-resolved ARPES measurements and hence a related observable is desiderable. The photoelectron spectroscopy is a pump-probe experimental setup, in which an intense radiation *pumps* the system into an excited states that, after a delay time, is subjected to a weak *probe* pulse. The photoelectrons generated by this second pulse are then detected with energy and angle resolution.

The photoelectron spectroscopy intensity is related to the transition probability between a scattering photoelectron state $|\chi_{\mathbf{p}}(t_f)\rangle$ with momentum $\mathbf{p}$ at t_f and a given state $|\Psi_0(t_i)\rangle$ at time t_i such that the transition matrix element is

$$\mathcal{M}_{\mathbf{p}}(t_f, t_i) = \langle \chi_{\mathbf{p}}(t_f)| \, U^{\text{driving}}(t_f, t_i) \, |\Psi_0(t_i)\rangle \, , \tag{6.26}$$

where U^{driving} describes the evolution operator of the external fields, in this case the pump and probe drivings [86]. Then, the transition probability is $P(\mathbf{p}) = |\mathcal{M}_{\mathbf{p}}(t_f, t_i)|^2$ and it is proportional to the measured intensity.

If the effect of the probe on the states is neglected, the former expression leads to

$$P(\Omega) = \left| \int_{-\infty}^{\infty} dt \; e^{i\Omega t} \langle \psi(t) | \psi(0) \rangle \right|^2 \, , \tag{6.27}$$

that is the Fourier transform of the projection on the initial state $|\psi(0)\rangle$ of the solution of the TDSE $|\psi(t)\rangle$, considering only the pump driving.

In the case of a periodic driving, $|\psi(t)\rangle$ is expressed by the decomposition (6.3) such that, upon time integration, yields

$$P(\Omega) = \sum_{b,m} |f_b|^2 |f_{m,b}|^2 \; \delta(\xi_b/\hbar + m\omega - \Omega) \, , \tag{6.28}$$

where $f_{m,b} \equiv \langle u_b^{(m)} | \psi(0) \rangle$ is the projection of the initial state over the m-th replica. In view of this expression, $|f_b|^2$ is interpreted as the occupations of the FBZ and the intensity of the photoelectron spectrosctopy signal is proportional to this magnitude.

The expression (6.27) gives a first insight into the expected ARPES measurements. However, if other electron-light interactions become important in ARPES measurements, the effect of the probe pulse must be taken into account. In fact, besides the Floquet-Bloch states, the light

can interact with the electronic states by other processes such as the dressing of the free electron states near the surface of a solid [76, 237, 238, 240]. This process, known as laser-assisted photoemission (LAPE), is usually modelled by Bloch states that transit into Volkov states[1]. Both Floquet and Volkov states show sidebands. Distinguishing the two contributions is of primary importance for the correct interpretation of ARPES intensities.

The interaction of the emitted electrons with the pump is strongly suppressed in certain configurations. In particular, when the driving field is polarised in the surface plane [117, 167], the Volkov states are minimised. Another indicator of the Floquet replicas in the spectra is the hybridisation of the sidebands (that leads to gaps) [167], which is absent in the Volkov states. Hence, from the theoretical perspective, the information encoded in the transition probability is comparable with the experimental ARPES for the linearly polarised configuration. For the other polarizations, the appearance of Floquet gaps in the experimental spectra is a signature that the Floquet states are also playing an important role in the dynamics of the system, however the contribution of the Volkov states could be important.

Floquet observables in the linear Dirac model

In this subsection, the linear Dirac Hamiltonian is discussed as a first example of a driven Floquet system. $\mathcal{H}_0$ comprises two bands obtained by taking only the linear terms in the effective Hamiltonian (1.43) for the surface states of a 3D TI.

$$\mathcal{H}_0(\mathbf{k}) = \hbar v \left(\sigma_x k_y - \sigma_y k_x\right) \ , \tag{6.29}$$

where v is a matrix element having dimensions of velocity.

For simplicity, a general elliptic driving is considered, as described by the following in-plane vector potential

$$\mathbf{A}(t) = [A_x \sin(\omega t), A_y \sin(\omega t + \theta_0), 0] \ , \tag{6.30}$$

where A_x and A_y are the amplitudes of the driving and ω is the driving frequency. The term θ_0 takes into account an initial phase. The circular driving is obtained for $\theta_0 = \pi/2$ and $A_x = A_y$. The linearly polarised pulses are obtained by setting one of the amplitudes to zero, for example

[1] The Volkov states are the solutions of the TDSE for a free electron interacting with an electromagnetic field. See for example reference [198] for a derivation of the Floquet and Volkov states in a Dirac Hamiltonian.

$A_y = 0$. By the minimal substitution, the vector potential enters the Dirac Hamiltonian as

$$\mathcal{H}(k_x, k_y, t) = \hbar v \left(k_x \sigma_y - k_y \sigma_x\right) + V_x(t) + V_y(t) \ , \tag{6.31a}$$

$$V_x(t) = evA_x \sin(\omega t)\sigma_y \ , \tag{6.31b}$$

$$V_y(t) = -evA_y \sin(\omega t + \theta_0)\sigma_x \ , \tag{6.31c}$$

where e is the elementary charge.

In this case, the expansion over the Fourier harmonics (6.10) leads to an affective Hamiltonian with the simplified structure of a monocromatic field

$$H_F(k_x, k_y) = \begin{pmatrix} \ddots & P & 0 & & \\ P^\dagger & H_0 + \hbar\omega & P & 0 & \\ 0 & P^\dagger & H_0 & P & 0 \\ & 0 & P^\dagger & H_0 - \hbar\omega & P \\ & & 0 & P^\dagger & \ddots \end{pmatrix} \ , \tag{6.32}$$

where the momentum dependence was omitted in the Dirac Hamiltonian $H_0 = H_0(k_x, k_y)$. The term that connects the replicas is

$$P = -i\frac{evA_x}{2}\sigma_y + \frac{evA_y[i\cos(\theta_0) - \sin(\theta_0)]}{2}\sigma_x \ . \tag{6.33}$$

The diagonalization of H_F (6.32) yields the Floquet quasienegies in figure 6.1 for a linearly polarised light and the spectrum 6.2 for the circularly polarised case.

The case of linear polarization is particularly instructive for the interpretation of the sidebands and the time-averaged DOS. In fact, the spectrum of the linearly polarised case for $k_y = 0$ is not modified by the external driving. Moreover, the TDSE for the Dirac Hamiltonian with linearly polarised driving can be integrated, leading to the time evolution of the states [70]

$$|\psi_{k_x,k_y=0,\tau}\rangle = e^{-i\tau v k_x t} \ e^{isa_x \cos(\omega t)} \ |\psi^0_{k_x,k_y=0,\tau}\rangle \ , \tag{6.34}$$

where $\tau = \pm 1$ is the index of the band, ψ^0 denotes the eigenstates of the original Dirac cone and $a_x = evA_x/(\hbar\omega)$. This expression shows that the driving only causes a phase change in the states and affects the spectral weighting. Indeed, the time-averaged DOS in the colour scale of figure 6.1 reports a shift of spectral weight towards the replicas, which are interpreted as photon-dressed bands.

The time-averaged DOS provides important complementary information about the distribution of Floquet states over the discrete harmonics [188, 222]. This is specially apparent in the limit of a driving pulse

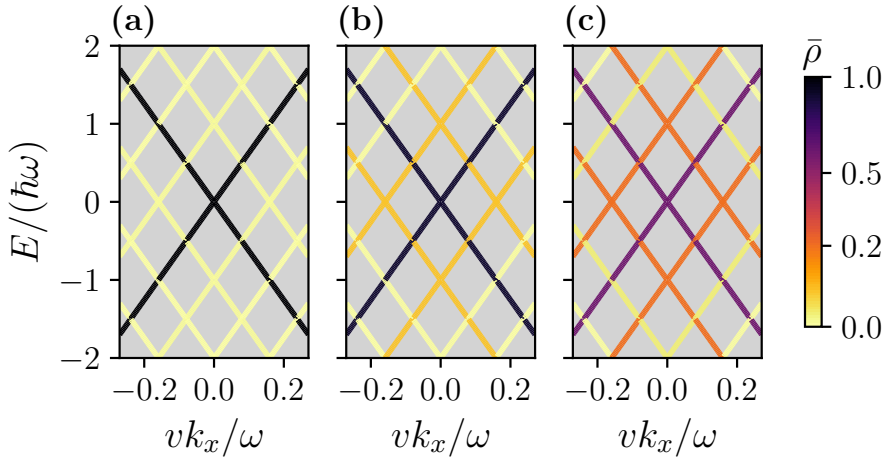

Figure 6.1: Quasienegies of the driven Dirac Hamiltonian with a linearly polarised driving with $evA_x/(\hbar\omega) = 0.1, 0.5, 1$ in panels (a), (b) and (c), respectively. The colorcode corresponds to the time-averaged DOS calculated from expression (6.25). The colormap is not linear, as shown in the colorbar, to improve the visibility of the colours in the range of lower DOS.

with frequency ω and vanishing amplitude. For vanishing amplitude, the expansion in the harmonic Fourier series becomes a purely mathematical tool, and the sidebands do not describe any physical state in the system. However, the replicas are still present in the quasienergies spectrum due to the non-zero frequency. In this case, even if the Floquet spectrum still shows the sidebands, the time-averaged DOS is only weighted in the bands of the unperturbed Dirac cone, see for example the panel 6.1(a) where the amplitude A_x is small.

For circular polarization, the operator describing the time-periodic field and the original Hamiltonian do not commute, in contrast to the linear polarization [70]. The driving then produces not only a rigid shift of the bands, but also a hybridisation of the Floquet replicas which gaps the spectrum. Avoided crossings appear at zero energy and at resonances where the conduction and valence bands of the unperturbed cone were separated by multiples of $\hbar\omega$.

The transition probability amplitude associated with the photoemission is calculated according to expression (6.27). The cases of linearly and circularly polarised light are shown in figures 6.3 and 6.4, respectively. In both figures, the initial state $|\psi(0)\rangle$ is chosen as a valence band state of $\mathcal{H}_0$. Regardless of the polarization, the initial state in the valence band of the Dirac cone is pumped to the nearby replicas with an increasing

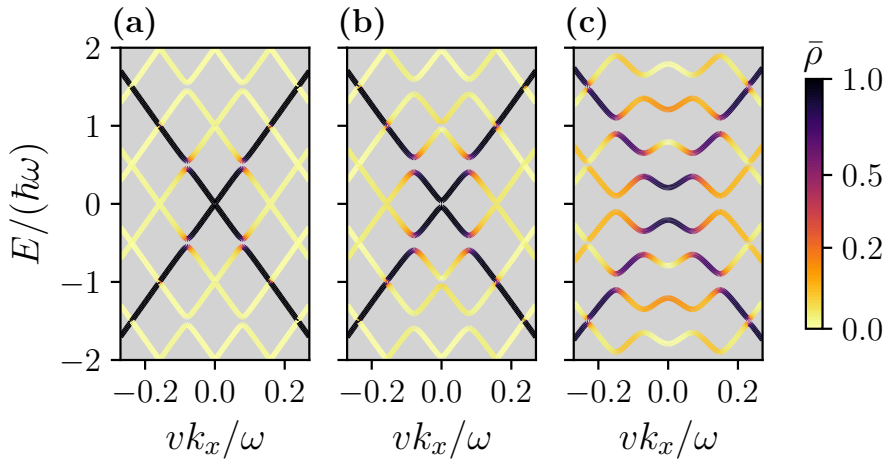

Figure 6.2: Floquet spectrum and time-averaged DOS for the circularly driven Dirac cone (i.e. $A_x = A_y$ and $\theta_0 = \pi/2$ in equation (6.30)). The pulse amplitudes are $evA_x/(\hbar\omega) = 0.1, 0.5, 1$ in panels (a), (b) and (c), respectively. The colorcode is the same as in figure 6.1.

effect depending on the pulse amplitude. Thus, in panel (c) of figure 6.3, which corresponds to the higher amplitude examined, the state is spread over the two upper and lower replicas. In contrast, in panels (a) and (b) the density is mainly located in the first FBZ.

Finally, in contrast to the circularly polarised case, the linear polarization exhibits a non-zero transition probability between replicas of the same band. Hence, in figure 6.3, the initial valence state only spreads over valence replicas. On the other hand, for the circularly polarised driving, the two bands are coupled. This allows transitions between the replicas of opposite bands, as shown in figure 6.4(c). By comparing the results of the DOS and the transition amplitudes, even if they are found to be very close and interpretable in the same manner, $P(\Omega)$ contains additional information about the accessible states starting from a given initial state.

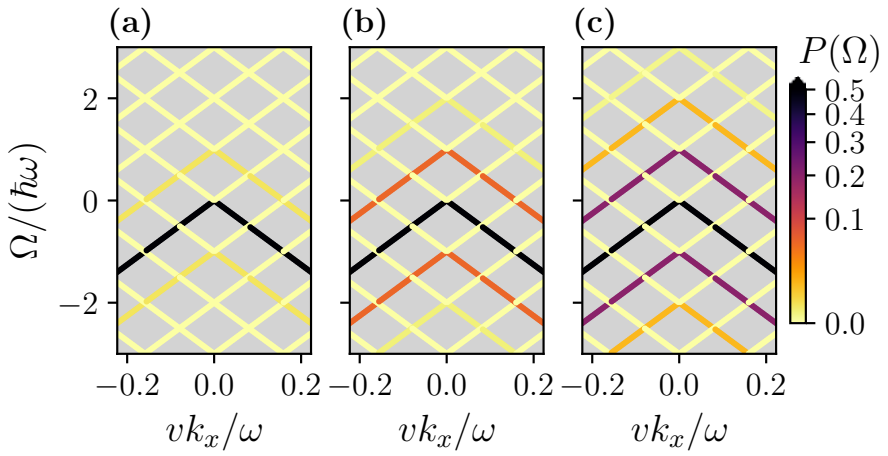

Figure 6.3: Transition probability amplitude for the Dirac Floquet spectrum in the case of the linearly polarised driving (i.e. by setting $A_y = 0$). The pulse amplitudes are $evA_x/(\hbar\omega) = 0.1, 0.5, 1$ in panels (a), (b) and (c), respectively. The colorcode corresponds to the amplitude of the $P(\Omega)$, computed using expression (6.27). The initial state $\psi(0)$ considered is in the valence band for $\mathcal{H}_0$.

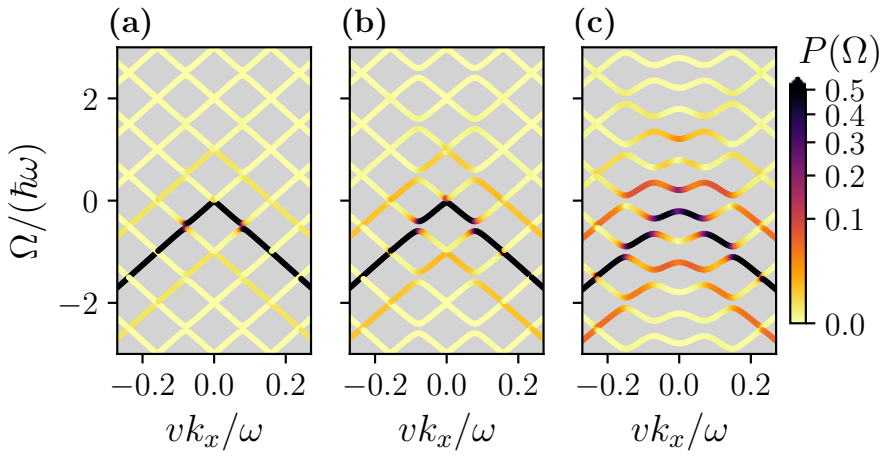

Figure 6.4: Transition probability amplitude $P(\Omega)$ for the Dirac Floquet spectrum with circularly polarised driving (i.e. $A_x = A_y$ and $\theta_0 = \pi/2$). The pulse amplitudes are $evA_x/(\hbar\omega) = 0.1, 0.5, 1$ in panels (a), (b) and (c), respectively. The colorcode is the same as in figure 6.3. The initial state considered is in the valence band for $\mathcal{H}_0$.

6.2 Extending the Floquet theory for non-periodic drivings

This section is devoted to non-period drivings. As already mentioned in the preamble of this chapter, the interest in describing non-periodic drivings is twofold. On the one hand, in condensed matter systems, the strong driving regime is usually accessible only with short pulses. On the other hand, recent measurements of time-resolved ARPES open the way to experimentally access the build-up regime of the photodressed electrons [117]. In these experiments, the pump pulses are usually of the order of 10 THz (i.e. with $T^{\text{pulse}} \sim 10$ fs) and thus the subcycle regime can be accessed with the typical femptosecond resolution of the time-resolved ARPES setups [209, 210, 216].

6.2.1 Floquet fidelity

In the case of non-periodic driving, the Floquet expansion in equation (6.3) is not given by the constant coefficients f_b. On the contrary, f_b becomes time-dependent and is computed by the projection of the TDSE solution over the Floquet states, as expressed in equation (6.7). To quantify the consistency of the Floquet states in this context, the Floquet fidelity is defined as follows

$$F(t) = \frac{1}{T}\int dt' \left| \sum_b \langle \psi(t') | f_b^F | \phi_\alpha^F(t') \rangle \right|^2 , \tag{6.35}$$

such that $F(t) = 1$ for a pure Floquet evolution and diminishing otherwise. In the former expression, the Floquet states $|\phi_\alpha^F\rangle$ are computed for a reference periodic system where the evolution is dictated by time-independent coefficients f_b^F obtained from equation (6.7) for a periodic driving.

In figure 6.5, a pulse with a switching-on ramp is considered. The pulse amplitude is described by replacing the constant amplitude in equation (6.30) by

$$A_x(t) = A_y(t) = \begin{cases} A_c \; t/\tau & \text{if } 0 \leq t \leq \tau \; , \\ A_c & \text{if } x > \tau \; , \end{cases} \tag{6.36}$$

where A_c and τ are two constant parameters. In this case, the pure Floquet driving is defined by the regime of $t \geq \tau$ and it might be informative to quantify the fidelity of a Floquet description within this basis. For this purpose, the fidelity is calculated by equation (6.35) and plotted in

panel (b) of figure 6.5. This quantity is time-dependent during the ramp, while it stacks at $F \sim 0.75$ for $t > \tau$. In panel (a) of the same figure, the Floquet expansion coefficients f_b are computed using expression (6.7) by projecting the numerical solution of the TDSE for the ramp pulse. The f_b also become time dependent for $t < \tau$. When the periodic Floquet driving is achieved, i.e. $t \geq \tau$, f_b becomes constant, as expected.

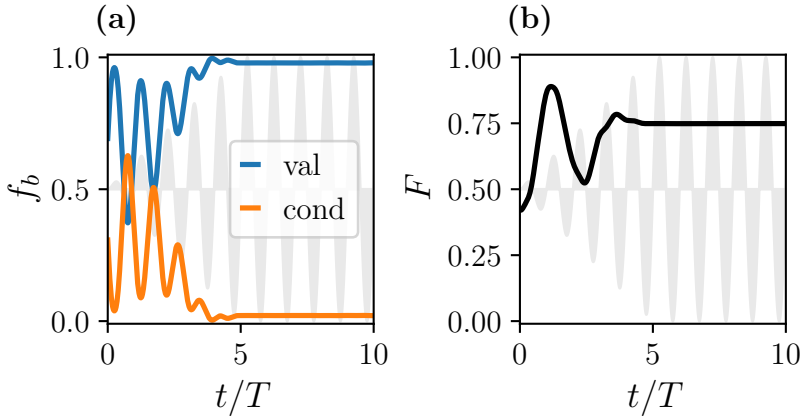

Figure 6.5: In (a) the time-dependent Fourier expansion coefficient f_b is plotted as a function of time; in (b) the Floquet fidelity F is calculated. Both panels consider a circularly polarised driving. The shaded area in the figure corresponds to the shape of the external pulse in arbitrary units. The parameters of the pulse, with aplitude given by equation (6.36), are $\tau/T = 5$, $evA_i/(\hbar\omega) = 0.5$ for $i = x, y$ and $\theta_0 = \pi/2$. The initial state is the valence state for $vk_x = 0.1\omega$. Panel (a) shows the coefficients f_b for the valence and conduction bands, as indicated in the legend.

6.2.2 $t - t'$ formalism

In the previous example, the Floquet basis naturally results from the long time limit. However, this is not the case for the drivings considered in the majority of the ARPES experiments. The usual time dependence of the driving resembles a Gaussian shaped pulse. Therefore, a Floquet basis does not arise as a limit in the time domain. Nevertheless, a Floquet-like formalism could be of interest in interpreting the appearance of sidebands.

To this end, a generalization of the Floquet formalism for varying pulse amplitudes is presented below. This formalism is called $t - t'$ due to the separation of time into two scales, one related to the evolution of the envelope function and the other to the periodic oscillations. The $t - t'$

formalism was first developed by Holthaus and collaborators [61, 112] and has recently been applied to the case of strong pulses in two-level systems [116].

In the case of a Gaussian pulse, the vector potential of a general elliptically polarised driving is split into two contributions

$$\mathbf{A}(t) = [a_x(t)\sin(\omega t), a_y(t)\sin(\omega t + \theta_0), 0] \ , \tag{6.37a}$$

$$a_i(t) = A_i \exp\left[-\frac{(t-t_0)^2}{\tau^2}\right] \ , \tag{6.37b}$$

where $i = x, y, z$, A_i is the maximum amplitude and θ_0 is an initial phase. The Gaussian envelope is centred around t_0, with the width given by τ. The Hamiltonian of the driven system is then factorised as

$$\mathcal{H}_{\text{pulse}}(t) = \mathcal{H}_0 + a(t)V(t) \ , \tag{6.38}$$

so that $V(t) = V(t+T)$ is periodic and $a(t)$ describes the envelope amplitude. The simplified expression (6.38) translates into multiple terms for $a(t)V(t)$ in the case of elliptical polarization with $a_x(t)$ and $a_y(t)$ given by equation (6.37a). To indicate the general dependence on the envelope without specifying the different contributions, the abbreviated notation $a(t)$ is used in the following. In fact, as will be shown below, the $t - t'$ formalism is very general. Its only main assumption is that a factorization of the driving into an envelope and a fast oscillation are appropriate for the non-periodic pulse.

If the evolution of the envelope is considered separately from the sinusoidal part, the TDSE for the Hamiltonian (6.38) can be expressed as

$$i\hbar\frac{d}{dt}\,|\psi(t)\rangle = \mathcal{H}_{\text{pulse}}(a(t), t)\,|\psi(t)\rangle \ , \tag{6.39}$$

where $\mathcal{H}_{\text{pulse}}(a(t), t)$ has a parametric dependence on the amplitude due to the factorization of the vector potential. For a fixed amplitude $a(t)$, equation (6.39) is the same as a periodic Floquet driving, whose solution is given by the *instantaneous* Floquet basis (6.3) such that

$$|\psi(t)\rangle = \sum_b f_b(t)\,|\phi_b^F(a,t)\rangle \ , \tag{6.40}$$

where the expansion coefficients are generally time-dependent and the Floquet basis depends on the amplitude a and, parametrically, on time. The instantaneous Floquet states involved in the former expansion are given, as in the periodic Floquet formalism, by a periodic function and a non-periodic exponent related to the quasi-energy

$$|\phi_b^F(t)\rangle = e^{-i\xi_b(a)t/\hbar}\,|u_b(a,t)\rangle \ . \tag{6.41}$$

Substituting this factorization into equation (6.40), the following expression is obtained for the solution of the TDSE with parametric dependence on the amplitude

$$|\psi(t)\rangle = \sum_b f_b(t)\ e^{-i\xi_b(a)t/\hbar}\ |u_b(a,t)\rangle\ . \tag{6.42}$$

Finally, the following quantities related to the Fourier expansion are defined

$$|u_\alpha(a,t)\rangle\ \equiv e^{il\omega t}\ |u_b(a,t)\rangle\ , \tag{6.43}$$

where $\alpha \equiv (b,l)$ is an abbreviation of the double index for the band and the harmonic decomposition. The quasi-energy is also related to the replicas by

$$\xi_\alpha(a)\ \equiv \xi_b(a) + l\hbar\omega\ . \tag{6.44}$$

Using the harmonic decomposition, the evolution of $\mathcal{H}_{\text{pulse}}$ is then written as a function of the instantaneous Floquet states by

$$|\psi(t)\rangle = \sum_\alpha c_\alpha(t)\ |u_\alpha(a(t),t)\rangle\ , \tag{6.45}$$

where $c_\alpha(t)$ denotes the expansion coefficients in the harmonic basis. Note that even though f_b and c_α have a similar construction, $c_\alpha(t)$ includes in its definition the contribution of the (instantaneous) Floquet quasi-energy. Therefore, a direct identification of the two quantities is incorrect, even in the context of the time-dependent $f_b(t)$. Using equation (6.45) as an *ansatz* for the TDSE, the following expression is obtained for the evolution of the expansion coefficients

$$i\hbar\frac{dc_\alpha}{dt} = \sum_\beta \mathcal{H}^{tt'}_{\alpha\beta}(a(t))\ c_\beta(t)\ , \tag{6.46}$$

where the Hamiltonian $\mathcal{H}^{tt'}_{\alpha\beta}$ is given by

$$\mathcal{H}^{tt'}_{\alpha\beta} \equiv \delta_{\alpha\beta}\xi_\alpha(a(t)) - i\frac{da}{dt}\mathcal{G}^{tt'}_{\alpha\beta}(a(t))\ , \tag{6.47a}$$

$$\mathcal{G}^{tt'}_{\alpha\beta}(a(t)) \equiv \int_0^T \frac{dt}{T}\langle u_\alpha(a,t)|\partial_a|u_\beta(a,t)\rangle\ , \tag{6.47b}$$

where the abbreviated notation for the derivative is $\partial_a = \partial/\partial_a$. The two contributions in expression (6.47a) account for the phase acquisition associated with the quasi-energies and the transition between Floquet replicas given by the $\mathcal{G}^{tt'}_{\alpha\beta}$ term.

The instantaneous Floquet states in (6.47b) are assumed to be differentiable. In order to satisfy this condition and not to show an expureous phase, the overall parallel transport condition is required by

$$\langle u_\alpha(a,t)|\partial_a|u_\alpha(a,t)\rangle = 0 \ . \tag{6.48}$$

This way, the arbitrary phase of the eigenvectors is fixed given a first initial phase at $t = 0$.

The central problem of the $t - t'$ formalism is to solve the differential equation (6.46) for the evolution of the expansion coefficients $c_\alpha(t)$. The instantaneous Floquet basis, used for factorizing the states, provides a more convenient interpretation of the dynamics in terms of the Floquet replicas for time-dependent driving amplitudes.

6.3 Effect of the pulse driving on the surface states of Bi_2Se_3

In this section, the surface states of Bi_2Se_3 are studied in detail within the periodic Floquet formalism and in the presence of a pulse. The effective Hamiltonian of the surface states in this material is determined by the usual linear Dirac cone with the addition of a trigonal warping [78, 155, 242], as introduced in section 1.3.2. The Hamiltonian in the absence of the pulse is then given by

$$\mathcal{H}_0(k_x,k_y) = (c_0 + c_2\mathbf{k}^2)\mathbb{1}_2 + \hbar v(k_y\sigma_x - k_x\sigma_y) + r(k_+^3 + k_-^3)\sigma_z \ , \tag{6.49}$$

where $\mathbf{k}^2 = k_x^2 + k_y^2$. The equation corresponds to expression (1.43) and the constants c_0, c_2, v and r are related to the bulk spectrum parameters, see equations (1.44).

The external driving is included by the minimal substitution, i.e. by replacing $\hbar k_x \to eA_x(t) + \hbar k_x$ and $\hbar k_y \to eA_y(t) + \hbar k_y$. Due to the more complicated momentum dependence in the warping term, the potential is cast in multiple terms so that it can be written as

$$\mathcal{H}(k_x,k_y,t) = \mathcal{H}_0 + V_x(t) + V_y(t) + V_{xy}(t) \tag{6.50}$$

where the following potentials are defined

$$\begin{aligned} V_x(t) = \ & 2r\sigma_z A_x^3(t) + (c_2\sigma_0 + 6rk_x\sigma_z)A_x^2(t) \\ & + [6r(k_x^2 - k_y^2)\sigma_z + 2c_2k_x\sigma_0 - \hbar v\sigma_y]A_x(t) \ , && \text{(6.51a)} \\ V_y(t) = \ & (c_2\sigma_0 - 6rk_x\sigma_z)A_y^2(t) \\ & + (2c_2k_y\sigma_0 - 12rk_xk_y\sigma_z + \hbar v\sigma_x)A_y(t) \ , && \text{(6.51b)} \\ V_{xy}(t) = & -6r\sigma_z A_x(t)A_y^2(t) - 12rk_y\sigma_z A_x(t)A_y(t) \ . && \text{(6.51c)} \end{aligned}$$

In the former expressions, the elementary charge e has been included in the units of the vector potential A_i for $i = x, y$ to simplify the notation. Next, the trigonal warping Hamiltonian is studied for the periodic driving in section 6.3.1 and for the Gaussian pulse in section 6.3.2. The vector potentials considered are the periodic sinusoidal driving of equation (6.30) and the time-dependent Gaussian pulse of equation (6.37a), without considering the corrections from the Volkov states. The linear polarization is studied and therefore the LAPE effect is expected to be negligible [167].

6.3.1 Periodic driving in the trigonally warped surface states

In this section, the methods applied to the linear Dirac Hamiltonian in section 6.1.4 are extended to the case of the trigonally warped Hamiltonian (6.50). The trigonal warping terms turned out to be indispensable for understanding the high harmonic spectra in Bi_2Te_3 under short pulses [231]. Therefore, they are expected to have an important effect on the Floquet dynamics. First, the time-averaged DOS is computed for the periodic drivings for the linear and circular polarization. In this Hamiltonian, due to the contributions in higher orders of $\mathbf{k}$ in equations (6.51), the external driving couples replicas up to third order. In addition, the coupling breaks the three-fold rotational symmetry of the system for general vector potentials. For instance, the linear polarization in the x-direction is described by a vector potential aligned with only one of the rotational axes, and thus the three-fold rotation is broken.

Figures 6.6 and 6.7 show the time averaged DOS for a linearly and circularly polarised pulse, respectively. Unless otherwise stated, the sinusoidal driving considered in this section has a frequency in the mid-infrared range of 160 meV, which corresponds to 38.7 THz. This value for the pump pulse is taken as a reference from the experiment reported in reference [167].

In the case of the linear polarization shown in figure 6.6, the spectrum inherits the inversion symmetry with respect to the exchange $k_x \to -k_x$. However, the Hamiltonian is not inversion symmetric and therefore the DOS is not invariant under the sign change of k_x.

Even though figure 6.6 shows no clear signature of gaps between Floquet replicas, the Hamiltonian for $k_y = 0$ in equation (6.49) and linear potential V_x from expression (6.51a) do not conmute. The anticommutator of the pristine Hamiltonian $\mathcal{H}_0$ and the potential is given by

$$[\mathcal{H}_0(k_x, k_y = 0), V_x(t)] = -4ivrk_xA_x(t)(A_x^2(t) + 3A_x(t)k_x + 2k_x^2)\ \sigma_x\ . \quad (6.52)$$

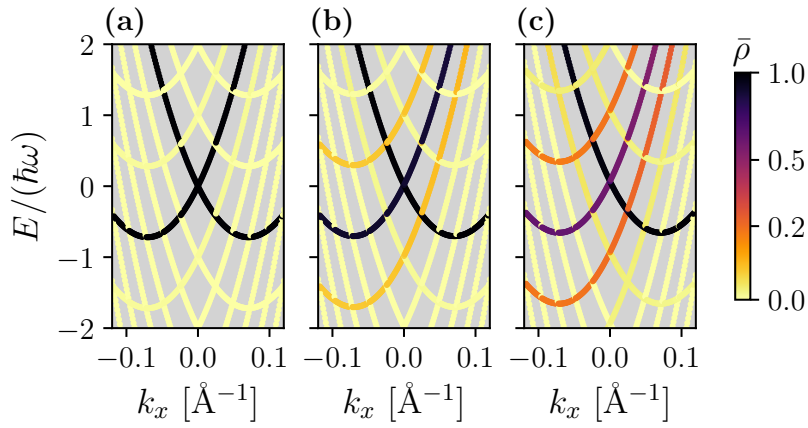

Figure 6.6: Time-averaged DOS for the Bi_2Se_3 Hamiltonian. The driving is linearly polarised with $A_y = A_x$ and $veA_x/(\hbar\omega) = 0.01, 0.05, 0.1$ in panels (a), (b) and (c), respectively. The time-averaged DOS is computed using expression (6.25).

This term is of high order in the momentum and vector potential and therefore gives a small coupling between the replicas. The intersection of the replicas produces avoided crossings of less than 10 meV for the drivings considered, and the gap increases with the pulse amplitude. For the amplitude $veA_x/(\hbar\omega) = 0.05$ the zoomed spectrum is shown in the inset of figure 6.8.

On the other hand, in the circularly polarised case, the coupling between the replicas is enhanced by the term V_{xy} (6.51c). More pronounced gaps appear even at small amplitudes, as shown in panel 6.7(b).

In a similar way to the previously studied linear Dirac cone, the transition probability amplitude is calculated from expression (6.27) for an initial state $|\psi(0)\rangle$ being a valence band state for $\mathcal{H}_0$. The results are plotted in figures 6.9 and 6.10 for the linearly and circularly polarised cases. Again, the transition probability matches the results of the time-averaged DOS, but it contains information about the allowed transitions between replicas from a given initial state, in this case the valence state of $\mathcal{H}_0$. In this way, the asymmetry between k_x and $-k_x$ becomes apparent and accounts for the asymmetric values of $P(\Omega)$ with respect to the exchange of the momentum sign. In particular, for the linearly polarised field, the valence band is more strongly coupled to the replicas for the negative k_x. This can be seen by comparing the transition probabilities for the two signs of k_x in figure 6.9(c).

In the following, the study is restricted to the linear polarization in order to focus on the effect of the sideband formation, rather than on the

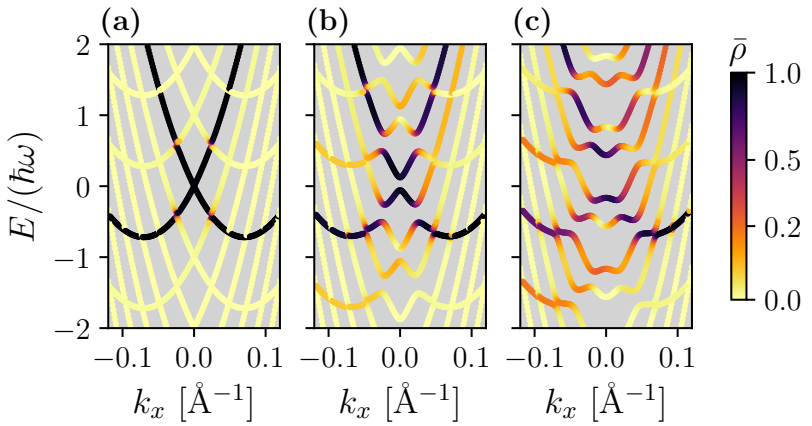

Figure 6.7: Time-averaged DOS for the cicurlarly polarised driving, i.e. by setting $\theta_0 = \pi/2$ and $A_x = A_y$ in expression (6.30). The pulse amplitude is set to $veA_x/(\hbar\omega) = 0.01, 0.05, 0.1$ in panels (a), (b) and (c), respectively.

modification of the spectrum due to the coupling between replicas. As already discussed in section 6.1.4, the configuration of the linearly polarised field reduces the LAPE effect and thus permits an easier interpretation in terms of the intensity of the time-resolved ARPES measurements without the need of considering the contribution of the Volkov states.

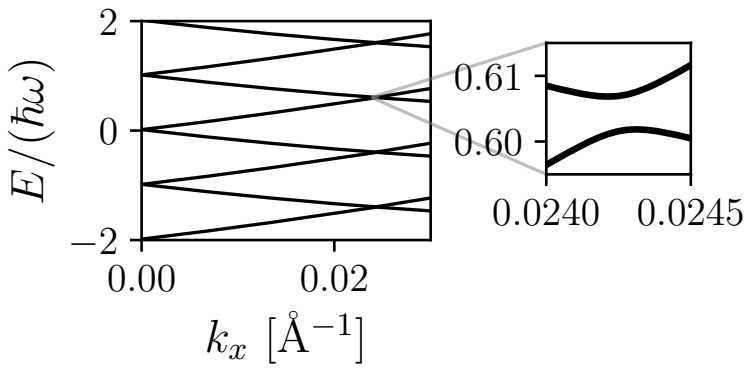

Figure 6.8: Floquet quasi-energy spectrum for the linearly polarised driving with amplitude $veA_x/(\hbar\omega) = 0.05$ as a function of k_x at $k_y = 0$. In the inset, the first (avoided) crossing is zoomed.

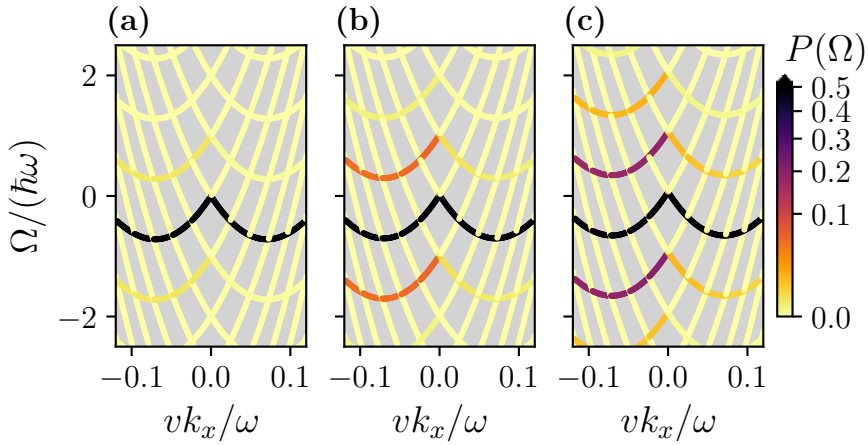

Figure 6.9: Transition probability amplitude $P(\Omega)$ for the Bi_2Se_3 surface states with linearly polarised driving (i.e. $A_y = 0$) computed from expression (6.27). The amplitud is set to $evA_x/(\hbar\omega) = 0.1, 0.5, 1$ in panels (a), (b) and (c), respectively. The initial state corresponds to a valence state for $\mathcal{H}_0$.

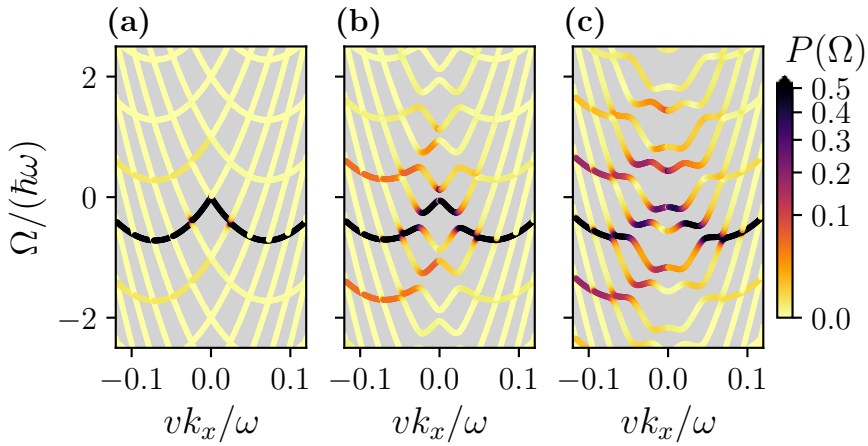

Figure 6.10: Transition probability amplitude $P(\Omega)$ for the Bi_2Se_3 surface states with circularly polarised driving (i.e. $A_x = A_y$ and $\theta_0 = \pi/2$). The amplitud is set to $evA_x/(\hbar\omega) = 0.1, 0.5, 1$ in panels (a), (b) and (c), respectively. The initial state corresponds to a valence state for $\mathcal{H}_0$.

6.3.2 Pulse driving in the trigonally warped surface states

This section is devoted to the study of the effect of non-periodic drivings in the surface states of Bi_2Se_3. In particular, the linearly polarised pulse described by equation (6.37a) for $A_y = 0$ is considered.

Transmission probability

A first insight into the formation of sidebands in the Gaussian driving case is provided by the transmission probability. After numerical integration, the solution of the TDSE is projected over the initial state using equation (6.27). The Fourier transform leads to a time-independent decomposition of the energy, where the emergence of replicas is apparent even if the dynamics is not periodic.

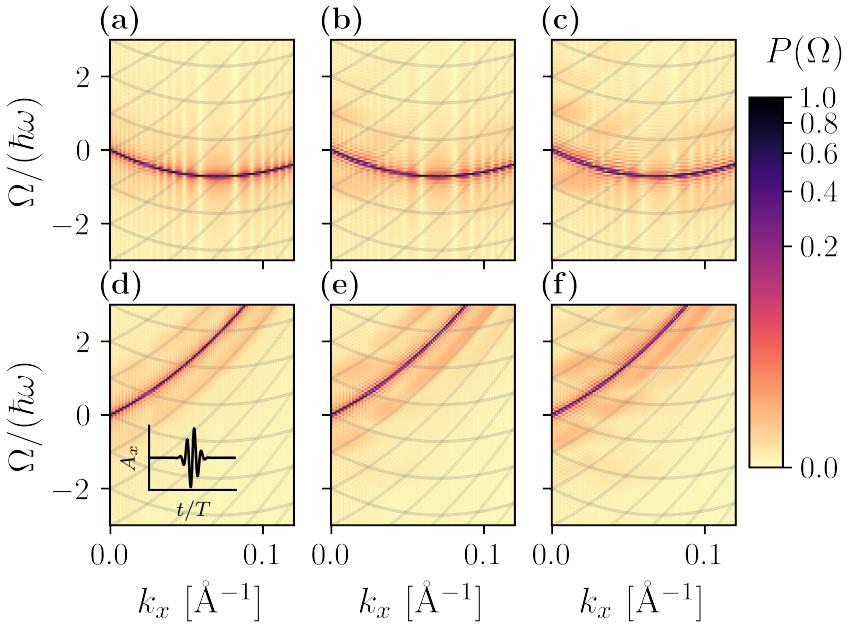

Figure 6.11: Transition probability computed numerically from expression (6.27) for a linearly polarised Gaussian pulse of width $\tau/T = 1$. The maximum amplitude is given by the strength $evA_x/(\hbar\omega) = 0.1$ in (a), (d); 0.5 in (b), (e); 1 in (c), (f). In light grey, the Floquet replicas generated by a rigid shifting of the dispersion relation are depicted to facilitate the visualization of the side-bands. The inset in (d) shows pictorically the pulse dependence on time given by equation (6.37a).

The results are shown in figures 6.11 and 6.12. The initial state $|\psi(0)\rangle$ in the upper panels of both figures corresponds to a valence state of $\mathcal{H}_0$, while the lower ones are conduction states. The increasing of the pulse length τ populates the side-bands, as can be seen by comparing panels (b) and (e) of figures 6.11 and 6.12. The vector potential undergoes oscillations of about $2\tau/T$. Therefore, for $\tau = T$ there are few oscillations, as shown in the sketch inset of figure 6.11, and the sidebands appear slightly. On the other hand, in figure 6.12, where $\tau = 3T$, the pulse is broader and the first sidebands are clearly revealed.

The numerically computed transition probability spectra also reveal the appearance of gaps for the avoided crossings, in agreement with the prediction of periodic drivings. Both the maximum pulse strength and the pulse length increase the size of the gaps.

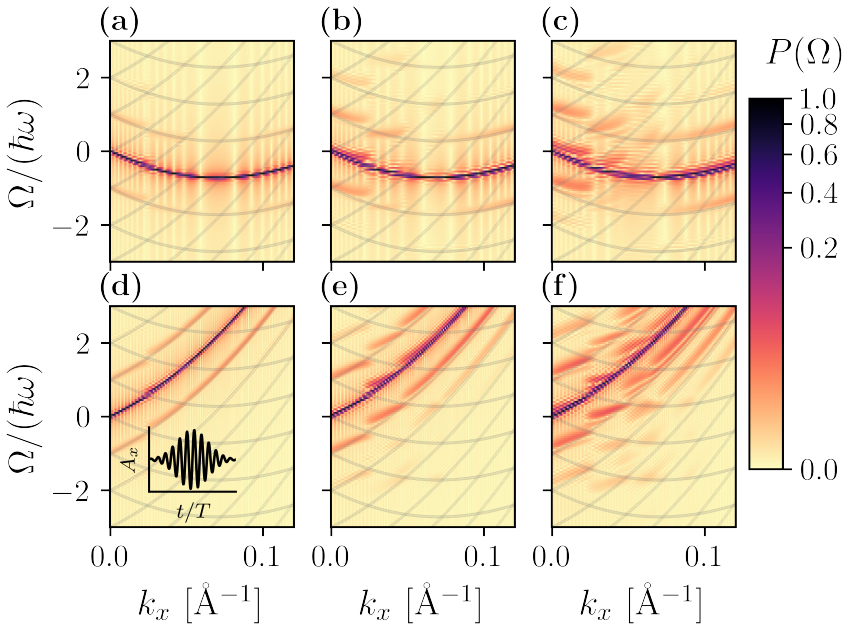

Figure 6.12: Transition probability computed numerically from expression (6.27) for a linearly polarised Gaussian pulse of width $\tau/T = 3$. The maximum amplitude is $evA_x/(\hbar\omega) = 0.1$ in (a), (d); 0.5 in (b), (e); 1 in (c), (f). In light grey, the Floquet replicas generated by a rigid shifting of the dispersion relation are depicted. The inset in (d) shows the pulse dependence on time.

$t - t'$ formalism applied to the Bi_2Se_3 surface states

Finally, the $t - t'$ formalism derived in section 6.2.2 is applied to the surface states of Bi_2Se_3 for a linearly polarised Gaussian pulse, given by equation (6.37a). This formalism allows solving the problem in a basis equivalent to Floquet replicas by considering the pulse amplitude as time-dependent. The TDSE is then mapped onto the evolution of the coefficients $c_\alpha(t)$ in equation (6.46). By solving $c_\alpha(t)$, the time dependence of the state is obtained from equation (6.45). The state calculated by this method can be compared with the numerical integration of the TDSE to check the accuracy of the $t - t'$ formalism. Along this section, the frequency considered is still $\hbar\omega = 160\,\text{meV}$.

In figure 6.13 a valence band state near the Dirac point ($k_x = -0.01\,\text{Å}^{-1}$ and $k_y = 0$) is evolved within the $t - t'$ formalism for a short pulse of $\tau = T$. The coefficients of the evolution appearing in equation (6.46) are shown in panel (b). Most of them are close to zero, except for the two closest replicas, which are populated by the pulse. However, they are also depopulated as the envelope decays, so that at the end of the pulse the original cone state is mostly occupied. The occupied replicas come both from the valence band, reflecting that the coupling to the conduction band is suppressed for the linearly polarised drive, as already expected from the results of the static Floquet picture.

Figure 6.13(a) shows the quasi-energies as a function of time. However, it is important to stress that the time dependence in this calculation is of a parametric type. In fact, the quasi-energies are computed in the usual Floquet formalism for a fixed $a(t)$. Furthermore, in panel 6.13(c), the absolute value of the components of the calculated states from the $t - t'$ formalism are compared with the solution from the numerical integration of the TDSE, finding a perfect agreement.

Next, the dependence of the pulse amplitude is examined, and the expected trend is found: as the pulse strength grows, the replica occupancy increases. This is shown in figure 6.14 for the selected expansion coefficients $c_{(b,l)}$. In panel 6.14(b) the coefficient for the conduction band of the first FBZ is plotted. The weak coupling between the conduction and valence bands slightly populates the conduction replica $(b, l) = (1, 0)$ with a contribution three orders of magnitude lower than the first valence replica $(b, l) = (0, 1)$ plotted in the panel (c).

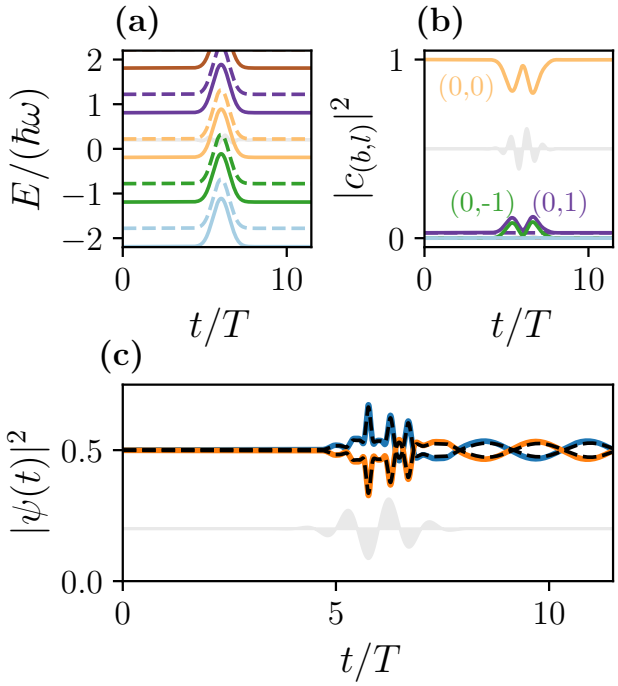

Figure 6.13: Evolution within the $t - t'$ formalism of a pulse with parameters $\tau/T = 1$, $evA_x/(\hbar\omega) = 0.4$ and an initial valence state with $k_x = -0.01\,\text{Å}^{-1}$ and $k_y = 0$. In (a) the Floquet quasienegies are plotted as a function of time for the first two upper and lower replicas. In (b) the coefficients are plotted as a function of time. The notation between brackets is (b, l), where b is the band of the replica and l is the harmonic. The curves of $(0, 1)$ and $(0, -1)$ are superposed and have been slightly shifted to improve visibility. In (c) the absolute value of the components of the solution for the $t - t'$ formalism are compared with the numerical solution of the TDSE. The colored lines correspond to the $t - t'$ solution while the dotted black lines are the TDSE. It has been numerically checked that $|\langle\psi^{\text{TDSE}}(t)|\psi^{t-t'}(t)\rangle|^2 \simeq 1$ for all t. In the background, the pulse is plotted in arbitrary units as a reference.

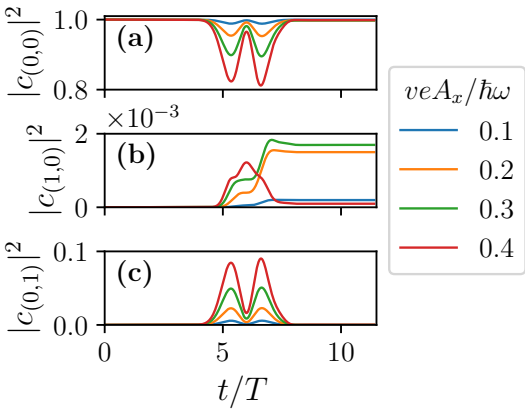

Figure 6.14: Selected expansion coefficients as a function of time corresponding to the valence state in the first FBZ in panel (a), i.e. $(b, l) = (0, 0)$; the conduction state in the first FBZ in panel (b), i.e. $(b, l) = (1, 0)$; and the first Floquet valence replica in panel (c), $(b, l) = (0, 1)$. The pulse width is set to $\tau/T = 1$ and the maximum amplitude is indicated in the legend. The initial state is the valence band state near the Dirac point employed in figure 6.13.

The transitions between replicas are given by the non-diagonal term in the Hamiltonian (6.47a), which is proportional to the derivative $da(t)/dt$. The derivative preceding the second term is the only dependence on the actual shape of the envelope. In fact, the term $\mathcal{G}^{tt'}_{\alpha,\beta}$ is only parametrically dependent on time, since it is a function of the pulse amplitude at a fixed time. Thus, the increase in the derivative of the pulse envelope is related to a higher rate change in the $c_\alpha(t)$. Oppositely, in the limit of an infinitely slow envelope variation, the second term in equation (6.47a) tends to zero and the expansion coefficients are easily solved by

$$c_\alpha(t) = c_\alpha(t = 0)\ e^{-i\xi_b^{1\mathrm{FBZ}} t/\hbar}\ . \tag{6.53}$$

Hence, in the adiabatic limit the $|c_\alpha|$ remains constant.

In the case of the Gaussian pulse, increasing the pulse width τ causes the derivative and the expansion coefficients to decrease towards the limit of the time-independent c_α. This is investigated in figure 6.15 where two pulses with different width are compared. The shorter pulse, which accounts for less than two complete cycles, generates a stronger driving towards the first replicas.

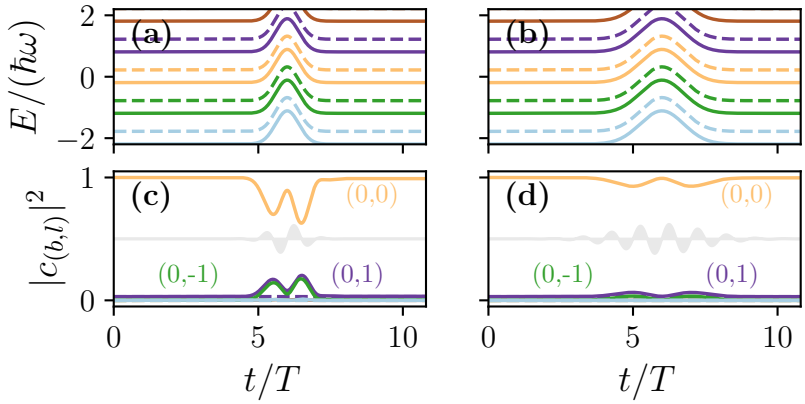

Figure 6.15: The pulse width is set to $\tau/T = 0.8$ and $\tau/T = 2$ in panels (a,c) and (b,d), respectively. The maximum amplitude is set to $evA_x/(\hbar\omega) = 0.4$ and the initial state correspond to the valence state near the Dirac cone employed in figure 6.13. In (a) and (c) the Floquet quasienergies up to $|l| \leq 2$ are plotted as a function of time. In (b) and (d) the absolute value of the expansion coefficients in the $t - t'$ formalism are represented.

Finally, it is interesting to briefly discuss the case of non-zero k_y. In this regime, the coupling between the valence and conduction bands is stronger due to the k_y dependent terms in the potential (6.51a). Therefore, non-zero transition probabilities between the valence and conduction replicas are found with a residual population in the conduction replica when the pulse is over, see figure 6.16(a). The $t - t'$ formalism does not take into account the relative phase between the envelope and the fast oscillations due to the integral over the period T implicit in the construction of the Floquet basis. Therefore, for increasing momenta, or for momenta with components in the k_y-direction, the $t - t'$ formalism is not accurate in describing the evolution of the system. Figure 6.16(c) compares the evolution from the TDSE and from the $t-t'$ formalism, finding less agreement for the state with non-zero k_y.

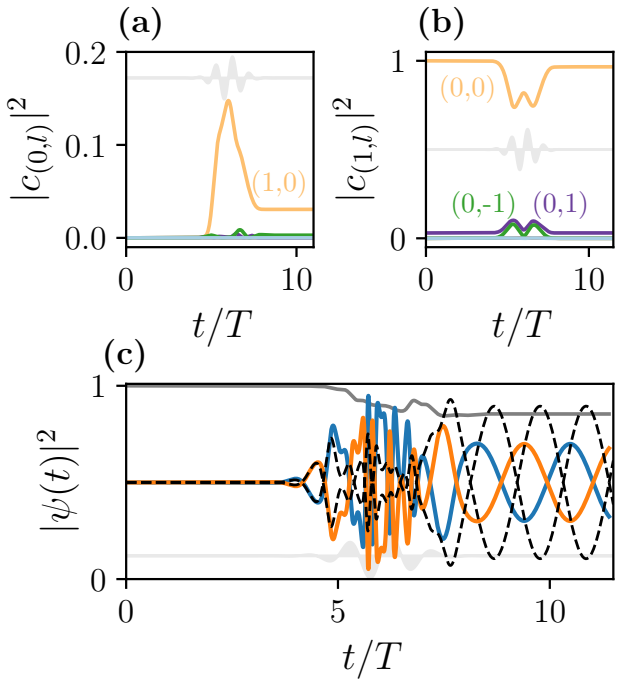

Figure 6.16: The absolute value of the expansion coefficients in the $t-t'$ formalism are represented, separating the contributions form the valence and conduction replicas in (a) and (b), respectively. The initial state corresponds to the valence state with $k_x = -0.01\,\text{Å}^{-1}$ and $k_y = 0.005\,\text{Å}^{-1}$. In (c) the reconstructed wavefunction is superposed with the solution of the TDSE. The grey line indicates the projection of this solution over the TDSE showing that it is less than 1 when the pulse is over. The pulse width is set to $\tau/T = 1$ and the maximum amplitude is $evA_x/(\hbar\omega) = 0.4$.

6.4 Conclusions and outlook

This chapter discussed the Floquet formalism. The study was mainly focused on reviewing the different methods and observables of interest in describing a driven system. Finally, the last part of the chapter is devoted to the $t - t'$ formalism and its implementation in the case of the Bi_2Se_3 surface state in a derivation which, to the author's knowledge, has not yet been reported.

The usual Floquet techniques for periodically driven systems are introduced in the first part of the chapter to fix the notation and to describe the observables used in the description of Floquet systems. Special emphasis is given to the dual derivation of the Floquet states either by the time evolution operator or by the harmonic decomposition to emphasize the physical interpretation of the Floquet basis.

The driven linear Dirac model is used as a valuable example in the introductory section to illustrate the calculation of the observables such as the time-averaged DOS and the transition probability. Next, the concept of Floquet fidelity is introduced for the turn-on pulse, where a well-defined final Floquet state is reached. However, for shorter Gaussian-shaped driving, the Floquet basis cannot be defined in such a tight way. Therefore, the $t - t'$ formalism appears as a natural extension for time-dependent pulse envelopes.

In particular, the $t - t'$ formalism is used in the last part of the chapter to describe the surface states of Bi_2Se_3 under Gaussian-shaped pulses. Starting from the results of the periodic driving in the usual Floquet formalism, the short pulses are described by the extended $t - t'$ basis, finding a quantitatively good agreement for evolution of the states with momentum in the direction of the polarization.

The results presented suggest that the $t - t'$ is a valuable tool to interpret the dynamics on an auxiliary Floquet basis and to compute the time evolution of the states, thus providing an interpretation of the ARPES experiments in the context of the Floquet formalism. Further studies could complement the research presented in this chapter. In fact, the details of the pulse envelope have proven to be indispensable for reproducing the experimental results. For example, the dephasing and the chirp of the pulse have been found to be crucial to understand the results of the high harmonic generation in Bi_2Te_3 under short pulses within the semiconductor Bloch equations [99, 292]. Therefore, it is expected that the details of the envelope and the oscillation also play an important role in the $t - t'$ formalism. In this formalism, a phase shift between the envelope and the pulse oscillations could be easily included, but the chirp or dephasing needs a careful implementation because it affects the static Floquet basis.

Moreover, there are many possibilities to extend the work on understanding the physical meaning of the Floquet observables in the context of the time-dependent $t - t'$ formalism.

In conclusion, the results of this chapter provide a solid basis for further investigations of the interplay between the Floquet states and the short pulses.

7 CONCLUSIONS

In this thesis, the effect of external perturbations and disorder in topological materials such as TSMs, TIs and graphene-based systems is investigated. The first part of the thesis focuses on external electric fields applied to TSMs and magnetically doped TIs. The electric field modifies important properties of the topological states by breaking symmetries of the system either by an onsite potential or by a RSOC generated by the coupling with the substrate. In both cases, the spatial extent and bands of the topological states are modified, and the external electric field provides a tool for tuning the states.

In the case of WSMs and DSMs considered in chapter 2, the external electric field in the direction of decay of the states modifies the velocity and shifts the degeneracy point in energy and momentum, according to the chirality of the Fermi arc. In DSMs with RSOC, the chirality and the spin are no longer conserved for each Dirac band. Therefore, this effect can be exploited in devices with spin-polai leads. In section 2.3, a device comprising a slab of Na_3Bi connected to two metallic leads is studied. One of the surfaces is in contact with the substrate and the RSOC is induced in this region. The system can be tuned into a spin-switching device by increasing the RSOC. Indeed, the spin flip is found to be the dominant contribution to the conductance for certain regimes of material parameters and sizes.

In chapter 3, devices formed by stacking layers of doped and undoped TIs under an external electric field in the growth direction are addressed. In this case, the electric field modifies the coupling of the different topological bands and generates multiple band crossings. This leads to a change in the Chern number of the system as a function of the external field. The transport properties of the device are then modified by the external field, which controls the number of topological channels contributing to the transverse conductance.

Chapter 4 is dedicated to study realistic graphene systems. Two effects are considered in this chapter: first, the e-e interaction in graphene nanoribbons is addressed in section 4.2, and then the effect of the hBN substrate in non-local resistance measurements is studied in section 4.3. The e-e interaction is found to produce an effective magnetisation which locally breaks the TR symmetry. This enables the scattering of the helical-edge channels in the KM model and breaks the conductance quantization

of the topological states. On the other hand, the hBN substrate breaks the valley degeneracy in graphene and induces valley currents in opposite spatial directions. With the addition of a magnetic field, the valley currents show a chiral behaviour, which can be studied by non-local transport measurements. Indeed, a different signal related to different carriers, electrons or holes, is measured depending on the direction of the field and the spatial direction of the injector-collector leads. In this section, a long-range hopping model is used to understand the experimental measurements.

The systematic study of disorder in Dirac cones is covered in chapter 5. The effect of the impurities is analysed using methods based on obtaining an effective medium by averaging. The treatment is mainly analytical and compares different approximations, namely the SCBA and the CPA. The DOS is obtained as a function of the disorder strength and the impurity fraction in 2D Dirac cones. A comparison of the two methods shows that the SCBA overestimates the effect of disorder for high-disorder concentrations and/or strong coupling with impurities.

Finally, in chapter 6, the effect of external time-dependent electromagnetic fields is addressed by means of Floquet formalism. In particular, the case of 2D Dirac bands describing the surface states of Bi_2Se_3 under a short pulse irradiation is studied. The Floquet formalism is extended by the so-called $t - t'$ formalism to describe time-dependent amplitudes. It is found that the Floquet basis correctly describes the evolution even if it is not periodic as long as the regime is adiabatic.

In summary, in this thesis the topological states are studied from a dual perspective. On the one hand, the external fields are used to tune intrinsic properties of the states such as the Fermi velocity, the spin, the number of topological channels or by inducing Floquet transitions. On the other hand, the resilience of the states to external perturbations and disorder is studied by analytical tools and numerical transport calculations. The thesis relates the theoretical results to two experimental measurements in DSMs under external electric and magnetic fields [181] and to non-local measurements in graphene nanoribbons encapsulated in hBN [227].

A TIME-REVERSAL SYMMETRY

The TR operation reverses the direction of the time evolution. The position operator is unchanged by the change in time evolution, but the momentum operator, which is related to velocity, is inverted. In summary, TR symmetry has the following effect:

$$t \to -t \ , \tag{A.1a}$$
$$x \to x \ , \tag{A.1b}$$
$$k \to -k \ . \tag{A.1c}$$

The TR operator then needs to have the following effect on the operators:

$$\Theta x \Theta^{-1} = x \ , \tag{A.2a}$$
$$\Theta p \Theta^{-1} = -p \ . \tag{A.2b}$$

For the conmutator of x and p this implies

$$\Theta [x,p] \Theta^{-1} = -[x,p] = +i\hbar \ . \tag{A.3}$$

The preceding equation leads to

$$\Theta i \Theta^{-1} = -[x,p] = -i \ , \tag{A.4}$$

from which it is clear that the TR operator is proportional to the complex conjugation.

A.1 Time-reversal symmetry in spinless systems

For spinless systems, the TR operator is expressed by the complex conjugation $\mathcal{K}$

$$\Theta = \mathcal{K} \ , \tag{A.5}$$

with the inverse $\Theta^{-1} = \mathcal{K}$. This operator is antilinear and antiunitary.

The implication of the TR symmetry in Bloch Hamiltonians is derived in the following. By expressing the Bloch Hamiltonian in terms of the creation $c^\dagger_{\alpha,\mathbf{k}}$ and annihilation $c_{\alpha,\mathbf{k}}$ operators, one obtains that

$$H = \sum_{\mathbf{k}} c^\dagger_{\alpha,\mathbf{k}} \mathcal{H}(\mathbf{k}) c_{\beta,\mathbf{k}} \ , \tag{A.6}$$

where α, β are matrix indices. The creation (annihilation) operator has to reverse the momentum due to the TR operation $\Theta c_{\mathbf{k}}^{(\dagger)} \Theta^{-1} = c_{-\mathbf{k}}^{(\dagger)}$. By imposing the TR symmetry on the Hamiltonian operator $\Theta H \Theta^{-1} = H$,

$$\sum_{\mathbf{k}} c_{\alpha,-\mathbf{k}}^{\dagger} \Theta \mathcal{H}(\mathbf{k}) \Theta^{-1} c_{\beta,-\mathbf{k}} = \sum_{\mathbf{k}} c_{\alpha,\mathbf{k}}^{\dagger} \mathcal{H}(\mathbf{k}) c_{\beta,\mathbf{k}} \ . \tag{A.7}$$

A TR invariant Bloch Hamiltonian has to fulfil

$$\mathcal{H}^{*}(\mathbf{k}) = \mathcal{H}(-\mathbf{k}) \ , \tag{A.8}$$

that is the condition for the Bloch Hamiltonians to be time invariant in the spinless case.

A.2 Time-reversal symmetry in spinfull systems

In the case of including the spin, the spin operator has to be included in the TR operator so that it is odd under the TR transformation:

$$\Theta \mathbf{s} \Theta^{-1} = -\mathbf{s} \ , \tag{A.9}$$

where $\mathbf{s}$ is the spin of the state. The spin flip implies the rotation by π around an arbitrary axis, traditionally set around the y axis [18]. The TR operator is then given by

$$\Theta = e^{-i\pi S_y/\hbar} \mathcal{K} \ , \tag{A.10}$$

where S_y is the spin operator in the y-direction and $\mathcal{K}$ is the complex conjugation. In the case of particles with spin 1/2, $S_y = (\hbar/2)\sigma_y$ leads to the following TR operator due to the properties of the exponential of the Pauli matrices

$$\Theta = i\sigma_y \mathcal{K} \ , \tag{A.11}$$

where the σ_y acts on the spin basis. Note that due to the antiunitary property of the TR operator, the TR symmetry in the Bloch Hamiltonian is given by

$$H(-\mathbf{k}) = \Theta H(\mathbf{k}) \Theta^{-1} \ . \tag{A.12}$$

A.3 Kramers' theorem

In particular, a TR symmetric Hamiltonian with spin 1/2 has a special degeneracy in the states, called Kramers' degeneracy, which arises from

TR symmetry. Kramers' degeneracy implies that in a TR symmetric Hamiltonian with spin 1/2, the eigenstates ψ and $\Theta\psi$ are degenerate and orthogonal to each other. This can be easily proved by considering a general TR symmetric Bloch Hamiltonian $H(\mathbf{k})$ with a Bloch state of spin s. The energy of the state is given by

$$H(\mathbf{k})u_{\mathbf{k},s} = \epsilon_{\mathbf{k}s}u_{\mathbf{k},s} \ . \tag{A.13}$$

Due to TR symmetry, the Bloch Hamiltonian satisfies equation (A.12) and hence

$$H(-\mathbf{k})\Theta u_{\mathbf{k},s} = \Theta H(\mathbf{k})\Theta^{-1}\Theta u_{\mathbf{k},s} = \Theta\epsilon_{\mathbf{k}s}u_{\mathbf{k},s} = \epsilon_{\mathbf{k}s}\Theta u_{\mathbf{k},s} \ , \tag{A.14}$$

where in the last step the TR operator skips the energy since it is a real number. Thus, the states $u_{\mathbf{k},s}$ and $\Theta u_{\mathbf{k},s}$ are degenerate with energy $\epsilon_{\mathbf{k}s}$. The orthogonality of the states can be proven by contradiction as follows. If the states are degenerate, they are related to a phase such that $\Theta\psi = e^{i\alpha}\psi$, with $\alpha \in \mathbb{R}$. Then,

$$-|\psi\rangle = \Theta^2|\psi\rangle = -\Theta|\Theta\psi\rangle = -e^{-i\alpha}\Theta|\psi\rangle = |\psi\rangle \ , \tag{A.15}$$

where the antiunitary property was used in the first step $\Theta^2 = -1$. Since the states might be zero to fulfil the linear dependence, it is clear that the ψ and its Kramers partner $\Theta\psi$ are orthogonal.

B LANDAUER-BÜTTIKER FORMALISM

In this thesis, the electronic transport is characterised by the Landauer-Büttiker formalism, which is an extension of the Landauer formula for multi-probe devices [27]. The main idea of the Landauer formula is to relate the transmission probability and the conductance of an electron propagating in a non-interacting system. In this appendix, the Landaur-Büttiker formalism is briefly commented on, and the reader is referred to more detailed explanations such as chapter 2 of reference [51].

In a macroscopic system, the conductance is given by the Ohm's law

$$G = \sigma W/L \ , \tag{B.1}$$

where W and L are the width and length. The conductivity σ does not depend on the size of the sample but only on the material itself.

The first formula implies that in the limit of a narrow sample, i.e. when $L \to 0$, the conductance diverges. However, this is not the case in the experimental measurements where a bounded maximum value of the resistance was found. If the system is in the regime of ballistic transport, i.e. whenever the mean free path of the electrons l satisfies $l > L$, the electrons can flow without any scattering in the lead. The resistance obtained must therefore be related to a contact resistance G_C in the interface between the contacts and the conductor.

Considering a 1D wire with two reflectionless leads with chemical potentials μ_1 and μ_2 such that $\mu_1 > \mu_2$ and zero temperature, the current flow is given by

$$I = \frac{2e}{\hbar} M(\mu_1 - \mu_2) \ , \tag{B.2}$$

where M is the number of modes in the energy range $E = \mu_1 \lesssim \mu_2$ and $2e/\hbar$ is the current carried per unit energy by an occupied state (with spin degeneracy) and it is independent on the dispersion relation [51].

From this expression, the conductance of the contacts can easily be obtained by

$$G_c = V/I = \frac{2e^2}{\hbar} M \ , \tag{B.3}$$

which relates the conductance of each channel to the conductance quantum $2e^2/\hbar$.

If a scattering region is considered so that the leads are still reflectionless but reflection is allowed in the scattering region, the transmission probability within the scattering region enters the former formula when considering the conductance of the whole system

$$G = \frac{2e^2}{\hbar} MT \ , \tag{B.4}$$

where T is the probability that an electron injected from the first lead is transmitted through the scattering region and collected in the second lead. This formula is known as the Landauer formula and can be extended to the multi-terminal case by

$$I_p = \sum_q \left[G_{qp} V_p - G_{pq} V_q \right] \ , \tag{B.5a}$$

$$G_{pq} = \frac{2e^2}{\hbar} T_{p \to q} \ , \tag{B.5b}$$

where the conductance is decomposed into coefficients that depend on the incoming lead q to the outgoing lead p and the current at lead p is given by I_p. To satisfy that the current is zero when all potentials are equal, the conductance must fulfil $\sum_q G_{qp} = \sum_q G_{pq}$, which leads to a more compact expression for equation (B.5a)

$$I_p = \sum_q G_{pq} \left[V_p - V_q \right] \ . \tag{B.5c}$$

Finally, it should be pointed out that the transmission function T_{pq} is given by the scattering matrix by

$$T_{pq} = \sum_{m \in q} \sum_{n \in p} |\mathcal{S}_{nm}|^2 \ , \tag{B.6}$$

where $\mathcal{S}_{nm}$ is the scattering matrix from the mode m of lead q to the mode n of lead p and the sum is performed over all occupied modes in the leads. Depending on the modes involved in the sum, the conductance can be factorised according to a specific operator, such as the spin or the chiral operator. This is the case of expression (4.36), where the spin is used to factorize the transmission matrix. In equations (2.19) and (2.45) the current is factorised by the chirality of the Weyl subblock.

The scattering matrix is the central result of scattering problems. Traditionally, this quantity has been obtained by recursive Green's function methods [253, 263]. In this thesis, an alternative method is used based on the wave function formulation of the scattering problem as implemented in the package `Kwant` [102]. This method is equivalent to the Green's function approach, but was found to be numerically more stable and efficient [102].

B.1 Local resistance calculation: example for a three-terminal device

In a multi-terminal device, equations (B.5a)-(B.5c) are actually a system of equations that can be expressed in matrix form. For example, for a three-terminal device like the one shown in figure B.1, equation (B.5c) can be expressed by

$$\begin{pmatrix} I_1 \\ I_2 \\ I_3 \end{pmatrix} = \begin{pmatrix} G_{12}+G_{13} & -G_{12} & -G_{13} \\ -G_{21} & G_{21}+G_{23} & -G_{23} \\ -G_{31} & -G_{32} & G_{31}+G_{32} \end{pmatrix} \begin{pmatrix} V_1 \\ V_2 \\ V_3 \end{pmatrix} . \tag{B.7}$$

Due to Kirchoff's law, the three equations are actually related by $I_1+I_2+I_3=0$ and therefore one of the three equations is linearly dependent. This is equivalent to the idea that only the potential difference is a physical quantity, so one of the voltages can be set to zero as a reference. If $V_3=0$, the system of equations is reduced to

$$\begin{pmatrix} I_1 \\ I_2 \end{pmatrix} = \begin{pmatrix} G_{12}+G_{13} & -G_{12} \\ -G_{21} & G_{21}+G_{23} \end{pmatrix} \begin{pmatrix} V_1 \\ V_2 \end{pmatrix} . \tag{B.8}$$

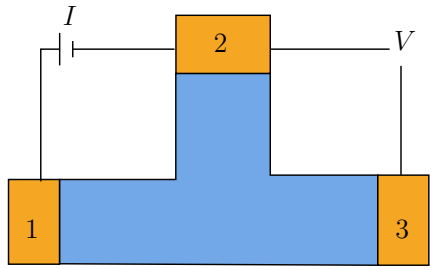

Figure B.1: Sketch of the three-terminal device. The leads are shown in orange and the scattering region in blue.

Given an applied current, the voltage drop between two leads can then be calculated by inverting the equation as follows

$$\begin{aligned} \begin{pmatrix} V_1 \\ V_2 \end{pmatrix} &= \begin{pmatrix} G_{12}+G_{13} & -G_{12} \\ -G_{21} & G_{21}+G_{23} \end{pmatrix}^{-1} \begin{pmatrix} I_1 \\ I_2 \end{pmatrix} \\ &= \frac{1}{A} \begin{pmatrix} G_{21}+G_{23} & G_{21} \\ G_{12} & G_{12}+G_{13} \end{pmatrix} \begin{pmatrix} I_1 \\ I_2 \end{pmatrix} \end{aligned} \tag{B.9}$$

where $A=(G_{12}+G_{13})(G_{21}+G_{23})-G_{12}G_{21}$ is the determinant of the 2×2 matrix in equation (B.8).

Once the voltage drops have been solved, the resistance is obtained by the usual expression $R = V/I$. However, in the case of a multi-terminal setup, the resistance obtained now depends on the indices of the injection and collection leads as well as the voltage probes. It is then defined by four indices as

$$R_{ij;kl} = \frac{V_i - V_j}{I_k - I_l} \ . \tag{B.10}$$

In the three-terminal device in this example, all resistance measurements are local due to the reduced number of leads. To calculate the resistance corresponding to the sketch in figure B.1, the following expression is used

$$R_{23;12} = \frac{V_2 - V_3}{I_1 - I_2} = \frac{G_{12}}{A} \ , \tag{B.11}$$

if the current $I_2 = 0$.

An equivalent approach is used in chapter 4 to calculate the local and non-local resistances for a aGNR and in chapter 2 to prove the topological currents of Fermi arcs.

C MAGNETIC FIELDS IN TIGHT-BINDING MODELS

The tight-binding models use the basis set of atomic-like orbitals to express the Hamiltonians of the systems. The basis set is generally denoted by $|n, \alpha\rangle$, where n is the spatial-site index and α refers to the orbital degree of freedom. The tight-binding Hamiltonian reads as

$$\mathcal{H} = \sum_{n} \epsilon_{n,\alpha} |n,\alpha\rangle\langle n,\alpha| - \sum_{n,m} t_{\alpha,\beta}(\mathbf{n}-\mathbf{m}) |n,\alpha\rangle\langle m,\beta| \ , \tag{C.1}$$

where the sums are over all the sites of the system. The term $\epsilon_{n,\alpha}$ is the onsite energy and the $t_{\alpha,\beta}(\mathbf{n}-\mathbf{m})$ is the hopping amplitude between the sites at distance $\mathbf{n}-\mathbf{m}$. Conversely, the onsite term and the hopping are related to the following projection of the Hamiltonian in this basis by

$$\epsilon_{n,\alpha} = \langle n,\alpha|\mathcal{H}|n,\alpha\rangle \ , \tag{C.2a}$$

$$t_{\alpha,\beta}(\mathbf{n}-\mathbf{m}) = -\langle n,\alpha|\mathcal{H}|m,\beta\rangle \ . \tag{C.2b}$$

Adding the external fields changes the onsite term and/or the hopping. This appendix focuses on the effect of the static magnetic and electric field on these terms.

The effect of the magnetic field is described by two terms: the orbital term and the Zeeman term. The orbital effect is related to the vector potential, which is introduced by the minimal substitution. In this way, the momentum $\mathbf{p}$ is replaced by $\mathbf{p} + e\mathbf{A}$. On the other hand, the Zeeman splitting is generated by the coupling between the spin and the external magnetic field, and it usually appears as a spin-dependent on-site energy shift. The effect of each term in the tight-binding formalism is discussed below, starting with the minimal substitution.

Given the Hamiltonian $\mathcal{H}(\mathbf{r},\mathbf{p})$, the minimal coupling to an external constant magnetic field $\mathbf{B}$ is described by the vector potential $\mathbf{A}$ such that $\mathbf{B}(\mathbf{r}) = \nabla \times \mathbf{A}(\mathbf{r})$. The vector potential is introduced by the following unitary transformation

$$e^{-i\phi}\mathcal{H}(\mathbf{r},\mathbf{p})e^{i\phi} = \mathcal{H}\left[\mathbf{r}, \mathbf{p} + e\mathbf{A}(\mathbf{r})\right] \ , \tag{C.3}$$

$$\phi(\mathbf{r}) = \frac{e}{\hbar}\int_{\mathbf{r}} \mathbf{A}(\mathbf{s}) \cdot d\mathbf{s} \ , \tag{C.4}$$

where the integral is performed over a line given by $\mathbf{r}$.

Using the Hamiltonian with the vector potential, the tight-binding representation of $\mathcal{H}$ is modified by the external field as

$$\langle n,\alpha|\mathcal{H}\left[\mathbf{r},\mathbf{p}+e\mathbf{A}(\mathbf{r})\right]|m,\beta\rangle = \exp\left[-\frac{ie}{\hbar}\int_{\mathbf{R}_{\mathbf{m},\beta}}^{\mathbf{R}_{\mathbf{n},\alpha}}\mathbf{A}(\mathbf{s})\cdot d\mathbf{s}\right]\langle n,\alpha|\mathcal{H}|m,\beta\rangle \ , \quad \text{(C.5)}$$

where the $\mathbf{R}_{\mathbf{n},\alpha}$ indicates the position of the site n. In a tight-binding, the most straightforward path is a straight line between sites. Assuming that the vector potential does not vary abruptly along this path, the integral can be approximated by the area:

$$\frac{e}{\hbar}\int_{\mathbf{R}_{\mathbf{m},\beta}}^{\mathbf{R}_{\mathbf{n},\alpha}}\mathbf{A}(\mathbf{s})\cdot d\mathbf{s} \simeq \phi(\mathbf{R}_{\mathbf{n},\alpha},\mathbf{R}_{\mathbf{m},\beta}) \ , \quad \text{(C.6a)}$$

$$\phi(\mathbf{R}_{\mathbf{n},\alpha},\mathbf{R}_{\mathbf{m},\beta}) \equiv \frac{e}{\hbar}(\mathbf{R}_{\mathbf{m},\beta}-\mathbf{R}_{\mathbf{n},\alpha})\frac{\mathbf{A}(\mathbf{R}_{\mathbf{n},\alpha})+\mathbf{A}(\mathbf{R}_{\mathbf{m},\beta})}{2} \ . \quad \text{(C.6b)}$$

Therefore, adding an external electromagnetic field modifies the following elements in the tight-binding Hamiltonian:

- The on-site elements has to include the scalar potential φ, related to the electric field and g, related to the Zeeman splitting:

$$\epsilon_{n,\alpha} = \epsilon^0_{n,\alpha} - e\varphi_{n,\alpha} + g \ , \quad \text{(C.7)}$$

  where $\epsilon^0_{n,\alpha}$ indicates the onsite term in the absence of external fields.

- The hoppings are modified according to equation (C.6b) by

$$t_{\alpha,\beta}(\mathbf{n}-\mathbf{m}) = e^{-i\phi(\mathbf{R}_{\mathbf{n},\alpha},\mathbf{R}_{\mathbf{m},\beta})}t^0_{\alpha,\beta}(\mathbf{n}-\mathbf{m}) \ , \quad \text{(C.8)}$$

  where the $t^0_{\alpha,\beta}(\mathbf{n}-\mathbf{m})$ is the hopping amplitude in the absence of external fields.

Next, the expressions are particularised for a graphene nanoribbon under a constant magnetic field pointing in the z-direction. In the Landau gauge, the vector potentials for a magnetic field in z-direction are

$$\mathbf{A}_1 = (-By,0,0) \ , \quad \text{(C.9a)}$$

$$\mathbf{A}_2 = (0,Bx,0) \ , \quad \text{(C.9b)}$$

where B is the strength of the magnetic field. In the case of the zGNR in section 4.3, the nanoribbon is elongated in the x-direction and the transverse leads are semi-infinite in the y-direction, as shown in figure 4.11. It is therefore particularly convenient to choose the gauge $\mathbf{A}_1$ in such a

way that only the hopping in the x-direction has to be modified and the translational symmetry in the transverse leads is automatically preserved. The phase entering the hopping amplitude is then given by

$$\phi(\mathbf{R_n}, \mathbf{R_m}) = \frac{\lambda_B(y_n + y_m)}{2}(x_n - x_m) \ , \tag{C.10}$$

where the magnetic field strength is related to λ_B, expressed in the units of inverse length, i.e. in nm^{-2}.

D FINITE TEMPERATURE IN THE T-MATRIX

In section 4.3, a temperature broadening is included in the resistance results. This appendix discusses the addition of a finite temperature to the Landauer-Büttiker formalism in order to obtain such a broadening. The expressions for the Landauer-Büttiker formula derived in appendix B consider zero bias and zero temperature.

The expression (B.5c) is generalised for a non-zero temperature and bias by[1]

$$I_p = \int i_p(E) dE \ , \tag{D.1a}$$

$$i_p(E) = \frac{2e}{\hbar} \sum_q [T_{pq}(E)(f_p(E) - f_q(E))] \ , \tag{D.1b}$$

where $T_{pq}(E)$ is the total transmission from terminal q to terminal p at the energy E. $f_p(E)$ is the Fermi distribution for the terminal p given by

$$f(E) = \left. \frac{1}{e^{(E-\mu)/k_B T} + 1} \right|_{\mu = E_F} \ , \tag{D.2}$$

where k_B is the Boltzmann constant, T is the temperature and E_F is the Fermi energy.

Equation (D.1a) is further simplified in the so-called linear response regime. In this case, the two potentials μ_p and μ_q are considered to be almost equal, so that a small current is produced by the deviation from the equilibrium state by

$$\delta I_p = \frac{2e}{\hbar} \sum_q \int dE \ \big([T_{pq}(E)]_{eq} \delta [f_p(E) - f_q(E)] + [f_p(E) - f_q(E)]_{eq} \delta T_{pq}(E) \big) \ . \tag{D.3}$$

At equilibrium $\mu_p = \mu_q$ and the second term is zero. The first term can be simplified by linearizing the Fermi distribution by

$$\delta [f_p(E) - f_q(E)] \approx (\mu_p - \mu_q) \left(\frac{\partial f}{\partial \mu} \right) = (\mu_p - \mu_q) \left(-\frac{\partial f}{\partial E} \right) \ . \tag{D.4}$$

[1] See sections 2.5 and 2.6 of reference [51] for a detailed derivation.

where the derivative of the Fermi distribution is

$$\frac{\partial f}{\partial E} = -\frac{\beta}{4\cosh^2(\beta(E-\mu)/2)} , \tag{D.5}$$

with $\beta = 1/k_B T$.

Substituting this result into equation (D.3) gives the following expression for the intensity

$$\delta I_p = \frac{2e}{\hbar} \sum_q \int dE \, \left(-\frac{\partial f}{\partial E}\right) [T_{pq}(E)]_{eq} \, (\mu_p - \mu_q) . \tag{D.6}$$

Conversely, this expression can be written in the usual form by defining the conductance G_{pq}

$$I_p = \sum_q G_{pq}[V_p - V_q] , \tag{D.7a}$$

$$G_{pq} = \frac{2e^2}{\hbar} \int dE \, T_{pq}(E) \left(-\frac{\partial f}{\partial E}\right) . \tag{D.7b}$$

where $V_i = \mu_i/e$ for $i = p, q$. The derivative of the Fermi distribution (D.5) is shown in figure D.1. The integration in energies in equation (D.6) is suitable for numerical integration due to the hyperbolic shape of $\partial f/\partial E$. Therefore, once the zero-temperature conductance is obtained, the temperature broadening in the conductance is implemented by numerically integrating expression (D.6) for each Fermi energy E_F. This method is used in section 4.3 to determine the resistances at non-zero temperature.

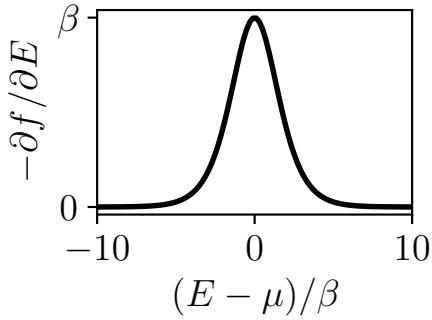

Figure D.1: Derivative of the Fermi distribution as a function of energy.

The zero-temperature limit is easily derived by approximating the Fermi distribution at zero temperature by $f(E) \approx \theta(\mu - E)$. The derivative is then

$$-\frac{\partial f}{\partial E} \approx \delta(\mu - E) . \tag{D.8}$$

Replacing the delta function in equation (D.7b) leads to the usual form of the conductance at zero-temperature (B.5b).

E EXPLICIT AVERAGING OVER DISORDER REALISATION

As an example, the first orders of the explicit averaging of the Green's function in the disordered system are calculated in this appendix. Given N sites and N_i impurities with fraction c such that $N_i = cN$, the structure factor is expressed by

$$\begin{aligned}\left\langle \rho_{\mathbf{q}} \right\rangle_{\text{av}} &= \sum_{\{\mathbf{R_j}\}} P\{\mathbf{R_j}\} \sum_{j=1}^{N_i} e^{-i\mathbf{q}\mathbf{R}_j} \\ &= c \sum_{j=1}^{N} e^{-i\mathbf{q}\mathbf{R}_j} = cN\delta_{\mathbf{q},0} = N_i \delta_{\mathbf{q},0} \end{aligned} \tag{E.1}$$

where $P\{\mathbf{R_j}\}$ indicates the probability distribution in the real space. The replacement $\sum_{\{\mathbf{R_j}\}} P\{\mathbf{R_j}\} \sum_{j=1}^{N_i} \to c \sum_{\text{all sites}}$ is done by considering a probability distribution of N_i impurities are distributed uniformly with fraction c [224]. Similarly, for the processes involving two structure factors one obtains

$$\begin{aligned}\left\langle \rho_{\mathbf{q_1}} \rho_{\mathbf{q_2}} \right\rangle_{\text{av}} &= \Big\langle \sum_{j_1,j_2}^{N_i} e^{-i\mathbf{q_1}\mathbf{R}_{j_1}} e^{-i\mathbf{q_2}\mathbf{R}_{j_2}} \Big\rangle_{\text{av}} \\ &= \Big\langle \sum_{j_1=j_2}^{N_i} e^{-i(\mathbf{q_1}+\mathbf{q_2})\mathbf{R}_{j_1}} + \sum_{j_1}^{N_i} e^{-i\mathbf{q_1}\mathbf{R}_{j_1}} \sum_{j_2\neq j_1}^{N_i} e^{-i\mathbf{q_2}\mathbf{R}_{j_2}} \Big\rangle_{\text{av}} \\ &= N_i \delta_{\mathbf{q_1}+\mathbf{q_2},0} + N_i \delta_{\mathbf{q_1},0} (N_i - 1)\delta_{\mathbf{q_2},0} \\ &\simeq N_i \delta_{\mathbf{q_1}+\mathbf{q_2},0} + N_i^2 \delta_{\mathbf{q_1},0}\delta_{\mathbf{q_2},0} \ , \end{aligned} \tag{E.2}$$

where in the last step $N_i \gg 1$ is considered.

Replacing the results for the structure factors in the expression of

$\mathcal{G}^{(n)}$ (5.28) for the first two orders are obtained

$$\left\langle \mathcal{G}^{(1)}_{\mathbf{k},\mathbf{k}'} \right\rangle_{\text{av}} = \mathcal{G}^0_{\mathbf{k}} \frac{1}{V} \left\langle \rho_{\mathbf{k}-\mathbf{k}'} \right\rangle_{\text{av}} U_{\mathbf{k},\mathbf{k}'} \mathcal{G}^0_{\mathbf{k}'} = \mathcal{G}^0_{\mathbf{k}} \left(U_{\mathbf{k},\mathbf{k}'} n_i \delta_{\mathbf{k},\mathbf{k}'} \right) \mathcal{G}^0_{\mathbf{k}'} \tag{E.3}$$

$$\left\langle \mathcal{G}^{(2)}_{\mathbf{k},\mathbf{k}'} \right\rangle_{\text{av}} = \mathcal{G}^0_{\mathbf{k}} \frac{1}{V^2} \sum_{\mathbf{q_1}} \left\langle \rho_{\mathbf{k}-\mathbf{q_1}} \rho_{\mathbf{q_1}-\mathbf{k}'} \right\rangle_{\text{av}} U_{\mathbf{k},\mathbf{q_1}} \mathcal{G}^0_{\mathbf{q_1}} U_{\mathbf{q_1},\mathbf{k}'} \mathcal{G}^0_{\mathbf{k}'} \tag{E.4}$$

$$= \mathcal{G}^0_{\mathbf{k}} \, n_i \delta_{\mathbf{k},\mathbf{k}'} \frac{1}{V} \sum_{\mathbf{q_1}} U_{\mathbf{k},\mathbf{q_1}} \mathcal{G}^0_{\mathbf{q_1}} U_{\mathbf{q_1},\mathbf{k}'} \mathcal{G}^0_{\mathbf{k}'}$$
$$+ \mathcal{G}^0_{\mathbf{k}} \, n_i^2 \sum_{\mathbf{q_1}} \delta_{\mathbf{k},\mathbf{q_1}} \delta_{\mathbf{q_1},\mathbf{k}'} U_{\mathbf{k},\mathbf{q_1}} \mathcal{G}^0_{\mathbf{q_1}} U_{\mathbf{q_1},\mathbf{k}'} \mathcal{G}^0_{\mathbf{k}'} \tag{E.5}$$

$$= \mathcal{G}^0_{\mathbf{k}} \left(n_i \frac{1}{V} \sum_{\mathbf{q_1}} U_{\mathbf{k},\mathbf{q_1}} \mathcal{G}^0_{\mathbf{q_1}} U_{\mathbf{q_1},\mathbf{k}'} \right) \delta_{\mathbf{k},\mathbf{k}'} \mathcal{G}^0_{\mathbf{k}'}$$
$$+ \mathcal{G}^0_{\mathbf{k}} \left(n_i^2 \, U_{\mathbf{k},\mathbf{k}'} \, \mathcal{G}^0_{\mathbf{k}'} \, U_{\mathbf{k}',\mathbf{k}'} \right) \delta_{\mathbf{k},\mathbf{k}'} \mathcal{G}^0_{\mathbf{k}'} \, . \tag{E.6}$$

where the impurity density is defined as $n_i \equiv N_i/V$.

The external propagators are explicitly separated in the equations in order to make clear the interaction part of the diagram. In this way, from the obtained expression, the Feynman rules reported in table 5.1 can be directly read out.

For higher values of n, calculating the average of ρ is straightforward but tedious. The process is the same as in equation (E.2): the sum is split into a factor which takes into account the same position (i.e. the same impurity) and a second factor which takes into account two different positions (i.e. two impurities), then three and so on. Then all the combinations have to be summed up correctly. This process is easier to do with diagrams: it is simpler to draw topologically different graphs than to construct all the non-equivalent subsets of n interactions with 1 to n impurities.

F ONE-BAND APPROXIMATION FOR POINT-LIKE IMPURITIES

This appendix is devoted to the calculation of equation (5.65). Starting from equation (5.13), the Green's function operators associated to $\mathcal{H}_{\text{eff}}$ and $\mathcal{H}_0$ satisfy [67]

$$\mathcal{G}^{\text{eff}} = \mathcal{G}^0 + \mathcal{G}^0 \sum_n |\, \omega_n \,\rangle \lambda_{\text{CPA}}(z) \langle\, \omega_n \,|\, \mathcal{G}^{\text{eff}} \ . \tag{F.1}$$

In the basis of the plane waves the closure relation is expressed as

$$\sum_{\mathbf{k}} |\, \mathbf{k} \,\rangle\langle\, \mathbf{k} \,| = \mathbb{1} \ , \tag{F.2}$$

$\mathbb{1}$ being the identity operator. By employing it and using equation (5.48a) one obtains

$$\begin{aligned} \langle\, \mathbf{k} \,|\, \mathcal{G}^{\text{eff}} \,|\, \mathbf{k}' \,\rangle &= \mathcal{G}^0_{\mathbf{k}}(z)\delta_{\mathbf{k},\mathbf{k}'} \\ &\quad + \frac{\lambda_{\text{CPA}}(z)}{a^2}\, \mathcal{G}^0_{\mathbf{k}}(z)\, \omega(\mathbf{k}) \sum_{\mathbf{K}} \omega^*(\mathbf{k}+\mathbf{K}) \langle\, \mathbf{k}+\mathbf{K} \,|\, \mathcal{G}^{\text{eff}} \,|\, \mathbf{k}' \,\rangle \ , \end{aligned}$$

where the index $\mathbf{K}$ runs over the vectors of the reciprocal lattice of the impurity lattice. In the one-band approximation, the Fourier transform of the shape function is assumed to vanish outside the BZ [88, 251]. In this way, the only term considered is the one of $\mathbf{K} = 0$, leading to

$$\langle\, \mathbf{k} \,|\, \mathcal{G}^{\text{eff}} \,|\, \mathbf{k}' \,\rangle = \left[1 - \frac{\lambda_{\text{CPA}}(z)}{a^2}\, \mathcal{G}^0_{\mathbf{k}}(z) |\, \omega(\mathbf{k})|^2 \right]^{-1} \mathcal{G}^0_{\mathbf{k}}(z)\delta_{\mathbf{k},\mathbf{k}'} \ . \tag{F.3}$$

The translational invariance of the effective medium ensures that the Green's function operator is diagonal in the basis of plane waves. The general relation between operators $(A-B)^{-1} = A^{-1}B(A-B)^{-1}$ allows to rewrite (F.3) as

$$\langle\, \mathbf{k} \,|\, \mathcal{G}^{\text{eff}} \,|\, \mathbf{k}' \,\rangle = \mathcal{G}^0_{\mathbf{k}} \big[z - \Sigma^{\text{CPA}}_{\mathbf{k}}(z) \big]\, \delta_{\mathbf{k},\mathbf{k}'} \ , \tag{F.4}$$

where $\Sigma^{\text{CPA}}_{\mathbf{k}}(z)$ was defined in equation (5.37).

Using the closure relation (F.2) we get

$$\begin{aligned} \langle\, \omega_n \,|\, \mathcal{G}^{\text{eff}}(z) \,|\, \omega_n \,\rangle &= \sum_{\mathbf{k}} \langle\, \mathbf{k} \,|\, \mathcal{G}^{\text{eff}} \,|\, \mathbf{k} \rangle\, |\langle\, \mathbf{k} \,|\, \omega_n \,\rangle|^2 \\ &= \frac{1}{V} \sum_{\mathbf{k}} \langle\, \mathbf{k} \,|\, \mathcal{G}^{\text{eff}} \,|\, \mathbf{k} \rangle\, |\omega(\mathbf{k})|^2 \ , \end{aligned} \tag{F.5}$$

where V is the volume of the system. After converting the sum over $\mathbf{k}$ into an integration it equation (5.65) is finally obtained.

BIBLIOGRAPHY

[1] D. A. Abanin et al. “Giant Nonlocality Near the Dirac Point in Graphene”. In: *Science* 332.6027 (2011), pp. 328–330. DOI: 10.1126/science.1199595.

[2] C. M. Acosta and A. Fazzio. “Spin-Polarization Control Driven by a Rashba-Type Effect Breaking the Mirror Symmetry in Two-Dimensional Dual Topological Insulators”. In: *Physical Review Letters* 122.3 (2019), p. 036401. DOI: 10.1103/PhysRevLett.122.036401.

[3] A. Agarwala and V. B. Shenoy. “Topological Insulators in Amorphous Systems”. In: *Physical Review Letters* 118.23 (2017), p. 236402. DOI: 10.1103/physrevlett.118.236402.

[4] A. Aharon-Steinberg, A. Marguerite, D. J. Perello, K. Bagani, T. Holder, Y. Myasoedov, L. S. Levitov, A. K. Geim, and E. Zeldov. “Long-range nontopological edge currents in charge-neutral graphene”. In: *Nature* 593.7860 (2021), pp. 528–534. DOI: 10.1038/s41586-021-03501-7.

[5] T. Aktor, J. H. Garcia, S. Roche, A.-P. Jauho, and S. R. Power. “Valley Hall effect and nonlocal resistance in locally gapped graphene”. In: *Physical Review B* 103.11 (2021), p. 115406. DOI: 10.1103/physrevb.103.115406.

[6] A. Altland and M. R. Zirnbauer. “Nonstandard symmetry classes in mesoscopic normal-superconducting hybrid structures”. In: *Physical Review B* 55.2 (1997), pp. 1142–1161. DOI: 10.1103/physrevb.55.1142.

[7] F. Amet, J. R. Williams, K. Watanabe, T. Taniguchi, and D. Goldhaber-Gordon. “Insulating Behavior at the Neutrality Point in Single-Layer Graphene”. In: *Physical Review Letters* 110.21 (2013), p. 216601. DOI: 10.1103/physrevlett.110.216601.

[8] P. W. Anderson. “Absence of diffusion in certain random lattices”. In: *Physical Review* 109.5 (1958), p. 1492. DOI: 10.1103/PhysRev.109.1492.

[9] H. Aoki, N. Tsuji, M. Eckstein, M. Kollar, T. Oka, and P. Werner. "Nonequilibrium dynamical mean-field theory and its applications". In: *Reviews of Modern Physics* 86.2 (2014), pp. 779–837. DOI: 10.1103/revmodphys.86.779.

[10] D. A. Areshkin, D. Gunlycke, and C. T. White. "Ballistic Transport in Graphene Nanostrips in the Presence of Disorder: Importance of Edge Effects". In: *Nano Letters* 7.1 (2006), pp. 204–210. DOI: 10.1021/nl062132h.

[11] N. P. Armitage, E. J. Mele, and A. Vishwanath. "Weyl and Dirac semimetals in three-dimensional solids". In: *Review of Modern Physics* 90.1 (2018), p. 015001. DOI: 10.1103/RevModPhys.90.015001.

[12] J. K. Asbóth, L. Oroszlány, and A. Pályi. *A Short Course on Topological Insulators*. Springer International Publishing, 2016. DOI: 10.1007/978-3-319-25607-8.

[13] Y. Baba, M. Amado, E. Diez, F. Domínguez-Adame, and R. A. Molina. "Effect of external fields in high Chern number quantum anomalous Hall insulators". In: *Physical Review B* 106.24 (2022), p. 245305. DOI: 10.1103/physrevb.106.245305.

[14] Y. Baba, A. Díaz-Fernández, E. Díaz, F. Domínguez-Adame, and R. A. Molina. "Electric field manipulation of surface states in topological semimetals". In: *Physical Review B* 100.16 (2019), p. 165105. DOI: 10.1103/PhysRevB.100.165105.

[15] Y. Baba, F. Domínguez-Adame, G. Platero, and R. A. Molina. "Rashba coupling and spin switching through surface states of Dirac semimetals". In: *New Journal of Physics* 23.2 (2021), p. 023008. DOI: 10.1088/1367-2630/abda56.

[16] D. N. Basov, R. D. Averitt, and D. Hsieh. "Towards properties on demand in quantum materials". In: *Nature Materials* 16.11 (2017), pp. 1077–1088. DOI: 10.1038/nmat5017.

[17] E. Benito-Matías and R. A. Molina. "Surface states in topological semimetal slab geometries". In: *Physical Review B* 99.7 (2019), p. 075304. DOI: 10.1103/PhysRevB.99.075304.

[18] B. A. Bernevig. *Topological Insulators and Topological Superconductors*. Princeton: Princeton University Press, 2013, p. 247. DOI: 10.1515/9781400846733.

[19] B. A. Bernevig, T. L. Hughes, and S.-C. Zhang. "Quantum Spin Hall Effect and Topological Phase Transition in HgTe Quantum Wells". In: *Science* 314.5806 (2006), pp. 1757–1761. DOI: 10.1126/science.1133734.

[20] G. Bhimanapati, N. Glavin, and J. Robinson. "2D Boron Nitride". In: *Semiconductors and Semimetals*. Elsevier, 2016, pp. 101–147. DOI: 10.1016/bs.semsem.2016.04.004.

[21] S. Bhowal and G. Vignale. "Orbital Hall effect as an alternative to valley Hall effect in gapped graphene". In: *Physical Review B* 103.19 (2021), p. 195309. DOI: 10.1103/physrevb.103.195309.

[22] R. R. Biswas and A. V. Balatsky. "Impurity-induced states on the surface of three-dimensional topological insulators". In: *Physical Review B* 81.23 (2010), p. 233405. DOI: 10.1103/PhysRevB.81.233405.

[23] H. Bruus, K. Flensberg, and O. U. Press. *Many-Body Quantum Theory in Condensed Matter Physics: An Introduction*. Oxford: Oxford University Press, 2004.

[24] A. Budewitz, K. Bendias, P. Leubner, T. Khouri, S. Shamim, S. Wiedmann, H. Buhmann, and L. W. Molenkamp. *Quantum anomalous Hall effect in Mn doped HgTe quantum wells*. 2017. DOI: 10.48550/ARXIV.1706.05789.

[25] J. C. Budich, F. Dolcini, P. Recher, and B. Trauzettel. "Phonon-Induced Backscattering in Helical Edge States". In: *Physical Review Letters* 108.8 (2012), p. 086602. DOI: 10.1103/physrevlett.108.086602.

[26] A. Burkov. "Weyl Metals". In: *Annual Review of Condensed Matter Physics* 9.1 (2018), p. 359. DOI: 10.1146/annurev-conmatphys-033117-054129.

[27] M. Büttiker. "Absence of backscattering in the quantum Hall effect in multiprobe conductors". In: *Physical Review B* 38.14 (1988), pp. 9375–9389. DOI: 10.1103/physrevb.38.9375.

[28] J. Cai et al. "Atomically precise bottom-up fabrication of graphene nanoribbons". In: *Nature* 466.7305 (2010), pp. 470–473. DOI: 10.1038/nature09211.

[29] K. E. Cakmak, A. Altıntas, and A. D. Güclü. "Effects of random atomic disorder on the magnetic stability of graphene nanoribbons with zigzag edges". In: *Physical Review B* 98.11 (2018), p. 115428. DOI: 10.1103/physrevb.98.115428.

[30] J. Callaway. *Quantum Theory of the Solid State*. v. 1. Academic Press, 1976.

[31] J. Cayssol, B. Dóra, F. Simon, and R. Moessner. "Floquet topological insulators". In: *Phys. Status Solidi Rapid Res. Lett.* 7.1-2 (2013), pp. 101–108. DOI: 10.1002/pssr.201206451.

[32] C.-K. Chan, P. A. Lee, K. S. Burch, J. H. Han, and Y. Ran. "When Chiral Photons Meet Chiral Fermions: Photoinduced Anomalous Hall Effects in Weyl Semimetals". In: *Physical Review Letters* 116 (2 2016), p. 026805. DOI: 10.1103/PhysRevLett.116.026805.

[33] C.-Z. Chang et al. "Experimental Observation of the Quantum Anomalous Hall Effect in a Magnetic Topological Insulator". In: *Science* 340.6129 (2013), pp. 167–170. DOI: 10.1126/science.1234414.

[34] C.-Z. Chang et al. "Thin Films of Magnetically Doped Topological Insulator with Carrier-Independent Long-Range Ferromagnetic Order". In: *Advanced Materials* 25.7 (2013), pp. 1065–1070. DOI: 10.1002/adma.201203493.

[35] T.-R. Chang et al. "Prediction of an arc-tunable Weyl Fermion metallic state in $Mo_xW_{1-x}Te_2$". In: *Nature Communications* 7.1 (2016), p. 10639. DOI: 10.1038/ncomms10639.

[36] M. Charlebois, D. Sénéchal, A.-M. Gagnon, and A.-M. S. Tremblay. "Impurity-induced magnetic moments on the graphene-lattice Hubbard model: An inhomogeneous cluster dynamical mean-field theory study". In: *Physical Review B* 91.3 (2015), p. 035132. DOI: 10.1103/physrevb.91.035132.

[37] C.-C. Chen, M. L. Teague, L He, X Kou, M Lang, W Fan, N Woodward, K.-L. Wang, and N.-C. Yeh. "Magnetism-induced massive Dirac spectra and topological defects in the surface state of Cr-doped Bi_2Se_3-bilayer topological insulators". In: *New Journal of Physics* 17.11 (2015), p. 113042. DOI: 10.1088/1367-2630/17/11/113042.

[38] Y. L. Chen et al. "Experimental Realization of a Three-Dimensional Topological Insulator, Bi_2Te_3". In: *Science* 325.5937 (2009), pp. 178–181. DOI: 10.1126/science.1173034.

[39] Y. Chen et al. "Ferromagnetism in van der Waals compound $MnS_{1.8}Bi_{0.2}Te_4$". In: *Physical Review Materials* 4.6 (2020), p. 064411. DOI: 10.1103/physrevmaterials.4.064411.

[40] J. Chesta Lopez, L. E. F. Foa Torres, and A. S. Nunez. "Multiterminal conductance at the surface of a Weyl semimetal". In: *Physical Review B* 97.12 (2018), p. 125419. DOI: 10.1103/PhysRevB.97.125419.

[41] H. Chi and J. S. Moodera. "Progress and prospects in the quantum anomalous Hall effect". In: *APL Materials* 10.9 (2022), p. 090903. DOI: 10.1063/5.0100989.

[42] C. Chiu, J. C. Y. Teo, A. P. Schnyder, and S. Ryu. "Classification of topological quantum matter with symmetries". In: *Reviews of Modern Physics* 88.3 (2016), p. 035005. DOI: 10.1103/revmodphys.88.035005.

[43] S. K. Chong, K. B. Han, T. D. Sparks, and V. V. Deshpande. "Tunable Coupling between Surface States of a Three-Dimensional Topological Insulator in the Quantum Hall Regime". In: *Physical Review Letters* 123.3 (2019), p. 036804. DOI: 10.1103/physrevlett.123.036804.

[44] J. L. Collins et al. "Electric-field-tuned topological phase transition in ultrathin Na_3Bi". In: *Nature* 564.7736 (2018), pp. 390–394. DOI: 10.1038/s41586-018-0788-5.

[45] P. Corbae, J. D. Hannukainen, Q. Marsal, D. Muñoz-Segovia, and A. G. Grushin. "Amorphous topological matter: Theory and experiment". In: *Europhysics Letters* 142.1 (2023), p. 16001. DOI: 10.1209/0295-5075/acc2e2.

[46] R. M. Corless, G. H. Gonnet, D. E. G. Hare, D. J. Jeffrey, and D. E. Knuth. "On the Lambert-W function". In: *Adv. Comput. Math.* 5.1 (1996), p. 329. DOI: 10.1007/BF02124750.

[47] M. Corso, E. Carbonell-Sanromà, and D. G. de Oteyza. "Bottom-Up Fabrication of Atomically Precise Graphene Nanoribbons". In: *On-Surface Synthesis II*. Springer International Publishing, 2018, pp. 113–152. DOI: 10.1007/978-3-319-75810-7_6.

[48] I. Crassee, R. Sankar, W.-L. Lee, A. Akrap, and M. Orlita. "3D Dirac semimetal Cd_3As_2: A review of material properties". In: *Physical Review Materials* 2.12 (12 2018), p. 120302. DOI: 10.1103/physrevmaterials.2.120302.

[49] A. Cresti, N. Nemec, B. Biel, G. Niebler, F. Triozon, G. Cuniberti, and S. Roche. "Charge transport in disordered graphene-based low dimensional materials". In: *Nano Research* 1.5 (2008), pp. 361–394. DOI: 10.1007/s12274-008-8043-2.

[50] B. Datta S. Das. "Electronic analog of the electro-optic modulator". In: *Applied Physics Letters* 56 (1990), p. 665. DOI: 10.1063/1.102730.

[51] S. Datta. *Electronic transport in mesoscopic systems*. Cambridge University Press, 1997, p. 377.

[52] C. R. Dean et al. "Boron nitride substrates for high-quality graphene electronics". In: *Nature Nanotechnology* 5.10 (2010), pp. 722–726. DOI: 10.1038/nnano.2010.172.

[53] R. Decker, Y. Wang, V. W. Brar, W. Regan, H.-Z. Tsai, Q. Wu, W. Gannett, A. Zettl, and M. F. Crommie. "Local Electronic Properties of Graphene on a BN Substrate via Scanning Tunneling Microscopy". In: *Nano Letters* 11.6 (2011), pp. 2291–2295. DOI: 10.1021/nl2005115.

[54] H. Dehghani, T. Oka, and A. Mitra. "Out-of-equilibrium electrons and the Hall conductance of a Floquet topological insulator". In: *Physical Review B* 91 (15 2015), p. 155422. DOI: 10.1103/PhysRevB.91.155422.

[55] Díaz-Fernández A., Chico Leonor, González J. W., and Domínguez-Adame F. "Tuning the Fermi velocity in Dirac materials with an electric field". In: *Scientific Reports* 7.1 (2017), p. 8058. DOI: 10.1038/s41598-017-08188-3.

[56] A. Díaz-Fernández and F. Domínguez-Adame. "Quantum-confined Stark effect in band-inverted junctions". In: *Physica E: Low-Dimensional Systems and Nanostructures* 93 (2017), pp. 230–233. DOI: 10.1016/j.physe.2017.06.026.

[57] P. Dirac. "The quantum theory of the electron". In: *Proceedings of the Royal Society of London. Series A, Containing Papers of a Mathematical and Physical Character* 117.778 (1928), pp. 610–624. DOI: 10.1098/rspa.1928.0023.

[58] F. Domínguez-Adame, E. Diez, and A. Sánchez. "Three-dimensional effects on extended states in disordered models of polymers". In: *Physical Review B* 51.13 (1995), p. 8115. DOI: 10.1103/PhysRevB.51.8115.

[59] F. Domínguez-Adame, B. Méndez, E. Maciá, and M. A. González. "Non-local separable potential approach to multicentre interactions". In: *Molecular Physics* 74.5 (1991), p. 1065. DOI: 10.1080/00268979100102801.

[60] B. Dóra, K. Ziegler, and P. Thalmeier. "Effect of weak disorder on the density of states in graphene". In: *Physical Review B* 77.11 (11 2008), p. 115422. DOI: 10.1103/PhysRevB.77.115422.

[61] K. Drese and M. Holthaus. “Floquet theory for short laser pulses”. In: *The European Physical Journal D - Atomic, Molecular and Optical Physics* 5.1 (1999), pp. 119–134. DOI: 10.1007/s100530050236.

[62] G. Dresselhaus. “Spin-Orbit Coupling Effects in Zinc Blende Structures”. In: *Physical Review* 100 (1955), p. 580. DOI: 10.1103/PhysRev.100.580.

[63] Y. Du, N. Xu, X. Lin, and A.-P. Jauho. “Moiré effects in graphene-hBN heterostructures”. In: *Physical Review Research* 2.4 (2020), p. 043427. DOI: 10.1103/physrevresearch.2.043427.

[64] D. H. Dunlap and V. M. Kenkre. “Dynamic localization of a charged particle moving under the influence of an electric field”. In: *Physical Review B* 34.6 (1986), pp. 3625–3633. DOI: 10.1103/physrevb.34.3625.

[65] L. Q. Duong, H. Lin, W.-F. Tsai, and Y. P. Feng. “Quantum anomalous Hall effect with field-tunable Chern number near $\mathbb{Z}_2$ topological critical point”. In: *Physical Review B* 92.11 (2015), p. 115205. DOI: 10.1103/physrevb.92.115205.

[66] A. Eckardt. “Colloquium: Atomic quantum gases in periodically driven optical lattices”. In: *Reviews of Modern Physics* 89.1 (2017), p. 011004. DOI: 10.1103/revmodphys.89.011004.

[67] E. Economou. *Green’s functions in quantum physics*. Berlin: Springer, 2006. DOI: 10.1007/978-3-662-11900-6.

[68] R. J. Elliott, J. A. Krumhansl, and P. L. Leath. “The theory and properties of randomly disordered crystals and related physical systems”. In: *Review of Modern Physics* 46.3 (1974), p. 465. DOI: 10.1103/RevModPhys.46.465.

[69] C. Fang, M. J. Gilbert, and B. A. Bernevig. “Large-Chern-Number Quantum Anomalous Hall Effect in Thin-Film Topological Crystalline Insulators”. In: *Physical Review Letters* 112 (4 2014), p. 046801. DOI: 10.1103/PhysRevLett.112.046801.

[70] A. Farrell, A. Arsenault, and T. Pereg-Barnea. “Dirac cones, Floquet side bands, and theory of time-resolved angle-resolved photoemission”. In: *Physical Review B* 94.15 (2016), p. 155304. DOI: 10.1103/physrevb.94.155304.

[71] H. Feldner, Z. Y. Meng, A. Honecker, D. Cabra, S. Wessel, and F. F. Assaad. “Magnetism of finite graphene samples: Mean-field theory compared with exact diagonalization and quantum Monte Carlo simulations”. In: *Physical Review B* 81.11 (2010), p. 115416. DOI: 10.1103/physrevb.81.115416.

[72] X. Feng et al. “Thickness Dependence of the Quantum Anomalous Hall Effect in Magnetic Topological Insulator Films”. In: *Advanced Materials* 28.30 (2016), pp. 6386–6390. DOI: 10.1002/adma.201600919.

[73] J. Fernández-Rossier and J. J. Palacios. “Magnetism in Graphene Nanoislands”. In: *Physical Review Letters* 99.17 (2007), p. 177204. DOI: 10.1103/physrevlett.99.177204.

[74] E. Fradkin. “Critical behavior of disordered degenerate semiconductors. I. Models, symmetries, and formalism”. In: *Physical Review B* 33 (5 1986), pp. 3257–3262. DOI: 10.1103/PhysRevB.33.3257.

[75] E. Fradkin. “Critical behavior of disordered degenerate semiconductors. II. Spectrum and transport properties in mean-field theory”. In: *Physical Review B* 33.5 (1986), pp. 3263–3268. DOI: 10.1103/physrevb.33.3263.

[76] J. K. Freericks, H. R. Krishnamurthy, and T. Pruschke. “Theoretical Description of Time-Resolved Photoemission Spectroscopy: Application to Pump-Probe Experiments”. In: *Physical Review Letters* 102.13 (2009), p. 136401. DOI: 10.1103/physrevlett.102.136401.

[77] H.-H. Fu, J.-T. Lü, and J.-H. Gao. “Finite-size effects in the quantum anomalous Hall system”. In: *Physical Review B* 89.20 (2014), p. 205431. DOI: 10.1103/physrevb.89.205431.

[78] L. Fu. “Hexagonal Warping Effects in the Surface States of the Topological Insulator Bi_2Te_3”. In: *Physical Review Letters* 103.26 (2009), p. 266801. DOI: 10.1103/physrevlett.103.266801.

[79] L. Fu and C. L. Kane. “Time reversal polarization and a Z_2 adiabatic spin pump”. In: *Physical Review B* 74.19 (2006), p. 195312. DOI: 10.1103/physrevb.74.195312.

[80] L. Fu, C. L. Kane, and E. J. Mele. “Topological Insulators in Three Dimensions”. In: *Physical Review Letters* 98.10 (2007), p. 106803. DOI: 10.1103/physrevlett.98.106803.

[81] M. Fujita, K. Wakabayashi, K. Nakada, and K. Kusakabe. “Peculiar Localized State at Zigzag Graphite Edge”. In: *Journal of the Physical Society of Japan* 65.7 (1996), pp. 1920–1923. DOI: 10.1143/jpsj.65.1920.

[82] T. Fukui, Y. Hatsugai, and H. Suzuki. "Chern Numbers in Discretized Brillouin Zone: Efficient Method of Computing (Spin) Hall Conductances". In: *Journal of the Physical Society of Japan* 74.6 (2005), pp. 1674–1677. DOI: 10.1143/jpsj.74.1674.

[83] T. Fukuzawa, M. Koshino, and T. Ando. "Weak-field Hall effect in graphene calculated within self-consistent Born approximation". In: *J. Phys. Soc. Jpn.* 78.9 (2009), p. 094714. DOI: 10.1143/JPSJ.78.094714.

[84] Q. D. Gibson, L. M. Schoop, L. Muechler, L. S. Xie, M. Hirschberger, N. P. Ong, R. Car, and R. J. Cava. "Three-dimensional Dirac semimetals: Design principles and predictions of new materials". In: *Physical Review B* 91.20 (2015), p. 205128. DOI: 10.1103/PhysRevB.91.205128.

[85] G. Giovannetti, P. A. Khomyakov, G. Brocks, P. J. Kelly, and J. van den Brink. "Substrate-induced band gap in graphene on hexagonal boron nitride:Ab initiodensity functional calculations". In: *Physical Review B* 76.7 (2007), p. 073103. DOI: 10.1103/physrevb.76.073103.

[86] U. D. Giovannini and H. Hübener. "Floquet analysis of excitations in materials". In: *Journal of Physics: Materials* 3.1 (2019), p. 012001. DOI: 10.1088/2515-7639/ab387b.

[87] C. Girit et al. "Graphene at the Edge: Stability and Dynamics". In: *Science* 323.5922 (2009), pp. 1705–1708. DOI: 10.1126/science.1166999.

[88] M. L. Glasser and P. R. Sievert. "Interband Effects in the Coherent Potential Approximation: Simple Two Band Model". In: *Canadian Journal of Physics* 53.11 (1975), p. 1109. DOI: 10.1139/p75-140.

[89] N. Goldman, J. C. Budich, and P. Zoller. "Topological quantum matter with ultracold gases in optical lattices". In: *Nature Physics* 12.7 (2016), pp. 639–645. DOI: 10.1038/nphys3803.

[90] A. Gómez-León and G. Platero. "Floquet-Bloch Theory and Topology in Periodically Driven Lattices". In: *Physical Review Letters* 110.20 (2013), p. 200403. DOI: 10.1103/physrevlett.110.200403.

[91] A. Gonis. *Green functions for ordered and disordered systems*. Amsterdam: North-Holland, 1992.

[92] C González-Santander, T Apostolova, and F Domínguez-Adame. "Binding energy of hydrogenic impurities in quantum dots under intense laser radiation". In: *Journal of Physics: Condensed Matter* 25.33 (2013), p. 335802. DOI: 10.1088/0953-8984/25/33/335802.

[93] J. González and R. A. Molina. "Topological protection from exceptional points in Weyl and nodal-line semimetals". In: *Physical Review B* 96 (4 2017), p. 045437. DOI: 10.1103/PhysRevB.96.045437.

[94] J. González and R. A. Molina. "Macroscopic Degeneracy of Zero-Mode Rotating Surface States in 3D Dirac and Weyl Semimetals under Radiation". In: *Physical Review Letters* 116 (15 2016), p. 156803. DOI: 10.1103/PhysRevLett.116.156803.

[95] V. Gorbachev R. et al. "Detecting topological currents in graphene superlattices". In: *Science* 346.6208 (2014), pp. 448–451. DOI: 10.1126/science.1254966.

[96] E. V. Gorbar, V. A. Miransky, I. A. Shovkovy, and P. O. Sukhachov. "Dirac semimetals A_3Bi (A=Na,K,Rb) as $\mathbb{Z}_2$ Weyl semimetals". In: *Physical Review B* 91.12 (2015), p. 121101. DOI: 10.1103/PhysRevB.91.121101.

[97] E. V. Gorbar, V. A. Miransky, I. A. Shovkovy, and P. O. Sukhachov. "Surface Fermi arcs in $\mathbb{Z}_2$ Weyl semimetals A_3Bi (A= Na, K, Rb)". In: *Physical Review B* 91.23 (2015), p. 235138. DOI: 10.1103/PhysRevB.91.235138.

[98] G. Grabecki et al. "Nonlocal resistance and its fluctuations in microstructures of band-inverted HgTe/(Hg,Cd)Te quantum wells". In: *Physical Review B* 88.16 (2013), p. 165309. DOI: 10.1103/physrevb.88.165309.

[99] M. Graml, M. Nitsch, A. Seith, F. Evers, and J. Wilhelm. "Influence of chirp and carrier-envelope phase on noninteger high-harmonic generation". In: *Physical Review B* 107.5 (2023), p. 054305. DOI: 10.1103/physrevb.107.054305.

[100] D. Gresch, G. Autès, O. V. Yazyev, M. Troyer, D. Vanderbilt, B. A. Bernevig, and A. A. Soluyanov. "Z2Pack: Numerical implementation of hybrid Wannier centers for identifying topological materials". In: *Physical Review B* 95.7 (2017), p. 075146. DOI: 10.1103/physrevb.95.075146.

[101] C. W. Groth, M. Wimmer, A. R. Akhmerov, J. Tworzydło, and C. W. J. Beenakker. "Theory of the topological Anderson insulator". In: *Physical Review Letters* 103.19 (2009), p. 196805. DOI: 10.1103/PhysRevLett.103.196805.

[102] C. W. Groth, M. Wimmer, A. R. Akhmerov, and X. Waintal. "Kwant: a software package for quantum transport". In: *New Journal of Physics* 16.6 (2014), p. 063065. DOI: 10.1088/1367-2630/16/6/063065.

[103] D. Gunlycke, D. A. Areshkin, and C. T. White. "Semiconducting graphene nanostrips with edge disorder". In: *Applied Physics Letters* 90.14 (2007), p. 142104. DOI: 10.1063/1.2718515.

[104] G. M. Gusev, Z. D. Kvon, E. B. Olshanetsky, A. D. Levin, Y. Krupko, J. C. Portal, N. N. Mikhailov, and S. A. Dvoretsky. "Temperature dependence of the resistance of a two-dimensional topological insulator in a HgTe quantum well". In: *Physical Review B* 89.12 (2014), p. 125305. DOI: 10.1103/physrevb.89.125305.

[105] F. D. M. Haldane. "Model for a Quantum Hall Effect without Landau Levels: Condensed-Matter Realization of the Parity Anomaly". In: *Physical Review Letters* 61.18 (1988), pp. 2015–2018. DOI: 10.1103/physrevlett.61.2015.

[106] F. Haldane. "Continuum dynamics of the 1-D Heisenberg antiferromagnet: Identification with the O(3) nonlinear sigma model". In: *Physics Letters A* 93.9 (1983), pp. 464–468. DOI: 10.1016/0375-9601(83)90631-x.

[107] M. Z. Hasan and C. L. Kane. "*Colloquium*: Topological insulators". In: *Reviews of Modern Physics* 82.4 (2010), pp. 3045–3067. DOI: 10.1103/revmodphys.82.3045.

[108] M. Z. Hasan and J. E. Moore. "Three-Dimensional Topological Insulators". In: *Annual Review of Condensed Matter Physics* 2.1 (2011), pp. 55–78. DOI: 10.1146/annurev-conmatphys-062910-140432.

[109] Y. Hatsugai. "Chern number and edge states in the integer quantum Hall effect". In: *Physical Review Letters* 71.22 (1993), pp. 3697–3700. DOI: 10.1103/PhysRevLett.71.3697.

[110] K. He, Y. Wang, and Q.-K. Xue. "Topological Materials: Quantum Anomalous Hall System". In: *Annual Review of Condensed Matter Physics* 9.1 (2018), pp. 329–344. DOI: 10.1146/annurev-conmatphys-033117-054144.

[111] J. L. Hernando, Y. Baba, E. Díaz, and F. Domínguez-Adame. "Many-impurity scattering on the surface of a topological insulator". In: *Scientific Reports* 11.1 (2021). DOI: 10.1038/s41598-021-84801-w.

[112] M. Holthaus. "Floquet engineering with quasienergy bands of periodically driven optical lattices". In: *Journal of Physics B: Atomic, Molecular and Optical Physics* 49.1 (2015), p. 013001. DOI: 10.1088/0953-4075/49/1/013001.

[113] D. Hsieh, D. Qian, L. Wray, Y. Xia, Y. S. Hor, R. J. Cava, and M. Z. Hasan. "A topological Dirac insulator in a quantum spin Hall phase". In: *Nature* 452.7190 (2008), pp. 970–974. DOI: 10.1038/nature06843.

[114] D. Hsieh et al. "A tunable topological insulator in the spin helical Dirac transport regime". In: *Nature* 460.7259 (2009), pp. 1101–1105. DOI: 10.1038/nature08234.

[115] B. Y. K. Hu, E. H. Hwang, and S. Das Sarma. "Density of states of disordered graphene". In: *Physical Review B* 78.16 (2008), p. 165411. DOI: 10.1103/PhysRevB.78.165411.

[116] T. N. Ikeda, S. Tanaka, and Y. Kayanuma. "Floquet-Landau-Zener interferometry: Usefulness of the Floquet theory in pulse-laser-driven systems". In: *Physical Review Research* 4.3 (2022), p. 033075. DOI: 10.1103/physrevresearch.4.033075.

[117] S. Ito et al. "Build-up and dephasing of Floquet–Bloch bands on subcycle timescales". In: *Nature* 616.7958 (2023), pp. 696–701. DOI: 10.1038/s41586-023-05850-x.

[118] R. Jackiw and C. Rebbi. "Solitons with fermion number $\frac{1}{2}$". In: *Physical Review D* 13.12 (1976), pp. 3398–3409. DOI: 10.1103/physrevd.13.3398.

[119] W. Jones and N. March. *Theoretical solid state physics: Non-equilibrium and disorder*. New York: Dover Publications, 1985.

[120] G. Jotzu, M. Messer, R. Desbuquois, M. Lebrat, T. Uehlinger, D. Greif, and T. Esslinger. "Experimental realization of the topological Haldane model with ultracold fermions". In: *Nature* 515.7526 (2014), pp. 237–240. DOI: 10.1038/nature13915.

[121] F. de Juan, E. H. Hwang, and M. A. H. Vozmediano. "Spectral and optical properties of doped graphene with charged impurities in the self-consistent Born approximation". In: *Physical Review B* 82.24 (2010), p. 245418. DOI: 10.1103/PhysRevB.82.245418.

[122] J. Jung, A. M. DaSilva, A. H. MacDonald, and S. Adam. "Origin of band gaps in graphene on hexagonal boron nitride". In: *Nature Communications* 6.1 (2015). DOI: 10.1038/ncomms7308.

[123] C. L. Kane and E. J. Mele. "Quantum Spin Hall Effect in Graphene". In: *Physical Review Letters* 95.22 (2005), p. 226801. DOI: 10.1103/physrevlett.95.226801.

[124] C. L. Kane and E. J. Mele. "$\mathbb{Z}_2$ Topological Order and the Quantum Spin Hall Effect". In: *Physical Review Letters* 95 (14 2005), p. 146802. DOI: 10.1103/PhysRevLett.95.146802.

[125] C. Kane. "Topological Band Theory and the $\mathbb{Z}_2$ Invariant". In: *Topological Insulators*. Ed. by M. Franz and L. Molenkamp. Vol. 6. Contemporary Concepts of Condensed Matter Science. Elsevier, 2013, pp. 3–34. DOI: 10.1016/B978-0-444-63314-9.00001-9.

[126] M. Kargarian, M. Randeria, and Y.-M. Lu. "Are the surface Fermi arcs in Dirac semimetals topologically protected?" In: *Proceedings of the National Academy of Sciences* 113.31 (2016), pp. 8648–8652. DOI: 10.1073/pnas.1524787113.

[127] M. I. Katsnelson. "Graphene: carbon in two dimensions". In: *Materials Today* 10.1-2 (2007), pp. 20–27. DOI: 10.1016/s1369-7021(06)71788-6.

[128] M. Kim et al. "Control of electron-electron interaction in graphene by proximity screening". In: *Nature Communications* 11.1 (2020). DOI: 10.1038/s41467-020-15829-1.

[129] M. Kim, C. H. Kim, H.-S. Kim, and J. Ihm. "Topological quantum phase transitions driven by external electric fields in Sb_2Te_3 thin films". In: *Proc. Natl. Acad. Sci. U.S.A.* 109.3 (2012), pp. 671–674. DOI: 10.1073/pnas.1119010109.

[130] M. Kindermann, B. Uchoa, and D. L. Miller. "Zero-energy modes and gate-tunable gap in graphene on hexagonal boron nitride". In: *Physical Review B* 86.11 (2012), p. 115415. DOI: 10.1103/physrevb.86.115415.

[131] A. Kitaev, V. Lebedev, and M. Feigel'man. "Periodic table for topological insulators and superconductors". In: *AIP Conference Proceedings*. AIP, 2009. DOI: 10.1063/1.3149495.

[132] T. Kitagawa, T. Oka, A. Brataas, L. Fu, and E. Demler. "Transport properties of nonequilibrium systems under the application of light: Photoinduced quantum Hall insulators without Landau levels". In: *Physical Review B* 84.23 (2011), p. 235108. DOI: 10.1103/physrevb.84.235108.

[133] J. Klier, I. V. Gornyi, and A. D. Mirlin. "From weak to strong disorder in Weyl semimetals: Self-consistent Born approximation". In: *Physical Review B* 100.12 (2019), p. 125160. DOI: 10.1103/PhysRevB.100.125160.

[134] K. v. Klitzing, G. Dorda, and M. Pepper. "New Method for High-Accuracy Determination of the Fine-Structure Constant Based on Quantized Hall Resistance". In: *Physical Review Letters* 45.6 (1980), pp. 494–497. DOI: 10.1103/physrevlett.45.494.

[135] K. von Klitzing. "Quantum Hall Effect: Discovery and Application". In: *Annual Review of Condensed Matter Physics* 8.1 (2017), pp. 13–30. DOI: 10.1146/annurev-conmatphys-031016-025148.

[136] B. W. Knight and G. A. Peterson. "Solvable three-dimensional lattice models". In: *Physical Review* 132.3 (1963), p. 1085. DOI: 10.1103/PhysRev.132.1085.

[137] K. Kobayashi, T. Ohtsuki, K.-I. Imura, and I. F. Herbut. "Density of States Scaling at the Semimetal to Metal Transition in Three Dimensional Topological Insulators". In: *Physical Review Letters* 112.1 (1 2014), p. 016402. DOI: 10.1103/PhysRevLett.112.016402.

[138] K. Komatsu, Y. Morita, E. Watanabe, D. Tsuya, K. Watanabe, T. Taniguchi, and S. Moriyama. "Observation of the quantum valley Hall state in ballistic graphene superlattices". In: *Science Advances* 4.5 (2018). DOI: 10.1126/sciadv.aaq0194.

[139] M. König, S. Wiedmann, C. Brüne, A. Roth, H. Buhmann, L. W. Molenkamp, X.-L. Qi, and S.-C. Zhang. "Quantum Spin Hall Insulator State in HgTe Quantum Wells". In: *Science* 318.5851 (2007), pp. 766–770. DOI: 10.1126/science.1148047.

[140] J. M. Kosterlitz and D. J. Thouless. "Long range order and metastability in two dimensional solids and superfluids. (Application of dislocation theory)". In: *Journal of Physics C: Solid State Physics* 5.11 (1972), pp. L124–L126. DOI: 10.1088/0022-3719/5/11/002.

[141] J. M. Kosterlitz and D. J. Thouless. "Ordering, metastability and phase transitions in two-dimensional systems". In: *Journal of Physics C: Solid State Physics* 6.7 (1973), pp. 1181–1203. DOI: 10.1088/0022-3719/6/7/010.

[142] V. N. Kotov, B. Uchoa, V. M. Pereira, F. Guinea, and A. H. C. Neto. "Electron-Electron Interactions in Graphene: Current Status and Perspectives". In: *Reviews of Modern Physics* 84.3 (2012), pp. 1067–1125. DOI: 10.1103/revmodphys.84.1067.

[143] S. S. Krishtopenko, M. Antezza, and F. Teppe. "Disorder-induced phase transition in Dirac systems beyond the linear approximation". In: *Physical Review B* 101.20 (20 2020), p. 205424. DOI: 10.1103/PhysRevB.101.205424.

[144] S. Kudła, A. Dyrdał, V. K. Dugaev, J. Berakdar, and J. Barnás. "Conduction of surface electrons in a topological insulator with spatially random magnetization". In: *Physical Review B* 100.20 (2019), p. 205428. DOI: 10.1103/PhysRevB.100.205428.

[145] M. König et al. “Spatially Resolved Study of Backscattering in the Quantum Spin Hall State”. In: *Physical Review X* 3.2 (2013), p. 021003. DOI: 10.1103/physrevx.3.021003.

[146] H. Lee, K. Wakabayashi, Y.-W. Son, and Y. Miyamoto. “A single particle Hamiltonian for electro-magnetic properties of graphene nanoribbons”. In: *Carbon* 50.10 (2012), pp. 3454–3458. DOI: 10.1016/j.carbon.2012.03.009.

[147] J. Li, R.-L. Chu, J. K. Jain, and S.-Q. Shen. “Topological Anderson Insulator”. In: *Physical Review Letters* 102.13 (13 2009), p. 136806. DOI: 10.1103/PhysRevLett.102.136806.

[148] T. Li et al. “Quantum anomalous Hall effect from intertwined moiré bands”. In: *Nature* 600.7890 (2021), pp. 641–646. DOI: 10.1038/s41586-021-04171-1.

[149] W. Li et al. “Density of states and its local fluctuations determined by capacitance of strongly disordered graphene”. In: *Scientific Reports* 3.1 (2013), p. 1772. DOI: 10.1038/srep01772.

[150] J. Liao et al. “Observation of Anderson Localization in Ultrathin Films of Three-Dimensional Topological Insulators”. In: *Physical Review Letters* 114.21 (2015), p. 216601. DOI: 10.1103/physrevlett.114.216601.

[151] H. Lignier, C. Sias, D. Ciampini, Y. Singh, A. Zenesini, O. Morsch, and E. Arimondo. “Dynamical Control of Matter-Wave Tunneling in Periodic Potentials”. In: *Physical Review Letters* 99.22 (2007), p. 220403. DOI: 10.1103/physrevlett.99.220403.

[152] L. R. F. Lima and C. Lewenkopf. “Breakdown of topological protection due to nonmagnetic edge disorder in two-dimensional materials in the quantum spin Hall phase”. In: *Physical Review B* 106.24 (2022), p. 245408. DOI: 10.1103/physrevb.106.245408.

[153] N. H. Lindner, G. Refael, and V. Galitski. “Floquet topological insulator in semiconductor quantum wells”. In: *Nature Physics* 7.6 (2011), pp. 490–495. DOI: 10.1038/nphys1926.

[154] C.-X. Liu, X.-L. Qi, X. Dai, Z. Fang, and S.-C. Zhang. “Quantum Anomalous Hall Effect in $Hg_{1-y}Mn_yTe$ Quantum Wells”. In: *Physical Review Letters* 101.14 (2008), p. 146802. DOI: 10.1103/physrevlett.101.146802.

[155] C.-X. Liu, X.-L. Qi, H. Zhang, X. Dai, Z. Fang, and S.-C. Zhang. “Model Hamiltonian for topological insulators”. In: *Physical Review B* 82.4 (2010), p. 045122. DOI: 10.1103/physrevb.82.045122.

[156] C.-X. Liu, S.-C. Zhang, and X.-L. Qi. "The Quantum Anomalous Hall Effect: Theory and Experiment". In: *Annual Review of Condensed Matter Physics* 7.1 (2016), pp. 301–321. DOI: 10.1146/annurev-conmatphys-031115-011417.

[157] C. Liu and S. Zhang. "Models and Materials for Topological Insulators". In: *Contemporary Concepts of Condensed Matter Science*. Elsevier, 2013, pp. 59–89. DOI: 10.1016/b978-0-444-63314-9.00003-2.

[158] J. Y. Liu et al. "Spin-valley locking and bulk quantum Hall effect in a noncentrosymmetric Dirac semimetal $BaMnSb_2$". In: *Nature Communications* 12.1 (2021). DOI: 10.1038/s41467-021-24369-1.

[159] Z. K. Liu et al. "A stable three-dimensional topological Dirac semimetal Cd_3As_2". In: *Nature Materials* 13.7 (2014), pp. 677–681. DOI: 10.1038/nmat3990.

[160] Z. K. Liu et al. "Discovery of a three-dimensional topological Dirac semimetal Na_3Bi". In: *Science* 343.6173 (2014), p. 864. DOI: 10.1126/science.1245085.

[161] Z. Liu, K. Suenaga, P. J. F. Harris, and S. Iijima. "Open and Closed Edges of Graphene Layers". In: *Physical Review Letters* 102.1 (2009), p. 015501. DOI: 10.1103/physrevlett.102.015501.

[162] S. López and F. Domínguez-Adame. "Non-local potential approach to the ground state of confined excitons in quantum dots". In: *Semiconductor Science and Technology* 17.3 (2002), p. 227. DOI: 10.1088/0268-1242/17/3/308.

[163] H.-Z. Lu, J. Shi, and S.-Q. Shen. "Competition between Weak Localization and Antilocalization in Topological Surface States". In: *Physical Review Letters* 107.7 (2011), p. 076801. DOI: 10.1103/physrevlett.107.076801.

[164] A. M. Lunde and G. Platero. "Helical edge states coupled to a spin bath: Current-induced magnetization". In: *Physical Review B* 86.3 (2012), p. 035112. DOI: 10.1103/physrevb.86.035112.

[165] J. Maciejko, T. L. Hughes, and S.-C. Zhang. "The Quantum Spin Hall Effect". In: *Annual Review of Condensed Matter Physics* 2.1 (2011), pp. 31–53. DOI: 10.1146/annurev-conmatphys-062910-140538.

[166] J. Maciejko, C. Liu, Y. Oreg, X.-L. Qi, C. Wu, and S.-C. Zhang. "Kondo Effect in the Helical Edge Liquid of the Quantum Spin Hall State". In: *Physical Review Letters* 102.25 (2009), p. 256803. DOI: 10.1103/physrevlett.102.256803.

[167] F. Mahmood, C.-K. Chan, Z. Alpichshev, D. Gardner, Y. Lee, P. A. Lee, and N. Gedik. "Selective scattering between Floquet–Bloch and Volkov states in a topological insulator". In: *Nature Physics* 12.4 (2016), pp. 306–310. DOI: 10.1038/nphys3609.

[168] A. Manchon, H. C. Koo, J. Nitta, S. M. Frolov, and R. A. Duine. "New perspectives for Rashba spin–orbit coupling". In: *Nature Materials* 14.9 (2015), pp. 871–882. DOI: 10.1038/nmat4360.

[169] J. M. Marmolejo-Tejada, J. H. García, M. D. Petrović, P.-H. Chang, X.-L. Sheng, A Cresti, P Plecháč, S Roche, and B. K. Nikolić. "Deciphering the origin of nonlocal resistance in multiterminal graphene on hexagonal-boron-nitride with ab initio quantum transport: Fermi surface edge currents rather than Fermi sea topological valley currents". In: *Journal of Physics: Materials* 1.1 (2018), p. 015006. DOI: 10.1088/2515-7639/aad585.

[170] J. W. McIver, B. Schulte, F.-U. Stein, T. Matsuyama, G. Jotzu, G. Meier, and A. Cavalleri. "Light-induced anomalous Hall effect in graphene". In: *Nature Physics* 16.1 (2019), pp. 38–41. DOI: 10.1038/s41567-019-0698-y.

[171] H. Min, J. E. Hill, N. A. Sinitsyn, B. R. Sahu, L. Kleinman, and A. H. MacDonald. "Intrinsic and Rashba spin-orbit interactions in graphene sheets". In: *Physical Review B* 74.16 (2006), p. 165310. DOI: 10.1103/physrevb.74.165310.

[172] M. Mogi, R. Yoshimi, A. Tsukazaki, K. Yasuda, Y. Kozuka, K. S. Takahashi, M. Kawasaki, and Y. Tokura. "Magnetic modulation doping in topological insulators toward higher-temperature quantum anomalous Hall effect". In: *Applied Physics Letters* 107.18 (2015), p. 182401. DOI: 10.1063/1.4935075.

[173] P. Moon and M. Koshino. "Electronic properties of graphene/hexagonal-boron-nitride moiré superlattice". In: *Physical Review B* 90.15 (2014), p. 155406. DOI: 10.1103/physrevb.90.155406.

[174] J. E. Moore and L. Balents. "Topological invariants of time-reversal-invariant band structures". In: *Physical Review B* 75.12 (2007), p. 121306. DOI: 10.1103/physrevb.75.121306.

[175] S. Murakami. "Quantum Spin Hall Effect and Enhanced Magnetic Response by Spin-Orbit Coupling". In: *Physical Review Letters* 97.23 (2006), p. 236805. DOI: 10.1103/physrevlett.97.236805.

[176] M. Nakahara. *Geometry, Topology and Physics*. CRC Press, 2018.

[177] A. Narita, X.-Y. Wang, X. Feng, and K. Müllen. "New advances in nanographene chemistry". In: *Chemical Society Reviews* 44.18 (2015), pp. 6616–6643. DOI: 10.1039/c5cs00183h.

[178] A. H. C. Neto, F. Guinea, N. M. R. Peres, K. S. Novoselov, and A. K. Geim. "The electronic properties of graphene". In: *Reviews of Modern Physics* 81.1 (2009), pp. 109–162. DOI: 10.1103/revmodphys.81.109.

[179] M. Neupane et al. "Observation of a three-dimensional topological Dirac semimetal phase in high-mobility Cd_3As_2". In: *Nature Communications* 5.1 (2014), p. 3786. DOI: 10.1038/ncomms4786.

[180] H. B. Nielsen and M. Ninomiya. "The Adler-Bell-Jackiw anomaly and Weyl fermions in a crystal". In: *Physics Letters B* 130.6 (1983), pp. 389–396. DOI: 10.1016/0370-2693(83)91529-0.

[181] S. Nishihaya, M. Uchida, Y. Nakazawa, M. Kriener, Y. Taguchi, and M. Kawasaki. "Intrinsic coupling between spatially-separated surface Fermi-arcs in Weyl orbit quantum Hall states". In: *Nature Communications* 12.1 (2021). DOI: 10.1038/s41467-021-22904-8.

[182] S. Nishihaya, M. Uchida, Y. Nakazawa, R. Kurihara, K. Akiba, M. Kriener, A. Miyake, Y. Taguchi, M. Tokunaga, and M. Kawasaki. "Quantized surface transport in topological Dirac semimetal films". In: *Nature Communications* 10.1 (2019), p. 2564. DOI: 10.1038/s41467-019-10499-0.

[183] J. Nitta, T. Akazaki, H. Takayanagi, and T. Enoki. "Gate Control of Spin-Orbit Interaction in an Inverted $In_{0.53}Ga_{0.47}As/In_{0.52}Al_{0.48}As$ Heterostructure". In: *Physical Review Letters* 78 (7 1997), p. 1335. DOI: 10.1103/PhysRevLett.78.1335.

[184] M. Noro, M. Koshino, and T. Ando. "Theory of transport in graphene with long-range scatterers". In: *Journal of the Physical Society of Japan* 79.9 (2010), p. 094713. DOI: 10.1143/JPSJ.79.094713.

[185] P. Novelli, F. Taddei, A. K. Geim, and M. Polini. "Failure of Conductance Quantization in Two-Dimensional Topological Insulators due to Nonmagnetic Impurities". In: *Physical Review Letters* 122.1 (2019), p. 016601. DOI: 10.1103/physrevlett.122.016601.

[186] K. S. Novoselov, A. K. Geim, S. V. Morozov, D. Jiang, M. I. Katsnelson, I. V. Grigorieva, S. V. Dubonos, and A. A. Firsov. "Two-dimensional gas of massless Dirac fermions in graphene". In: *Nature* 438.7065 (2005), pp. 197–200. DOI: 10.1038/nature04233.

[187] K. S. Novoselov, A. K. Geim, S. V. Morozov, D. Jiang, Y. Zhang, S. V. Dubonos, I. V. Grigorieva, and A. A. Firsov. "Electric Field Effect in Atomically Thin Carbon Films". In: *Science* 306.5696 (2004), pp. 666–669. DOI: 10.1126/science.1102896.

[188] T. Oka and H. Aoki. "Photovoltaic Hall effect in graphene". In: *Physical Review B* 79.8 (2009), p. 081406. DOI: 10.1103/physrevb.79.081406.

[189] T. Oka and S. Kitamura. "Floquet Engineering of Quantum Materials". In: *Annual Review of Condensed Matter Physics* 10.introduction (2019), pp. 387–408. DOI: 10.1146/annurev-conmatphys-031218-013423.

[190] T. Okugawa, P. Tang, A. Rubio, and D. M. Kennes. "Topological phase transitions induced by disorder in magnetically doped $(Bi, Sb)_2Se_3$ thin films". In: *Physical Review B* 102.20 (2020), p. 201405. DOI: 10.1103/physrevb.102.201405.

[191] Y. Ominato and M. Koshino. "Quantum transport in a three-dimensional Weyl electron system". In: *Physical Review B* 89.5 (5 2014), p. 054202. DOI: 10.1103/PhysRevB.89.054202.

[192] Y. Onodera and Y. Toyozawa. "Persistence and amalgamation types in the electronic structure of mixed crystals". In: *Journal of the Physical Society of Japan* 24.2 (1968), p. 341. DOI: 10.1143/JPSJ.24.341.

[193] L. Ortiz, R. A. Molina, G. Platero, and A. M. Lunde. "Generic helical edge states due to Rashba spin-orbit coupling in a topological insulator". In: *Physical Review B* 93.20 (2016), p. 205431. DOI: 10.1103/PhysRevB.93.205431.

[194] P. M. Ostrovsky, I. V. Gornyi, and A. D. Mirlin. "Symmetries and weak localization and antilocalization of Dirac fermions in HgTe quantum wells". In: *Physical Review B* 86 (12 2012), p. 125323. DOI: 10.1103/PhysRevB.86.125323.

[195] Y. Ou et al. "Enhancing the Quantum Anomalous Hall Effect by Magnetic Codoping in a Topological Insulator". In: *Advanced Materials* 30.1 (2017), p. 1703062. DOI: 10.1002/adma.201703062.

[196] J. J. Palacios, J. Fernández-Rossier, and L. Brey. "Vacancy-induced magnetism in graphene and graphene ribbons". In: *Physical Review B* 77.19 (2008), p. 195428. DOI: 10.1103/physrevb.77.195428.

[197] H. Pan, M. Wu, Y. Liu, and S. A. Yang. "Electric control of topological phase transitions in Dirac semimetal thin films". In: *Scientific Reports* 5.1 (2015), p. 14639. DOI: 10.1038/srep14639.

[198] S. T. Park. "Interference in Floquet-Volkov transitions". In: *Physical Review A* 90.1 (2014), p. 013420. DOI: 10.1103/physreva.90.013420.

[199] V. M. Pereira, J. M. B. Lopes dos Santos, and A. H. Castro Neto. "Modeling disorder in graphene". In: *Physical Review B* 77.11 (11 2008), p. 115109. DOI: 10.1103/PhysRevB.77.115109.

[200] D. A. Pesin, E. G. Mishchenko, and A. Levchenko. "Density of states and magnetotransport in Weyl semimetals with long-range disorder". In: *Physical Review B* 92.17 (2015), p. 174202. DOI: 10.1103/PhysRevB.92.174202.

[201] L. A. Ponomarenko et al. "Cloning of Dirac fermions in graphene superlattices". In: *Nature* 497.7451 (2013), pp. 594–597. DOI: 10.1038/nature12187.

[202] A. C. Potter, I. Kimchi, and A. Vishwanath. "Quantum oscillations from surface Fermi arcs in Weyl and Dirac semimetals". In: *Nature Communications* 5.1 (2014). DOI: 10.1038/ncomms6161.

[203] E. Prodan, T. L. Hughes, and B. A. Bernevig. "Entanglement Spectrum of a Disordered Topological Chern Insulator". In: *Physical Review Letters* 105.11 (2010), p. 115501. DOI: 10.1103/physrevlett.105.115501.

[204] X.-L. Qi, T. L. Hughes, and S.-C. Zhang. "Topological field theory of time-reversal invariant insulators". In: *Physical Review B* 78.19 (2008), p. 195424. DOI: 10.1103/physrevb.78.195424.

[205] X.-L. Qi, Y.-S. Wu, and S.-C. Zhang. "Topological quantization of the spin Hall effect in two-dimensional paramagnetic semiconductors". In: *Physical Review B* 74.8 (2006). Ferromagnetic moments interacting with band electrons through the SOC, p. 085308. DOI: 10.1103/physrevb.74.085308.

[206] X.-L. Qi and S.-C. Zhang. "Topological insulators and superconductors". In: *Reviews of Modern Physics* 83.4 (2011), pp. 1057–1110. DOI: 10.1103/revmodphys.83.1057.

[207] M. Raczkowski, R. Peters, T. T. Phùng, N. Takemori, F. F. Assaad, A. Honecker, and J. Vahedi. "Hubbard model on the honeycomb lattice: From static and dynamical mean-field theories to lattice quantum Monte Carlo simulations". In: *Physical Review B* 101.12 (2020), p. 125103. DOI: 10.1103/physrevb.101.125103.

[208] J. P. Reed, B. Uchoa, Y. I. Joe, Y. Gan, D. Casa, E. Fradkin, and P. Abbamonte. "The Effective Fine- Structure Constant of Freestanding Graphene Measured in Graphite". In: *Science* 330.6005 (2010), pp. 805–808. DOI: 10.1126/science.1190920.

[209] J. Reimann, K. Sumida, M. Kakoki, K. A. Kokh, O. E. Tereshchenko, A. Kimura, J. Güdde, and U. Höfer. "Ultrafast electron dynamics in a topological surface state observed in two-dimensional momentum space". In: *Scientific Reports* 13.1 (2023). DOI: 10.1038/s41598-023-32811-1.

[210] J. Reimann et al. "Subcycle observation of lightwave-driven Dirac currents in a topological surface band". In: *Nature* 562.7727 (2018), pp. 396–400. DOI: 10.1038/s41586-018-0544-x.

[211] S. P. Repetsky, I. G. Vyshyvana, R. M. Kruchinin S. P. Melnyk, and A. P. Polishchuk. "The energy spectrum and the electrical conductivity of graphene with substitution impurity". In: *Condensed Matter Physics* 23.1 (2020), p. 1370. DOI: 10.5488/CMP.23.13704.

[212] S. P. Repetsky, I. G. Vyshyvana, V. B. Kruchinin, and S. Bellucci. "Effect of impurities ordering in the electronic spectrum and conductivity of graphene". In: *Physics Letters A* 384.19 (2020), p. 126401. DOI: 10.1016/j.physleta.2020.126401.

[213] M. Ribeiro, S. R. Power, S. Roche, L. E. Hueso, and F. Casanova. "Scale-invariant large nonlocality in polycrystalline graphene". In: *Nature Communications* 8.1 (2017). DOI: 10.1038/s41467-017-02346-x.

[214] K. A. Ritter and J. W. Lyding. "The influence of edge structure on the electronic properties of graphene quantum dots and nanoribbons". In: *Nature Materials* 8.3 (2009), pp. 235–242. DOI: 10.1038/nmat2378.

[215] S. Roche, S. R. Power, B. K. Nikolić, J. H. García, and A.-P. Jauho. "Have mysterious topological valley currents been observed in graphene superlattices?" In: *Journal of Physics: Materials* 5.2 (2022), p. 021001. DOI: 10.1088/2515-7639/ac452a.

[216] G. Rohde, A. Hendel, A. Stange, K. Hanff, L.-P. Oloff, L. X. Yang, K. Rossnagel, and M. Bauer. "Time-resolved ARPES with sub-15 fs temporal and near Fourier-limited spectral resolution". In: *Review of Scientific Instruments* 87.10 (2016), p. 103102. DOI: 10.1063/1.4963668.

[217] R. J. P. Román et al. "Band gap measurements of monolayer h-BN and insights into carbon-related point defects". In: *2D Materials* 8.4 (2021), p. 044001. DOI: 10.1088/2053-1583/ac0d9c.

[218] H. Rostami and E. Cappelluti. "Impurity effects and bandgap closing in massive Dirac systems". In: *Physical Review B* 96.5 (5 2017), p. 054205. DOI: 10.1103/PhysRevB.96.054205.

[219] A. Roth, C. Brune, H. Buhmann, L. W. Molenkamp, J. Maciejko, X.-L. Qi, and S.-C. Zhang. "Nonlocal Transport in the Quantum Spin Hall State". In: *Science* 325.5938 (2009), pp. 294–297. DOI: 10.1126/science.1174736.

[220] D. G. Rothe and E. M. Hankiewicz. "Tunable polarization in a beam splitter based on two-dimensional topological insulators". In: *Physical Review B* 89 (3 2014), p. 035418. DOI: 10.1103/PhysRevB.89.035418.

[221] D. G. Rothe, R. W. Reinthaler, C.-X. Liu, L. W. Molenkamp, S.-C. Zhang, and E. M. Hankiewicz. "Fingerprint of different spin–orbit terms for spin transport in HgTe quantum wells". In: *New Journal of Physics* 12.6 (2010), p. 065012. DOI: 10.1088/1367-2630/12/6/065012.

[222] M. S. Rudner and N. H. Lindner. "Band structure engineering and non-equilibrium dynamics in Floquet topological insulators". In: *Nature Reviews Physics* 2.5 (2020), pp. 229–244. DOI: 10.1038/s42254-020-0170-z.

[223] S. Ryu, A. P. Schnyder, A. Furusaki, and A. W. W. Ludwig. "Topological insulators and superconductors: tenfold way and dimensional hierarchy". In: *New Journal of Physics* 12.6 (2010), p. 065010. DOI: 10.1088/1367-2630/12/6/065010.

[224] U. Rössler. "Defects, Disorder, and Localization". In: *Advanced Texts in Physics*. Springer Berlin Heidelberg, 2004, pp. 255–279. DOI: 10.1007/978-3-662-09940-7_9.

[225] C. K. Safeer, J. Ingla-Aynés, F. Herling, J. H. Garcia, M. Vila, N. Ontoso, M. R. Calvo, S. Roche, L. E. Hueso, and F. Casanova. "Room-Temperature Spin Hall Effect in Graphene/MoSsub2/sub van der Waals Heterostructures". In: *Nano Letters* 19.2 (2019), pp. 1074–1082. DOI: 10.1021/acs.nanolett.8b04368.

[226] C. K. Safeer, J. Ingla-Aynés, N. Ontoso, F. Herling, W. Yan, L. E. Hueso, and F. Casanova. "Spin Hall Effect in Bilayer Graphene Combined with an Insulator up to Room Temperature". In: *Nano Letters* 20.6 (2020), pp. 4573–4579. DOI: 10.1021/acs.nanolett.0c01428.

[227] J. Salvador-Sánchez et al. "Generation and control of non-local chiral currents in graphene superlattices by orbital Hall effect". In: (2022). DOI: 10.48550/ARXIV.2206.04565.

[228] I. Sánchez-Ramírez, Y. Baba, L. Chico, and F. Domínguez-Adame. "Impact of electron-electron interactions on the thermoelectric efficiency of graphene quantum point contacts". In: *Physical Review B* 106.4 (2022), p. 045129. DOI: 10.1103/physrevb.106.045129.

[229] B. Sbierski, K. A. Madsen, P. W. Brouwer, and C. Karrasch. "Quantitative analytical theory for disordered nodal points". In: *Physical Review B* 96.6 (2017), p. 064203. DOI: 10.1103/PhysRevB.96.064203.

[230] B. Sbierski, G. Pohl, E. J. Bergholtz, and P. W. Brouwer. "Quantum Transport of Disordered Weyl Semimetals at the Nodal Point". In: *Physical Review Letters* 113.2 (2 2014), p. 026602. DOI: 10.1103/PhysRevLett.113.026602.

[231] C. P. Schmid et al. "Tunable non-integer high-harmonic generation in a topological insulator". In: *Nature* 593.7859 (2021), pp. 385–390. DOI: 10.1038/s41586-021-03466-7.

[232] T. L. Schmidt, S. Rachel, F. von Oppen, and L. I. Glazman. "Inelastic Electron Backscattering in a Generic Helical Edge Channel". In: *Physical Review Letters* 108.15 (2012), p. 156402. DOI: 10.1103/physrevlett.108.156402.

[233] A. P. Schnyder, S. Ryu, A. Furusaki, and A. W. W. Ludwig. "Classification of topological insulators and superconductors in three spatial dimensions". In: *Physical Review B* 78.19 (2008), p. 195125. DOI: 10.1103/physrevb.78.195125.

[234] A. P. Schnyder, S. Ryu, A. Furusaki, A. W. W. Ludwig, V. Lebedev, and M. Feigel'man. "Classification of Topological Insulators and Superconductors". In: *AIP Conference Proceedings*. AIP, 2009. DOI: 10.1063/1.3149481.

[235] M Schultz, F Heinrichs, U Merkt, T. Colin, T Skauli, and S Løvold. "Rashba spin splitting in a gated HgTe quantum well". In: *Semiconductor Science and Technology* 11 (1999), p. 1168. DOI: 10.1088/0268-1242/11/8/009.

[236] T. Schumann, L. Galletti, D. Kealhofer, H. Kim, M. Goyal, and S. Stemmer. "Observation of the Quantum Hall Effect in Confined Films of the Three-Dimensional Dirac Semimetal Cd_3As_2". In: *Physical Review Letters* 120.1 (2018), p. 016801. DOI: 10.1103/physrevlett.120.016801.

[237] M. Schüler and S. Beaulieu. "Probing topological Floquet states in WSe_2 using circular dichroism in time- and angle-resolved photoemission spectroscopy". In: *Communications Physics* 5.1 (2022). DOI: 10.1038/s42005-022-00944-w.

[238] M. Schüler and M. A. Sentef. "Theory of subcycle time-resolved photoemission: Application to terahertz photodressing in graphene". In: *Journal of Electron Spectroscopy and Related Phenomena* 253 (2021), p. 147121. DOI: 10.1016/j.elspec.2021.147121.

[239] G. W. Semenoff. "Condensed-Matter Simulation of a Three -Dimensional Anomaly". In: *Physical Review Letters* 53.26 (1984), pp. 2449–2452. DOI: 10.1103/physrevlett.53.2449.

[240] M. Sentef, A. F. Kemper, B. Moritz, J. K. Freericks, Z.-X. Shen, and T. P. Devereaux. "Examining Electron-Boson Coupling Using Time-Resolved Spectroscopy". In: *Physical Review X* 3.4 (2013), p. 041033. DOI: 10.1103/physrevx.3.041033.

[241] M. Serlin, C. L. Tschirhart, H. Polshyn, Y. Zhang, J. Zhu, K. Watanabe, T. Taniguchi, L. Balents, and A. F. Young. "Intrinsic quantized anomalous Hall effect in a moiré heterostructure". In: *Science* 367.6480 (2020), pp. 900–903. DOI: 10.1126/science.aay5533.

[242] W.-Y. Shan, H.-Z. Lu, and S.-Q. Shen. "Effective continuous model for surface states and thin films of three-dimensional topological insulators". In: *New Journal of Physics* 12.4 (2010), p. 043048. DOI: 10.1088/1367-2630/12/4/043048.

[243] A. L. Sharpe, E. J. Fox, A. W. Barnard, J. Finney, K. Watanabe, T. Taniguchi, M. A. Kastner, and D. Goldhaber-Gordon. "Emergent ferromagnetism near three-quarters filling in twisted bilayer graphene". In: *Science* 365.6453 (2019), pp. 605–608. DOI: 10.1126/science.aaw3780.

[244] S.-Q. Shen, W.-Y. Shan, and H.-Z. Lu. "Topologial insulator and the Dirac equation". In: *SPIN* 01.01 (2011), pp. 33–44. DOI: 10.1142/s2010324711000057.

[245] S.-Q. Shen. *Topological Insulators*. Vol. 187. Springer Series in Solid-State Sciences. Singapore: Springer, 2017, p. 266. DOI: 10.1007/978-981-10-4606-3.

[246] D. N. Sheng, Z. Y. Weng, L. Sheng, and F. D. M. Haldane. "Quantum Spin-Hall Effect and Topologically Invariant Chern Numbers". In: *Physical Review Letters* 97.3 (2006), p. 036808. DOI: 10.1103/physrevlett.97.036808.

[247] M. Shiranzaei, F. Parhizgar, J. Fransson, and H. Cheraghchi. "Impurity scattering on the surface of topological-insulator thin films". In: *Physical Review B* 95.23 (2017), p. 235429. DOI: 10.1103/PhysRevB.95.235429.

[248] J. H. Shirley. "Solution of the Schrödinger Equation with a Hamiltonian Periodic in Time". In: *Physical Review* 138.4B (1965), B979–B987. DOI: 10.1103/physrev.138.b979.

[249] N. H. Shon and T. Ando. "Quantum transport in 2D graphite system". In: *Journal of the Physical Society of Japan* 67.7 (1998), p. 2421. DOI: 10.1143/JPSJ.67.2421.

[250] C. Sias, H. Lignier, Y. P. Singh, A. Zenesini, D. Ciampini, O. Morsch, and E. Arimondo. "Observation of Photon-Assisted Tunneling in Optical Lattices". In: *Physical Review Letters* 100.4 (2008), p. 040404. DOI: 10.1103/physrevlett.100.040404.

[251] P. R. Sievert and M. L. Glasser. "Interband Effects in the Coherent-Potential Approximation. I". In: *Physical Review B* 7.4 (1973), p. 1265. DOI: 10.1103/PhysRevB.7.1265.

[252] Y. V. Skrypnyk and V. M. Loktev. "Electronic properties of graphene with point defects". In: *Low Temperature Physics* 44.12 (2018), p. 1112. DOI: 10.1063/10.0000565.

[253] F. Sols. "Recursive Tight-Binding Green's Function Method: Application to Ballistic and Dissipative Transport in Semiconductor Nanostructures". In: *Quantum Transport in Ultrasmall Devices*. Springer US, 1995, pp. 329–338. DOI: 10.1007/978-1-4615-1967-6_16.

[254] A. A. Soluyanov and D. Vanderbilt. "Computing topological invariants without inversion symmetry". In: *Physical Review B* 83.23 (2011), p. 235401. DOI: 10.1103/physrevb.83.235401.

[255] J. C. W. Song, A. V. Shytov, and L. S. Levitov. "Electron Interactions and Gap Opening in Graphene Superlattices". In: *Physical Review Letters* 111.26 (2013), p. 266801. DOI: 10.1103/physrevlett.111.266801.

[256] P. Soven. "Coherent-potential model of substitutional disordered alloys". In: *Physical Review* 156.3 (1967), p. 809. DOI: 10.1103/PhysRev.156.809.

[257] P. V. Sriluckshmy, K. Saha, and R. Moessner. "Interplay between topology and disorder in a two-dimensional semi-Dirac material". In: *Physical Review B* 97.2 (2018), p. 024204. DOI: 10.1103/PhysRevB.97.024204.

[258] T. Stauber, N. M. R. Peres, and A. H. Castro Neto. "Conductivity of suspended and non-suspended graphene at finite gate voltage". In: *Physical Review B* 78.8 (2008), p. 085418. DOI: 10.1103/PhysRevB.78.085418.

[259] J. A. Steinberg, S. M. Young, S. Zaheer, C. L. Kane, E. J. Mele, and A. M. Rappe. "Bulk Dirac Points in Distorted Spinels". In: *Physical Review Letters* 112.3 (2014), p. 036403. DOI: 10.1103/PhysRevLett.112.036403.

[260] Y. Tanaka, A. Furusaki, and K. A. Matveev. "Conductance of a Helical Edge Liquid Coupled to a Magnetic Impurity". In: *Physical Review Letters* 106.23 (2011), p. 236402. DOI: 10.1103/physrevlett.106.236402.

[261] D. W. Taylor. "Vibrational properties of imperfect crystals with large defect concentrations". In: *Physical Review* 156.3 (1967), p. 1017. DOI: 10.1103/PhysRev.156.1017.

[262] D. J. Thouless. "Quantization of particle transport". In: *Physical Review B* 27.10 (1983), pp. 6083–6087. DOI: 10.1103/physrevb.27.6083.

[263] D. J. Thouless and S Kirkpatrick. "Conductivity of the disordered linear chain". In: *Journal of Physics C: Solid State Physics* 14.3 (1981), pp. 235–245. DOI: 10.1088/0022-3719/14/3/007.

[264] D. J. Thouless, M. Kohmoto, M. P. Nightingale, and M. den Nijs. "Quantized Hall Conductance in a Two-Dimensional Periodic Potential". In: *Physical Review Letters* 49.6 (1982), pp. 405–408. DOI: 10.1103/physrevlett.49.405.

[265] Y. Tokura, K. Yasuda, and A. Tsukazaki. "Magnetic topological insulators". In: *Nature Reviews Physics* 1.2 (2019), pp. 126–143. DOI: 10.1038/s42254-018-0011-5.

[266] L. E. F. F. Torres, S. Roche, and J.-C. Charlier. *Introduction to Graphene-Based Nanomaterials*. Cambridge University Press, 2014. DOI: 10.1017/cbo9781139344364.

[267] P. E. Trevisanutto, C. Giorgetti, L. Reining, M. Ladisa, and V. Olevano. "*Ab Initio GW* Many-Body Effects in Graphene". In: *Physical Review Letters* 101.22 (2008), p. 226405. DOI: 10.1103/physrevlett.101.226405.

[268] D. C. Tsui, H. L. Stormer, and A. C. Gossard. "Two-Dimensional Magnetotransport in the Extreme Quantum Limit". In: *Physical Review Letters* 48.22 (1982), pp. 1559–1562. DOI: 10.1103/physrevlett.48.1559.

[269] D. V. Tuan, J. Marmolejo-Tejada, X. Waintal, B. Nikolić, S. Valenzuela, and S. Roche. "Spin Hall Effect and Origins of Nonlocal Resistance in Adatom-Decorated Graphene". In: *Physical Review Letters* 117.17 (2016), p. 176602. DOI: 10.1103/physrevlett.117.176602.

[270] A. M. Turner and A. Vishwanath. "Beyond band insulators: Topology of semimetals and interacting phases". In: *Contemporary Concepts of Condensed Matter Science*. Vol. 6. Elsevier, 2013, pp. 293–324. DOI: 10.1016/B978-0-444-63314-9.00011-1.

[271] K. Uchida, S. Kusaba, K. Nagai, T. N. Ikeda, and K. Tanaka. "Diabatic and adiabatic transitions between Floquet states imprinted in coherent exciton emission in monolayer WSe_2". In: *Science Advances* 8.51 (2022). DOI: 10.1126/sciadv.abq7281.

[272] M. Uchida et al. "Quantum Hall states observed in thin films of Dirac semimetal Cd_3As_2". In: *Nature Communications* 8.1 (2017). DOI: 10.1038/s41467-017-02423-1.

[273] G. S. Uhrig, M. H. Kalthoff, and J. K. Freericks. "Positivity of the Spectral Densities of Retarded Floquet Green Functions". In: *Physical Review Letters* 122.13 (2019), p. 130604. DOI: 10.1103/physrevlett.122.130604.

[274] G. Usaj, P. M. Perez-Piskunow, L. E. F. Foa Torres, and C. A. Balseiro. "Irradiated graphene as a tunable Floquet topological insulator". In: *Physical Review B* 90 (11 2014), p. 115423. DOI: 10.1103/PhysRevB.90.115423.

[275] D. Vanderbilt. *Berry Phases in Electronic Structure Theory*. Cambridge University Press, 2018. DOI: 10.1017/9781316662205.

[276] B. Velický. "Theory of electronic transport in disordered binary alloys: Coherent-potential approximation". In: *Physical Review* 184.3 (1969), p. 614. DOI: 10.1103/PhysRev.184.614.

[277] J. A. Vergés, F. Guinea, and E. Louis. "Unrestricted Hartree-Fock study of the two-band Hamiltonian in doped CuO_2 planes". In: *Physical Review B* 46.6 (1992), pp. 3562–3572. DOI: 10.1103/physrevb.46.3562.

[278] J. A. Vergés, E. Louis, P. S. Lomdahl, F. Guinea, and A. R. Bishop. "Holes and magnetic textures in the two-dimensional Hubbard model". In: *Physical Review B* 43.7 (1991), pp. 6099–6108. DOI: 10.1103/physrevb.43.6099.

[279] K. Wakabayashi, K. ichi Sasaki, T. Nakanishi, and T. Enoki. "Electronic states of graphene nanoribbons and analytical solutions". In: *Science and Technology of Advanced Materials* 11.5 (2010), p. 054504. DOI: 10.1088/1468-6996/11/5/054504.

[280] P. R. Wallace. "The Band Theory of Graphite". In: *Physical Review* 71.9 (1947), pp. 622–634. DOI: 10.1103/physrev.71.622.

[281] J. Wang, B. Lian, H. Zhang, Y. Xu, and S.-C. Zhang. "Quantum Anomalous Hall Effect with Higher Plateaus". In: *Physical Review Letters* 111.13 (2013), p. 136801. DOI: 10.1103/physrevlett.111.136801.

[282] J. Wang, B. Lian, and S.-C. Zhang. "Electrically Tunable Magnetism in Magnetic Topological Insulators". In: *Physical Review Letters* 115.3 (2015), p. 036805. DOI: 10.1103/physrevlett.115.036805.

[283] Q.-Z. Wang, X. Liu, H.-J. Zhang, N. Samarth, S.-C. Zhang, and C.-X. Liu. "Quantum Anomalous Hall Effect in Magnetically Doped InAs/GaSb Quantum Wells". In: *Physical Review Letters* 113.14 (2014), p. 147201. DOI: 10.1103/physrevlett.113.147201.

[284] Y. H. Wang, H. Steinberg, P. Jarillo-Herrero, and N. Gedik. "Observation of Floquet-Bloch States on the Surface of a Topological Insulator". In: *Science* 342.6157 (2013), pp. 453–457. DOI: 10.1126/science.1239834.

[285] Y.-X. Wang and F. Li. "High Chern number phase in topological insulator multilayer structures". In: *Physical Review B* 104.3 (2021), p. 035202. DOI: 10.1103/physrevb.104.035202.

[286] Z. Wang, H. Weng, Q. Wu, X. Dai, and Z. Fang. "Three-dimensional Dirac semimetal and quantum transport in Cd_3As_2". In: *Physical Review B* 88.12 (2013), p. 125427. DOI: 10.1103/PhysRevB.88.125427.

[287] Z. Wang, Y. Sun, X. Q. Chen, C. Franchini, G. Xu, H. Weng, X. Dai, and Z. Fang. "Dirac semimetal and topological phase transitions in A_3Bi (A=Na, K, Rb)". In: *Physical Review B* 85.19 (2012), p. 195320. DOI: 10.1103/PhysRevB.85.195320.

[288] Z. Wang et al. “Composite super-moiré lattices in double-aligned graphene heterostructures”. In: *Science Advances* 5.12 (2019). DOI: 10.1126/sciadv.aay8897.

[289] K. Watanabe, T. Taniguchi, and H. Kanda. “Direct-bandgap properties and evidence for ultraviolet lasing of hexagonal boron nitride single crystal”. In: *Nature Materials* 3.6 (2004), pp. 404–409. DOI: 10.1038/nmat1134.

[290] P. Weinberger. *Electron scattering theory for ordered and disordered matter*. Oxford: Clarendon Press, 1990.

[291] H. Weng, R. Yu, X. Hu, X. Dai, and Z. Fang. “Quantum anomalous Hall effect and related topological electronic states”. In: *Advances in Physics* 64.3 (2015), pp. 227–282. DOI: 10.1080/00018732.2015.1068524.

[292] J. Wilhelm, P. Grössing, A. Seith, J. Crewse, M. Nitsch, L. Weigl, C. Schmid, and F. Evers. “Semiconductor Bloch-equations formalism: Derivation and application to high-harmonic generation from Dirac fermions”. In: *Physical Review B* 103.12 (2021), p. 125419. DOI: 10.1103/physrevb.103.125419.

[293] R. Winkler. “Rashba spin splitting in two-dimensional electron and hole systems”. In: *Physical Review B* 62 (7 2000), p. 4245. DOI: 10.1103/PhysRevB.62.4245.

[294] R. Winkler. *Spin-Orbit Coupling Effects in Two-Dimensional Electron and Hole Systems*. Springer Berlin Heidelberg, 2003. DOI: 10.1007/b13586.

[295] C. Wu, B. A. Bernevig, and S.-C. Zhang. “Helical Liquid and the Edge of Quantum Spin Hall Systems”. In: *Physical Review Letters* 96.10 (2006), p. 106401. DOI: 10.1103/physrevlett.96.106401.

[296] S. Wu, V. Fatemi, Q. D. Gibson, K. Watanabe, T. Taniguchi, R. J. Cava, and P. Jarillo-Herrero. “Observation of the quantum spin Hall effect up to 100 kelvin in a monolayer crystal”. In: *Science* 359.6371 (2018), pp. 76–79. DOI: 10.1126/science.aan6003.

[297] S. Wu, L. Jing, Q. Li, Q. W. Shi, J. Chen, H. Su, X. Wang, and J. Yang. “Average density of states in disordered graphene systems”. In: *Physical Review B* 77.19 (2008), p. 195411. DOI: 10.1103/PhysRevB.77.195411.

[298] Y. Xia et al. “Observation of a large-gap topological-insulator class with a single Dirac cone on the surface”. In: *Nature Physics* 5.6 (2009), pp. 398–402. DOI: 10.1038/nphys1274.

[299] D. Xiao, M.-C. Chang, and Q. Niu. "Berry phase effects on electronic properties". In: *Reviews of Modern Physics* 82.3 (2010), pp. 1959–2007. DOI: 10.1103/revmodphys.82.1959.

[300] D. Xiao, W. Yao, and Q. Niu. "Valley-Contrasting Physics in Graphene: Magnetic Moment and Topological Transport". In: *Physical Review Letters* 99.23 (2007), p. 236809. DOI: 10.1103/physrevlett.99.236809.

[301] C. Xu and J. E. Moore. "Stability of the quantum spin Hall effect: Effects of interactions, disorder, and $\mathbb{Z}_2$ topology". In: *Physical Review B* 73.4 (2006), p. 045322. DOI: 10.1103/physrevb.73.045322.

[302] S.-Y. Xu et al. "Observation of Fermi arc surface states in a topological metal". In: *Science* 347.6219 (2015), p. 294. DOI: 10.1126/science.1256742.

[303] J. Xue, J. Sanchez-Yamagishi, D. Bulmash, P. Jacquod, A. Deshpande, K. Watanabe, T. Taniguchi, P. Jarillo-Herrero, and B. J. LeRoy. "Scanning tunnelling microscopy and spectroscopy of ultra-flat graphene on hexagonal boron nitride". In: *Nature Materials* 10.4 (2011), pp. 282–285. DOI: 10.1038/nmat2968.

[304] M. Yankowitz, J. Xue, D. Cormode, J. D. Sanchez-Yamagishi, K. Watanabe, T. Taniguchi, P. Jarillo-Herrero, P. Jacquod, and B. J. LeRoy. "Emergence of superlattice Dirac points in graphene on hexagonal boron nitride". In: *Nature Physics* 8.5 (2012), pp. 382–386. DOI: 10.1038/nphys2272.

[305] Y. Yao, F. Ye, X.-L. Qi, S.-C. Zhang, and Z. Fang. "Spin-orbit gap of graphene: First-principles calculations". In: *Physical Review B* 75.4 (2007), p. 041401. DOI: 10.1103/physrevb.75.041401.

[306] A. F. Young, J. D. Sanchez-Yamagishi, B. Hunt, S. H. Choi, K. Watanabe, T. Taniguchi, R. C. Ashoori, and P. Jarillo-Herrero. "Tunable symmetry breaking and helical edge transport in a graphene quantum spin Hall state". In: *Nature* 505.7484 (2013), pp. 528–532. DOI: 10.1038/nature12800.

[307] S. M. Young, S. Zaheer, J. C. Y. Teo, C. L. Kane, E. J. Mele, and A. M. Rappe. "Dirac semimetal in three dimensions". In: *Physical Review Letters* 108.14 (2012), p. 140405. DOI: 10.1103/PhysRevLett.108.140405.

[308] R. Yu, W. Zhang, H.-J. Zhang, S.-C. Zhang, X. Dai, and Z. Fang. "Quantized Anomalous Hall Effect in Magnetic Topological Insulators". In: *Science* 329.5987 (2010), pp. 61–64. DOI: 10.1126/science.1187485.

[309] C. Zhang, Y. Zhang, H.-Z. Lu, X. C. Xie, and F. Xiu. "Cycling Fermi arc electrons with Weyl orbits". In: *Nature Reviews Physics* 3.9 (2021), pp. 660–670. DOI: 10.1038/s42254-021-00344-z.

[310] C. Zhang et al. "Evolution of Weyl orbit and quantum Hall effect in Dirac semimetal Cd_3As_2". In: *Nature Communications* 8.1 (2017). DOI: 10.1038/s41467-017-01438-y.

[311] C. Zhang et al. "Quantum Hall effect based on Weyl orbits in Cd_3As_2". In: *Nature* 565.7739 (2019), pp. 331–336. DOI: 10.1038/s41586-018-0798-3.

[312] F. Zhang, C. L. Kane, and E. J. Mele. "Surface states of topological insulators". In: *Physical Review B* 86.8 (2012), p. 081303. DOI: 10.1103/physrevb.86.081303.

[313] H. Zhang, C.-X. Liu, X.-L. Qi, X. Dai, Z. Fang, and S.-C. Zhang. "Topological insulators in Bi2Se3, Bi2Te3 and Sb2Te3 with a single Dirac cone on the surface". In: *Nature Physics* 5.6 (2009), pp. 438–442. DOI: 10.1038/nphys1270.

[314] J. Zhang et al. "Topology-Driven Magnetic Quantum Phase Transition in Topological Insulators". In: *Science* 339.6127 (2013), pp. 1582–1586. DOI: 10.1126/science.1230905.

[315] T. Zhang, J. Ha, N. Levy, Y. Kuk, and J. Stroscio. "Electric-Field Tuning of the Surface Band Structure of Topological Insulator Sb_2Te_3 Thin Films". In: *Physical Review Letters* 111 (5 2013), p. 056803. DOI: 10.1103/PhysRevLett.111.056803.

[316] Y. Zhang, D. Bulmash, P. Hosur, A. C. Potter, and A. Vishwanath. "Quantum oscillations from generic surface Fermi arcs and bulk chiral modes in Weyl semimetals". In: *Scientific Reports* 6.1 (2016). DOI: 10.1038/srep23741.

[317] Y. Zhang, Y.-W. Tan, H. L. Stormer, and P. Kim. "Experimental observation of the quantum Hall effect and Berry's phase in graphene". In: *Nature* 438.7065 (2005), pp. 201–204. DOI: 10.1038/nature04235.

[318] Z.-Q. Zhang, C.-Z. Chen, Y. Wu, H. Jiang, J. Liu, Q. feng Sun, and X. C. Xie. "Chiral interface states and related quantized transport in disordered Chern insulators". In: *Physical Review B* 103.7 (2021), p. 075434. DOI: 10.1103/physrevb.103.075434.

[319] Y.-F. Zhao et al. "Tuning the Chern number in quantum anomalous Hall insulators". In: *Nature* 588.7838 (2020), pp. 419–423. DOI: 10.1038/s41586-020-3020-3.

[320] Y. Zhou and M. W. Wu. "Optical response of graphene under intense terahertz fields". In: *Physical Review B* 83.24 (2011), p. 245436. DOI: 10.1103/physrevb.83.245436.

[321] M. R. Zirnbauer. "Riemannian symmetric superspaces and their origin in random-matrix theory". In: *Journal of Mathematical Physics* 37.10 (1996), pp. 4986–5018. DOI: 10.1063/1.531675.

[322] E. de Prunelé. "Solvable model for three-dimensional quantum scattering of a particle off several separable interactions centred at n arbitrary points". In: *Journal of Physics A: Mathematical and General* 30.22 (1997), p. 7831. DOI: 10.1088/0305-4470/30/22/021.